DIPARTIMENTO SCIENZE DELLA VITA

DOTTORATO DI RICERCA IN SCIENZE DELLA VITA

CICLO XXXIV

COORDINATORE Prof. Massimo Valoti

DESIGN AND OPTIMIZATION OF A COMPUTER-ASSISTED TOOL FOR ERYTHROCYTE PHENOTYPING: IN SEARCH OF A NEW BIOMARKER FOR AUTISM SPECTRUM DISORDERS

SETTORE SCIENTIFICO-DISCIPLINARE: BIO/06

TUTOR: Prof. Pietro Lupetti

DOTTORANDA: Dr.ssa Paola Petrone

CO-RELATORI:

Dott. Alessandro Barducci
(I.C.S. srl)

Dott. Claudio De Felice
(Azienda Ospedaliera Universitaria Senese)

Dott. Eugenio Paccagnini

A.A. 2021-2022

To my grandmothers Dina and Teresa,
my grandfather Vincenzo
and my aunt Anna Teresa.

ABSTRACT

The morphology of a red blood cell (RBC) in physiological conditions (discocyte) is of primary importance for its main physiological role (i.e., the transport of respiratory gases to and from the tissues). The erythrocyte membrane-cortical cytoskeleton-complex structure, ensuring both shape resilience and marked physiological deformability, also allows erythrocytes to undergo peculiar shape changes, from spherical globes (spherocytes), concave shapes (stomatocytes), cells provided with spines (echinocytes) or with a central crest (knizocytes). Several pathological conditions are associated with characteristic RBC shape alterations. For instance, typical thorny red cells (acanthocytes) are prevalent in neuroacanthocytosis, a group of rare genetic diseases; hereditary spherocytosis, elliptocytosis, and stomatocytosis are RBC disorders resulting from mutations in genes encoding various membrane and skeletal proteins; codocytes are a common occurrence in beta-thalassemia. Furthermore, aberrant erythrocytic shapes are observed in renal and liver disease, and in case of hemoglobinopathies and toxemias. Leptocytes, as well as other abnormal erythrocyte shapes, are reported in patients diagnosed with Rett syndrome, an X-linked genetically determined neurodevelopmental disorder. Abnormal RBC shapes have been described also in patients diagnosed with autism spectrum disorders (ASD). ASD represent a complex set of neurodevelopmental disorders, characterized by social and behavioral impairments. These disorders have a prevalent genetic etiology; however, epigenetically acting environmental factors (e.g., immune dysregulation, pollutants) seem to play a key role in the development of the disease. This condition is associated with a high social impact and strong suggestions of a dramatically rising prevalence in the general pediatric population over the last decades.

In the present thesis work, we started to investigate the potential value of the RBC shape as a biomarker candidate for an early ASD diagnosis, illustrating and discussing the results achieved so far within this broad research project. One of these results is the optimization of a new protocol, based on the acupuncture method, for blood samples preparation aimed at SEM (Scanning Electron Microscopy) morphological analysis of RBC. Indeed, to reach the final research goal it is necessary to carry out many bloods drawn from young children in a practical way. The novel preparation and imaging method, both minimally invasive and cheap, consists in aspirating by a capillary tube (preloaded with anticoagulant solution) a drop of peripheral blood obtained from a prick in a human subject's fingertip. Samples are subsequently processed by *ad hoc* protocols and imaged at SEM. Another goal successfully achieved through this work is the favorable opinion and approval from local ethics committee. Preliminary results from blood samples analysis at SEM confirm the presence

of morphologically abnormal erythrocytes in ASD patients in a greater extent than in healthy volunteers. Nevertheless, given the small sample size searched to date, more accurate information and a high caseload of subjects are still needed.

The last and most consistent part of this thesis work illustrates development and validation of a new computer-assisted tool for erythrocyte phenotyping in SEM micrographs. Indeed, achieving our final research goal involves the analysis of many blood samples, each of which needing a time-consuming manual search, count and classification of a large number of RBC. In this context a software capable to semi-automatically associate a distribution of erythrocytes among the relevant morphological classes to each examined patient would represent a powerful tool towards a more rapid and reproducible analysis of RBC morphology. Furthermore, observations from studying of intra-operator variability of the manual RBC morphological analysis by SEM carried out in this thesis work suggest the need of a high number of replicate counts, supporting the key relevance of implementing reliable computer-assisted algorithms and machine learning systems for our research project. Our own software, developed using Microsoft Visual Studio 2010 as a working environment and the C^{++} language as a programming language, has shown to be able to detect RBC in SEM micrographs and to intercept erythrocyte morphological categories, albeit with different degrees of efficiency. This new software represents a promising and powerful tool with many potential applications, from early ASD diagnostic to basic research in hematology.

This thesis work presents the initial phases of an ambitious research project about erythrocyte morphological changes in pediatric ASD patients, laying solid foundations for its continuation. Indeed, further investigations are needed to establish the statistical significance of the differences about erythrocyte morphological alterations in blood micro-samples from ASD patients and neurotypical controls. Moreover, our work will continue validating the data - obtained by our software - about the distribution of erythrocytes among several morphometric classes in SEM micrographs from peripheral blood samples. These aspects are of seminal importance in the research aimed at discovering potential novel biomarkers for ASD diagnosis based on the SEM analysis of peripheral blood micro-samples.

ABBREVIATIONS

ADOS: Autism Diagnostic Observation Schedule

AFM: Atomic Force Microscopy

ANOVA: Analysis of Variance

ASD: Autism Spectrum Disorders

CARS2: Childhood Autism Rating Scale, Second edition

CDC: Centers for Disease Control and Prevention

CHT: Circular Hough Transform

CSV: Comma-Separated Values

DIC: Differential Interference Contrast

DNA: DeoxyriboNucleic Acid

DSM-V: Diagnostic and Statistical Manual of Mental Disorders, fifth edition

FN: False Negatives

FP: False Positives

G6PD: Glucose-6-Phosphate Dehydrogenase

HDL: High-Density Lipoprotein

HFA: High Functioning Autism

IQ: Intelligence Quotient

LFA: Low Functioning Autism

MeCP2: X-linked methyl-CpG-binding protein 2 gene

MFA: Medium Functioning Autism

MLP: Multi-Layer Perceptron

NADPH: reduced Nicotinamide Adenine Dinucleotide Phosphate

PUFA: Polyunsaturated Fatty Acids

RBC: Red Blood Cell/Red Blood Cells

RGB: Red, Green, Blue

RNA: RiboNucleic Acid

ROS: Reactive Oxygen Species

RTT: Rett syndrome

SD: Standard Deviation

SEM: Scanning Electron Microscopy

SVM: Support-Vector Machines

TP: True Positive

INDEX

1. INTRODUCTION

1.1. Erythrocyte morphology and related analysis techniques

Erythrocytes are unique anuclear cells, with their cytoplasm consisting of 95% hemoglobin (Buys et al., 2013). Under physiological conditions, a normal human red blood cell (RBC) assumes a biconcave disc shape (discocyte). In general, there is a close relationship between cell shape and its function: muscle fibers are somewhat elongated in order to perform contraction; neurons have a strongly branched structure to be able to receive (through the dendrites) impulses, which come from other neurons or are produced by environmental stimuli. Very often changes in cell morphology are signals of an altered ability of the cell, or the tissue of which it is part, to carry out its physiological functions. Erythrocytes are no exception, as the retention of their disc-shape is of primary importance for their main physiological role (e.g. transport of respiratory gases to and from tissues; Ciccoli et al., 2013; Pierre, 2002). Changes in morphology, mechanical features or integrity of erythrocyte have implications on correct functioning of the cell, as it can be observed in several dysfunctional erythrocyte states (Buys et al., 2013). In particular, the study of erythrocyte morphology assumes critical importance in the field of rheology. In fact, considerable evidence indicates that erythrocytes shape is directly related to their deformability, with a critical influence on rheological properties of blood (Ciccoli et al., 2012; Simpson, 1989; Vromen and McCane, 2009). For example, in the case of sickle cell anemia, sickle-shaped erythrocytes are found, which are rigid and cause dramatic changes in viscosity and rheological properties of the blood. These cells within the circulation block the blood flow in thin capillaries, causing stasis and poor oxygen supply to the tissues, and finally painful abdominal crises, splenic or cerebral infarcts and kidney damage (Bessis, 1974).

1.1.1. Erythrocyte membrane

The peculiarities of the erythrocyte plasma membrane allow the cell to have an extended surface area for gas exchanges. In order to be able to pass through small capillaries (some of which with a cross section 1/3 of erythrocyte's diameter) and to be able to withstand high shear stresses, erythrocyte membrane must be highly deformable and robust at the same time (Bolotta et al., 2018a; Buys et al., 2013). Erythrocyte membrane consists of an asymmetrical phospholipid bilayer, supported by an underlying cytoskeleton complex, which is responsible for the unusual features of erythrocyte's plasma membrane (Bolotta et al., 2018a; Buys et al., 2013). In the erythrocyte membrane cytoskeleton, vertical and horizontal interactions are established between cytoskeletal

proteins, integral membrane proteins and phospholipid bilayer; the integrity of erythrocyte membrane is based on these interactions. Vertical linkages are based on spectrin, ankyrin, and band 3 protein, and on spectrin, protein 4.1 and glycophorin. These interactions also include the spectrin - ankyrin - Rh multiprotein complex association and the weak interactions between skeletal proteins and negatively charged lipids of membrane phospholipid bilayer's inner layer. Instead, horizontal interactions are based mainly on spectrin, protein 4.1 and actin (Ciccoli et al., 2013; Cortelazzo et al., 2015; Fig. 1.1). The plasma membrane, together with its cytoskeletal support, is considered to be responsible for maintaining cell shape and stability and for possibility of large deformations when necessary (Buys et al., 2013).

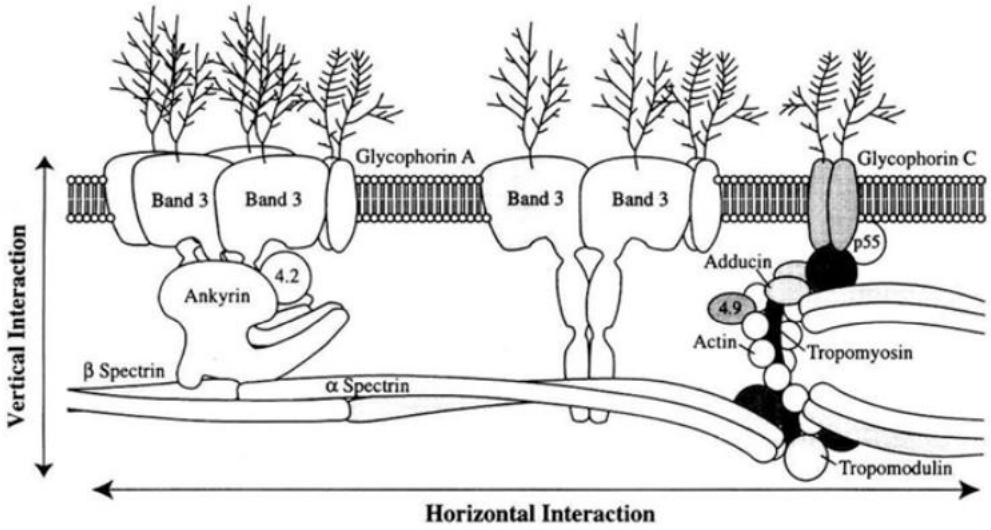

Figure 1.1 - Cytoskeletal proteins of red blood cells (Gallagher, 2005).

Abnormalities of the erythrocyte membrane are related to inherited hemolytic anemias. In *hereditary spherocytosis* syndromes (characterized by the presence of spherical-shaped erythrocytes), in *hereditary elliptocytosis* (characterized by the presence of elliptical, cigar-shaped erythrocytes on peripheral blood smear) and in *hereditary pyropoikilocytosis* (characterized by erythrocyte morphology reminiscent of that seen in patients after a thermal burn) there is a mechanical weakness or fragility due to defects in proteins of the erythrocyte membrane. In hereditary spherocytosis, destruction of abnormal erythrocytes in the spleen is the principal cause of hemolysis. As it regards hereditary elliptocytosis, erythrocyte life span is decreased in a subset of patients: in this case, patients experience hemolysis, anemia, splenomegaly and intermittent jaundice. In *hereditary stomatocytosis* syndromes (characterized by erythrocytes with a mouth-shaped area of central pallor on peripheral blood smear) there are abnormalities in red cell cation permeability leading to changes in red cell volume. Patients can experience hemolysis and anemia, along with predisposition to thrombosis after splenectomy (Gallagher, 2005).

The bulk of evidence on the existence of a close correlation between erythrocyte morphology and their function justifies the development and use of several techniques for the morphological study of RBC. Morphological data regarding erythrocytes are of crucial importance in basic research on cell biology, as well as for translational research and medical diagnostics.

1.1.2. Automated hematological analyzers

Automated analyzer peripheral blood counts provide accurate and precise RBC counts and red cell indices, information on RBC population distribution, size and haemoglobin content (Palmer et al., 2015). Technologies used by hematology flow analyzers can be traced back to two fundamental principles: the impedance principle and the optical or light scattering principle (Buttarello, 2016). The impedance principle is based on detecting the increase in electrical resistance produced by the passage of a cell through a hole filled with high conductivity liquid. The change in resistance is - in a first approximation - directly proportional to the cell volume (Kubitschek, 1960). In optical methods, the suspended cells are introduced in sequence through a flow cell where they are intercepted by a suitably focused light beam. The interaction between the light beam and the cell determines the dispersion of light in all directions. This light is collected by one or more detectors (photodiodes or photomultipliers) positioned at well-defined angles. The amount of light measured in the "forward" direction mainly depends on the cell size, while in the "side" direction it mainly depends on the refractive index and on the level of cell's structural complexity (Brunsting and Mullaney, 1972; Mullaney and Dean, 1969; Salzman et al., 1975).

1.1.3. Light microscopy

Despite the advances in technology of automated hematology analyzers, specialized flow cytometry, molecular diagnostic, cytogenetics, and chemical studies of the blood cells, the use of conventional microscopy still forms the basis of the morphologic evaluation of erythrocytes (Pierre, 2002; Yturralde et al., 2020). In patients with anemia, or other diseases with abnormal erythrocytes, the peripheral smear permits interpretation of diagnostically significant RBC findings. These include assessment of RBC shape, size, color, inclusions, and arrangement (Ford, 2013). According to the Rümke table distribution, a minimum of 1000 RBC should be evaluated to provide a precise percentage of the cells having a particular morphological abnormality (Palmer et al., 2015). Commonly, in laboratory hematology diagnostics, peripheral blood smears are dried and then stained with Giemsa and May-Grunwald solutions. In this case, normal erythrocytes examined in the center

of a smear appear isolated from each other, about 7.5-8 μm in diameter, round or slightly oval in shape, dark pink on the outside and gradually fading towards the center (the area of central pallor occupying approximately the middle third of the cell; Palmer et al., 2015). The preparations can also be set up for *in vivo* observation, for example with the interference contrast technique (also known as Differential Interference Contrast, DIC). This method is based on the interference of two light rays polarized perpendicularly to each other. The images obtained with this method have a characteristic relief effect (similar to that obtained by scanning electron microscopy, SEM). Erythrocytes in this type of images have very sharp outlines, unlike what occurs in phase contrast images - in which erythrocytes are surrounded by characteristic pericellular halos.

1.1.4. Scanning electron microscopy

SEM is a versatile tool for morphological imaging, for surface features and structures in the order of microns and nanometers and can be used in many fields, including life sciences, biology and nanotechnology (Swanepoel and Pretorius, 2012). SEM uses a high-energy electron beam to scan the sample (Bhowmick et al., 2012). Some advantages of this tool are its considerable depth of field (which is responsible for the three-dimensional appearance of the sample), the ability to obtain the image in a few seconds and a high resolution (Pretorius et al., 2016; Russell et al., 2001). SEM works in a high vacuum environment (with pressures below 10^{-3} Pa). The interaction between the electron beam and the metallized sample generates secondary electrons which are captured by a detector offset from the sample holder. The signal is converted into electrical pulse which are sent to a monitor: one pixel on the monitor is related to one point on the sample. A monochrome image with high resolution and great depth of field is obtained as a result. It is made up of fundamental elements defined as pixels, with light intensity that is a function of how many electrons have been captured by the detector. The image observed on the monitor can be saved as a digital file on the computer. In SEM microgrphs discocytes appear gray in color with a bright luminous outline and a dark central depression (Fig. 1.2).

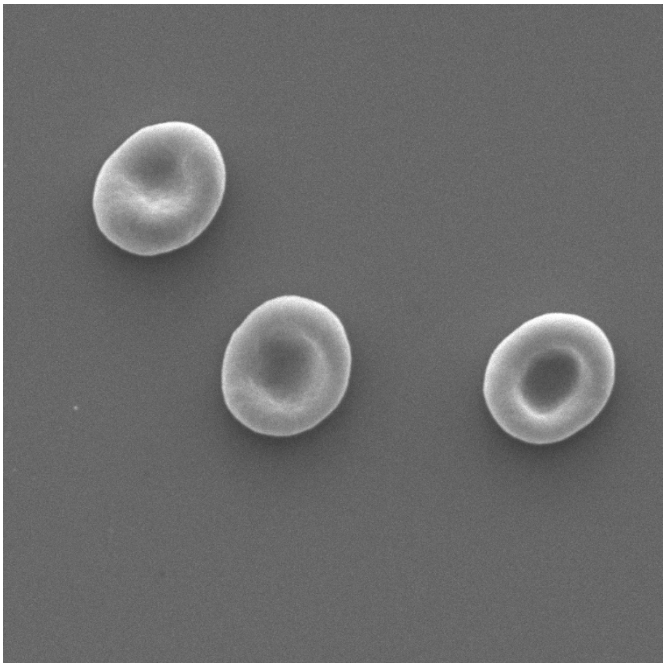

Figure 1.2 - Scanning electron micrograph of three discocytes.

In their work, Pretorius et al. (2016) suggest that, although light microscopy represents one of the main tools for clinical hematologists to classify and diagnose pathological conditions based on study of erythrocyte morphology, SEM technology should be employed as a recurrent morphological analysis tool. The question about technique cost and ease of use may arise, however the preparation of erythrocytes for SEM does not involve samples staining. Furthermore, erythrocytes visualization with SEM is probably simpler than focusing under light microscope, and the cost of a low-end SEM is in line with that of a high-end light microscope (Pretorius et al., 2016).

1.2. Red cell morphotypes and diseases characterized by abnormally shaped erythrocytes

Erythrocytes can be considered as key cellular indicators of an individual's overall well-being (Pretorius and Kell, 2014), also due to the short duration of their lifetime (Pretorius et al., 2016). There are several pathological conditions associated with characteristic changes in erythrocyte morphology (Bolotta et al., 2018a). Anomalies in erythrocyte shape are indicated by the word *poikilocytosis*, introduced by Quincke in 1877, while variation in erythrocyte size is called *anisocytosis*. Shape changes in patient's circulating blood can represent hereditary or acquired abnormalities. Such anomalies can be non-specific and associated with several mechanisms or highly specific and essential for the diagnosis of acquired or hereditary conditions (Pierre, 2002). In their work, Pretorius et al. (2016) provide examples of how diagnostic significance of erythrocytes as an important morphological indicator can have a great prognostic value, in particular in the study of erythrocyte structure during diagnosis of the disease and then in monitoring erythrocyte structure's health status after intervention therapies (Pretorius et al., 2016). Hypothesis according to which erythrocyte alterations may represent real-time biosensors of pathologies progression had previously been advanced by other authors (Berliner et al., 2005; Lucantoni et al., 2006; Rogowski et al., 2005).

1.2.1. Macrocytes

Macrocytes are mature erythrocytes with volume, area and diameter larger than discocytes (Bessis and Weed, 1973; Pierre, 2002; Fig. 1.3). In a peripheral blood smear, their diameter measures 8.5 microns or more. Erythrocytes with a diameter greater than 10 microns are called *gigantocytes*. Their hemoglobin concentration is generally lower than normal. Macrocytes can be found in severe anemias (Bessis and Weed, 1973). In newborns and premature babies, erythrocytes have both a large diameter and a large volume, even if this condition is not generally considered as macrocytosis since it

represents a physiological state. Macrocytosis can be due to an increase in reticulocytes. Macrocytes can have a round or oval shape. In many cases, round macrocytes are caused by chronic liver failure. On the other hand, if macrocytes have got an oval configuration, it means that erythrocytic precursors are dyserythropoietic. There may be a vitamin B12 or folate deficiency or exposure to drugs that inhibit DNA synthesis. Indeed, damage to DNA synthesis prolongs the cell cycle, but does not interfere with the rate of cytoplasmic hemoglobin synthesis. The level of cytoplasmic hemoglobin that signals nuclear division cutoff and expulsion of nucleus is reached before the normal number of cell divisions has occurred, leading to larger mature cells (Pierre, 2002).

1.2.2. Microcytes

Microcytes are erythrocytes with smaller diameter and area than discocytes, generally with no change in thickness/diameter ratio (Pierre, 2002; Fig. 1.3). They may be associated with decreased amounts of hemoglobin (hypochromia; Palmer et al., 2015). Hypochromic microcytes are found in anemia caused by iron deficiency (Pierre, 2002) and thalassemia (Palmer et al., 2015). Hypochromic microcytic erythrocytes with siderotic granules (iron-containing inclusions) are observed in patients with both hereditary and acquired refractory sideroblastic anemia. Chronic lead poisoning also produces hypochromic microcytic anemia with siderotic granules (Pierre, 2002).

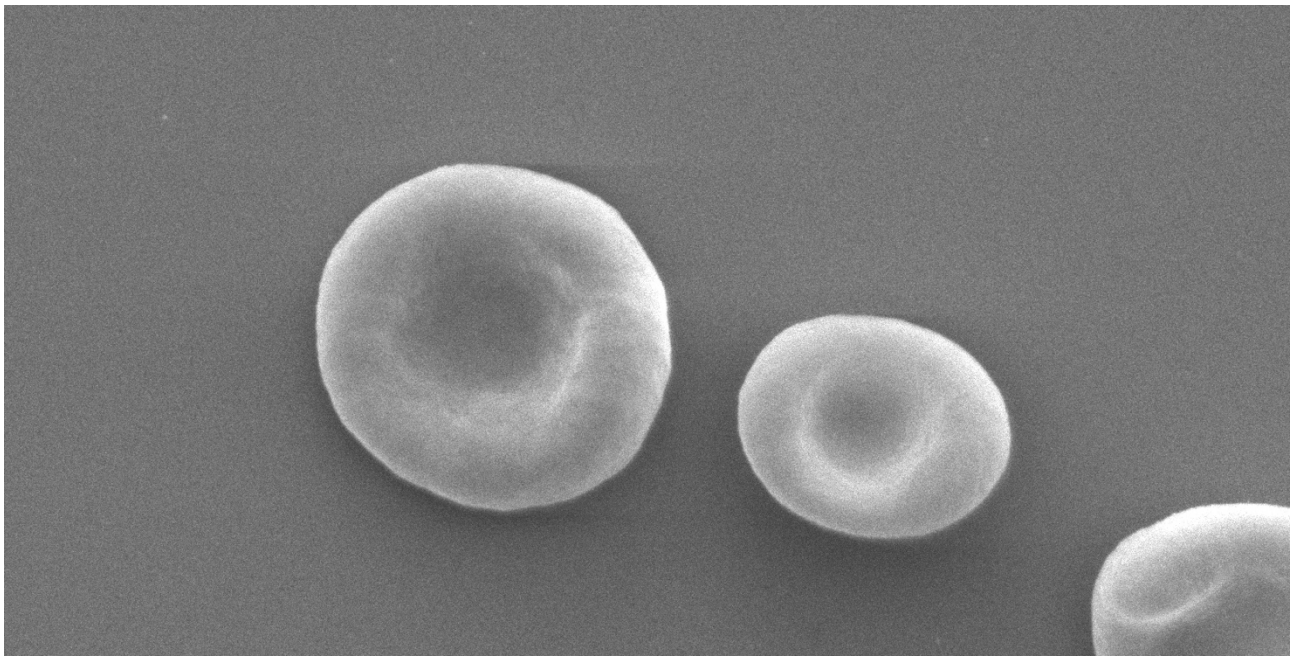

Figure 1.3 - Scanning electron micrograph of a macrocyte (on the left) and a microcyte (on the right).

1.2.3. Spherocytes

Spherocytes are spheroidal erythrocytes with a markedly reduced surface area/volume ratio (Fig. 1.4). In a peripheral blood smear these spherocytes appear denser and darker (absence of central pallor) due to their thickness (Palmer et al., 2015; Pierre, 2002). According to Bessis and Weed (1973), spherocytes class includes several morphologically and etiologically different cell types:

- *Macrospherocytes*, produced by the osmotic swelling of normal erythrocytes;
- *Sphero-echinocytes* and *sphero-stomatocytes* (described later);
- *Microspherocytes*, resulting from erythrocyte fragmentation processes. They can be produced in cases of severe frostbite or frozen extremities (Pierre, 2002); microspherocytes may also be a feature of microangiopathic hemolytic anemia (Palmer et al., 2015). In addition, a marked microspherocytosis is observed in the case of exotoxin produced by *Clostridium* species, which leads to significant erythrocytic damage and intravascular hemolysis (Pierre, 2002).
- Spherocytes observed in hereditary spherocytosis. Some patients with hereditary spherocytosis demonstrate occasional variants called "mushroom cell" or "pincer cell", which resemble spherocytes with mirror indentations, resulting in an appearance similar to a button mushroom (Ford, 2013).

Spherocytes can also be found in other pathological conditions or in case of direct damage to red cell membrane (Palmer et al., 2015; Pierre, 2002). Acquired causes of spherocytosis are due to antibodies damage towards erythrocyte membrane; such damage can be isoimmune or autoimmune

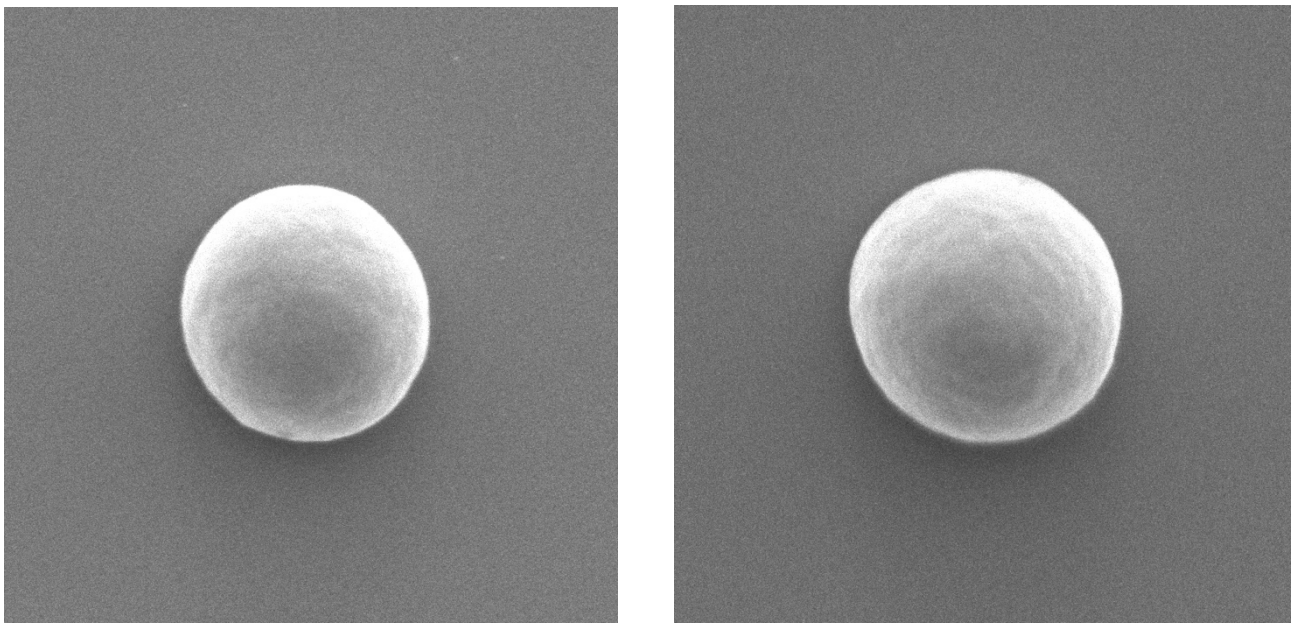

Figure 1.4 - Scanning electron micrographs of spherocytes.

in nature. A pseudospherocytosis is observed in patients who have received recent RBC transfusions: transfused erythrocytes may appear small and rounded in a peripheral blood smear (Pierre, 2002). Spherocytosis can also be observed in newborns with gram-negative sepsis and in patients with thermal burns, as well as in other hemolytic anemias including G6PD (Glucose-6-Phosphate Dehydrogenase) deficiency (Ford, 2013).

1.2.4. Elliptocytes

Elliptocytes are elliptical shaped red blood cells (Fig. 1.5). Approximately 1% of RBC are elliptical in normal cases. This shape ranges over a barely distinguishable ellipse to almost rod-shaped cells. Typically, elliptocytes are present as macro-elliptocytes in case of vitamin B12 and folate deficiency, or are the result of chemotherapeutic agents that affect DNA or RNA synthesis (Pierre, 2002). In all type of anemia, the percentage of elliptocytes can increase up to 10% (Bessis and Weed, 1973). Indeed, these cells can in fact be found in patients with megaloblastic anemia, dyserythropoietic anemia, such as 5q minus syndrome, and in myelodysplastic syndromes (Ford, 2013; Pierre, 2002). Additionally, hypochromic microcytic anemias due to iron deficiency and thalassemic syndromes frequently go along with elliptocytic changes in RBC. Elliptocytes are also found in an autosomal dominant hereditary pathology: hereditary elliptocytosis. In the homozygous form of the disease, elliptocytes can represent up to 90% of peripheral RBC (Pierre, 2002). Parents with typical hereditary elliptocytosis may have infants with a much more abnormal phenotype, with severe microschistocytosis, as well as elliptocytosis. These children can have either hereditary elliptocytosis

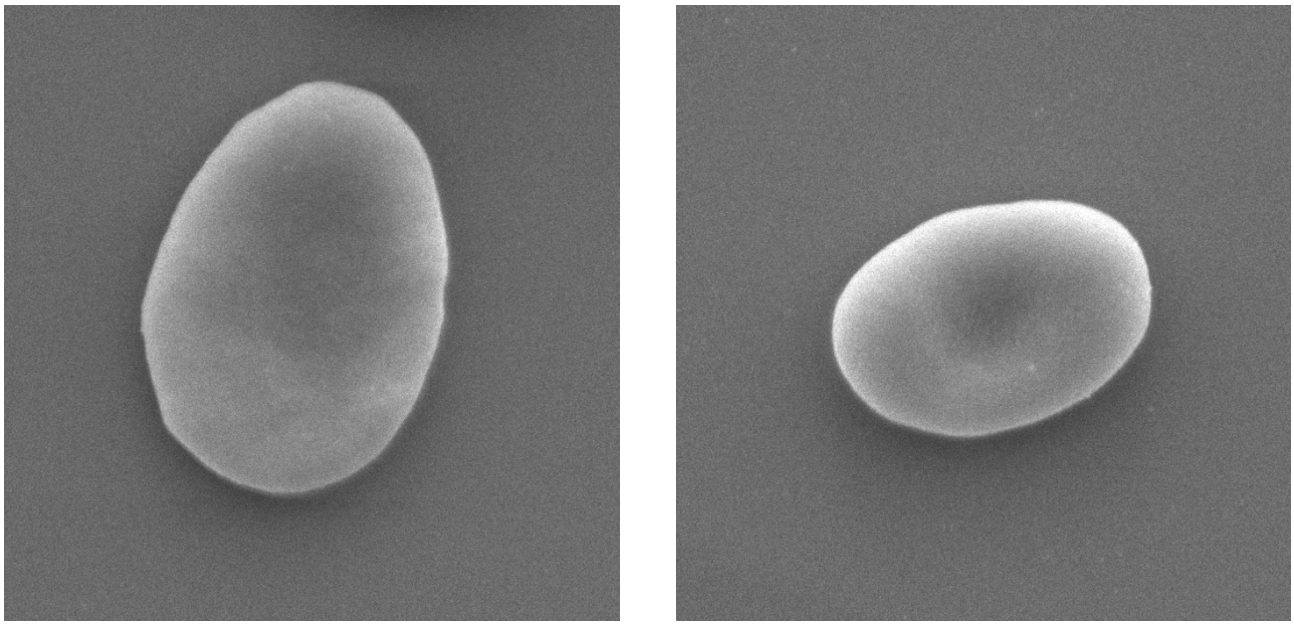

Figure 1.5 - Scanning electron micrographs of elliptocytes.

with infantile poikilocytosis or hereditary pyropoikilocytosis. In Southeast Asian ovalocytosis, elliptocytes show a central transverse (not longitudinal) pale region, or pale regions separated by a transverse cytoplasmic line, or even a central pale region divided into two or three rays (Ford, 2013).

1.2.5. Echinocytes

Echinocytes are erythrocytes covered with 10-30 short blunt projections or spicules of fairly regular shape (the term *echinocyte* derives from the Greek word that means "sea urchin"; Lim et al., 2002; Palmer et al., 2015). Such red blood cells can represent artifacts: it has been shown that if erythrocytes are washed with saline solution and placed between a glass microscope slide and a coverslip, they transform into echinocytes. When a plastic slide is used, no echinocytes are formed (Pierre, 2002). In the transformation from discocyte to echinocyte, the following stages can be recognized: echinocyte I (an irregularly contoured disc), echinocyte II (a flattened cell with spines, Fig. 1.6A), echinocyte III (a spherical or ovoid cell with 10-30 spines distributed on its surface, Fig. 1.6B; Bessis et al., 1973). If RBC are exposed to high concentrations of certain chemicals or to a very high pH (10.0) the spicules become smaller and more numerous and eventually bud irreversibly, forming extracellular vesicles composed of material derived from the plasma membrane and leaving behind spherical bodies with a small area and volume: sphero-echinocytes I and II (Fig. 1.7). In addition to high pH and proximity to a glass surface, echinocytes can be induced by: plasma incubated at 37°C for 24 hours, lysolecithin, fatty acids, ATP depletion, erythrocytes aging, amphipathic anions, high concentration of salts and cholesterol enrichment (Bessis, 1974; Bessis et al., 1973; Brecher and Bessis, 1972). Under some conditions, discocyte-echinocyte transformation is reversible by washing

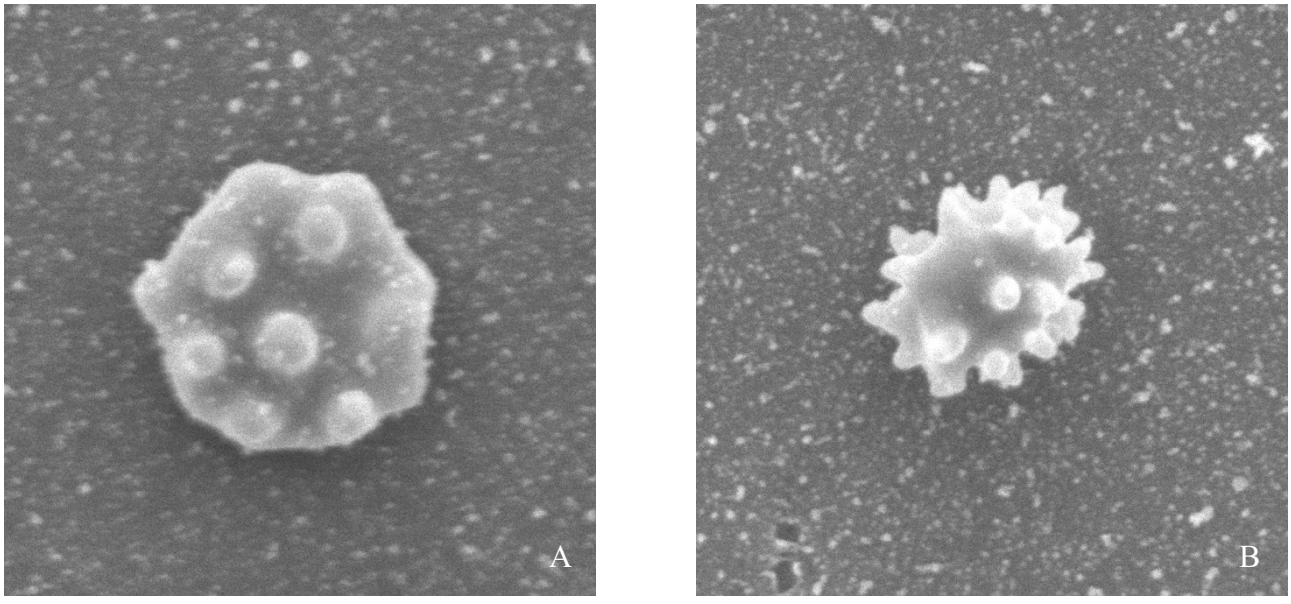

Figure 1.6 – Scanning electron micrograph of an echinocyte II (A) and an echinocyte III (B).

cells with fresh normal plasma (Brecher and Bessis, 1972). It has been observed that spicules always appear (or reappear) in the same place on the cell surface (Bessis, 1974). Echinocytic changes can occur with RBC of any type, for example: echino-spherocytes, echino-elliptocytes, echino-drepanocytes, and so on; Pierre, 2002). Echinocytes have been observed in patients with chronic liver disease (Turchetti et al., 1997), in cases of renal failure, following transfusion, phosphate deficiency, burns (Ford, 2013), uremia, pyruvate kinase deficiency and phosphoglycerate kinase deficiency (Brecher and Bessis, 1972).

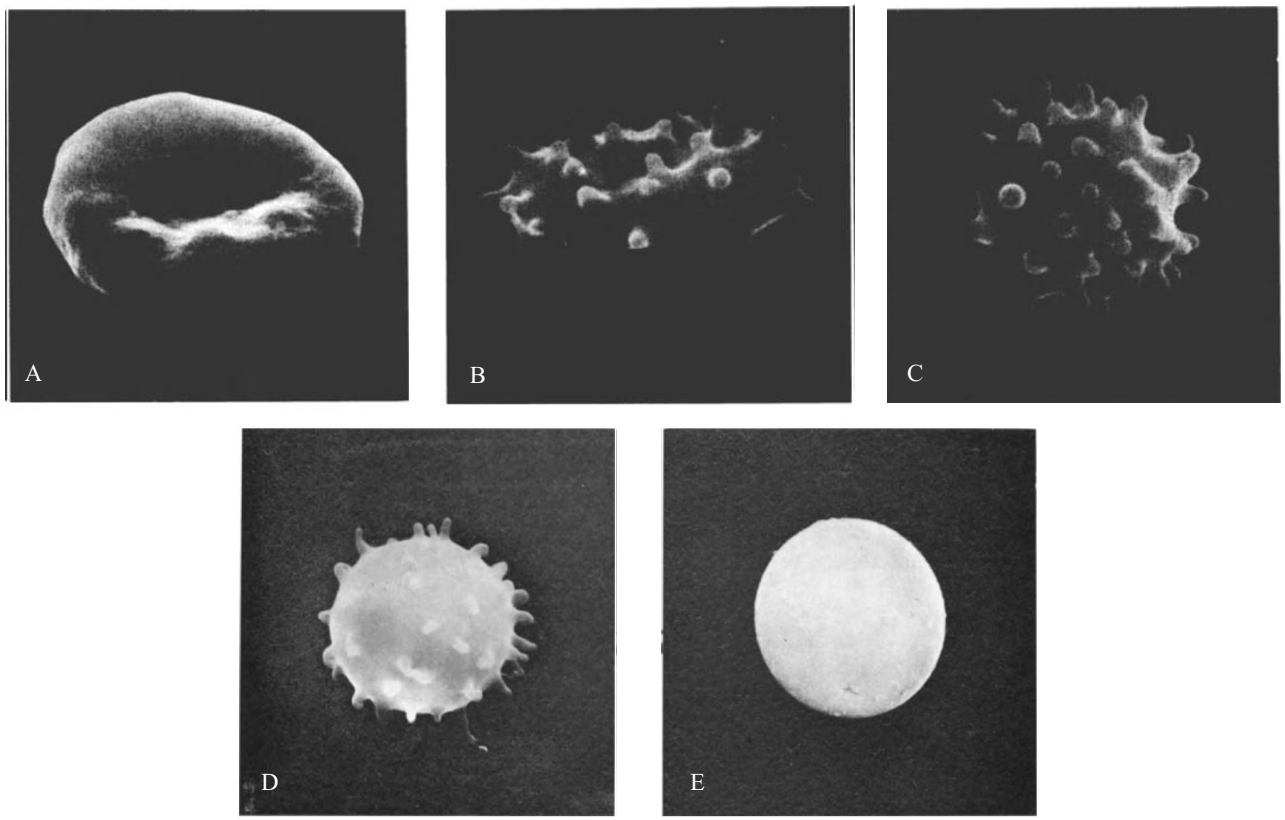

Figure 1.7 - Discocyte-echinocyte transformation. (A) Echinocyte I: a discocyte with an irregular contour; (B) Echinocyte II: a flat red blood cell with spicules; (C) Echinocyte III: spherical or ovaloid cell with 30-50 spicules distributed evenly over its surface; (D) Sphere-echinocyte I: a sphere with short spicules; (E) Sphere-echinocyte II: a sphere with spicules that can only be clearly seen with the scanning electron microscope (they are too small to be seen with a light microscope; Bessis et al., 1973).

1.2.6. Stomatocytes

Stomatocytes are concave, cup-shaped erythrocytes (Fig. 1.8). The term “stomatocytes” derives from the Greek word which means "mouth"; in fact the stomatocytes’ enfolding appears in a blood smear prepared for light microscopy as an elongated depression surrounded by two lips (Bessis, 1974). The stomatocytes’ “line of pallor” usually runs parallel to the main axis of the erythrocyte, but in certain variants (for example in South East Asian ovalocytosis), the line may run across the main

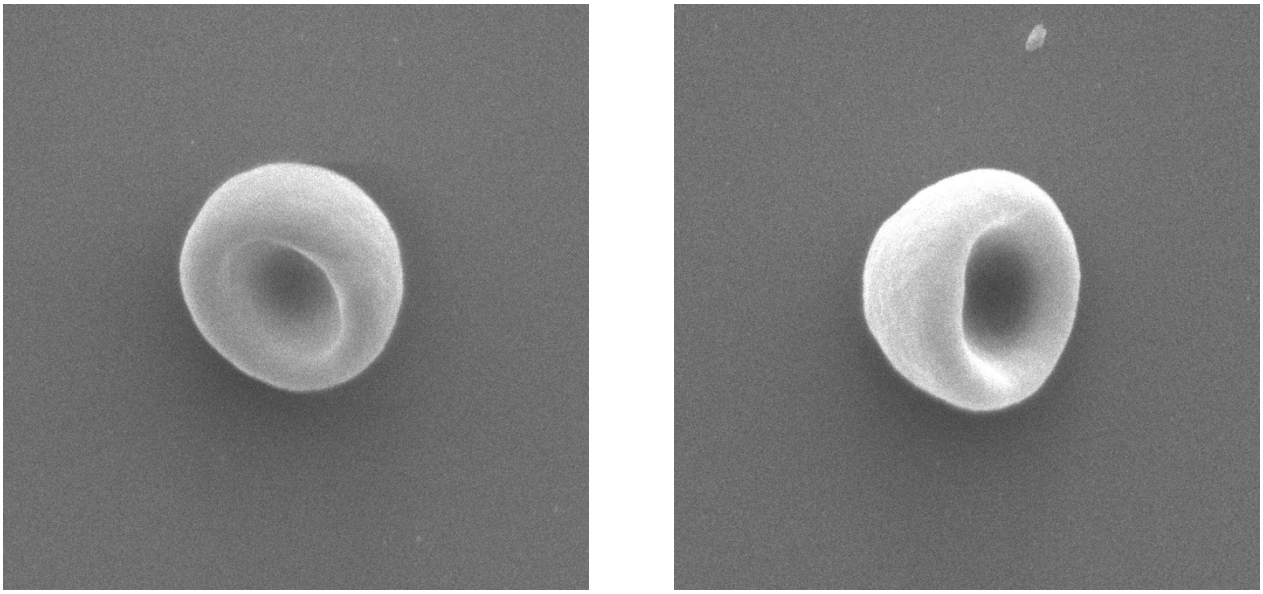

Figure 1.8 - Scanning electron micrographs of stomatocytes.

axis or may be nonlinear, for example bifurcated or trifurcated (Ford, 2013). Stomatocytes can represent both real anomalies and artifacts. In the first case, they are found in hereditary stomatocytosis (Pierre, 2002). Furthermore, these cells have been observed in certain hemolytic anemias in which this morphological change appears to be characteristic (Bessis and Weed, 1973), in obstructive liver disease and alcoholic liver disease, Rh null syndrome, as well as in the aforementioned South East Asian ovalocytosis (Ford, 2013; Palmer et al., 2015). Stomatocytic transformation represents the opposite of echinocytic transformation. It occurs progressively over time and if RBC are exposed to a low pH (3.0), multiple concave invaginations are produced, which eventually bud to form internal vesicles, leaving a **sphero-stomatocyte**. Stomatocytes return to a normal configuration when placed in normal plasma (Fig. 1.9). In addition to low pH, stomatocytes can also be induced by chemicals including amphipathic cations and drugs (phenothiazine and chlorpromazine), or by low salt concentration and cholesterol depletion (Bessis et al., 1973). As with discocyte-echinocyte transformation, disc-stomatocyte transformation can occur in pathological erythrocytes. This transformation overlaps with the underlying structural pathology of the cell (Bessis, 1974).

1.2.7. Knizocytes

Knizocytes are three-concave erythrocytes (Fig. 1.10). In fresh blood they can be observed in certain hemolytic anemias, such as hereditary spherocytosis. These shapes have also been observed in patients with cirrhosis after acute alcoholic intoxication and in patients with chronic liver disease.

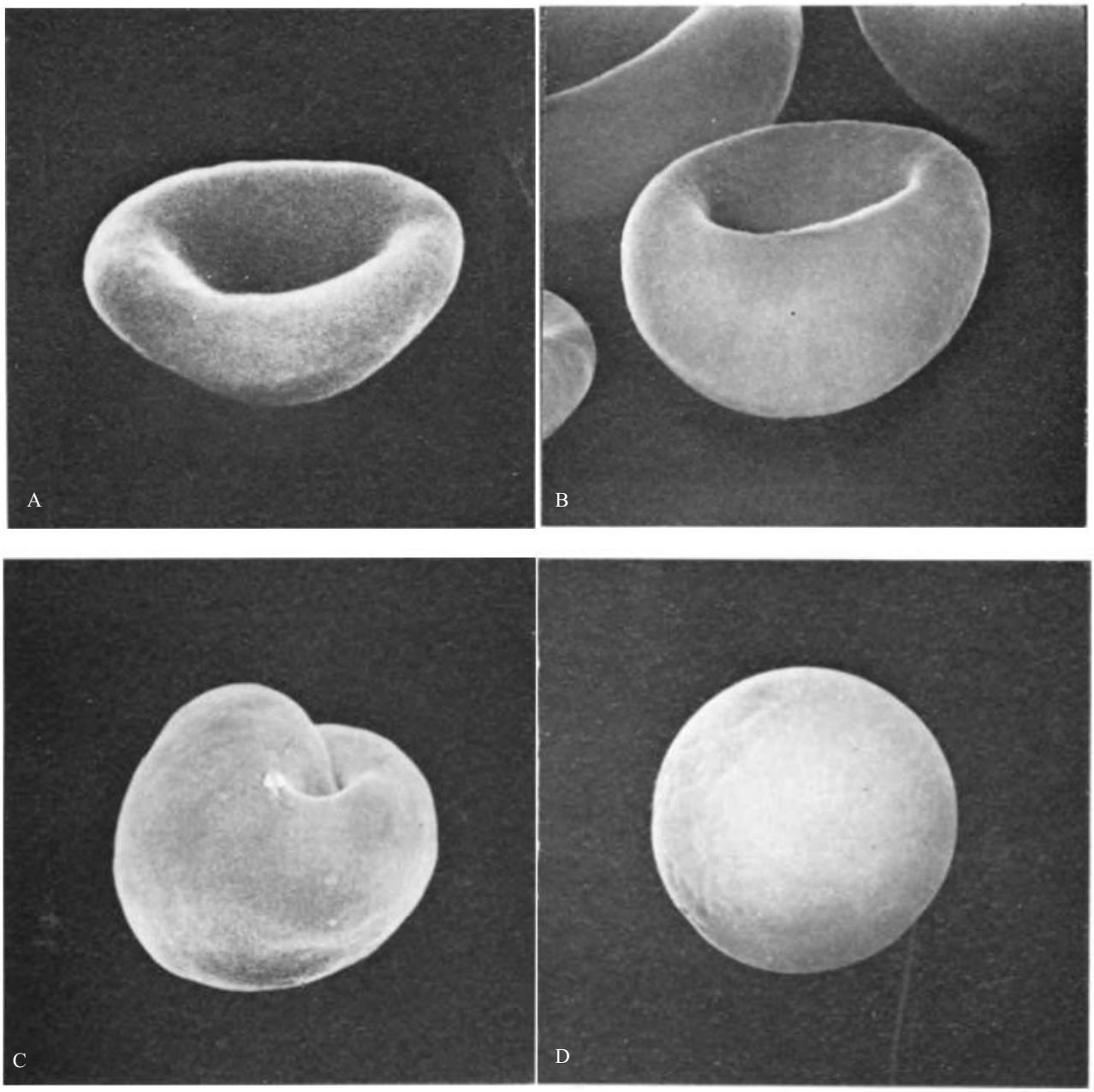

Figure 1.9 - Discocyte - stomatocyte transformation: (A) Stomatocyte I: this shape can be observed in certain states of hereditary or acquired haemolytic disease; (B) Stomatocyte II: cell that has got the shape of a cup deeper than stomatocyte I; (C) Sphere-stomatocyte I: stomatocyte with minimal central depression; (D) Sphere-stomatocyte II: a sphere with an irregularly shaped contour on one side (which can only be clearly observed by scanning electron microscope; Bessis et al., 1973).

The number of knizocytes is also elevated in diabetic vasculopathy (Bessis et al., 1973; Turchetti et al., 1998, 1997). Furthermore, this shape can be produced by exposure of RBC to a hypotonic medium with anti-echinocytic factors, or it can be caused by a slight deformation of the cells by a stream of liquid passed between a slide and a cover slip, after letting the RBC settle on the glass (Pierre, 2002). Finally, it should be reminded that knizocytes can represent an artifact due to drying, during preparation for scanning electron microscopy (Bessis et al., 1973).

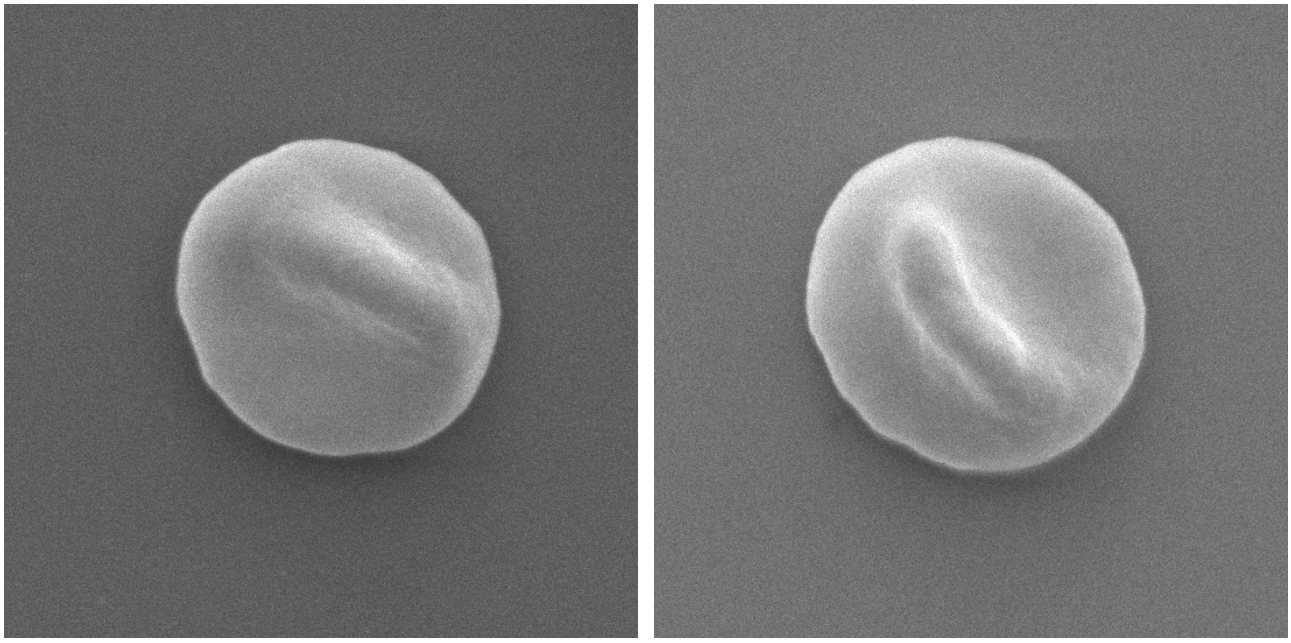

Figure 1.10 - Scanning electron micrograph of knizocytes.

1.2.8. Acanthocytes

Acanthocytes (or spur cells) are hyperchromic and "spiny" erythrocytes (Palmer et al., 2015; Fig. 1.11). Indeed, the term *acanthocytes*, introduced by Singer et al. (1952), derives from the Greek word that means "thorn". These spines are of variable length, size, thickness and shape (Palmer et al., 2015; Pierre, 2002). Their ends are described as *knobby* by Brecher and Bessis (1972) and, conversely, *pointed* by Ford (2013); Palmer et al. (2015) describe them as club-shaped, while Pierre (2002) reports that these spines arise from a dense, small and round central structure and have the ends bent backwards. All these authors agree that the spines are distributed in an irregular manner at the level of the cell surface. Pierre (2002) reports that these spicules are much less numerous than those of echinocytes: from 5 to 10 according to Brecher and Bessis (1972) and from 2 to 20 according to Palmer et al. (2015). These spines may also be provided with branches in acantho-echinocytes (Brecher and Bessis, 1972; Pierre, 2002).

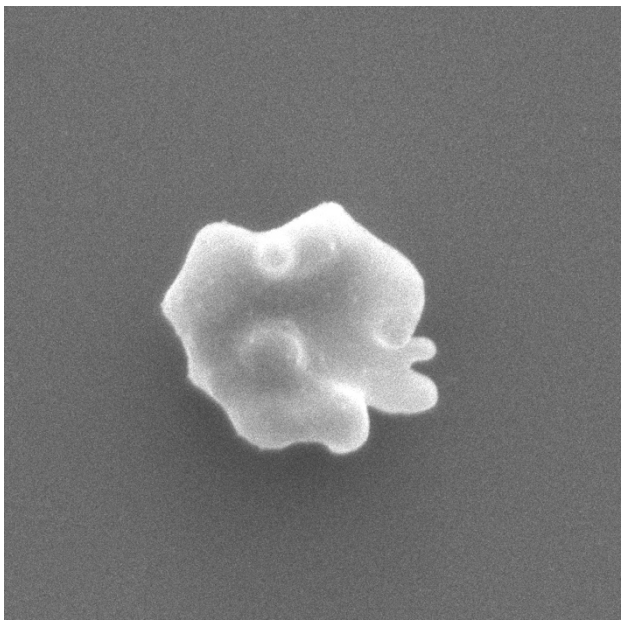

Fig. 1.11 - Scanning electron micrograph of an acanthocyte.

Acanthocytes are found in hereditary acanthocytosis, characterized by plasma abetalipoproteinemia. Acanthocytes are also found in cases of terminal liver failure associated with low serum cholesterol (an association which has been called spur cell anemia (Pierre, 2002). Furthermore, acanthocytes have been found in a familial disorder with neuronal degeneration, but without abetalipoproteinemia and in severe neonatal liver disease with hemolytic anemia (Brecher and Bessis, 1972). Presence of acanthocytes may suggest pyruvate kinase deficiency (in this case there are also irregularly contracted cells) or the McLeod phenotype. Acanthocytes are most commonly seen in patients with some dyslipidemia and also with anorexia nervosa (Ford, 2013). This erythrocyte morphotype is also found in cases of vitamin E deficiency (Palmer et al., 2015). Finally, acanthocytes have been found in patients without any recognizable hematological disorder in which the spleen has been removed by traumatic rupture or related to kidney transplantation (Brecher and Bessis, 1972) and also in patients with hyposplenism (Ford, 2013).

1.2.9. Codocytes

Codocytes are bell-shaped hypochromic erythrocytes. In fact, the term codocytes derives from the Greek word that means “bell”. The mean corpuscular volume of hemoglobin and the mean corpuscular concentration of hemoglobin of codocytes are always low. Codocytes can be thought as cells whose envelope is too large for their hemoglobin content. As a result, their resistance to hypotonic saline is increased and lysis occurs only when the cell membrane is fully stretched. Codocytes can therefore be considered as the antithesis of spherocytes, which have too little membrane for their volume and therefore have an increased susceptibility to lysis or an increase in "osmotic fragility" (Bessis, 1974). Codocytes can be found in many hypochromic anemias, particularly in thalassemia. When a drop of blood is prepared, bell-shaped hypochromic erythrocytes often appear as **target cells** when they lie flat on the slide (Fig. 1.12, 1.13). The appearance of target cell can also arise from other causes, for example in the case of echino I-lepto-torocytes (Fig. 1.14; Bessis et al., 1973). Under light microscope, target cells appear as erythrocytes having a central red area within the area of central pallor. Target cells are found in liver diseases, hyposplenism, hemoglobin C or S-C disease and xerocytosis (a type of stomatocytosis with decresed red cell cation permeability; Gallagher, 2005); they can also be observed in case of iron deficiency (Ford, 2013). If the bell-shaped hypochromic cells lean on one side, they resemble **helmet cells** (Fig. 1.15; Bessis et al., 1973).

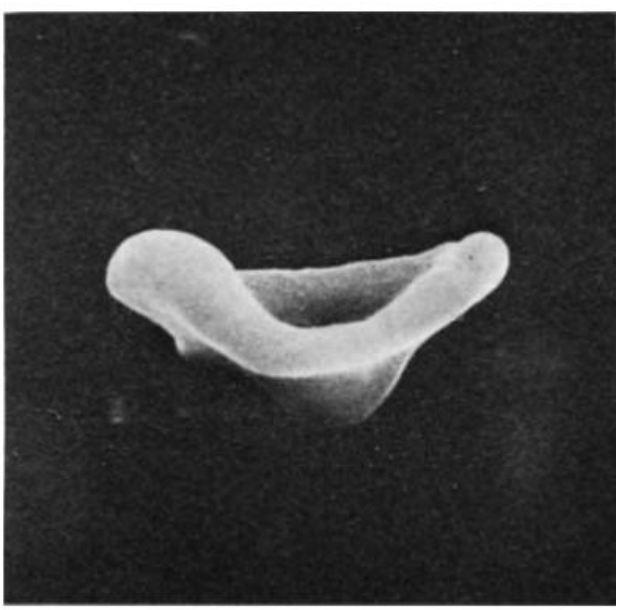

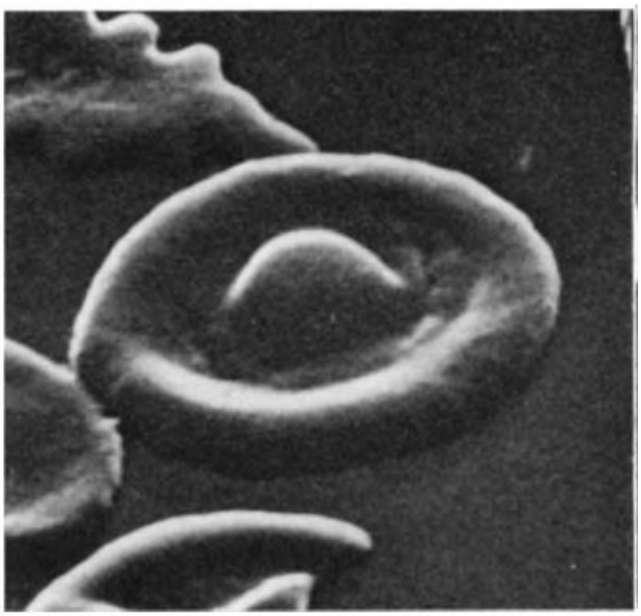

Figure 1.12 - Codocytes/target cells: when a drop of blood is prepared, if the bell-shaped hypochromic erythrocytes lie flat on the slide, they appear as target cells (Bessis et al., 1973).

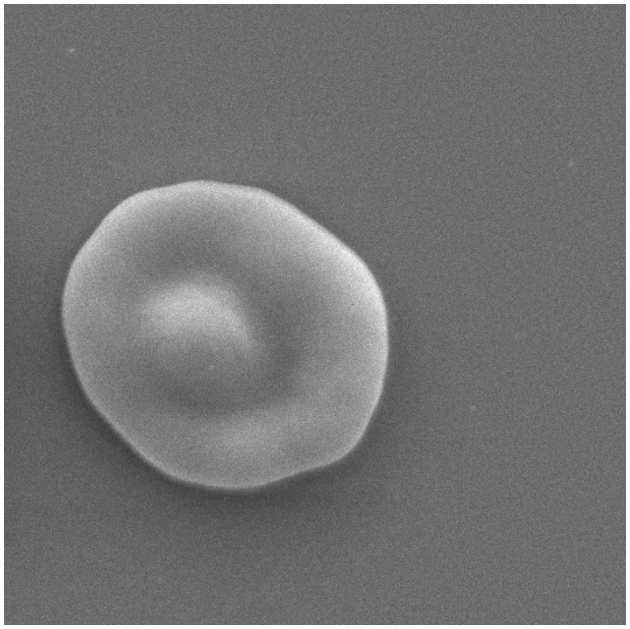

Figure 1.13 - Scanning electron micrographs of a target cell.

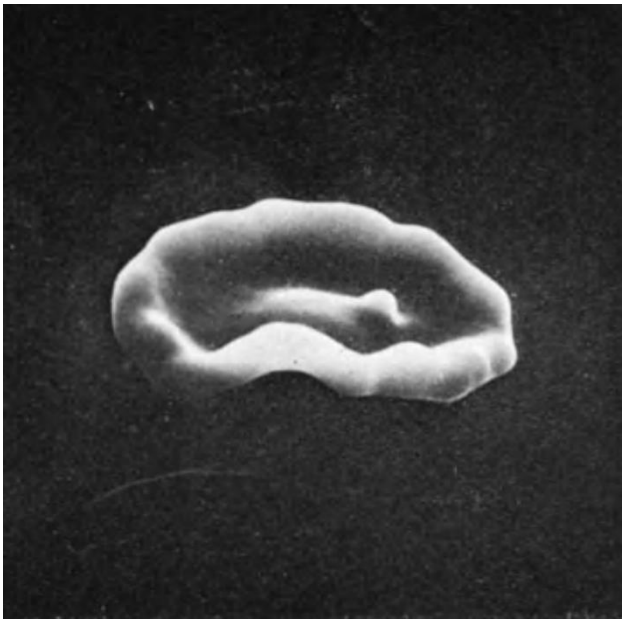

Figure 1.14 - Scanning electron micrograph of an echino I-lepto-thorocyte: this combination generates the appearance of a target cell (Bessis et al., 1973).

1.2.10. Leptocytes

Leptocytes are flat erythrocytes with thin edges: the term derives from the Greek word for "thin". They have a larger diameter and a comparable volume to those of discocytes (Fig. 1.16). These cells appear pale in color in a peripheral blood smear. Leptocytes can be seen in a broad spectrum of

conditions including thalassemia, iron deficiency (e.g. in dogs), drug adverse effects (phenothiazine), liver or biliary tract disease, or may even represent a familiar trait (Bessis et al., 1973; Pierre, 2002).

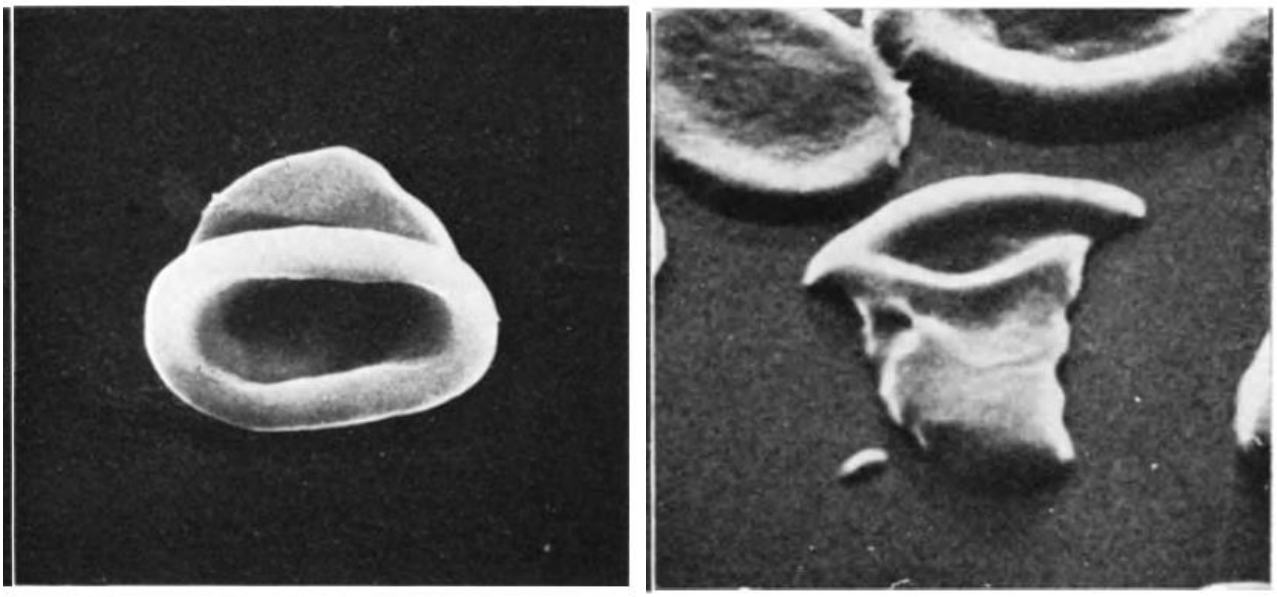

Figure 1.15 - Codocytes/helmet cells: when a drop of blood is prepared, if the bell-shaped hypochromic erythrocytes lean to one side, they resemble helmet cells (Bessis et al., 1973).

1.2.11. Other abnormal red cell morphotypes

- *Keratocytes* (from the Greek word that means "horn") are RBC with peculiar pointed projections (Pierre, 2002). Keratocytes are yield in case of microangiopathic hemolytic anemias, because of mechanical damage or exposure of erythrocytes to oxidative drugs in vivo (Palmer et al., 2015; Pierre, 2002). The following RBC morphotypes can be considered subtypes of keratocytes:
    - *Bite cells*, RBC with peripheral single or multiple arcuate defects (bites) caused by the removal of Heinz bodies by the spleen. They are a feature of oxidant haemolysis (Suppl. Fig. 1);
    - *Blister cells*, RBC in which the haemoglobin appears retracted

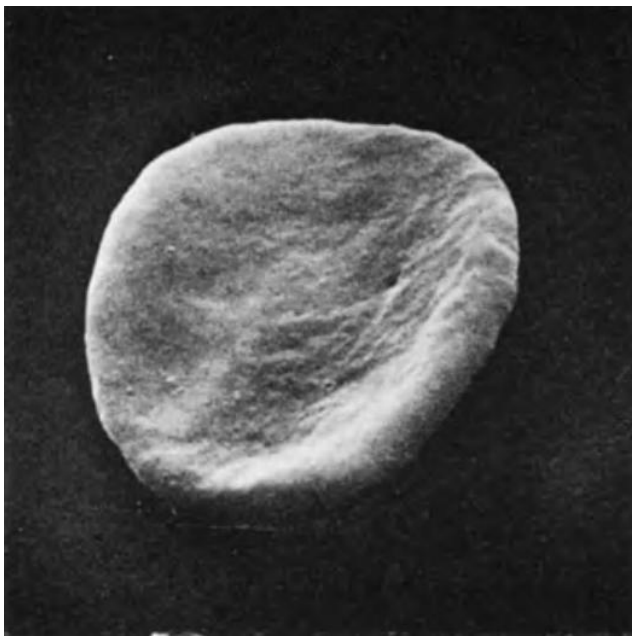

Figure 1.16 - Scanning electron micrograph of a leptocyte (Bessis et al., 1973).

into one half of the cell to form a dense mass leaving the remainder of the cell as an empty membrane;

- *Irregularly contracted cells*, smaller and denser RBC which lack an area of central pallor but are not as regular in shape as spherocytes (Palmer et al., 2015).

- *Myelinic figures* are phospholipids released from red cell membrane during cell necrosis; with interaction with plasma, they form filaments, spheres, or strings of spheres. They are most commonly seen in the blood of burn victims with large amounts of tissue damage (Pierre, 2002).
- *Dacryocytes* (from the Greek word meaning "drop") are erythrocytes with a single spicule, wide and tapered, which gives the cell the shape of a drop (Suppl. Fig. 2). Dacryocytes are found in chronic idiopathic myelofibrosis (and are occasionally observed in other myelodysplastic and myeloproliferative syndromes) and in many severe anemias (especially thalassemia major; Bessis et al., 1973; Pierre, 2002).
- *Fish cells* resemble dacryocytes because they have a round end and a tapered end but, unlike dacryocytes, the tapered end flares up in two buds, generating the appearance of a fish's tail. This type of erythrocyte has been found in cases of thalassemia (Ford, 2013).
- *Sickle cells* are found in sickle cell disease (or sickle cell anemia), a hereditary disease in which erythrocytes have got abnormal hemoglobin (hemoglobin S). When the oxygen tension decreases (for example at high altitude), the hemoglobin molecules polymerize and form thin and long rods inside the cell. These tiny rods of hemoglobin group into bundles that stretch the membrane and deform the discocyte (Bessis, 1974).
- *Schistocytes* (from the Greek word which means "to divide") are fragments of RBC produced by extrinsic mechanical damage within the circulation and are a diagnostic feature of microangiopathic haemolytic anaemia. Schistocytes are always smaller than intact red cells and can have the shape of fragments with sharp angles and straight borders, small crescents, helmet cells or keratocytes (Palmer et al., 2015; Suppl. Fig. 3).

1.2.12. Pathologies characterized by a systemic inflammatory profile

Erythrocytes with aberrant morphologies are typically observed in blood samples from patients diagnosed with a systemic inflammatory profile, such as type II diabetes, thromboembolic stroke, rheumatoid arthritis, Parkinson's disease and Alzheimer's disease, as well as conditions such as hereditary hemochromatosis and hyperferritinemia (Bester et al., 2013; Buys et al., 2013; Pretorius et al., 2015, 2014a, 2014b, 2013; Pretorius and Kell, 2014; Pretorius and Lipinski, 2013). It is believed

that these morphological changes are due precisely to alterations in inflammatory state, which are caused, for example, by the generation of ROS (Reactive Oxygen Species) and oxidative stress, and can directly affect coagulation and hematological system (Pretorius et al., 2016).

In inflammatory conditions, peculiar erythrocyte morphologies - not visible through a light microscope - are often observed. Two new terms have been coined to describe these erythrocyte morphologies: knot cells and balloon cells (Fig. 1.17). The **knot cells** twist into each other (through a light microscope they appear just as discocytes). In the presence of fibrin fibers, their membranes are so elastic that they twist and knot around the fibers. **Balloon cells** are modified drop-shaped cells, with an extended and long projection that can interact with fibrin fibers (Pretorius and Lipinski, 2013). Such projections are too thin to be observed with a light microscope (Pretorius et al., 2016). Through SEM, Buys et al. (2013) observed erythrocyte morphological changes in patients with diabetes: erythrocytes are elongated, their membranes form extensive projections, moreover cells spontaneously twist around fibrin fibers. These cells also appear visibly smoother than those of healthy erythrocytes (Fig. 1.18). Macroparameter measurements by atomic force microscopy (AFM) suggest that erythrocytes of these patients are smaller and with a reduced concavity depth (Buys et al., 2013).

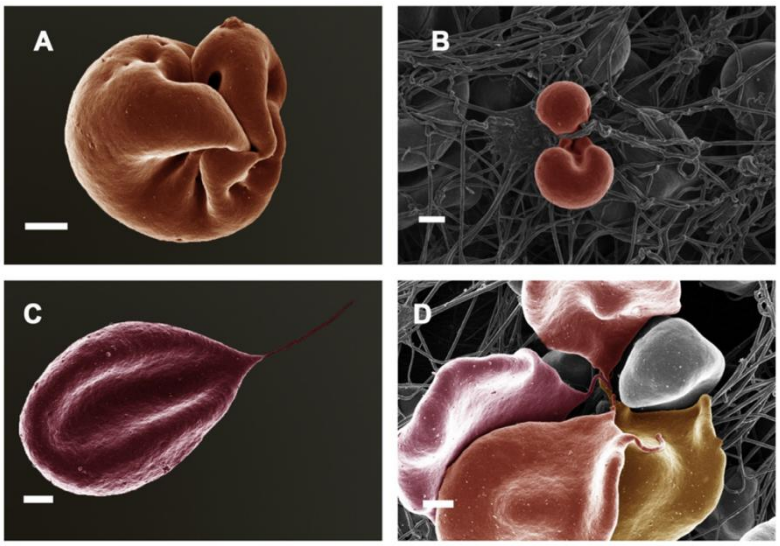

Figure 1.17: new erythrocyte morphologies, visible only by SEM. (A) Knot cell; (B) Knot cell with fibrin associations; (C) Balloon cell; (D) Balloon cells associated with each other. Scale bar: 1 micron (Pretorius et al., 2016).

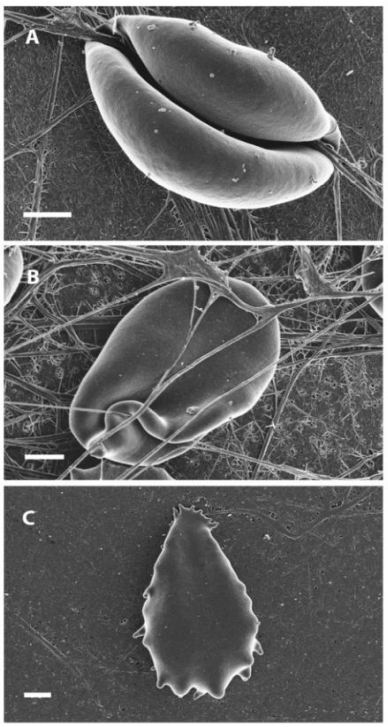

Figure 1.18: Scanning electron micrographs of erythrocytes from a diabetic subject. (A) Erythrocyte with very smooth membrane spontaneously twisted around fibrin fibers; (B) Erythrocyte showing an elongated ultrastructure. (C) Erythrocyte showing a smooth membrane. Scale = 1 micrometer (Buys et al., 2013).

1.2.13. Pathologies characterized by oxidative stress

Changes in erythrocyte morphology can occur via a biochemical mechanism in which oxidative stress leads to changes in lipids and membrane proteins. Oxidative stress is defined as the destruction of normal intracellular balance between ROS, yielding during aerobic metabolism or as a result of pathological processes, and antioxidant defense mechanisms (Ghezzo et al., 2013). As a result of oxidative stress, biophysical alterations of erythrocyte morphology occur, such as cell shrinkage and changes in cell rigidity or elasticity. These changes result in less deformability and greater aggregation of erythrocytes (Loyola-Leyva et al., 2019; Manzur-Jattin et al., 2016; Pretorius et al., 2016).

For example, in patients with **chronic obstructive pulmonary disease** chronic oxidative stress modifies red blood cells shape, but normal shape is restored following appropriate antioxidant medications (Lucantoni et al., 2006). Similarly, RBC storage in blood banks leads to formation of ROS and oxidation products such as malondialdehyde. The consequent oxidative stress leads to echinocytes formation, then to budding of micro and nano-vesicles from the spines (Greenwalt, 2006) and finally to hemolysis; all of these processes can be avoided by supplementing with antioxidants (Pallotta et al., 2014). Another pathology with a proven increase in oxidative stress in which morphological alterations of erythrocytes have been reported is **end-stage renal disease**. Distinctive morphological features of this condition are echinocytosis and stomatocytosis (Antonelou et al., 2011).

In addition, it has been reported that **hypercholesterolemia** modifies erythrocyte morphology through an increase in membrane cholesterol content and yielding biochemical changes (Fessler et al., 2013; Radosinska and Vrbjar, 2016). Indeed, hypercholesterolemia facilitates formation of free radicals, which can lead to lipid peroxidation and modify erythrocyte membrane proteins and, therefore, their morphology (Radosinska and Vrbjar, 2016). **Obesity** can also alter erythrocyte morphology. A possible mechanism for this type of alteration is the production of pro-inflammatory cytokines by adipose tissue, thus yielding lipid peroxidation in erythrocyte membrane and changes in cytoskeletal proteins, which alter erythrocyte morphology and membrane fluidity (Babitha and Gunasekaran, 2016). Loyola-Leyva et al. (2020) reported altered erythrocyte morphologies (analyzed by SEM) in metabolically unhealthy subjects (patients with hypercholesterolemia, hypertension or high levels of triglycerides or glucose) of normal weight, metabolically healthy subjects with obesity, and metabolically unhealthy subjects with obesity. In the metabolically unhealthy group, a greater erythrocyte diameter was observed compared to the metabolically healthy counterpart. The axis ratio was higher in metabolically unhealthy groups (more elongated RBC). The study shows that

hypercholesterolemia was associated with larger and more elongated erythrocytes, while obesity was associated with smaller erythrocytes. Furthermore, age, high-density lipoprotein (HDL), consumption of ultra-processed food were factors associated with altered erythrocyte morphologies (Fig. 1.19).

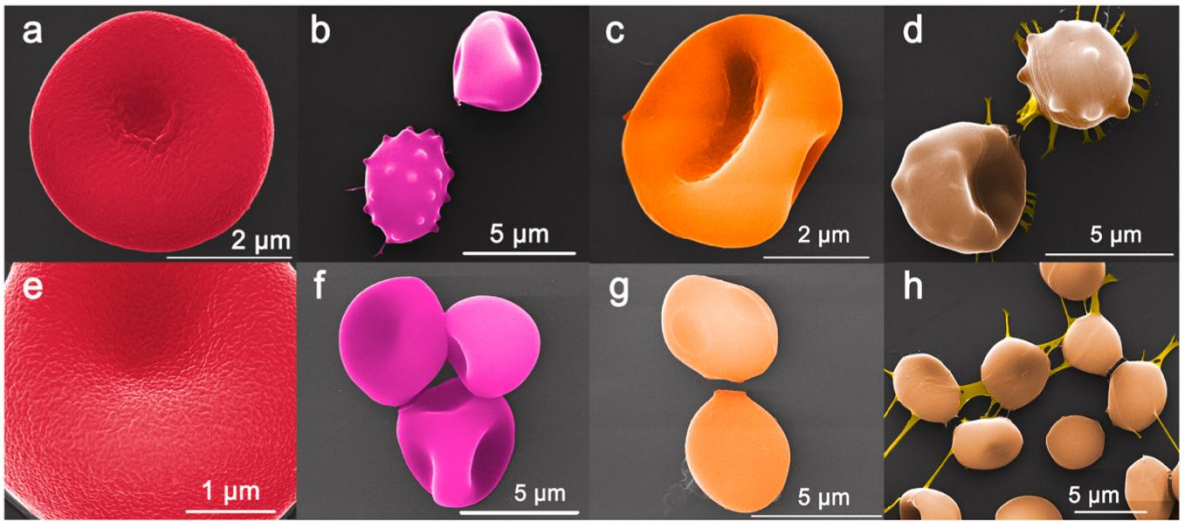

Figure 1.19: SEM images of red blood cells with normal and pathological morphologies observed in the different groups. (a) and (e) correspond to the healthy group and are normocytes. (b) and (f) correspond to the metabolically unhealthy group of normal weight, in (b) an echinocyte and an erythrocyte with an irregular shape can be observed. (c) and (g) belong to metabolically healthy participants with obesity, in (c) an erythrocyte with morphology similar to a normocyte can be observed and in (g) erythrocytes with "flat pancake" shapes can be observed. (d) and (h) correspond to the metabolically unhealthy group with obesity, in (d) a stomatocyte and an echinocyte can be observed, and in the image (h) there are different types of pathological erythrocyte morphologies. Both (d) and (h) contain what could be fibrin fibers, indicators of the inflammatory process (Loyola-Leyva et al., 2020).

1.2.14. Other conditions in which abnormally shaped RBC are found

- *Infantile pycnocytosis:* this term has been used to describe finding of acanthocytes with thin projections in newborns and premature babies. This condition, sometimes accompanied by hemolysis, is thought to be due to a vitamin E deficiency in the mother and in the baby. It is a disorder that disappears when the child begins to receive vitamin E, either through the diet or as a drug. The awareness of the need for proper nutrition during pregnancy and the almost universal administration of multivitamins to pregnant women have practically caused this pathology to disappear (Pierre, 2002).

- *Hereditary pyropoikilocytosis:* in this disease, extreme variation in the shape and size of red blood cells is found. It is an autosomal recessive disorder most frequently diagnosed in black children (Pierre, 2002). Hereditary pyropoikilocytosis is caused by defects in the horizontal interactions of erythrocyte membrane (Cortelazzo et al., 2015). There are both quantitative and structural changes in spectrin, which lead to a decrease in spectrin tetramers. This

pathology is associated with thermal instability of erythrocyte membrane. Peculiar features of this pathology are: a significant increase in the fragmentation of RBC, changes in shape when erythrocytes are heated to 46°C and a marked microcytosis (Pierre, 2002).

- *Extracorporeal circulation in cardiovascular surgery:* in their work, Deng et al. (2018) show that the percentage of erythrocyte malformations in the postoperative group was higher than in the pre-operative and intra-operative groups, through SEM and AFM image analysis. The authors of the study suggest that the dissection itself can induce erythrocyte damage due to disorders of blood coagulation system and hemodynamics.
- *Patients lacking G6PD:* Fang et al. (2016) reported significantly high percentages of altered erythrocyte shapes, predominantly echinocytes, in these patients (Fig. 1.20). G6PD is an X-linked enzyme catalyzing the first-rate limiting step in the pentose phosphate pathway, which produces reduced nicotinamide adenine dinucleotide phosphate (NADPH), a binding substrate for several redox systems. Erythrocytes from individuals lacking G6PD are vulnerable to oxidative stress, predisposing them to chemically induced hemolysis when certain oxidizing agents are administered. Ford (2013) instead reported that the G6PD deficiency condition often shows bite and blister cells, schistocytes and spherocytes.

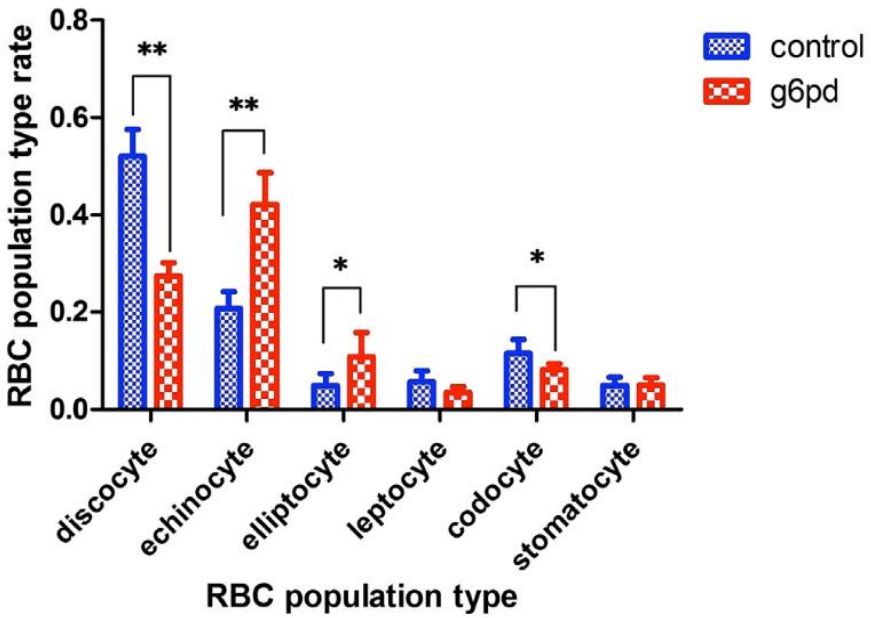

Figure 1.20 - RBC population type distribution in control individuals and G6PD deficient patients, N = 3. (*p < 0.05, **p < 0.01; Fang et al., 2016).

1.3. Autism spectrum disorders

Autism spectrum disorders (ASD) represent a heterogeneous and complex neurodevelopmental disorder consisting mainly of impaired social interaction, communication difficulties and restricted, repetitive and stereotyped patterns of behavior (Ciccoli et al., 2013; Ghezzo et al., 2013). Children with ASD also generally suffer from echolalia, hyperactivity, memory/learning/motor skills or other neurological functions deficits, abnormal excitability, hyper- or hypo-sensitivity to sensory stimuli, anxiety, difficulty adapting to new environments or habits, and excessive dependence on routines (Abruzzo et al., 2015; Parletta et al., 2016). Subjects with ASD may also suffer from a broad spectrum of somatic disorders, such as immunological, gastrointestinal, sleep disturbances and others, at a much higher rate compared to general population. Associated medical conditions negatively affect the main symptoms of ASD, and increase the probability of behaviors that are difficult to manage (Jasenovec et al., 2019).

ASD include several conditions: classical (non-syndromic) autism, which is the predominant phenotype, Asperger's syndrome, childhood disintegrative disorder, and pervasive developmental disorder not otherwise specified, according to the Diagnostic and Statistical Manual of Mental Disorders, fifth edition (DSM-V). This manual classifies ASD on three levels (mild, moderate or severe) based on the degree of support that the patient requires (Abruzzo et al., 2015)

It is believed that ASD result from a complex interaction between genetic background and environmental factors (Ciccoli et al., 2013). Immune dysregulation, inflammation, oxidative stress, mitochondrial dysfunction, and environmental toxicant exposures have been reported in a large number of studies on associated physiological abnormalities in ASD (Frustaci et al., 2012; Kaur et al., 2014; Rossignol and Frye, 2012). With particular regard to oxidative stress, this condition in ASD subjects damages deeply and in many ways erythrocytes and their plasma membrane: oxidative stress changes fluidity and lipid composition of erythrocyte membrane and affects the activity of Na^+/K^+-ATPase (Bolotta et al., 2018b; Ghezzo et al., 2013). Several possible risk factors for ASD have been investigated, which include advanced parental age, birth complications, prematurity, low birth weight, and assisted conception (Shen et al., 2019).

The epidemiology of ASD is continuously increasing all over the world with huge social and economic burdens (Shen et al., 2019). ASD affect four to five times more males than females (1/42 for boys versus 1/189 for girls). Centers for Disease Control and Prevention (CDC) estimated that 1/68 children (aged 8 years) in 2014 suffered from ASD in the USA. Another recent valuation points out the presence of ASD in 1 in 132 people with little variation globally. This discrepancy could be a sign of both a real increase in the presence of ASD and their diagnosis (in 2012 the CDC estimated

that ASD rate in American children was 1/88) and the fact that ASD diagnosis is often "lost" when children progress into adulthood, being replaced by a "generic" intellectual disability and/or hidden under late-developing neuropsychiatric illnesses (Abruzzo et al., 2015).

ASD begins early in childhood and lasts throughout life (Shen et al., 2019). A recent review (Brian et al., 2015) points out four broad domains of development that are predictive for ASD: sensory-motor, social-emotional, attention and communication. Deficits in these areas may appear as early as 6-9 months, although the clinical onset of ASD generally occurs during the second year of life. Indeed, a reliable diagnosis can be made at three years old children (since clinical diagnosis is difficult and uncertain in younger children); however, many children receive a final diagnosis only much later (Abruzzo et al., 2015): the mean age of clinical diagnosis has found stable at 4-5 years with no evidence of decline (Brett et al., 2016).

As the etiology of ASD is not completely understood, there is still no cure available for the treatment of this disorder. However, some behavioral interventions are available to improve the core and associated symptoms of autism, particularly when initiated at an early stage. Thus, there is an increasing demand for finding biomarkers for use in the prognosis and diagnosis of ASD patients (Shen et al., 2019). In particular, there is growing interest in the identification of biomarkers that could be implemented easily in clinical practice through conventional laboratory medicine, following the routine collection of body fluids such as blood, urine, or saliva. However, the availability of reliable biomarkers remains an unmet clinical need (Ruggeri et al., 2014). Although diagnostic biomarkers have not yet been established, research efforts have been carried out in neuroimaging and biological analyses including genomics and gene testing, proteomics, metabolomics, transcriptomics, and studies of the immune system, inflammation, and microRNAs (Shen et al., 2019).

1.3.1. Erythrocyte morphological alterations in patients with RTT

With their work, Ciccoli et al. (2012) reported the presence of oxidative stress, mild chronic hypoxia, and a high frequency of leptocytes (Fig. 1.21) in girls with Rett syndrome (RTT), which is a neurodevelopmental disorder with autistic features - but it has recently been separated from ASD as a nosologically distinct entity (DSM-V). It is a severe and relatively rare disorder that affects females (about 1: 10000-1: 15000) characterized, in addition to autistic behavior, by neurological regression and typical hands stereotypies. RTT represents the second most common cause of severe intellectual disability in females and is genetically determined as it is mainly due (approximately 90-95% of cases) to loss-of-function mutations in the X-linked methyl-CpG-binding protein 2 gene (MeCP2), a key gene for transcriptional regulation (Cortelazzo et al., 2015). Furthermore, the work

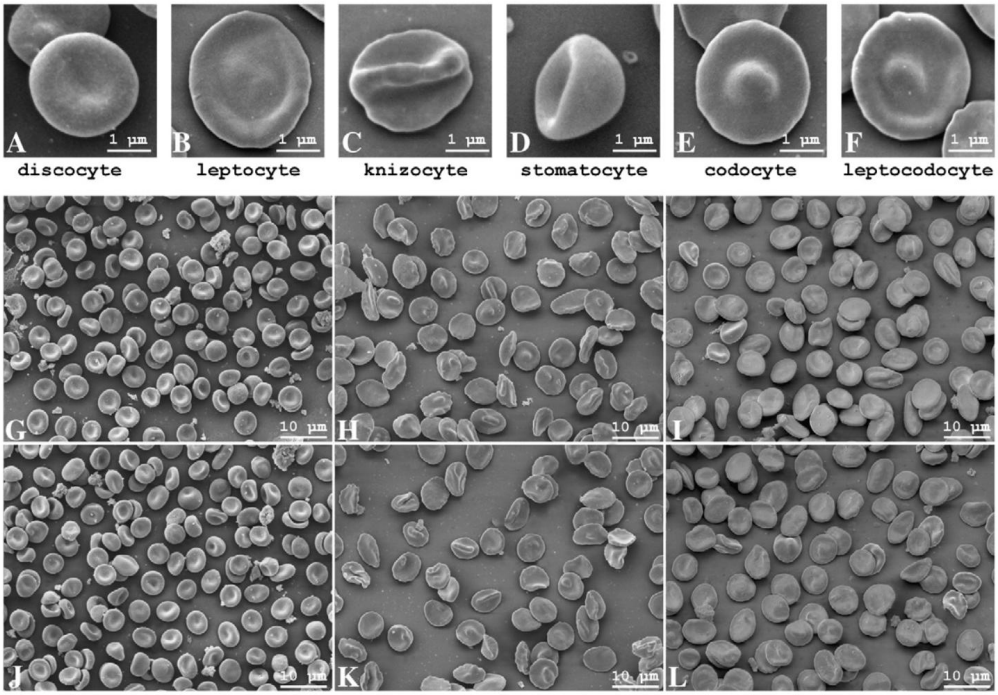

Figure 1.21 - Abnormal erythrocyte shapes in Rett syndrome observed by SEM. Top panel row: frames of main red cell shape changes from untreated RTT patients (A: normal shaped red blood cells (B-F: abnormal shaped red cells). Bottom panels: SEM red blood cells of RTT patients before and after omega-3 PUFA supplement (6 and 12 months) and healthy controls. (G, J) healthy controls. (H, K) typical RTT patients. (I) typical RTT patients after 6 months of PUFA omega-3 supplement. (L) typical RTT patients after 12 months of PUFA omega-3supplementation (Ciccoli et al., 2012).

by Ciccoli et al. (2012) shows that altered RBC morphology in RTT patients is partially restored by supplementing omega-3 polyunsaturated fatty acids (PUFA), a family of biologically active fatty acids with antioxidant potential. For the generation of the altered RBC shapes in these patients, the combination of oxidative stress and hypoxia plays a key role.

Furthermore, Cortelazzo et al. (2015) reported that oxidative stress could play an important role in influencing the state of the erythrocyte plasma membrane and its cytoskeleton. Authors of this study identified in RTT patients significant changes in the redox state for nearly all membrane cytoskeletal proteins and a reduced expression of more than half of membrane cytoskeletal proteins (with particular reference to five proteins showing expression changes proportional to the severity of MECP2 mutations: spectrin alpha chain, adducin, erythrocyte membrane protein 55 kDa, fructose-bisphosphate aldolase and tropomodulin). In this study, changes observed in membrane cytoskeletal proteins appear to be related to changes in cells shapes (leptocytes) and involve both vertical and horizontal interactions: this consideration is suggested by the peculiar morphological features of leptocytes, which appear slightly larger and elongated (possible involvement of horizontal interactions) and more thin (possible involvement of vertical interactions). This study also shows that an omega-3 PUFA supplement has got a strong impact on restoration of post-translational oxidative

modifications affecting proteins of critical importance for erythrocytes shape maintenance and structural stability.

1.3.2. Erythrocyte morphological alterations in ASD patients

After discovering altered erythrocyte morphologies in RTT patients, the same authors reported high percentage of **abnormal RBC shapes**, mainly elliptocytes, in patients with "classical" autism through SEM analysis (Fig. 1.22). In this study, morphologically abnormal RBC in autistic subjects were related to oxidative damage of erythrocyte membrane. Indeed, the study also highlighted an **increase in F2-isoprostanes** and in **4-hydroxynoneal protein adducts** of erythrocyte membrane. F2-isoprostanes are considered as specific and reliable markers of oxidative stress (Ciccoli et al., 2012). They are compounds similar to F2 prostaglandin originated from the peroxidation, catalyzed by free radicals, of arachidonic acid esterified in phospholipids. Instead, 4-hydroxynoneal is a highly reactive toxic aldehyde which, depending on its concentration and localization, can be considered as a "second toxic messenger" which disseminates and augments initial free radicals events. Indeed, 4-hydroxynoneal is generated as a degradation product following free radicals attack on omega-6 PUFA (arachidonic acid, linoleic acid) and can in turn covalently bind proteins, phospholipids and DNA; in particular, it easily reacts with nucleophilic groups of amino acid side chains and its covalent bond to proteins leads to alterations in their structure and biological activity (Ciccoli et al., 2013, 2012). The study by Ciccoli et al. (2013) also highlighted a **reduction and oxidative damage of β-**

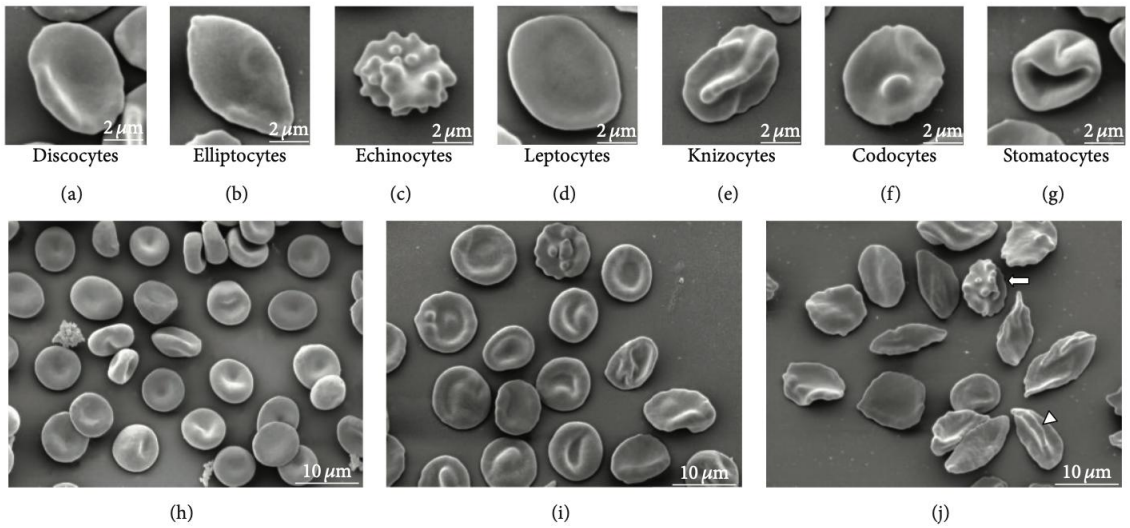

Figure 1.22 - Abnormal erythrocyte shapes in classical autism at the scanning electron microscopy (SEM). (a): normal discocyte shape; (b) to (g): main shape-altered RBC observed in autistic patients; (h): healthy controls; (i): a typical morphological pattern in nonautistic neurodevelopmental disorders (NA-NDDs); (j): typical picture in an autistic patient with predominant elliptocytosis. Symbols indicate intermediate-shaped RBC: the arrow indicates a disco-echinocyte shape, while the arrowhead indicates the presence of a knizo-echinocyte shape in autistic patients, bars correspond to 2 μm in (a) to (g) upper panels and to 10 μm in the (h), (i), and (j) lower panels (Ciccoli et al., 2013).

actin protein of erythrocyte membrane. The authors therefore hypothesize that these three factors (erythrocyte abnormalities, oxidative damage to membrane, and β-actin alterations) may be a promising candidate in the identification of new biological markers for ASD diagnostic process.

A subsequent study (Bolotta et al., 2018a) confirmed the results obtained by Ciccoli et al. (2013) about abnormally shaped erythrocytes in autistic children through SEM analysis (Fig. 1.23). In this work, more than 50% of ASD children's erythrocytes assumes an altered morphology, and codocytes and star-shaped cells were responsible for approximately 30% of all abnormalities. It is important to note that ASD patients' RBC do not show characteristic or bizarre morphologies; rather they have got a higher percentage of altered morphologies found in smaller quantities in control subjects' RBC.

In the study by Bolotta et al. (2018a) it is also shown that changes in RBC shapes are independent from the anticoagulant used (Na_2-EDTA or heparin), confirming that only a long storage in Na_2-EDTA could affect erythrocyte shape. In this study, changes in RBC shape were also shown not to be affected by treatment procedures prior to glutaraldehyde fixation, such as repeated centrifugations

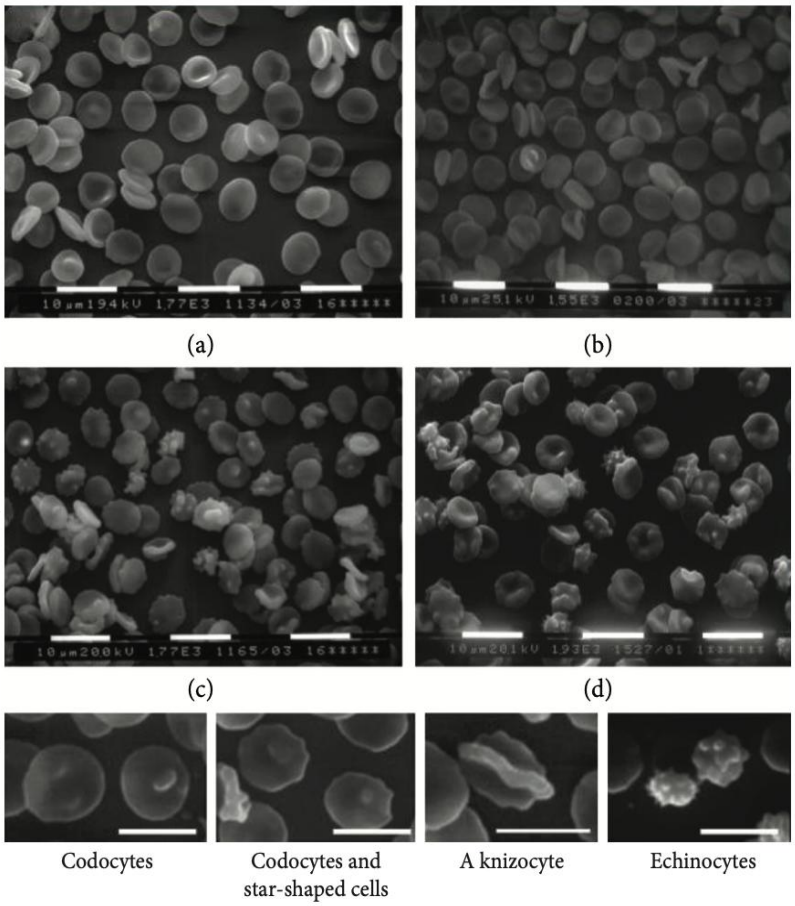

Figure 1.23 - Erythrocyte morphology at SEM. (a, b) Normal erythrocyte morphology (discocytes) found in neurotypically developing children. (c, d) A variety of abnormal red cell morphologies found in children with ASD. Bottom panel: a gallery of abnormal erythrocyte morphologies (Bolotta et al., 2018a).

carried out in saline buffer. These observations suggest that abnormal erythrocyte shapes found by the authors do not represent artifacts.

The authors also showed that in vitro treatment with antioxidants (tocotrienol and Q10) for 24 h brings the percentage of morphotypic erythrocytes in ASD patients from 47.5% to 82%, thus restoring normal morphology to control levels (Fig. 1.24). Considering this evidence and the fact that, in their study, the presence of quantitative differences in proteins playing a key role in membrane-cytoskeleton organization (beta-actin, band 3, stomatin) was not detected between ASD subjects and neurotypical development subjects, the authors hypothesize the presence in ASD subjects of oxidative stress-induced modifications in membrane proteins, or their associations, rather than quantitative differences.

Given that inside RBC there is a high cellular concentration of oxygen and hemoglobin (which has the peculiar property of undergoing self-oxidation), these cells represent a constant source of super oxide production and for this reason they are highly susceptible to oxidative damage. Despite this, as far as is known so far, oxidative stress in ASD children does not seem to be generated within

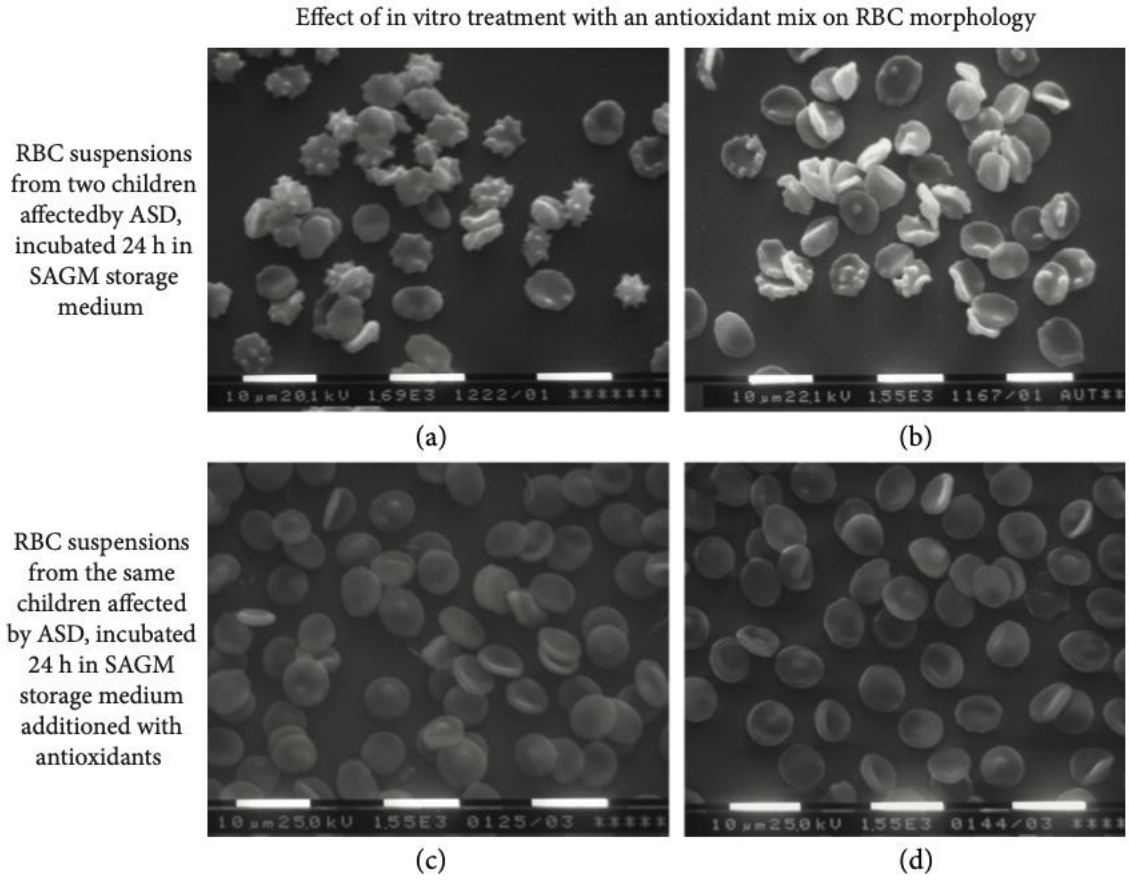

Figure 1.24 - Effect of antioxidant treatment on the morphology of RBC from children affected by autistic spectrum disorder. (a, b) Before the in vitro 24 h treatment. (c, d) After the treatment with tocotrienol and Q10. The percentage of abnormally shaped erythrocytes is clearly decreased.

erythrocytes and could be a consequence of chronic (neuro)inflammation. It is interesting to note that, despite several alterations in ASD erythrocytes, oxidative stress in these cells seems to be limited in its consequences, as suggested by the fact that no clinical signs of reduced erythrocyte activity (e.g. oxygenation) have been described so far in ASD patients (Bolotta et al., 2018a).

1.4. Computer-assisted methods for erythrocyte images analysis

Computer-assisted analysis of erythrocyte images has attracted considerable attention in the field of research on hematological diseases. Traditionally, the blood test under microscope, which plays an important role in the diagnosis of hematological and non-hematological pathologies, is carried out manually by expert operators. However, measuring the distribution of different RBC in a blood sample involves a great amount of tedious, time-consuming and repetitive work. The accuracy of recognition largely depends on subjective factors such as operator experience and fatigue. This limits the translation of results from studies concerning deformability, filterability and morphology of erythrocytes from research laboratories to clinical diagnosis (Durant et al., 2017; Nithyaa et al., 2013; Vromen and McCane, 2009; Wang, 2011). Hence the need to automate the entire process. This would not only reduce the hematologists workload but would also lead to accurate results in significantly shorter periods of time. The automation of this task would therefore be very useful for improving the hematological procedure and accelerating diagnosis of many diseases (Nithyaa et al., 2013).

1.4.1. Erythrocyte image segmentation and computerized recognition of erythrocyte morphotypes

In the computerized image analysis process, segmentation represents the bridge between the original image and intelligent processing (Wang, 2011). Segmentation is the operation through which an image is reduced into multiple segments (consisting of sets of pixels) corresponding to the object of interest. Relevant research has been done in trying to solve this problem, and several segmentation algorithms have been proposed in recent years. Among them there are segmentation methods applied to the analysis of several cell types or biological images. In fact, some practical applications of image segmentation are used in medical imaging to study anatomical structures, diagnosis, treatment planning or to locate tumors or other pathologies. There are several medical image segmentation techniques used for blood cells analysis. The goal of blood cell segmentation is to extract images of cells from complex backgrounds (Adollah et al., 2008; Devi et al., 2015; Vromen and McCane, 2009). Regarding erythrocytes in particular, many methods of segmentation have been reported for their

identification and enumeration. These methods use different techniques including morphological operations, filtering, thresholding and edge detection. Many of erythrocyte segmentation and counting methods use the Circular Hough Transform (CHT; Hegde et al., 2018). The Hough transform is a technique for extracting features of an object used in image analysis that is generally applied after edge detection (Maitra et al., 2012). Edge detection includes several mathematical operators that are designed to identify edges in the image. They are defined as segments consisting of digital image's pixels of rapid variation in intensity (Lindeberg, 2011; Szeliski, 2020). The Hough transform is computed using a primitive basic graphical, which in this case is a circle; each circle with the desired radius is drawn on each contours' edge point (i.e. the maximum points of the transform are highlighted), they are those circles that rest on the cellular contour already detected (Barducci and Pippi, 1999). If the cellular radius is known, the CHT can be applied to find the center of the circle, knowing the number of points that fall on cell perimeter, that is, on cell edge; if the cellular radius is not known, the points of image center and the radius are searched in the three dimensions (x, y and z), complicating the calculation (Mazalan et al., 2013).

Historically, efforts for automatic morphological classification have used statistical models based on an input derived in a similar way to the analysis performed by morphologists. Known as *feature engineering*, this science tries to quantify predetermined morphological features from digital images used as inputs for prediction algorithms (Durant et al., 2017). In the literature, most of the studies concerning automatic classification of erythrocytes are based on light microscopy images. The first study concerning this topic was the work by Bacus et al. (1976). It explored the feasibility of developing a technique for automatic classification of abnormal erythrocytes, applying digital image processing and pattern recognition techniques, and in particular gray level thresholding and labeling of contiguous regions for the segmentation step. Thresholding is a very simple image segmentation technique through which, starting from a grayscale or RGB (red, green, blue) image, a binary image (black and white) is produced. Image pixels are labeled as belonging to the object or to the background if their value is respectively higher or lower than an arbitrary cutoff value. In the work by Bacus et al. (1976), after segmentation step erythrocytes analyzed were then characterized by variations in size, roundness, presence of spicules, eccentricity, and distribution of gray levels in the center of the cell. These features allowed the authors to separate erythrocytes into distinct subgroups, each consisting of morphologically similar cells: (a) macrocytes, (b) normocytes, (c) schistocytes, (d) acanthocytes and burr cells, (d) microcytes and spherocytes, (e) elliptocytes, sickle cells, pencil-shaped cells and (f) target cells. The authors obtained an accuracy range from 88 to 100% for the subgroups considered, suggesting that a classification into multiple erythrocyte categories was possible.

The implementation of feature engineering was also explored by Albertini et al. (2003), who created a statistical analysis model based on 4 preselected erythrocyte indices (chromogenic index, size index, biconcavity index and density profile) to discriminate between 7 morphological classes (discocytes, echinocytes, microcytes, macrocytes, ovalocytes, target cell, cup-shaped cell) from images acquired with a light microscope processed with an image processing software. Results of the study showed an agreement of 70% between actual and predicted classification.

Many of the studies in the literature regarding automatic classification of erythrocytes about processing of light microscopy images are based on samples obtained from patients with anemia. The first of such works was carried out by Westerman & Bacus (1983), who reported the accurate evaluation of different erythrocyte morphological classes (normocytes, macrocytes, target cells and sickle cells) in peripheral blood images of adults with sickle cell disease. The automatic image processing system identifies cells based on size, hemoglobin content, central pallor and shape (circularity, elongation, spicularity) and provides concentrations of the different erythrocyte morphotypes. In this work, counts of sickle cells obtained through this image processing system were compared with counts obtained through more traditional methods of analysis, highlighting a close correlation. The authors also demonstrated a very good reproducibility of results obtained through image processing, analyzing nine pairs of duplicate slides, prepared simultaneously, from four different patients, and observing a high correlation between the two slides for cell types.

More recently, Chandrasiri e Samarasinghe (2014) have introduced an accurate fully automatic system to identify four types of red cell morphological abnormalities found in anemic patients (elliptocytes, macrocytes, hypochromic microcytes and spherocytes), and to carry out blood cell counts. Identification of erythrocyte typologies was achieved by extracting different erythrocyte features such as area, shape, central pallor, and rectangular factor. The new segmentation method introduced by the authors was developed above all to solve the problem of identification and separation of overlapping cells. The accuracy in the erythrocyte count was found to be greater than 99%, the range of accuracy in identifying abnormal erythrocyte morphologies was instead 91-97%.

Nithyaa et al. (2013) reported the automatic recognition of disease such as malaria, sickle cell anemia, elephantiasis, trypanosomiasis and polycythemiasis by extracting statistical features of blood smears images acquired under light microscope and processed using MATLAB software. Results of classification appeared more accurate and in synchrony with the results obtained by operators.

In the work by Bala and Doegar (2015) image processing techniques were applied to erythrocyte images to count normal and abnormal cells (sickle cells) using watershed segmentation. Watershed segmentation is a segmentation method whose name derives from an expression relating to geography: in fact, this algorithm operates on a digital grayscale image as if it were a topographic

surface with reliefs. Gray level of pixels indicates the elevation of these reliefs. All surface's pixels at a given minimum constitute a hydrographic basin associated with that minimum and the watersheds, defined as dams that divide adjacent hydrographic basins, determine boundaries that separate different image regions (Arganda-Carreras and Legland, 2014; Bala and Doegar, 2015). After applying watershed segmentation, a shape factor for each cell was calculated for the differentiation between normal and abnormal cells. Additionally, erythrocyte contour plots were drawn to visualize sickle cell and target cells. The simulation of this technique was performed on MATLAB 2013a.

Marzuki et al. (2017) proposed a method for identification of thalassemia using an active contour method for segmentation of blood smear images acquired under light microscope. The active contour model, also called *snake*s, is a structure in the context of computerized vision used for the delineation of an object profile starting from a potentially noisy two-dimensional image. A snake is a deformable tab influenced by image's constraints and forces that push it towards object's contours, and by internal forces that resist deformation (Kass et al., 1988). Following the segmentation phase, Marzuki et al. (2017) used the roundness and eccentricity of erythrocytes to identify abnormal cells, reporting the identification accuracy around 90%.

Sharma et al. (2016) proposed a method for recognition of sickle cells, dacryocytes and elliptocytes with the aim of detecting sickle cell anemia and thalassemia. The proposed method involves the acquisition of thin blood smear images under light microscope, and then their pre-processing by applying a filter to remove image noise. This is followed by watershed segmentation method for separation of overlapping erythrocytes and morphological operations to improve the image. Subsequently, feature extraction was carried out, including the metric value (measurement of object roundness) and the relationship between the two axes. Finally, for classification based on extracted features, *a k-nearest neighbor* classifier was used. Nearest neighbors represent a very simple technique of non-parametric supervised learning (i.e., it does not involve any learning parameters). On the contrary, the training examples are all maintained and at the time of estimation the closest k examples are found and averaged to produce the output (Szeliski, 2020), where k is an arbitrary number established by the developer. Using this technique, Sharma et al. (2016) reported the accuracy of their classifier to be around 80% with about 88% sensitivity.

Implementation of feature engineering was also studied as an input for modern machine learning algorithms, including artificial neural networks (Durant et al., 2017). Artificial neural networks are computer systems that mimic biological neural computation model (Szeliski, 2020). For example, these systems were used by Khot e Prasad (2012) in their work, which is based on development of an image analysis system for detection of erythrocyte abnormalities - such as sickle cells, teardrop

erythrocytes, acanthocytes, Howell-Jolly's bodies (nuclear residues consisting of erythrocyte nucleus's fragments which, after its expulsion, remain in the cytoplasm), macrocytes and microcytes - in blood samples images acquired under light microscope. For their purpose, the authors first applied color normalization on images, then extracted different physical red cell features. The latter were used by the authors for artificial neural networks training. The accuracy achieved by their classifier was 73.57%.

In their work, Kim et al. (2001) presented a new scheme capable of automatically analyzing, counting and classifying red and white blood cells efficiently in images of human peripheral blood samples. After identifying RBC and white blood cells in blood samples images acquired with a CCD camera connected to microscope, the authors extracted cell features. Cells were then classified using a back-propagation learning-based neural network model. The authors considered five different categories of white blood cells (neutrophils, eosinophils, basophils, lymphocytes, and monocytes) and fifteen different classes of RBC (normal, crenate, burr cells, target cells, spherocytes, oat-shaped, ovalocytes, sickle cells, stomatocytes, blister cells, helmet-shaped, pinched cells, drop-shaped, filamentous, triangular; Suppl. Fig. 4-5). Classification of RBC was based on boundary and inner border information. On average, recognition rate of RBC and white blood cells was 91% and 81% respectively.

Tomari et al. (2014) proposed a computer-assisted system to automate the process of RBC detection and identification from light microscope images of blood smears. First, erythrocyte-related regions were extracted from the background using global threshold method applied on images converted to monochromatic representation. The global threshold is a segmentation method by which the object can be extracted from the background through a simple operation that compares image values with a threshold value (Rogowska, 2009). After applying the global threshold method, noise and holes in erythrocytes were deleted through morphological filters and labeling of connected components. Subsequently, information relating to erythrocytes was extracted based on geometric properties. Finally, erythrocytes were classified as normal or abnormal using an artificial neural network classifier. The proposed method was tested on blood cells images, proving to be an effective and reliable system for classifying normal and abnormal erythrocytes (accuracy: 82%).

The commercial system CellaVision (*CellaVision® DM9600*) offers an image analysis solution for erythrocytes based on artificial neural networks, using 80 predetermined object's features to classify cells starting from 17 morphological classes, within 4 qualitative categories (Durant et al., 2017). However, reports published for erythrocytes classification with CellaVision demonstrate limited specificity and variable accuracy without re-classification by operators (Criel et al., 2016; Egelé et al., 2016).

Erythrocyte classification based on their morphological changes was also addressed using deep learning methods. Deep learning is a machine learning and artificial intelligence's research field that is based on different levels of representation, corresponding to hierarchies of factors or concepts' features, where high-level concepts are defined on the basis of low-level ones.

Durant et al. (2017) implemented a deep convolutional neural network for erythrocyte classification consisting of more than 150 layers. Convolutional neural networks are based on patterns that mimic human visual recognition fields, known as filters, which are mathematically convoluted with the image of interest. Unlike traditional artificial neural networks that take inputs along a whole image simultaneously, convolutional filters operate on limited areas to produce "feature maps" of local patterns, which are combined through successive layers into more summary features (Zeiler and Fergus, 2014). Durant et al. (2017) reported an accuracy of 90.60% for the correct classification.

Wąsowicz et al. (2017) proposed a method for automatic erythrocytes counting and classification in images of stained human blood smears. These authors used advanced image processing methods for erythrocyte identification and separation, followed by eigenfaces method coupled to neural networks for erythrocyte classification into normal and abnormal. The eigenfaces method allows to describe an image through a much smaller set of representative images (eigenfaces). Eigenfaces can be considered as a set of standardized elements of human face, obtained from the static analysis of many faces. Then, each face can be reconstructed as a linear combination of these eigenfaces plus an average image of the faces. In the case of the problem considered by Wąsowicz et al. (2017), blood cells (normal and abnormal) were analyzed by the algorithm instead of human faces. Vectors obtained by eigenfaces method, representing images of blood cells, were used to train the neural network. Accuracy and sensitivity of the system reached 88%, along with 90% specificity.

1.4.2. Computerized processing of erythrocytes SEM images

With regard to erythrocytes SEM images, Vromen and McCane (2009) proposed a segmentation method called the *contour tracing based approach* for automatic identification of normal erythrocytes' contours. This method focuses on solving the problem of correctly tracing overlapping erythrocytes' edges, based on information regarding changes in image brightness. The incorporation of this model into the contour tracing process allowed the authors to include a priori knowledge regarding shapes assumed by contours, rather than simply following the major change in brightness. The authors used a second order polynomial model with a simple Bayesian approach to ensure smooth contours and an ellipse fitting procedure to remove noising contours. Of all outlines detected, 95.7% are correct, with a 0.6% false negative rate, and 4.3% false positive rates.

The contour tracing approach described by Vromen and McCane (2009) was subsequently used by Wang (2011) with the aim of developing a sophisticated algorithm to accurately classify RBC into different groups. This method of recognition and classification was implemented based on RBC' real shape. In fact, unlike conventional segmentation methods for erythrocyte images, based on two-dimensional grayscale images, segmentation strategy proposed by Wang (2011) is based on extraction of surface features. In this work, first, the distribution of erythrocyte shapes was estimated from SEM images. Subsequently, the approach based on contour tracing described previously by Vromen and McCane (2009) for erythrocytes recognition and extraction was applied. Each three-dimensional cell shape was then reconstructed as 3D height field using the *Shape from Shading* technique (Fig. 1.25). It involves the computation of the three-dimensional shape of a surface starting from the brightness of the black and white image of that surface. Surface was then divided into different types: peak, pit, ridge, valley, flat, minimal surface, saddle ridge and saddle valley. 3D height field was then used to segment cell surface through a surface fitting segmentation algorithm (Fig. 1.26). Eventually, cells were divided into different categories according to the distribution of their surface types. Finally, a classifier was built to discriminate erythrocytes with regular morphology from those with irregular morphology, by means of a linear combination SVM (Support-Vector Machines). SVM is an automatic learning model that use supervised learning methods in which algorithm categorizes a set of training examples (Yturralde et al., 2020). In the work by Wang (2011) irregular erythrocyte shapes are seen as input samples from the classifier. The combined classifier shows efficient and easily to be implemented.

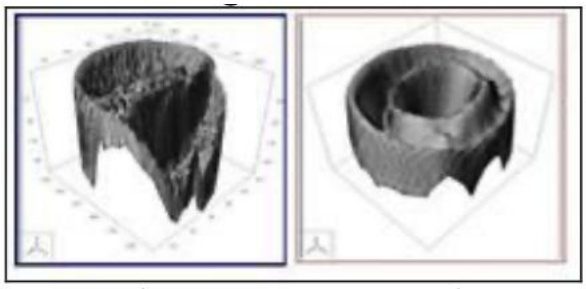

Figure 1.25 - Two three-dimensional erythrocyte shapes reconstructed using the *Shape from Shading* technique (Wang, 2011).

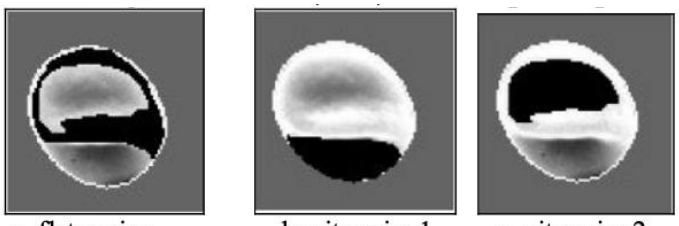

Figure 1.26 - Example of segmentation result using surface fitting method. The cell is perfectly segmented into three isolated parts. There are two different types of resulting surfaces: flat and pit (Wang, 2011).

The same author published another work (Wang, 2017), in which the distribution features of curved surfaces are extracted using a three-dimensional reconstruction of RBC shape. The methodology proposed in this study consists, first of all, in a reduction of noise (white lines of a grid superimposed on the SEM image) through local median filtering techniques (Fig. 1.27). After that, superimposed cells are extracted individually using the guided contour tracing method. A three-dimensional

reconstruction is then performed using the linear approximation and finally the shape distribution is established by calculating the curvatures (Fig. 1.28).

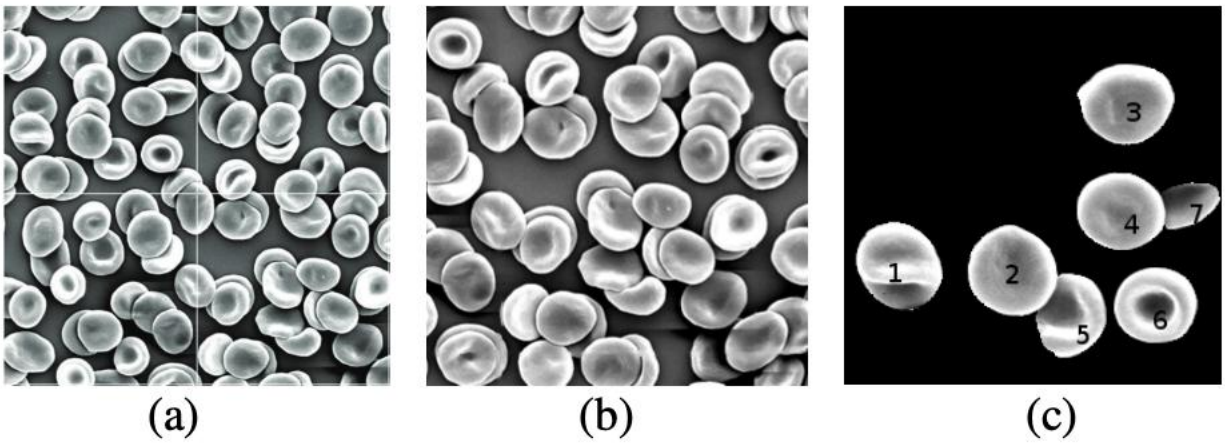

Figure 1.27 - Individually extracted cells in a SEM image. (a) noise image, (b) filtered image, (c) single cell image (Wang, 2017).

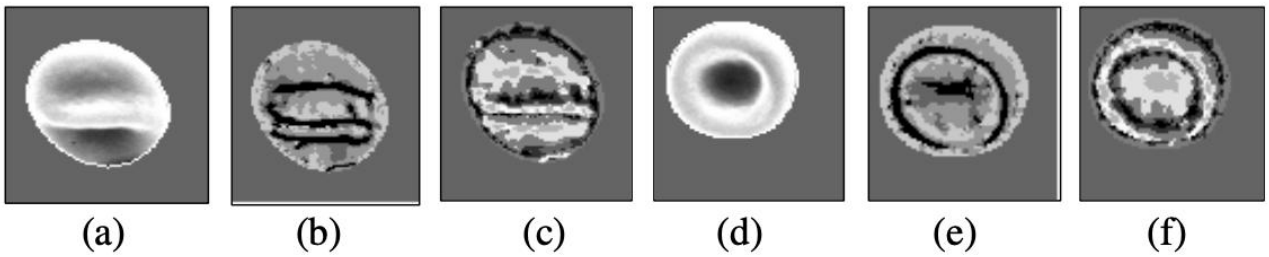

Fig. 1.28 - Results of curvature calculation. (a) and (d) are images of original cells, (b) and (e) are the main curvatures of (a) and (d): the black regions represent the main curvature value while the gray regions represent the value of secondary curvature. The region with the main curvature corresponds to the most prominent part of the shape change. (c) and (f) are mean curvature and Gaussian curvature illustration of (a) and (d) (Wang, 2017).

Instead, the work by Bhowmick et al. (2013) focused on the development of a computer-assisted method for classifying anemia types in SEM images of peripheral blood samples. This approach is based on morphological features and erythrocyte structure, such as shape, size and variation in the surface appearance of abnormal erythrocytes. In this study, erythrocytes were separated from blood samples and then processed for SEM imaging. Subsequently, erythrocytes were segmented from SEM images using gray level thresholding, morphological operators, and watershed algorithms (Fig. 1.29). Subsequently, erythrocytes in the foreground were extracted and then, through morphological operators, the unwanted and distorted cells were eliminated from the image. Starting from correctly segmented cells, features of the external surface profile and geometric features (area, perimeter, eccentricity, compactness) were extracted for anemia identification. All the extracted features were statistically evaluated with the intention of characterizing 7 classes of erythrocytes (1 normal and 6 of anemia: normochromic and hypochromic macrocytic, hypochromic and normochromic normocytic, normochromic and hypochromic microcytic). Finally, to automatically predict the

different types of anemia, a Bayesian classification (a statistical learning technique whereby pathology can be probabilistically predicted) was trained and tested.

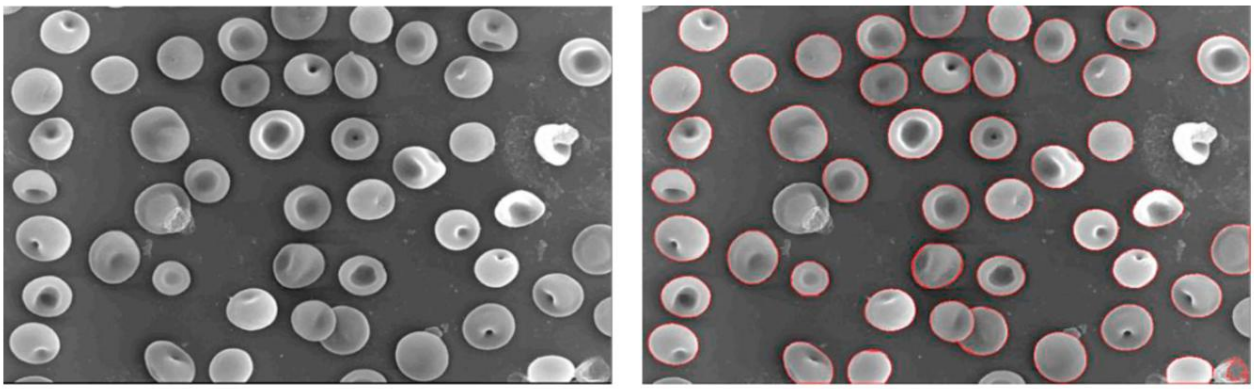

Figure 1.29 - Segmentation of erythrocytes SEM images. (a) input SEM image and (b) segmented image (Bhowmick et al., 2013).

The same research team also developed a computer-assisted methodology for thalassemia screening using multi-layer perceptron (MLP) neural networks based on morphological features of RBC from SEM images (Fig. 1.30; Bhowmick et al., 2012). This approach consists of several steps: (1) a segmentation step using watershed algorithms for RBC segmentation in SEM images, (2) a feature extraction and selection step by which features are extracted on the basis of morphological changes of RBC in thalassemia using different mathematical measures (9 out of 17 morphological features were found to be statistically significant in discriminating normal and thalassemic RBC), (3) a final classification step in which RBC were classified into two groups - normal and thalassemia - using MLP neural networks. The proposed machine learning methodology provides 90.38% sensitivity, 98.81% specificity, 98.93% positive predictive value and 94.59% overall accuracy for thalassemia screening.

1.5. Aim of the work

Because prior scanning electron microscopy (SEM) evidence show a significant percentage of altered erythrocyte shapes in ASD subjects (Bolotta et al., 2018a; Ciccoli et al., 2013), we want to investigate if the erythrocyte morphological alterations found in ASD patients can represent a biomarker to use as a component of a screening for early diagnosis of this group of disease. In absence of laboratory tests, ASD diagnosis is currently carried out by neuropsychiatric evaluation based on specific screenings, symptoms, clinical observations, and behavioral evaluations. Early diagnosis and prediction are however essential for ASD. In fact, several rehabilitative interventions with proven efficacy in reducing core symptoms of these disorders are currently available, but their clinical course

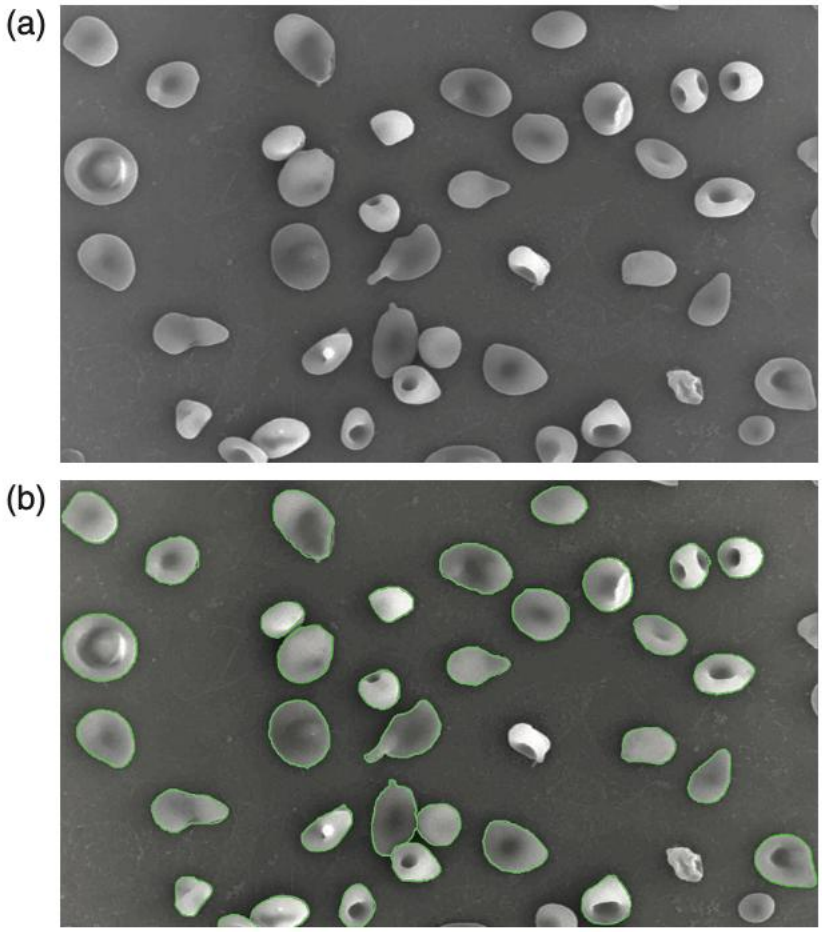

Figure 1.30 - Segmentation of erythrocytes SEM images from patients with thalassemia. (a) input SEM image and (b) segmented image (Bhowmick et al., 2012).

depends fundamentally on how early the intervention is established. Substantial improvements can be achieved by intensive behavioral intervention initiated prior to 24 months of age as neural plasticity is increased and challenging behavior are less prominent (Shen et al., 2019). Prior to the onset of behavioral abnormalities, behavioral interventions could conceivably minimize their severity - with a better neurodevelopmental outcome for the patient and improved performances in most life contexts - or even result in prevention of a full-blown autism (Dawson, 2008; Estes et al., 2015; Fossum et al., 2018; Kandasami et al., 2017; Kasari et al., 2015; Shen et al., 2019). However, without any biological determination, early diagnostics are difficult and subjective (Brett et al., 2016).

In order to test the hypothesis according to which the biomarker *erythrocyte morphological alterations* may be used as a component of a screening for early ASD diagnosis, it is necessary to carry out many bloods drawn from young children in a practical way. For this reason, our research team has developed a new preparation and imaging method, based on acupuncture technique, for SEM analysis of blood samples. This method, minimally invasive and cheap, consists in aspirating by a capillary tube (preloaded with anticoagulant solution) a drop of peripheral blood obtained from

a prick in a human subject's fingertip (Fortunato, 2016). Furthermore, in order to achieve the ultimate goal of our research project is necessary to manually search, count and classify a large number of RBC for each one of the numerous blood sample considered, as demonstrated by a previous thesis work (part of our research project; Zarra, 2017). As can be easily understood, this type of work takes a long time during which an operator is subject to fatigue, with possible repercussions on the precision and accuracy of the analysis. Therefore, for the optimization of our research work, an automated computer system which would relieve the operator from performing the analysis manually would be very important. Hence, it was thought to develop a new computerized morphometric analysis system for a quick and accurate work of semi-automatic detection and classification of human erythrocyte morphological variants in SEM micrographs. This software was developed precisely to operate on SEM micrographs obtained from blood samples prepared through the novel acupuncture method.

The aim of the present thesis work is to present the results achieved so far within this broad project: the optimization of the protocol for blood micro-samples preparation, the preliminary results of the clinical study about erythrocyte morphological changes in pediatric ASD patients and, above all, the development and validation of our new software for erythrocyte phenotyping in SEM micrographs.

2. MATERIALS AND METHODS

2.1. Ethical authorization

This study was conducted according to the guidelines established in the Declaration of Helsinki and all procedures involving human patients have been approved by the Local Ethics Committee (Local Health Company Umbria 2, prot. N. 19000/20/OV of 30/06/2020).

2.2. Protocol for blood samples preparation aimed at RBC morphological analysis by SEM

Blood samples for SEM were prepared using the following protocol which was previously fine-tuned in a master degree thesis work (Fortunato, 2016; Fig. 2.1):

- loading of a disposable 10 µl capillary (Hirshmann Instruments™) equipped with a pro-pipette (Hirschmann Instruments™) with anticoagulant solution (0.05 M sodium citrate in physiological solution). To do this, the capillary must be immersed in the anticoagulant solution and the latter rises by capillarity along the tube. The capillary must be loaded with anticoagulant solution for ¾ of its volume;
- disinfection of patient's fingertip;
- puncture of the fingertip, through an automatic lancing device (Roche Diabetes Care) or through a disposable lancet (Ascensia Diabetes Care Single-Let®);
- aspiration of the blood drop from the puncture site. To do this, the capillary with anticoagulant solution must be brought close to the blood drop and the latter rises by capillarity along the tube. To facilitate this operation, the capillary must be tilted with respect to the puncture site. If the meniscus of the anticoagulant solution does not contact the blood drop, the latter may not be aspirated. In this case it is necessary to occlude the hole at the upper end of the pro-pipette with a finger and apply a slight pressure on the upper part of the pro-pipette itself. The capillary must be loaded for ¼ of its capacity with the blood material;
- deposition of the mixture of blood and anticoagulant solution on the support, consisting of a glass slide (7x15mm) or a rectangle of aclar film (7x10 mm). To carry out this operation, the capillary must be brought close to the support, while the hole at the end of the pro-pipette must be occluded with a finger and at the same time a slight pressure must be applied on the upper part of the pro-

pipette itself. By this operation, the content of the capillary is deposited on the support. After that, it is necessary to wait 30 seconds to achieve better adhesion of the blood material to the support;

- immersion of the support with the RBC adhering to it in a 2 ml tube containing a solution of 2.5% glutaraldehyde in 0.1 M phosphate buffer (which will be stored at 4°C) for the ultrastructural preservation of the blood material. In fact, once the blood is taken from the human subject, the erythrocytes morphology begins to change over time. To avoid these morphological changes, instant erythrocyte fixation is an important step (Bhowmick et al., 2013).

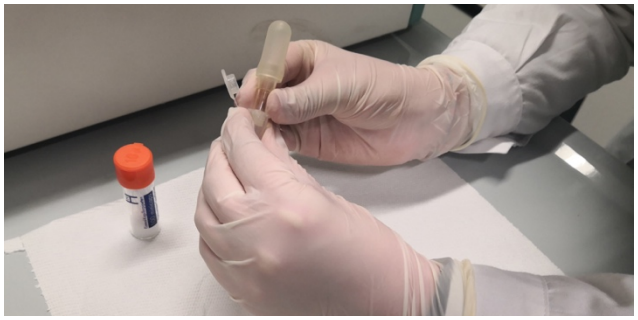

A. Loading of a disposable 10 µl capillary equipped with a pro-pipette with an anticoagulant solution.

B. Fingertip disinfection.

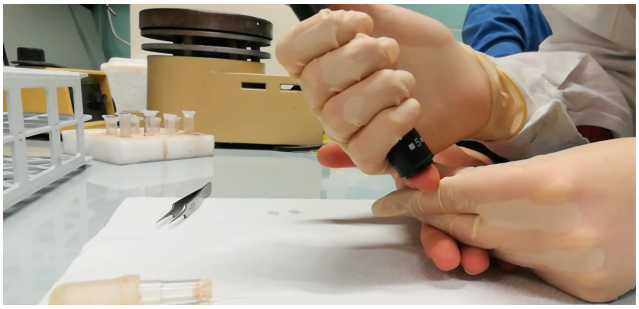

C. Puncture of the fingertip.

D. Blood drop aspiration.

E. Deposition of capillary's content on the support.

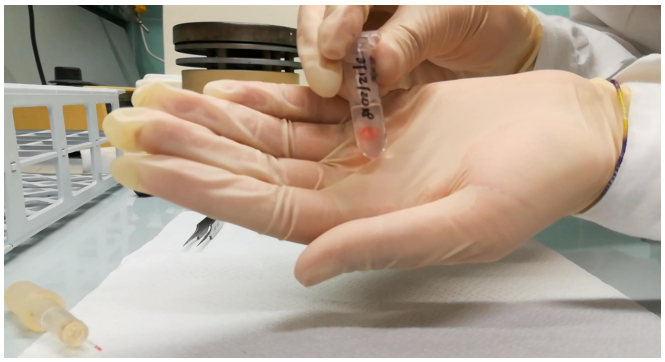

F. Immersion of the support in fixative solution.

Figure 2.1 – Preparation of blood samples for SEM analysis.

After this preparation, the samples were subjected to the following procedure for morphometric analysis by SEM:

- two consecutive washes at 4°C with 0.1M phosphate buffer (pH 7.2), each one for 10 minutes;
- fixation of lipid components in a 1% osmium tetroxide aqueous solution at 4 ° C for 1 hour;
- two washes at 4°C with water, each one for 10 minutes;
- dehydration in ascending scale of ethyl alcohol (30%, 50%, 70%, 90%, 100%), each step for 10 minutes at 4°C, and a further step in 100% ethyl alcohol at room temperature;
- CO_2 critical point drying using a CPD010 unit (Balzers Union, Liechtenstein);
- mounting of dried samples on aluminum stubs (Tedpella, Inc);
- metallization with gold by means of a sputtering device MED010 (Balzers Union, Liechtenstein);
- analysis at either SEM XL20 (Philips, Eindhoven, Netherlands), SEM XL30 (Philips, Eindhoven, Netherlands) or SEM Quanta 400 (FEI – Field Electron and Ion Company, Hillsboro, Oregon).

2.3. Pilot study on ASD patients and healthy volunteers

Through the protocol just described blood samples from 4 healthy volunteers (age: 21-25 years old) and 15 ASD patients were obtained. Table 2.1 shows the clinical data concerning ASD patients, whose neuropsychiatric evaluation was performed through CARS2 (Childhood Autism Rating Scale, Second edition, Schopler et al., 2010). The CARS2-ST (ST for "Standard Form") is used with younger or lower functioning individuals, while CARS2-HF (HF for "High Functioning") is used

#	Gender	Age	Diagnosis	Comorbidities
1	Unavailable	4	HFA (high functioning autism)	///
2	Unavailable	3.5	ASD moderate-severe	///
3	M	3.5	ASD moderate-severe	///
4	M	5.5	ASD moderate-severe	///
5	Unavailable	5	ASD mild-moderate	///
6	M	3.5	ASD moderate	///
7	M	9	ASD mild-moderate	///
8	M	7	ASD mild-moderate	hearing loss
9	Unavailable	3.5	ASD moderate-severe	///
10	M	7	LFA (low functioning autism) - MFA (medium functioning autism)	///
11	M	3.5	ASD moderate-severe	///
12	M	5	ASD mild	///
13	M	5	ASD mild-moderate	///
14	F	4	ASD mild-moderate	Attention-Deficit/Hyperactivity Disorder (ADHD)
15	F	3.5	ASD mild	///

Table 2.1 - Clinical data of patients enrolled for the pilot study. This table shows for each patient: gender, age at enrollment, diagnosis, and eventual comorbidities.

with higher functioning individuals[1]. The CARS2 scale is divided into 15 items relating to the main behavioral areas, each of which must be assigned a variable score from 1 to 4 in seven steps. The sum of all scores gives an overall value, which indicates the presence or the absence of the disease and – if present – also its severity.

2.4. Optimization of the protocol for blood samples preparation aimed at SEM morphological analysis

For the optimization of blood samples preparation protocol, 30 experimental tests were carried out starting from 19 blood samples from 7 different healthy volunteers. For protocol optimization, the following 3 variables were tested:

- *Times of permanence of the blood material in the fixative*
    - 1 day;
    - 4 days;
    - 5 days;
    - 7 days;
    - 2 months;
- *Support cleaning methodology*
    - by optical lens tissue;
    - by sonication (support dipped in acetone);
- *Deposition times of blood material on the support*
    - 30 seconds;
    - 1 minute;
    - 2 minutes;
    - 10 minutes;
    - 15 minutes.

[1] In ASD patients the level of functioning is indexed by overall intelligence quotient (IQ). High functioning autism (HFA) can be thought as within one standard deviation of population mean IQ (that is, IQ of 85 or above); medium functioning autism (MFA) can be thought of as between one and three standard deviations below the population mean (that is, IQ of 55– 84). Low functioning autism (LFA) can be thought of below this (that is, IQ of 54 or below; Baron-Cohen, 2006).

2.5. Neuropsychiatric parameters evaluated and clinical data collected for the clinical study

Blood samples from ASD patients enrolled for the clinical study were processed through the optimized protocol. For this clinical study, doctors of the Child and Adolescent Neuropsychiatry Unit of the local health unit Umbria 2 in Terni took care of the enrollment of the patients. Their team, also made up of psychologists and nurses, carried out the neuropsychiatric visit and the collection of biological material for each patient enrolled. They organized their work in sessions of 2-4 patients at a time, dedicating about half of their working day to this activity. The neuropsychiatric assessment of patients made use of a tool for the ASD diagnosis, that is nationally and internationally recognized: the Autism Diagnostic Observation Schedule (ADOS; Lord et al., 2012). It consists of a standardized and semi-structured assessment of communication, social interaction, play and imaginative use of materials for ASD subjects. ADOS consists of standardized activities that allow the examiner to observe behaviors critical for ASD diagnosis at different chronological ages and for different levels of development. Through this tool it is possible to evaluate behavior of the subject in response to stimulus situations and activities predetermined by the test, in order to obtain information on relational and communicative features. This test is based on an interactive evaluation context, capable of generating situations that provide stimuli on a social level, through play and verbal exchanges. The ADOS includes four different modules depending on the level of expressive language of the subject and the age. The scores are organized according to 5 main groups: A. Language and communication; B. Mutual social interaction; C. Game; D. Stereotypical behaviors and narrow interests; E. Other abnormal behaviors. ADOS score along with other clinical data of the enrolled patients are shown in Table 2.2.

#	Gender	Date of enrollment	Age at enrollment	Autism level at enrollment	Diagnosis date	Age at diagnosis	ADOS-2 score	Comparison score	Comorbidities
1	M	20/04/21	4 y 11 m	2	July 2020	4 y 2 m	10	3 mild	Attention-Deficit/Hyperactivity Disorder (ADHD)
2	M	20/04/21	5 y	3	Spet 2020	3 y 6 m	20	7 moderate	severe intellectual disability
3	M	20/04/21	6 y 6 m	3	July 2019	3 y 10 m	22	7 moderate	intellectual disability
4	F	20/04/21	5 y	1	April 2019	3 y 1 m	14	4 mild	///
5	M	02/08/21	17 y 4 m	1	unavailable	unavailable	unavailable	not available	dyslexia
6	M	02/08/21	6 y 3 m	3	April 2019	3 y 11 m	18	6 moderate	intellectual disability
7	M	02/08/21	6 y 10 m	2	April 2017	2 y 6 m	15	5 moderate	intellectual disability
8	M	19/11/21	10 y 2 m	3	June 2014	2 y 9 m	15	5 moderate	intellectual disability
9	M	19/11/21	7 y 1 m	2	December 2017	3 y 2 m	17	7 moderate	intellectual disability
10	M	30/12/21	8 y 4 m	1	March 2017	3 y 8 m	13	4 mild	///
11	M	30/12/21	6 y 6 m	3	April 2019	3 y 10 m	16	6 moderate	intellectual disability
12	M	30/12/21	11 y 5 m	2	May 2021	10 y 10 m	13	6 moderate	intellectual disability, stutter

Table 2.2 - Clinical data of patients enrolled for the clinical study. This table shows for each patient: gender, date of enrollment, age at enrollment, autism level at enrollment, diagnosis date, age at diagnosis, ADOS-2 score, comparison score, and eventual comorbidities. The comparison score, corresponding to a symptom level of the disorder, allows to standardize the ADOS modules.

2.6. SEM analysis of erythrocyte morphology

The analysis of erythrocyte morphology was carried out counting ≥ 1000 erythrocytes at a magnification of 1500x (for the SEM XL20 and XL30) and of 3000x (for SEM Quanta400) setting the microscopes at an electron accelerating voltage of 10kV. A *Numbers* file with a format previously created was used for each sample to classify erythrocytes observed at the SEM in the different morphological classes (an example is shown in Fig. 2.2). Counting and classification of erythrocytes

erythrocytes per area	echinocytes I	echinocytes II	echinocytes III	acanthocytes	spherocytes	sphero-stomatocytes	stomatocytes	leptocytes
12					1			
8					2			
11								
8					1			
11								
11					1			
11								
3					1			
3								
1								
2								
6								
2								
2								
1								
2								
1001	0	0	0	0	85	2	6	0
%	0.00	0.00	0.00	0.00	8.49	0.20	0.60	0.00

leptocytes	knizocytes	target cells	elliptocytes	microcytes	macrocytes	other anomalies	total abnormal morphotypes	discocytes
							1	11
							2	6
			1				1	10
	1						2	6
		1		1		1	3	8
		1					2	9
	1						1	10
							1	2
		1		1			2	1
							0	1
							0	2
	1						1	5
							0	2
							0	2
							0	1
							0	2
0	24	29	17	25	0	32	220	781
0.00	2.40	2.90	1.70	2.50	0.00	3.20	21.98	78.02

Figure 2.2 - Numbers table used to classify erythrocytes observed at SEM in the corresponding morphological classes. Each row of the table corresponds to a red blood cells area observed at SEM. The total number of erythrocytes present in the area was entered in the first column; the following columns, related to the different erythrocyte morphological classes, were filled with the corresponding number of erythrocytes. The sum of morphologically abnormal erythrocytes present in the area was automatically calculated in the penultimate column. In the last column, the number of discocytes present in the field was automatically calculated (by subtracting to the number of total erythrocytes the number of morphologically abnormal erythrocytes). In the last rows of the table, the total number of erythrocytes counted in the sample, the number of total erythrocytes for each morphological class and for the total of morphologically abnormal erythrocytes were calculated by adding the values present in all the previous rows of the table. For the latter two types of values, the respective percentage compared to the total number of erythrocytes counted in the sample was automatically calculated and displayed in the last row of the table.

in different SEM areas was done by proceeding from right to left, then moving down and continuing from left to right, and so on following a regular rasterized pattern.

2.7. Intra-operator variability of erythrocyte SEM analysis

In order to gauge intra-assay variability, relative standard deviation (SD; %) were used for triplicate measurements on n=3 different blood samples as assessed by the same operator (Suppl. Tab. 1). Data were extracted from the corresponding descriptive summary statistics. Variance values were calculated for the 15 main morphologic categories of circulating erythrocyte shapes observed at the SEM analysis: echinocyte I, echinocyte II, echinocyte III, acanthocyte, spherocyte, stomatocyte, sphero-stomatocyte, elliptocyte, macrocyte, microcyte, target cell, leptocyte, knizocyte, discocyte, other shapes, as well as total abnormal morphotypes. The relationship between cell shape frequency (as expressed as percentage value of total observed shapes) and relative SD (%) was tested by univariate regression analysis models. Analysis of variance was performed by one-way ANOVA test. The MedCalc version 20.013 statistical software package (*MedCalc Software Ltd.,* Ostend, Belgium) was used for data analysis, and a two-tailed $p < 0.05$ was considered to indicate statistical significance.

2.8. SEM micrographs for software development and evaluation

A micrograph obtained by an electron microscope fitted with digital imaging tools consists in computer file with information about a two-dimensional grid of pixels. Pixels are the smallest individual elements of the image, and they are characterized by numerical values. These values represent local intensities of image brightness and may range from white to black. Therefore, a digital image is an ordered set of rows and columns composed by pixels: the width and height of the image are defined by a number of pixels in the abscissa (rows) and a number of pixels in the ordinate (columns; Ferreira and Rasband, 2012). The digital images of RBC used for the development of our computer system, aimed at automatic recognition and classification of human erythrocytes in SEM micrographs, are in grayscale and measure:

- 3872x2904 pixels, when acquired at SEM XL20;
- 4096x3200 pixels, when acquired at SEM XL30;
- 3584x3301 pixels, when acquired at SEM Quanta 400.[2]

[2] The digital images, despite having been acquired through different SEM, do not have great differences in their resolution (and therefore in their pixel size).

Fig. 2.3 shows a sample SEM image of those used in our study. There are some notable features concerning these images that make our problem - that is, to recognize and semi-autonomously classify erythrocytes in these images - meaningful and challenging. On the one hand, the images produced by the SEM are of very high quality and high contrast. In these images there are varying shading, generated by the detection source. On the other hand, erythrocytes take on irregular shapes. In fact, although many cells are more or less circular in shape with smooth contours, some cells are not, and the latter type is the one of particular interest in the study of both ASD and other pathologies with abnormally shaped erythrocytes. SEM images of the blood drop consist of two regions: background and foreground. The foreground consists of erythrocytes, white blood cells, platelets and plasma protein aggregates, while the background consists of the support surface (aclar or glass). Most of the

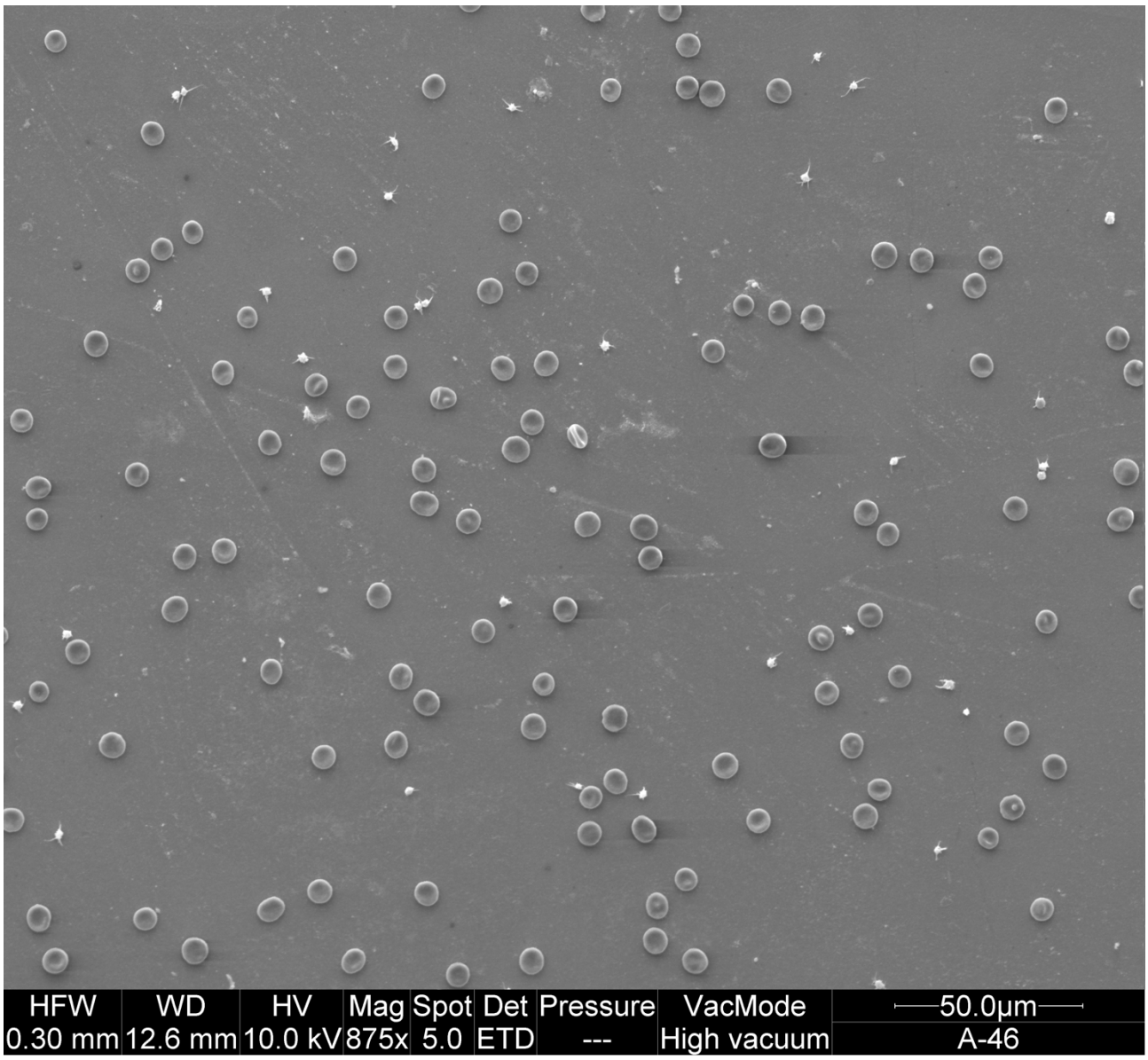

Figure 2.3 - Example of SEM micrograph of erythrocytes used for software development and evaluation.

cells are located perpendicular to the electron beam and, in the case of discocytes, show a flat surface with an almost circular shape.

2.9. SEM XL20 and SEM XL30 set-up for micrographs acquisition

- Magnification: 400x;
- sample placed orthogonally to the detector (tilt angle: 0°);
- acceleration voltage: 10.0 kV;
- spotsize: 5;
- working distance: 12 mm;
- contrast: about 12;
- brightness: about 47;
- file saving in .TIF format;

2.10. SEM Quanta 400 set-up for micrographs acquisition

- Magnification: 1000x;
- sample placed orthogonally to the detector (tilt angle: 0°);
- acceleration voltage: 10.0 kV-15.0 kV;
- spotsize: 5;
- working distance: 10 mm;
- contrast: about 12;
- brightnes: about 47;
- file saving in .TIF format;

2.11. Protocol for micrographs acquisition

The following requirements have proved to be indispensable for software development and use and they can be considered as an essential part of the standard protocol for SEM micrographs acquisition (which was previously established in a master degree thesis work; Pianigiani, 2018):

- images must contain an adequate number of blood cells: not too low, so as not to acquire too much micrographs and thus increase time for acquisition and analysis, nor too high in order to guarantee quick and simple data processing;
- the magnification used must allow, on the one hand, to accurately reconstruct the erythrocyte shape and, on the other hand, to show in a same image a number of cells suitable for optimizing the algorithm calculation speed (and consequently the image analysis process). For this reason, the decision was made to use a 400x magnification for SEM XL20 and for SEM XL30, which corresponds, as it was subsequently determined, to a 1000x magnification for SEM Quanta 400[3];
- there must be as few erythrocyte stacks (i.e., cells superimposed on each other) as possible and acquisitions must be made away from the edges of the blood drop, in order to avoid aggregated erythrocytes;
- the background (represented by the aclar/glass support placed on the stub) must be less noisy as possible, i.e. there must be the least possible quantity of plasma protein residues, fibrin clots and improperly metallized components;
- the contrast and brightness levels must be within the thresholds denoted by the SEM videoscope.

2.12. Software development: general overview

For software development, Microsoft Visual Studio 2010 was used as a working environment, and the C++ language as a programming language. The development steps of our computer-assisted tool for phenotyping erythrocytes in SEM micrographs that involved computer programming were carried out by Professor Alessandro Barducci (I.C.S. Srl). The first step within the image processing and analysis procedure for the development of a software whose purpose was to detect and classify erythrocytes in SEM micrographs, is represented by the *image segmentation* process. Segmentation consists of dividing the image into geometrically coherent segments (consisting of sets of pixels) corresponding to the object of interest in the image (in this case, an erythrocyte). The goal of segmentation is to simplify the representation of the original image into another one which is more meaningful and easier to analyze (Adollah et al., 2008). The segmentation represents a crucial step, since the accuracy of the subsequent steps such as feature extraction and erythrocyte morphotypes classification depend on the precision of single RBC segmentation process. Segmentation of this type

[3] That is, by acquiring photos of a sample through SEM Quanta 400, these photos will show cells having the same dimensions in mm as those in photos acquired at SEM XL20 and SEM XL30.

of images is a difficult and challenging problem due to the complex shaping of the cells recorded in digital microscope images (Tomari et al., 2014).

Following the segmentation step, the image was subjected to the so-called *instance classification*, that is the process by which all the segments belonging to the same *instance* (object of interest in the image, in this case an erythrocyte) are grouped into connected spatial units and are labeled one by one. Instance classification process therefore recognizes RBC as physical entities distinct from each other that at that point can also be labeled and counted.

Following the instance classification step, there was a step of features extraction, where the features were represented by cellular morphological parameters such as area, eccentricity, length of the cell perimeter, number of crosses, to name a few. Subsequently, a training step of the software was performed in order to make the semi-automatic classification of erythrocyte morphotypes possible. During this step, each recognized instance was manually assigned by the operator to a specific erythrocyte morphological type. At the end of this process, processing data are saved in a text or excel file, in which a certain set of numerical values - related to the identified cell morphological parameters - is associated with an erythrocyte, which is named according to its corresponding morphological class.

Based on the processing data, an erythrocyte classifier was developed with the aim of semi-automatically establishing which phenotypic class the instance belongs to, i.e. morphologically typical class or morphotype-atypical class with the different subclasses.

2.13. Data set for software development and evaluation

For the early stages of software development, 180 micrographs were used. These micrographs were obtained from blood samples of ASD patients enrolled for the pilot study. This first set of micrographs were acquired at the SEM XL20 using the acquisition protocol and the setup previously illustrated.

To evaluate the software ability of single erythrocytes detection in SEM micrographs, 112 photos acquired at SEM XL20 from 3 different samples were analyzed. These samples were obtained from ASD patients enrolled for the pilot study. The total number of erythrocytes in this set of photos was 3˙000, ranging from a minimum of 876 to a maximum of 1˙070 and an average of 1˙000 erythrocytes per sample.

To evaluate the software performance of detecting the total number of erythrocytes in SEM images, 380 photos acquired at SEM XL20 or at SEM Quanta 400 from 10 different samples were analyzed. These samples were obtained from ASD patients enrolled for the pilot study. The total number of

erythrocytes in this set of photos was 1˙3131, ranging from a minimum of 777 to a maximum of 2˙071 and around 1˙353 of erythrocytes per sample in average.

For the software training step, 215 photos acquired at SEM Quanta400 from 4 different samples (from ASD patients enrolled for the pilot study) plus 24 photos acquired at SEM XL-30 from a single sample (from ASD patient enrolled for the clinical study) were used[4]. The total number of erythrocytes which have been manually assigned to the respective morphological classes was 5˙244, ranging from a minimum of 250 to a maximum of 1˙253 in the different samples and an average of about 834 erythrocytes per sample. Most of these processing data were then used for the construction of scatterplot graphs, which allow to view erythrocytes belonging to different morphological classes according to the values of their respective morphological parameters differently coupled to each other. Information obtained from these graphs were used to guide the development of algorithms to cover the last calculation step: semi-automatic morphometric classification of erythrocytes in different morphological categories. After having combined all the processing data in a single excel file, so that in each sheet the data of erythrocytes belonging to a specific erythrocyte class were grouped, 59 scatterplots were constructed in total.

To evaluate the software's ability to recognize blobs (irregularities which resemble protuberances found sometimes in abnormal RBC), 28 target cells were analyzed in SEM micrographs from two different pathological samples. In particular, the number of false negatives (target cells with unrecognized blobs) and true positives (target cells with recognized blobs) were calculated with the relative percentages.

2.14. Erythrocyte morphotypes classifier

For transitioning from the sets of morphological parameters to the classification of erythrocyte morphotypes, a crossroad between the criterions of Bayes classification and the Neyman-Pearson classification was used. To represent morphological parameters at a probabilistic level, normal (Gaussian) probability densities and Poisson's probability densities were used for continuous variables (eg: area, perimeter) and for integers variables (eg: the number of crosses) respectively. A priori probabilities (likelihood ratio) were established empirically using the data generated by software training step.

The problem of erythrocyte morphotypes classification is a typical problem of decision theory. On the one hand, there are n erythrocyte classes A_k $k = 1, 2, ..., n$ (discocytes, elliptocytes, microcytes,

[4] It was possible to use images acquired at SEM XL30 for software training after having brought their resolution to the same value as those of the micrographs acquired at SEM Quanta 400 using Photoshop.

etc). On the other hand, there are m morphological parameters p_k k = 1, 2, ..., m associated with each erythrocyte. We want to define the conditional probability $P_k = P\,(A_k \mid \vec{p}\,)$ of belonging to the generic class A_k assuming that the vector of parameters $\vec{p}$ has occurred. We will choose as class $\tilde{A}$ the one that produces the highest membership probability value $\tilde{A} = \max\{A_k\}_k$.

A priori probabilities for each class are usually a rectangular function, that is, the function assumes 1.0 as value for morphological variable's certain ranges of values (domain), and 0.0 for values outside the domain. The range of values allowed for each morphological parameter is established by calculating statistical moments for each erythrocyte morphological class (Fig. 2.4), starting from the processing data of the available erythrocyte population. In particular, the permitted range of values is established by calculating the min-max interval on the population of erythrocytes observed. In the presence of a small number of erythrocytes per class (<100), the interval is extended by 10% on both extremes (0.9min-1.1max). Conversely, a safety margin of 3% (0.97min-1.03max) is taken in the case of a large number of erythrocytes per class. The exception is the "other anomaly" class which, for the a priori probability, admits any value of morphological parameters, but with a lower probability, equal to 0.03. The Poisson and Gaussian probability densities are entirely defined by a few statistical moments: only by the mean (μ) for the first one

$$(f_{m(k)}(m) = \frac{\mu^m}{m!} e^{-\mu})$$

and by the mean and standard deviation (σ) for the second one

$$(f_{x(k)}(x) = \frac{1}{\sqrt{2\pi\sigma_x^2}} e^{-\frac{(x-\mu_x)^2}{2\sigma_x^2}}).$$

In the case of multivariate probability density, the entire covariance matrix (Σ) is needed

$$(f_{\vec{x}(k)}(\vec{x}) = \frac{1}{[2\pi\|\Sigma\|]^{\frac{n}{2}}} e^{-\frac{(\vec{x}-\mu_x)^T\,\Sigma^{-1}(\vec{x}-\mu_x)}{2\sigma_x^2}}).$$

By using estimates of statistical moments, a priori probabilities and probability densities of each morphological class were defined. A multivariate probability density - which can include 3, 4 or 5 morphological parameters among the following: area, perimeter, maximum diameter, eccentricity, boundary Routh Mean Square - was defined. For all the other morphological parameters, variables are considered to be statistically independent. Based on this knowledge, it was possible to carry out the classification calculation (decision making).

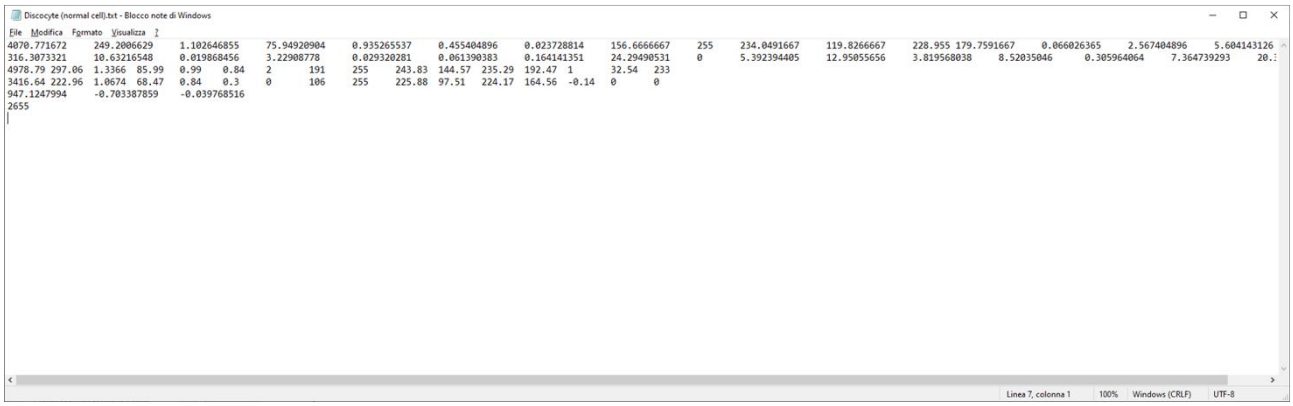

Figure 2.4 - Statistical moments for erythrocyte morphological class. This figure shows statistical moments for discocyte class as an example. For each column (relating to a morphological parameter) the following are displayed: mean value (first row), standard deviation (second row), maximum value (third row), minimum value (fourth row), covariances (fifth row), number of erythrocytes considered (sixth row).

3. RESULTS AND DISCUSSION

3.1. Pilot study on ASD patients and healthy volunteers

The pilot study conducted on healthy volunteers and ASD patients allowed to prepare and observe by SEM a set of RBC samples and to produce morphometric data from either healthy controls (Suppl. Tab. 2) and ASD patients (Suppl. Tab. 3). The pilot study also enabled to start testing the applicability on ASD patients of the mini-invasive protocol for blood samples collection and preparation aimed at SEM morphological analysis. Chart 3.1 and Chart 3.2 show the results, in terms of average values, obtained from the RBC morphological analysis at SEM for the 7 blood samples from healthy volunteers and for the 15 blood samples from ASD patients, respectively. These data are discussed in the paragraph "Erythrocyte shape analysis at SEM: discussion" of the present chapter.

3.2. Optimization of the protocol for blood samples preparation aimed at RBC morphological analysis by SEM

3.2.1. Times of permanence of the blood material in the fixative

It has been observed that storage of erythrocytes in fixative solution for up to 2 months does not negatively affect their morphological appearance (Fig. 3.1). This feature of the method allows to have adequate time available for the samples transmission from the sampling points to the electron microscopy laboratory, where their subsequent processing takes place.

3.2.2. Nature of the support

Glass was chosen as a support for the adhesion of the blood material, since through experimental tests carried out previously it was found that rectangles of aclar film were subject to breakage following exposure to the SEM electron beam (Fig. 3.2).

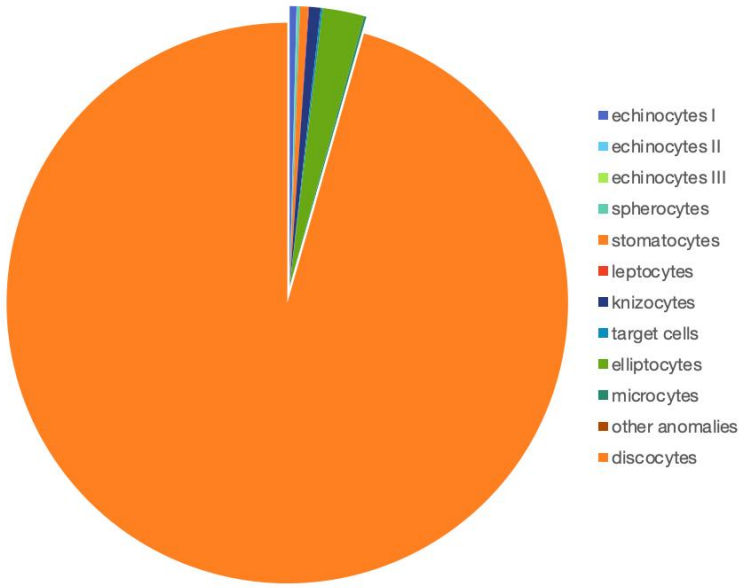

Chart 3.1 – RBC population type in healthy volunteers' blood samples prepared through the original version of protocol for blood samples preparation aimed at RBC morphological analysis by SEM.

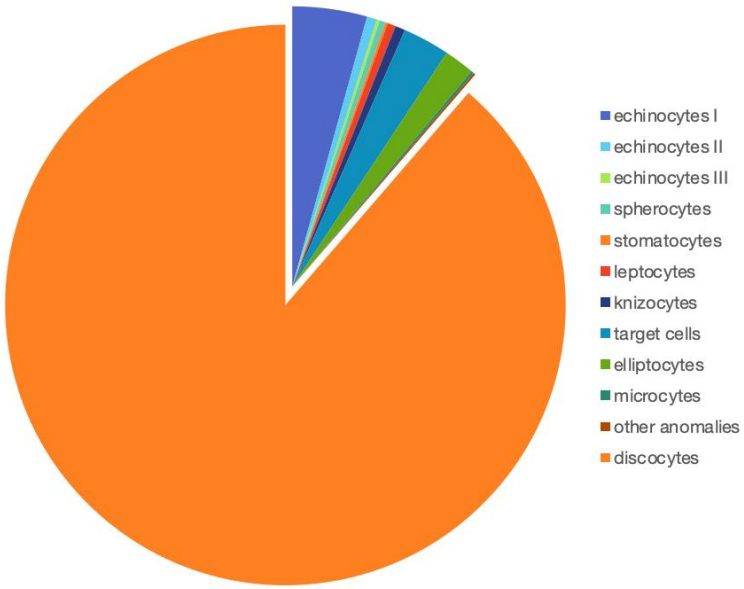

Chart 3.2 - RBC population type in ASD patients' blood samples prepared through the original version of protocol for blood samples preparation aimed at RBC morphological analysis by SEM.

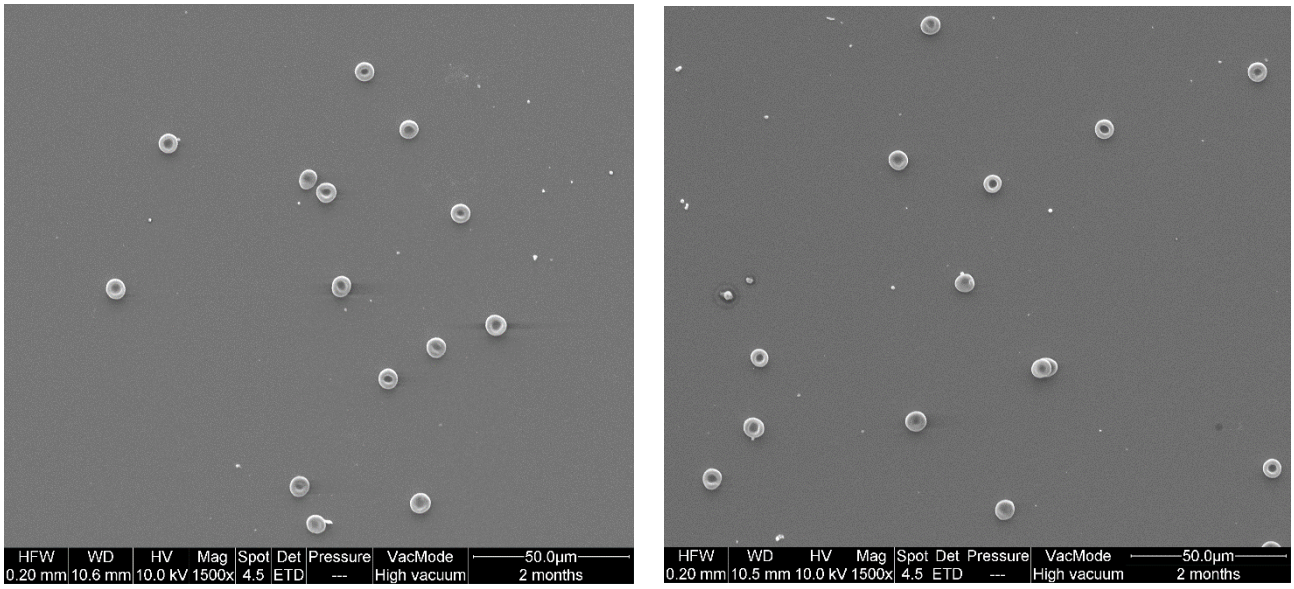

Figure 3.1 - SEM micrographs of RBC samples stored in fixative liquid for 2 months. RBC morphological appearance is preserved.

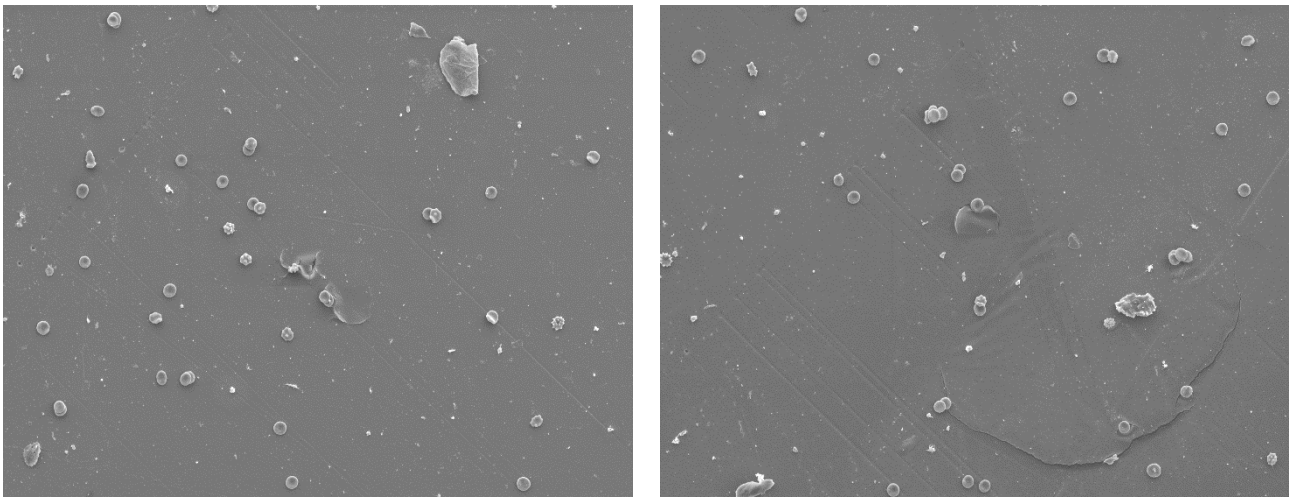

Figure 3.2 – Blood samples prepared through the original version of the protocol with aclar film used as support for RBC adhesion. The figure shows breaks in the aclar because of exposure to the SEM electron beam.

3.2.3. Cleaning methodology of the support

The best cleaning method of the support is found to be by optical lens tissue. This method, involving a coarser cleaning than the standard sonication method used in other routine preparation protocols, turned out as being more efficient in allowing the adhesion of a greater number of RBC to the support (Fig. 3.3).

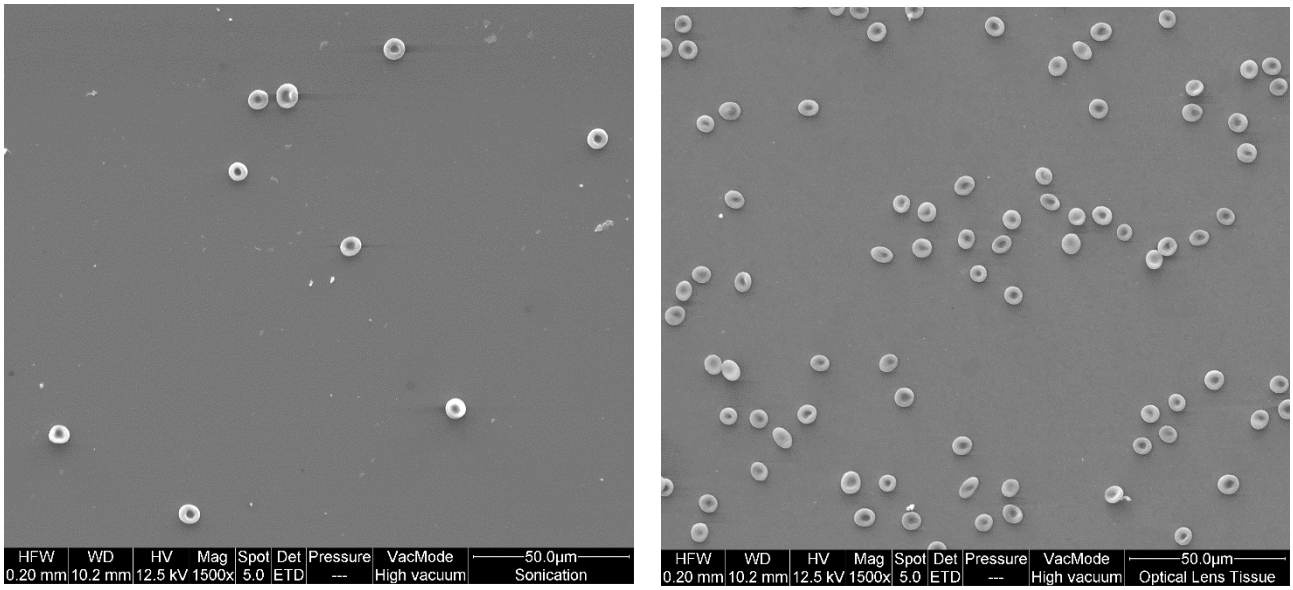

Figure 3.3 – Cleaning methodology of the support. The figure shows a small number of RBC adhering to the glass slide cleaned by sonication (on the left) and a greater number of RBC adhering to the glass slide cleaned by optical lens tissue (on the right).

3.2.4. Deposition times of blood material on the support

It was observed that the optimal deposition time of the blood material on the support, among those tested, was 15 minutes. This time allows the adhesion of an adequate number of cells to the support without, at the same time, causing the blood drop to dry out (Fig. 3.4).

3.2.5. Indicative protocol

After performing the acupuncture and taking the blood drop with a capillary preloaded with 0.05 M sodium citrate in physiological solution, the optimized protocol is structured as follows:

- Addition of the capillary content to 25 µl of fixative solution (2.5% glutaraldehyde in 0.1 M phosphate buffer) contained in a 1.5 ml tube;
- Centrifugation at 1˙000 RPM for 5 minutes (ALC microCENTRIFUGETTE®4214), then aspiration of the supernatant and addition of 10 µl of 0.1 M phosphate buffer (repeat this step 3 times);
- Deposition on the support of 2 µl of RBC diluted in buffer (15 minutes in a humid chamber at 4 ° C);
- Drip addition of 2 µl of 1% osmium (15 minutes at 4 ° C);
- Rinses in water (2x5 minutes) and then processing according to the original protocol described in “materials and methods”.

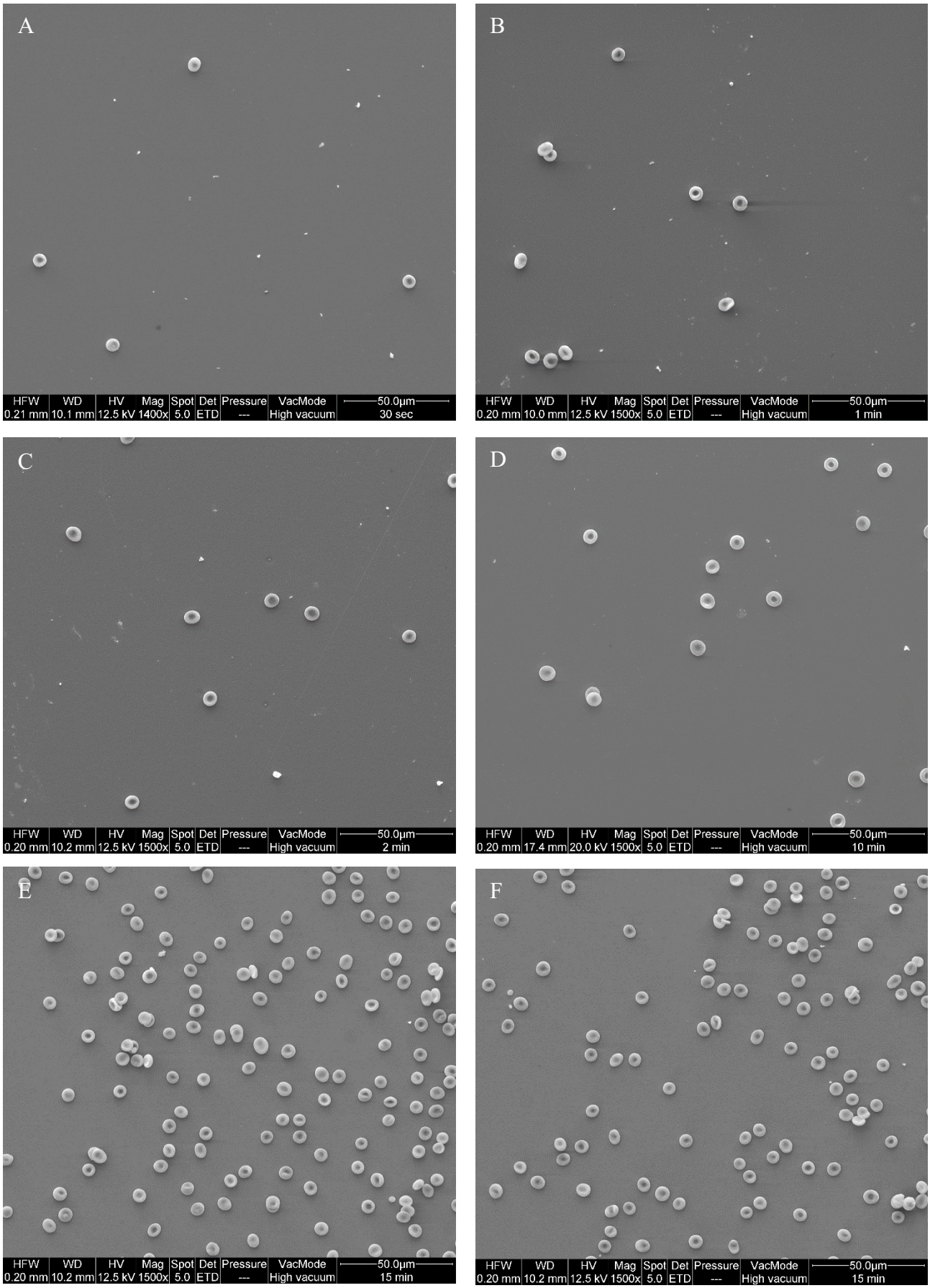

Figure 3.4 – Deposition times of blood material on the support. The figure shows different samples with RBC adhered to the slide according to different deposition times of the blood material on the support: 30 seconds (A), 1 minute (B), 2 minutes (C), 10 minutes (D), 15 minutes (E,F). It is noted that the deposition time of 15 minutes allows to obtain better results in terms of density of RBC adhered to the support.

The original protocol for blood samples preparation aimed at RBC morphological analysis by SEM suffers mainly from two limitations. The first one is represented by the possibility, starting from an acupuncture, to prepare only a single blood sample for subsequent processing and SEM imaging. The second limitation is that sometimes the RBC field appeared noisy under SEM due to the presence of plasma proteins. This presence was a problem especially during development and use of our software, altering the cellular contour recognized by the program or creating lighter regions within the cellular area. To overcome these limitations, it was decided to change the protocol of blood samples preparation in such a way that the fixation of the blood material took place in suspension, before the deposition of the blood material itself on the support. This feature of the optimized protocol allows to obtain samples in suspension that can be worked safely in the laboratory. Indeed, the optimized protocol allows on the one hand, to make multiple SEM samples starting from a single blood drop obtained through a single acupuncture, and on the other hand to separate the RBC from plasma by centrifugation, obtaining cleaner samples (Fig. 3.5).

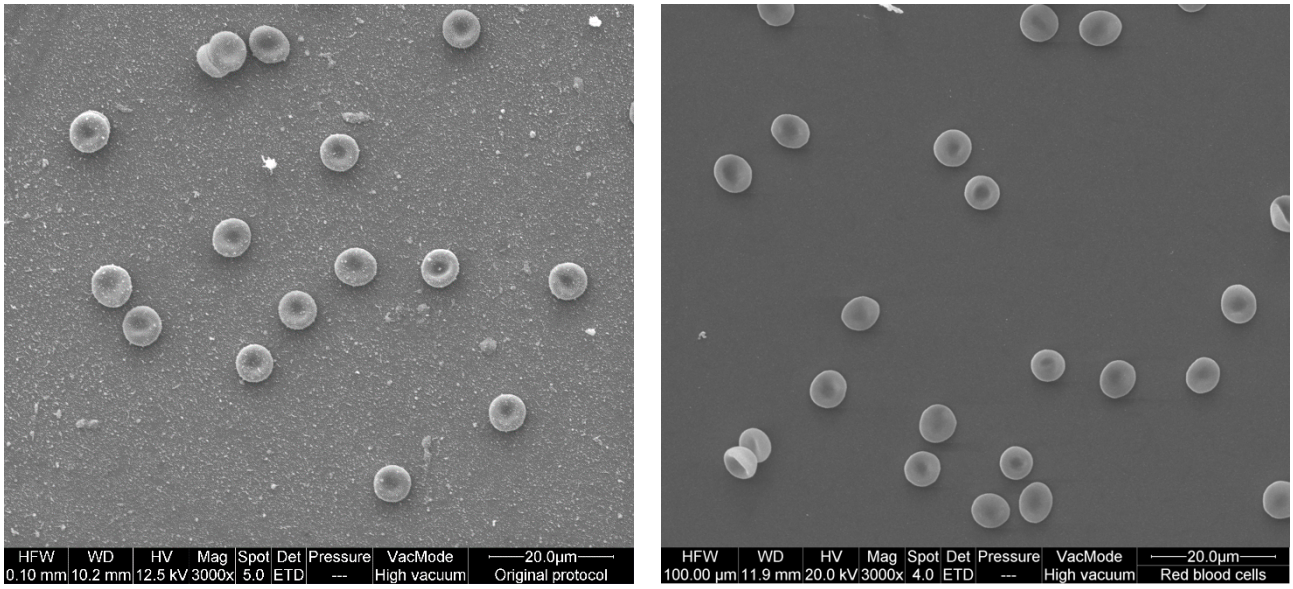

Figure 3.5 - SEM micrographs of blood samples prepared using the two different versions of the protocol in comparison. It is possible to notice the higher level of cleanliness of the samples prepared using the optimized protocol (figure on the right) compared to the samples prepared using the protocol in its original version (figure on the left).

In this new procedure, the step of immersion of the support with blood material in the fixative liquid - which guaranteed the simple and definitive adhesion of the RBC on the support - was not present anymore. This leads to two consequences. The first one is that during the development of the new protocol, among other things, the optimal time needed for adequate sedimentation of the RBC on the support could be tested and established. The second consequence is that manual steps that hospital staff must carry out at the time of acupuncture are reduced compared to what was foreseen by the original version of the protocol. Indeed, hospital staff are no longer expected to handle the support -

on which the blood material was previously deposited - with a pair of tweezers to submerge it in the fixative liquid: it is sufficient for hospital staff to settle the contents of the capillary directly into the fixative solution. Results of RBC samples from two healthy volunteers prepared by the optimized protocol and visualized at SEM are shown in Fig. 3.6. As can be seen, the normal erythrocyte morphology is preserved and, unlike classical preparation methods, where RBC are highly overlapping (Vromen and McCane, 2009), our method of preparing blood samples produced in most cases a monolayer of cells with rare aggregates. The optimized protocol was initially tested to prepare blood samples from 4 healthy volunteers, to then realize a set of RBC morphometric data about these healthy controls at SEM (Suppl. Tab. 4). Chart 3.3 shows the results obtained from the RBC morphological analysis of these samples, in terms of average values.

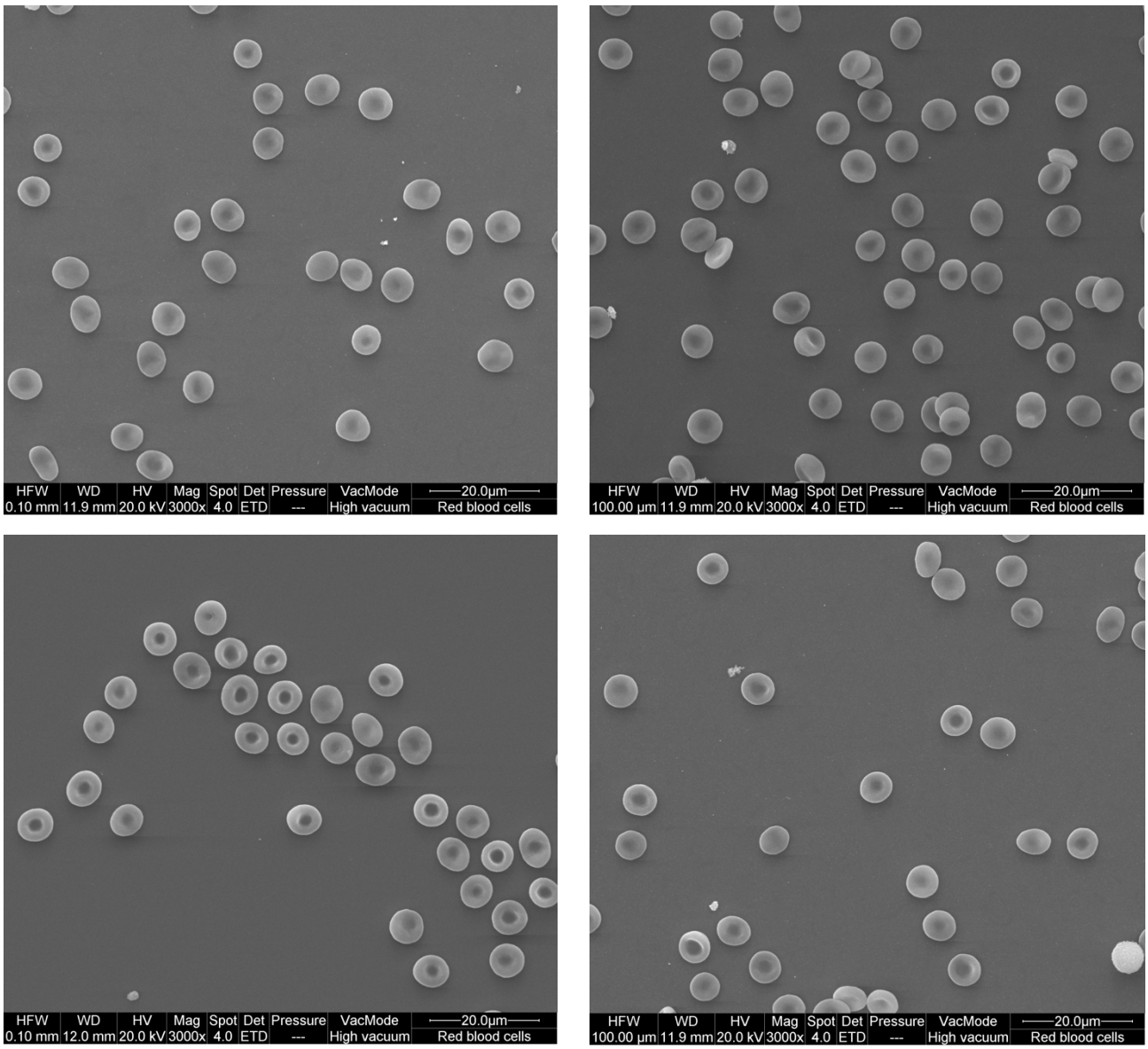

Figure 3.6 – SEM micrographs of RBC samples prepared by the optimized protocol. Monostratified and morphologically normal erythrocytes. Clean slide background.

3.3. Preliminary results of the clinical study

The first samples of the clinical study showed a high percentage of spherocytes (33.96% on average, Suppl. Tab. 5). This result aroused suspicion, so checks were carried out with the solutions (anticoagulant and fixative) from the same stock used for the patients in the clinical study, using blood samples from healthy volunteers. From these checks it emerged that the percentage of spherocytes was also in this case significant, albeit lower than in the first pathological samples of the clinical study (15.55%, Suppl. Tab. 6). It was thought that the problem might be generated by the anticoagulant solution; therefore, an experimental test was carried out on healthy volunteers using the anticoagulant solution from the same stock used for the pathological samples of the clinical study, together with another experimental test using the re-prepared anticoagulant solution. As can be seen from the table in supplementary materials, the sample prepared using the anticoagulant solution from the same stock used for the pathological samples of the clinical study showed a high percentage of spherocytes (22.91%, Suppl. Tab. 7), while the sample prepared using the re-prepared anticoagulant solution showed a low percentage of spherocytes (1.52%, Suppl. Tab. 8). The re-prepared solution was then supplied to the colleagues in Terni for the preparation of the subsequent samples. The results obtained from these last samples are shown in the Suppl. Tab. 9 and summarized in the Chart 3.4 in terms of average values. These data are discussed in the paragraph below.

3.4. Erythrocyte shape analysis at SEM: discussion

It is currently known from results published by two different research groups that indeed alterations of the erythrocyte morphology were observed by SEM in patients diagnosed positive for ASD (Bolotta et al., 2018a; Ciccoli et al., 2013). Our research project about the study of alterations of erythrocyte morphology in ASD patients aims however at answering some questions, such as at what age the erythrocyte morphological changes begin to appear in patients and whether such changes can be detectable even before the onset of symptoms routinely used for the diagnosis of the disorder on a neurobehavioral basis. Answering these questions is of fundamental importance to know if the presence of erythrocyte morphological alterations in ASD patients can be validated as a biomarker to be included in a screening for early ASD diagnosis.

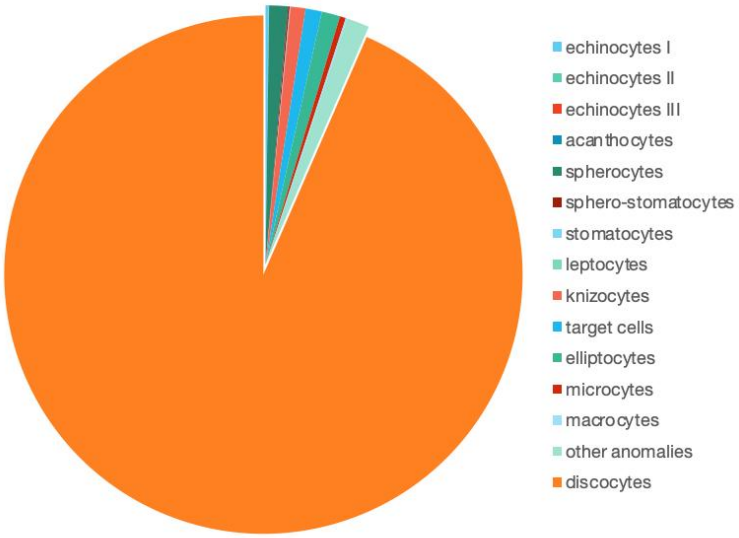

Chart 3.3 - RBC population type in healthy volunteers' blood samples prepared through the optimized protocol.

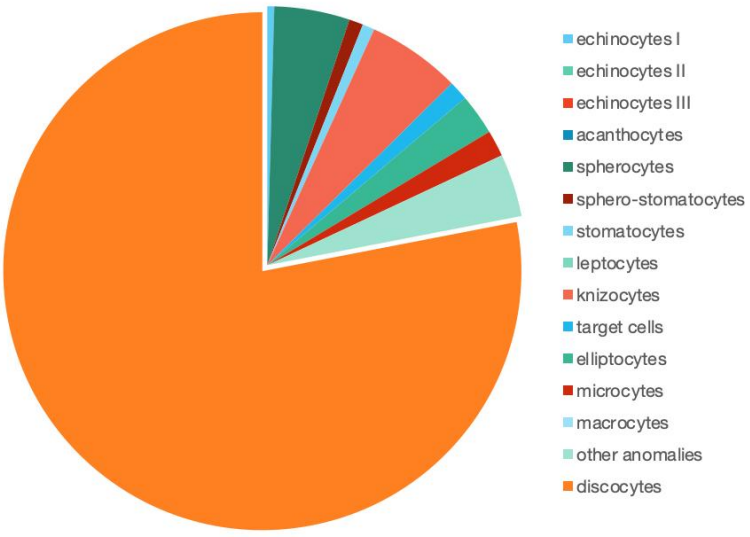

Chart 3.4 - RBC population type in ASD patients' blood samples prepared through the optimized protocol.

In addition to the knowledge already present in the literature, our study presents the development of a new minimally invasive protocol for blood samples preparation aimed at RBC morphological analysis by SEM, together with a set of initial RBC morphometric data at SEM derived from both ASD and controls' blood samples prepared using this new method. Our novel protocol is based on the acupuncture method, while data already published were obtained from blood taken by venous sampling. Indeed, the invasiveness of diagnostic practices is particularly critical in pediatric patients and, consequently, it is important to minimize the stress for the patient induced by sampling practices.

Regarding the presence of erythrocyte morphological changes in ASD patients, some considerations can be made, although it is worth remembering that ours are preliminary data and so, it is necessary to increase the caseloads of both ASD patients and control subjects, to provide more accurate information with statistical significance. From the data concerning erythrocyte shape analysis at SEM presented in this thesis, it is clear that the percentage of discocytes in healthy volunteers' blood samples, prepared both through the original version of the protocol (95.58%) and through the optimized one (93.48%), is in line with the percentage of discocytes in control subjects from the work by Bolotta et al. (2018a; ~90%) and significantly higher than that one in the work by Ciccoli et al. (2013; ~75%; Fig. 3.7). From this observation it can be deduced that the protocol based on acupuncture aimed at blood samples preparation for SEM morphological analysis described in this thesis does not appear to induce an excessively high number of laboratory artifacts concerning erythrocyte morphology, compared to similar data already published in the literature.

Regarding the quantity of discocytes present in ASD patients, differences can be observed between the data emerging from this thesis and those already published. The percentage of morphotypic erythrocytes in these patients in the study by Bolotta et al. (2018a) is ~45%, significantly higher than of ~15% in the study by Ciccoli et al. (2013; Fig. 3.7) and both are significantly lower than those that emerged from our study (respectively of 88.66% for ASD patients of the pilot study and 78.05% for ASD patients enrolled for the clinical study). The prevalent morphological anomalies found in blood samples of ASD patients enrolled for the pilot study, to a greater extent than in healthy volunteers, are echinocytes I and target cells. This observation is in line with the results shown in the studies by Ciccoli et al. (2013) and by Bolotta et al. (2018a) reporting the presence of a significantly higher percentage of both codocytes (which take shape of target cells) and echinocytes in ASD subjects compared to control subjects (Fig. 3.7). Instead, in blood samples of ASD patients enrolled for the clinical study, the prevalent morphological anomalies, which are found to a greater extent than in control subjects, are: spherocytes, knizocytes, elliptocytes and abnormal erythrocytes that fall into the category "other anomaly". As regards knizocytes, they were found to a greater extent in ASD patients than in control subjects both in the study by Ciccoli et al. (2013; in a statistically significant

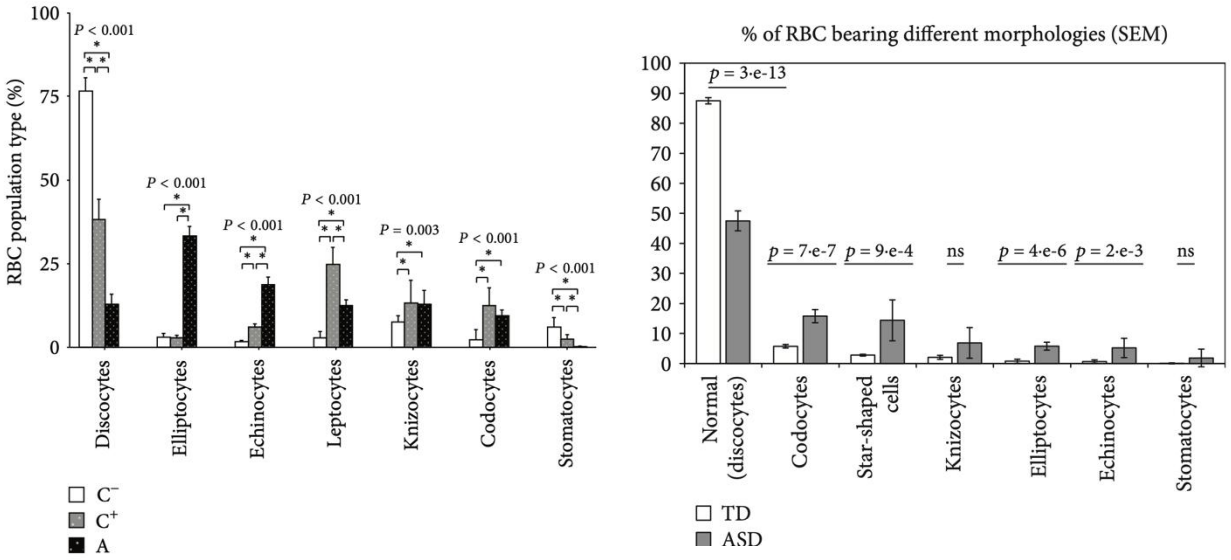

Figure 3.7 - Comparison of SEM analysis about erythrocyte morphologies in ASD and control subjects by Ciccoli et al. (2013; on the left) and by Bolotta et al. (2018a; on the right). Image on the left: RBC morphology distribution in autistic patients (A, black columns), subjects with nonautistic neurodevelopmental disorders (C^+, gray columns) and healthy controls (C^- white columns). Statistically significant differences are highlighted by a single asterisk (P> 0.05). The P values on the classification of each erythrocyte shape refer to one-way ANOVA. Image on the right: RBC morphology distribution in typically developing children (light columns) and in ASD children (dark column) are shown. The numbers above the columns indicate whether the difference was statistically significant (p> 0.05 by Student t-test).

way) and in that one by Bolotta et al. (2018a; in a statistically non-significant way; Fig. 3.7). As far as elliptocytes are concerned, they were found to a greater extent (in a statically significant way) in ASD patients than in control subjects both in the study by Ciccoli et al. (2013) and in the study by Bolotta et al. (2018a; Fig. 3.7). However, elliptocytes in autistic patients are found in a much greater percentage in the study by Ciccoli et al. (2013; ~35%) than in the study by Bolotta et al. (2018; ~5%; Fig. 3.7). The data of this thesis concerning the relationship between elliptocytes in ASD patients and control subjects seem to be more in line with those from the study of Bolotta et al. (2018a). As far as spherocytes and "other anomalies" are concerned, these RBC morphotypes represent a novelty as these classes have not been taken into consideration in the previously published works, presumably because no erythrocytes belonging to these morphological classes have been found in the samples analyzed in these works. Regarding erythrocyte morphological changes in ASD patients, future studies are needed to establish if a single predominant morphological abnormality or rather a combination of several morphological abnormalities with canonical relative percentages, should be considered for the correlation between erythrocyte morphological abnormalities and ASD. The second hypothesis seems more plausible.

Another aspect that remains to be clarified concerns the factors and cofactors that determine the presence of erythrocyte morphological abnormalities in ASD patients. It is reasonable to hypothesize that among these factors and cofactors there are the modifications induced by oxidative stress on

erythrocyte membrane's proteins or their associations. In fact, it is known that defects in erythrocyte membrane skeleton's components, and the consequent loss of functional and structural integrity, gives rise to characteristic alterations of the erythrocyte morphology in some other pathological conditions (e.g. hereditary spherocytosis, elliptocytosis and stomatocytosis; Gallagher, 2005). Besides, a SEM morphological study (Ciccoli et al., 1994) on mouse erythrocytes incubated with oxidizing agents reported that these cells exhibited several alterations in shape, including transformation into echinocytes and the presence of codocyte-like, stomatocyte-like and knizocyte-like shapes. Reconnecting to that, it is worth noting that several publications highlight the presence of oxidative stress' deep effect in the erythrocyte membrane of ASD patients (Bolotta et al., 2018b; Ciccoli et al., 2013; Ghezzo et al., 2013). The hypothesis according to which modifications induced by oxidative stress on erythrocyte membrane's proteins can be responsible for erythrocyte morphological abnormalities in ASD patients is reinforced by scientific works showing the presence of abnormal erythrocyte morphologies in pathological conditions characterized by oxidative stress - such as chronic obstructive pulmonary disease (Lucantoni et al., 2006) and end-stage renal disease (Antonelou et al., 2011) – and, above all, two published papers (Ciccoli et al., 2012; Cortelazzo et al., 2015) involving RTT patients, a neurodevelopmental disorder with autistic features which has recently been separated from ASD as a nosological distinct entity (DSM-V). With their work, Ciccoli et al. (2012) reported the presence in these patients of abnormal RBC shapes (mainly leptocytes), for the generation of which oxidative stress - together with a situation of hypoxia - plays a key role. Cortelazzo et al. (2015) identified in RTT patients significant changes in the redox state for nearly all membrane cytoskeletal proteins, suggesting that oxidative stress could play an important role in influencing the state of the erythrocyte plasma membrane and its cytoskeleton. In this study, changes observed in membrane cytoskeletal proteins appear to be related to changes in cells shapes (leptocytes). Even if a key role of membrane cytoskeleton proteins would be confirmed, it remains to be precisely determined whether changes in cytoskeletal proteins and, consequently, in erythrocyte morphology of ASD subjects always occur in the same way in different RBC and/or in different ASD patients.

Considering the ascertained presence of alterations in the fatty acid composition of the erythrocyte membrane in ASD patients (Ghezzo et al., 2013), erythrocyte morphological changes of these subjects could also have a correlation with the composition of erythrocyte membrane's lipid bilayer, or with the nature of its interaction with the erythrocyte membrane's proteins. It is also reasonable to hypothesize that morphological, lipid and protein changes of the erythrocyte membrane in ASD patients are the result of systemically altered physiological conditions of these patients, such as a pro-

inflammatory state, the presence of which in ASD subjects is reported in the literature (Rose et al., 2012; Rossignol and Frye, 2012; Vargas et al., 2005). Further and continuous studies are necessary to clarify in a precise and detailed manner which are the factors and cofactors leading to the onset of erythrocyte morphological alterations in ASD patients.

3.5. Intra-operator variability of erythrocyte SEM analysis

Mean intra-assay variability for discocytes and total abnormal morphotypes was 3.06 ± 0.61% and 10.67 ± 8.24%, respectively (Chart 3.5). Consistently larger intra-operator variabilities were evidenced for the remaining erythrocyte shape classes, while the intra-assay variance for echinocytes II and III was not evaluable (Chart 3.6). A statistically significant exponential regression was observed between intra-operator variability and cell shape frequency ($y=57.782-2.64x+0.0248\ x^2$; $R^2=0.14$, $p=0.034$; Chart 3.7).

While intra-operator variability was found to be acceptable for the most frequently observed circulating erythrocyte shape classes (i.e., discocytes) and total abnormal cell shapes, intra-assay variance was found to be inversely related to cell shape frequency. These observations strongly suggest the need of a high number of replicate counts and the key relevance of implementing reliable computer-assisted algorithms and machine learning systems in order to discover potential novel disease biomarkers at the SEM analysis of peripheral blood micro-samples.

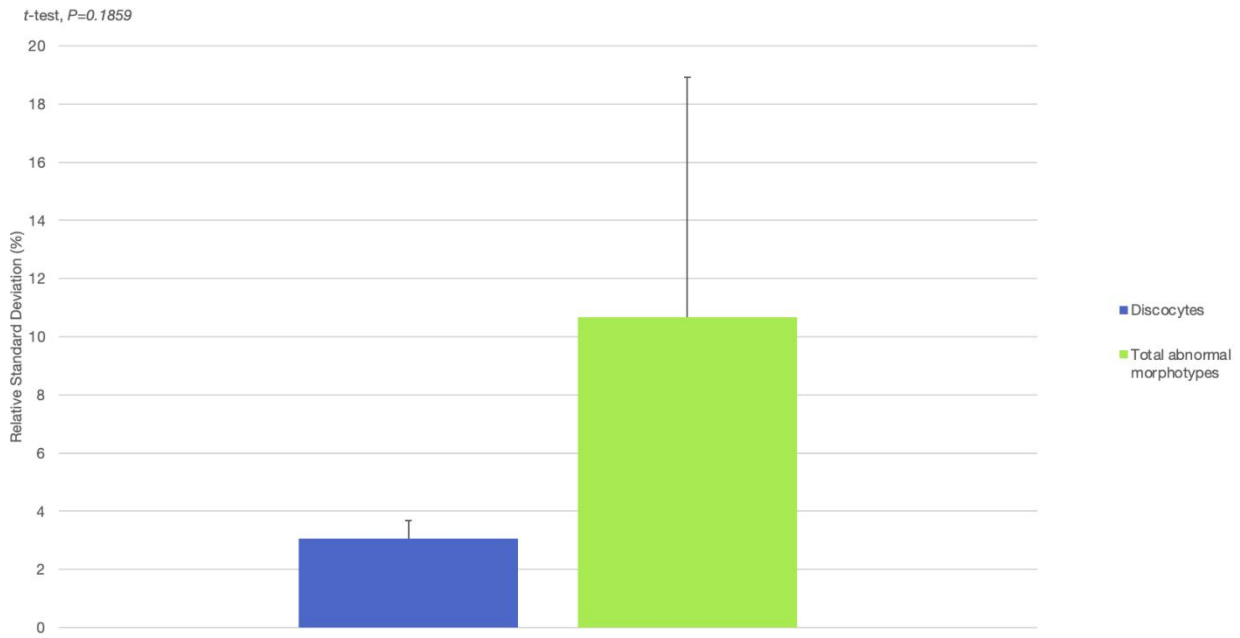

Chart 3.5 – Relative Standard Deviation (%) for discocytes and total abnormal morphotypes. Histograms describe intra-operator variability, as expressed as mean ± 1 standard deviation of percentage relative SD, for discocytes and total abnormal morphotypes. These data result from erythrocyte counts at SEM in triplicate for 3 samples.

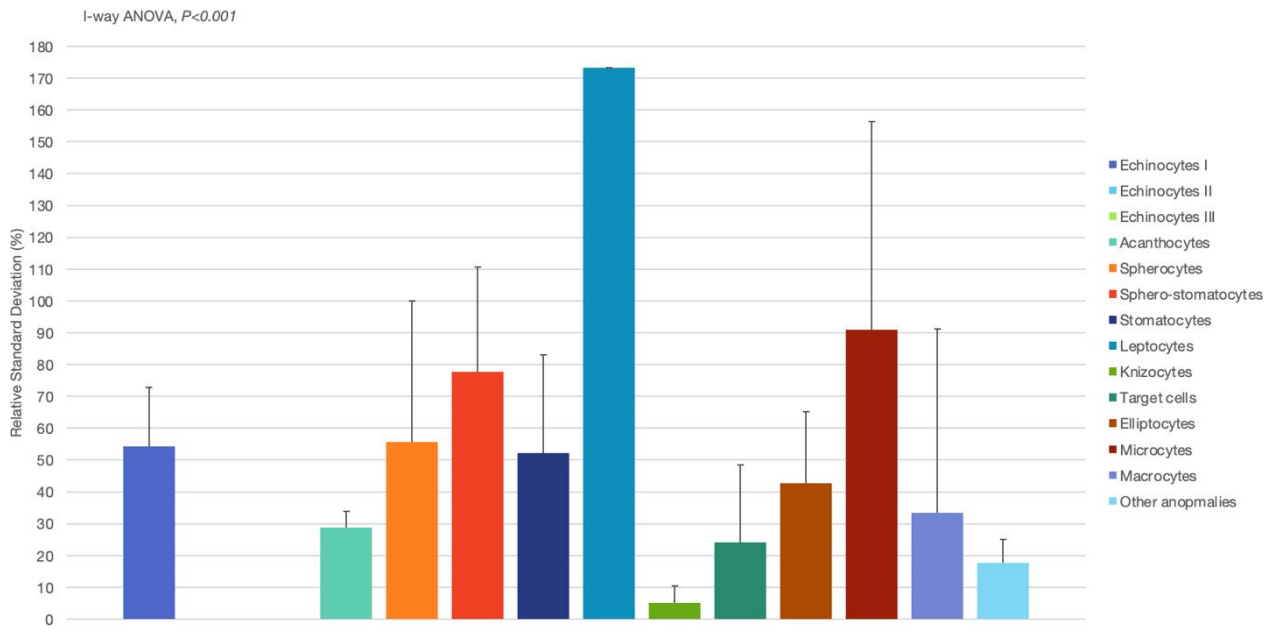

Chart 3.6 – Relative Standard Deviation (%) for each abnormal erythrocyte morphological class. Histograms describe intra-operator variability, as expressed as mean ± 1 standard deviation of percentage relative SD, for each abnormal erythrocyte morphological class. These data result from erythrocyte counts at SEM in triplicate for 3 samples.

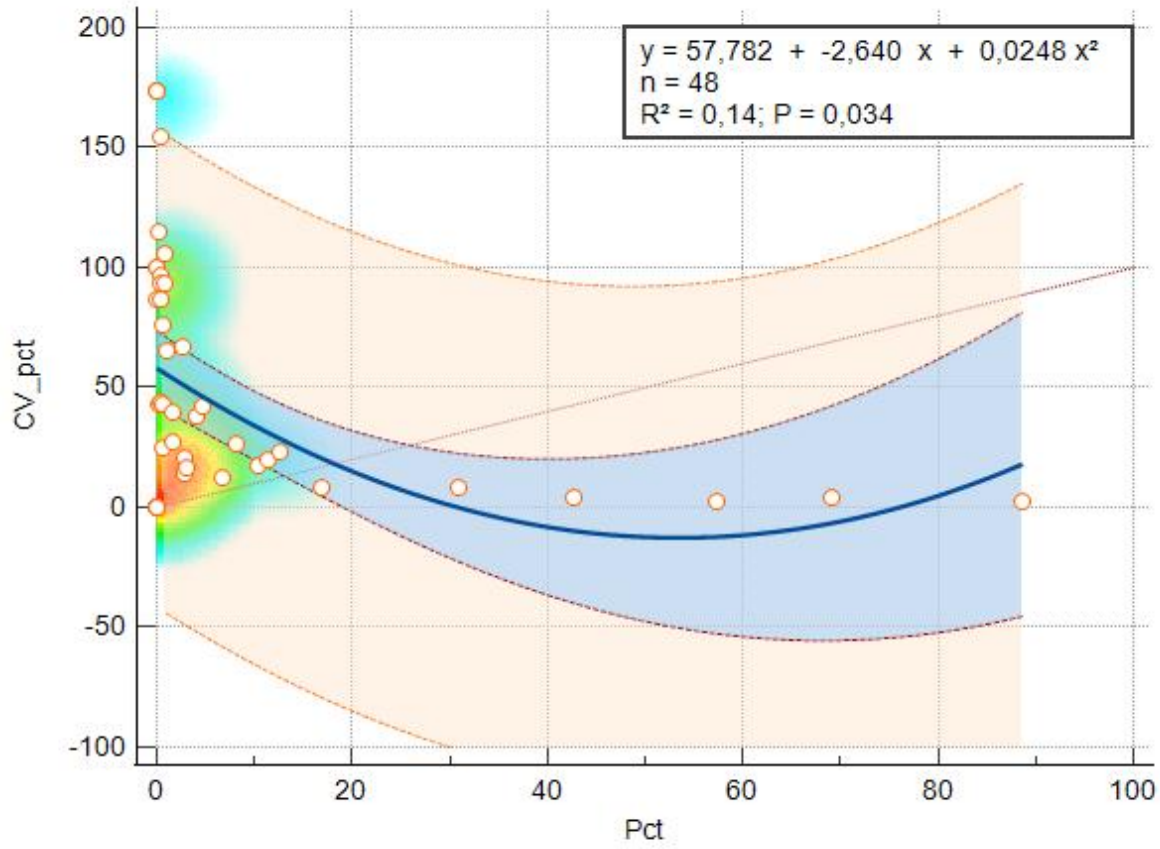

Chart 3.7 - Correlation between intra-operator variability and cell shape frequency. Univariate exponential regression between intra-operator variability (Y axis, percentage values) and frequency (X axis, percentage values of total cell counts) of erythrocyte morphotypes observed at the SEM analysis. Open circles represent single observations. Note: the negative curve graph reconstruction is for didactical purpose only.

3.6. Software functionalities and erythrocyte semi-automatic detection

3.6.1. Software's graphic interface

In the software user interface, there is the *open image* button at the bottom left. After executing this command, a dial-needle window opens - the operator can use it to select the digital image which he wants to analyze. At this point, the software performs a test to make sure that the image has been loaded. If this step is performed correctly, the image appears in the software window with a significantly reduced resolution, to allow full viewing.

On the right of the software window there is a column of options, in which a square sub-image is easily visible at the top. By clicking on any point of the image, inside the sub-image (zoom box) an image's detail at its natural resolution can be seen; the center of the image in the zoom box coincides with the point of the image on which the mouse pointer has been placed. Each time this operation is done, the software normalizes the image in the zoom box, bringing its contrast and brightness to preset values. The software is provided with a test to verify that the small image in the zoom box has been loaded.

3.6.2. Horizontal plot and vertical plot

Below the zoom box two figures show the plots of the horizontal and vertical transects extracted from the above sub-image. These plots show the profile of the image's intensity (gray level) as a function of the pixel coordinate, i.e., horizontal coordinate for the horizontal plot and vertical coordinate for the vertical plot. The importance of these plots relates to the circumstance that the SEM signal depends on the inclination to the detector direction of the surface of the observed object. Thus, these two profiles can be considered as a signature of the three-dimensional shape of the observed cell. Almost always, two tall peaks (maxima) separated by a rather wide valley and surrounded by two minima define the cell area.

The software analyzes many horizontal and vertical transects as to fill the entire image available. Each transect is calculated as the average between the current row (or column) and the two neighboring ones to drastically reduce the noise amplitude and improve the accuracy of the processing results. It is worth noting that averaging of the image signal always occurs in a direction orthogonal to the plot arrangement, in order to reduce its random component, while preserving its information content. In Fig. 3.8 it is shown the software interface as it appeared during the first development steps.

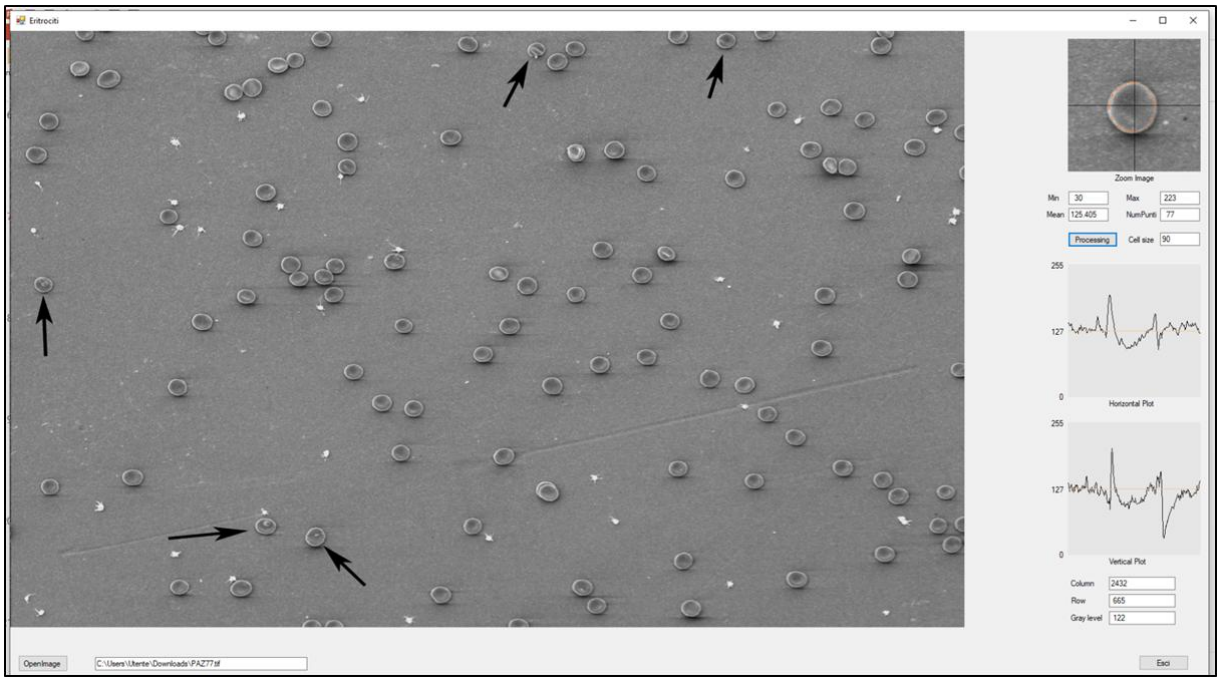

Figure 3.8 - Software interface as it appeared during the first development steps. Left: the image as it appears once opened within the software; the *Open image* button is located at the bottom left. Right: the 200x200 pixel sub-image, followed by horizontal plot and vertical plot. Below the zoom box and above the plots, it can be found some textboxes concerning the sub-image in the zoom box: *Min* (minimum pixel intensity value), *Max* (maximum pixel intensity value), *Mean* (average pixel intensity value), *NumPunti* (number of pixels that are found inside the cell – this value gives a first indication about cell size). Next it can be found the *Processing* button (through which it is possible to process the image in the zoom box) and the *Cell size* textbox (which indicates the average size of cell diameter; it is a parameter that can be modified by operator as it changes according to the image resolution; this value stays the same for the images obtained at that particular microscope with the same experimental acquisition conditions). Below the plots there are three other textboxes which refer respectively to the column number, the row number and the gray level value related to the point of the whole image on which the mouse cursor is placed.

3.6.3. Segmentation algorithm

By clicking the processing button in the software window's right column, the image shown by the zoom box is processed to identify a red blood cell. To do this, the software looks for a starting minimum on horizontal transects, first, and on the vertical ones, then. After finding the first minimum, the algorithm searches for the first maximum within a fairly short lag, then for the second maximum and finally for the second minimum.

To identify features of transects profiles, the procedure evaluates a fairly extensive list of parameters with which it reports the main features of transects; these parameters include the average value of the transect, the values of the first and second maximum, the values of the first and second minimum, the average of the transect between the first and second maximum, the distance between the first minimum and the first maximum and the one between the second minimum and the second maximum. In order that all erythrocytes can be recognized by the software, the distance between the first maximum and the second maximum (roughly corresponding to the width of the cell) must fall within

a rather wide range of acceptable values, deduced in an empirical way. This distance range is about 3-13 microns, which is wide enough to include abnormal cells as well.

It is necessary to underline that all the images darken by moving down and to the right, as if they had a virtual source of illumination in the upper left corner: this effect is due to the position of the sample with respect to the electron source and to the detector and to the self-shielding effect of secondary electrons operated by the cell. This means that, in the plots, the second maximum always is less toll than the first one and that the second minimum always is deeper than the first one.

When the algorithm recognizes the pair of maxima that define the cell extremes, and after all the named conditions are validated, the pixels contained between the maxima are assigned to the image segment classified as belonging to the cell (visually, the space between the starting pixels and the ending ones is filled with an orange line in the middle). This process is applied first to rows and then to the columns of the sub-image within the zoom box. Any erythrocytes in the zoom box become orange: this represents the graphic display of segmentation operated by the algorithm within the selected area. In other words, the cell colored in orange is a set of orthogonal segments identified by the software and all labeled in the same way (Fig. 3.9).

It is necessary to note that only healthy erythrocytes show the typical pattern of profiles within the plots, represented by two maxima accompanied by two minima and separated by a valley, while sometimes erythrocytes with abnormal morphology show remarkably different profiles. Fibrin clots, and all other impurities in the sample that do not belong to the morphological class of RBC, also have an irregular plot profile (Fig. 3.10).

3.6.4. Segmentation: discussion

Edge-based techniques for segmentation are based on the idea that rapid changes in intensity values occur when passing from one region of interest to another. The aim is the detection (and therefore the classification) of the discontinuities (edges) of the image (gray levels). Instead, *class-based* techniques rely on the analysis of the whole image to group the pixels through thresholding or clustering operations. The segmentation procedure proposed resembles *edge detection* segmentation methods (which represent a type of edge-based techniques), although not belonging to them properly. Edge detection algorithms usually calculate the derivative of the image intensity according to a given mathematical operator. Many edge detection algorithms compute the first order derivative (image gradient), then search for peak values to detect object boundaries. Other edge detection operators are based on the calculation of the second derivative operator (e.g.: the Laplace operator), which roughly

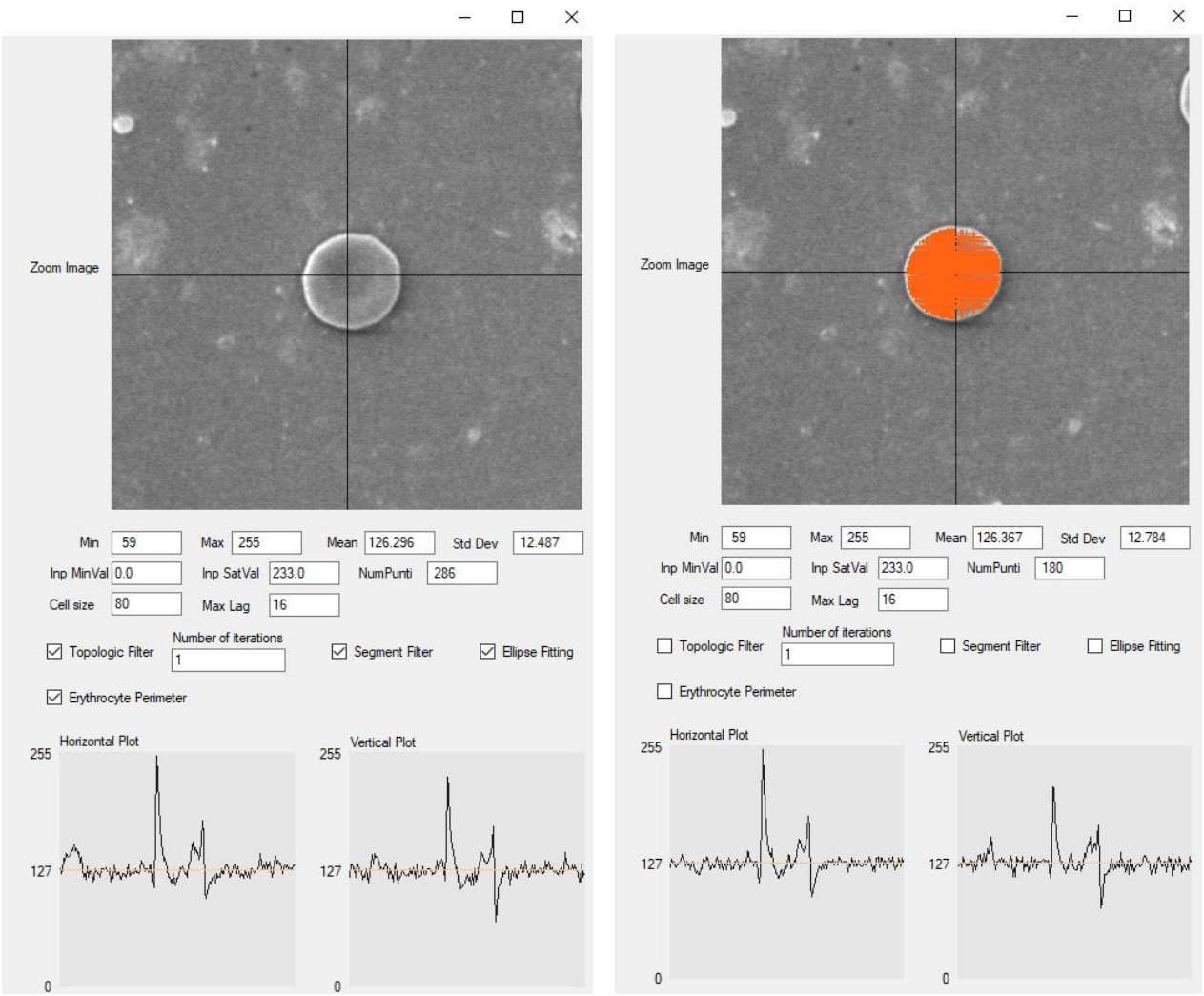

Figure 3.9 - Segmentation. Left: example of a selected erythrocyte with its relative plots. Right: after clicking on the *Processing* button it is possible to appreciate how the erythrocyte is filled with vertical and horizontal orange segments. In the plots it can be seen how, in correspondence of erythrocyte edges, there are always two peaks (two maxima), separated by a rather wide valley and surrounded by of two minima. It is also noted that the first maximum is higher than the second one and that the second minimum is deeper than the first one.

corresponds to the gradient's speed of change. A general-purpose algorithm, such as that of gradient or edge detection methods, would be applied to every point of the image, regardless of whether to start the processing from a dark or light pixel. On the other hand, the segmentation method here adopted has the advantage of considering a trigger (black border which is always present around the cells) which allows to start the next part of processing. In this way our segmentation procedure becomes specialized for cells recognition.

The classic *edge-based* approach was excluded from the present study because, if a contour extractor was applied to an image with high field noise, many false positives would result. In our case, if the *edge-based* approach was applied to an image containing several fibrin clots, these fibrin clots, having a gradient on the edges even greater than that of RBC, would be highlighted even more than erythrocytes, causing confusion in count and distinction between cells of interest and noising

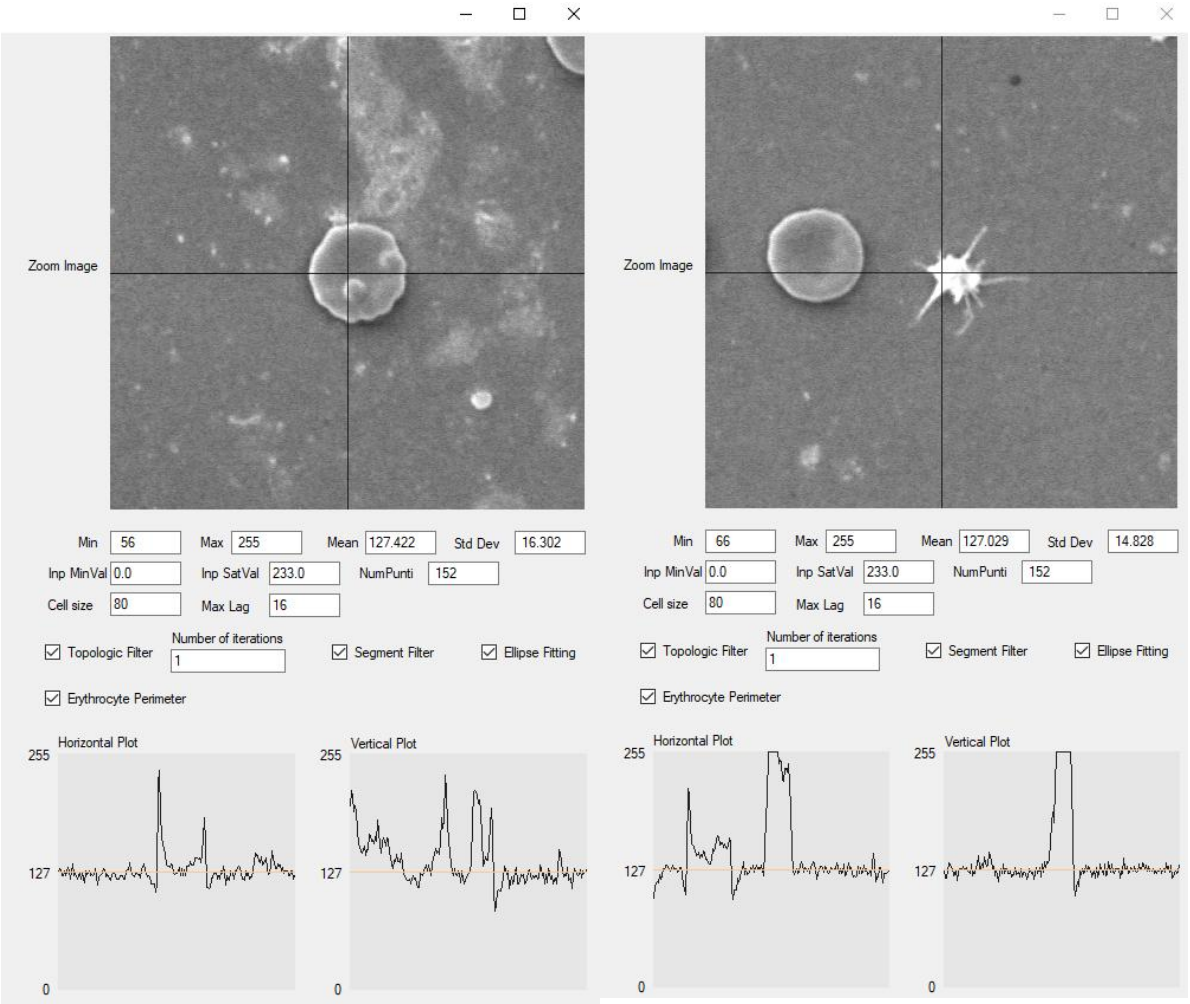

Figure 3.10 - Examples of atypical erythrocyte morphology and fibrin clots' plot profiles. In both images it is possible to appreciate how plot profile of erythrocytes with atypical morphology (left) and of fibrin clots (right) are visibly different from RBC with canonical morphology's plot profiles shown above.

elements. Fibrin clots are in fact very bright elements on a dark background, while RBC are gray objects on a dark background. In this case, it would then be desirable to first apply a pixel threshold with a cutoff value, such as to eliminate a set of pixels below that value, to which subsequently apply a contour extractor. But, in this case, the cutoff value could cut out some cells of interest that are characterized by an area generally smaller than that of a healthy erythrocyte. To exclude fibrin clots and other disturbing elements, shape or size could be used as discriminants, but in this case one would risk, once again, not admitting an abnormal RBC, or instead retaining and scoring fibrin clots of larger size than an erythrocyte.

The *thresholding* segmentation method, belonging to the *class-based* methods, is found in the literature for the segmentation of erythrocytes in micrographs produced by either light or electron microscopes (Bacus et al., 1976; Bhowmick et al., 2013; Tomari et al., 2014). This method was also disregarded, since the threshold's cutoff value could lead to an over-segmentation or to the exclusion

of erythrocytes with altered morphology, or to the inclusion of disturbing elements, such as fibrin clots.

Another kind of segmentation methods is represented by the *region-based* techniques. Among these, there is the *watershed* segmentation method. It has been used by several authors for erythrocyte segmentation in both light and electron microscope images (Bala and Doegar, 2015; Bhowmick et al., 2013, 2012; Garnier et al., 2019; Malpica et al., 1997; Sharma et al., 2016). The segmentation method based on the watershed algorithm was not taken into consideration for this project, because it gives an over-segmentation where there are many local minima, as in the case of erythrocytes whose center has levels of gray intensity clearly different from those of the cellular contours: for example, in the case of target cell, which have a thin area with a central lighter area. The watershed algorithm gives over-segmentation even in images with a very noisy background (Arganda-Carreras and Legland, 2014).

The Hough transform is widely used in the literature (Agrawal and Verma, 2015), for example to identify and count erythrocytes on the basis of the range of RBC radius, which extends from the minimum - to the maximum radius of the cell (Cruz et al., 2019; Mazalan et al., 2013). Although the average diameter of an erythrocyte is known, in each image there are cells with a different radius, which must therefore be determined before proceeding with the Hough transform. Moreover, the shape of real cells never is a perfect circle, making it complex to find a general curve to accurately match the generic cell shape. As an instance, elliptocytes, having an elliptical or sometimes rod shape, acanthocytes and echinocytes, which have a spheroidal shape with spines on the surface, or the knizocytes, which are even triconcave, could have a radius range that differs greatly from the average one. This means that this type of cell may not be correctly recognized through the CHT due to the incompleteness of the circle drawn (Mazalan et al., 2013). Furthermore, to find out if one RBC's outline passes in a point of the image, it is necessary to add on the extracted contours all the possible circular profiles that pass through that point. Having to repeat this operation on each single cell's extracted outline of in the image, the calculation becomes long and laborious (Barducci and Pippi, 1999).

In conclusion, it is possible to state that our segmentation method aimed at the recognition of RBC is the best one suited for the specific type of SEM micrographs used in our work, compared to the methods found in the literature for similar purposes.

3.6.5. Instance classification

As a result of the segmentation process, the image is reduced to a set of many adjacent pixel segments placed horizontally and vertically; at this level, it is impossible to discriminate between the pixels that belong to the same physical element and those that are extraneous to it. After the segmentation process there is the instance classification process, which consists in establishing whether the set of pixels belonging to the class of erythrocyte segments constitutes a compact and connected set or not. Whenever it is possible to find in the set a couple pixels for which no path exists laying entirely in the set itself that joins them, we state this set as unconnected (composed by two or more connected sets, which are not connected to each other). The instance classification is used to join segments of connected pixels, that is, those for which there is a path that connects them in extension. In other words, instance classification process rejoins all adjacent pixel segments. With this operation, all connected segments become an object, that is, a class or instance.

3.6.6. Filtering

Following segmentation and instance classification processes, the algorithm can identify regions corresponding to erythrocytes, however in the image obtained there are false positives, unwanted foreground elements and noise. To overcome these problems, some filtering methods were applied. This step is critical as noise can significantly impair the system's ability to accurately identify and classify extracted objects (Kass et al., 1988).

First, the *topological filter* is applied, thanks to which sets of segments with a smaller area than the expected area of an average erythrocyte are removed. These set of segments presumably are not erythrocytes (false positives) or they are wrongly segmented erythrocytes (i.e. erythrocytes for which the software has recognized so few pixels for which it is not worth doing further processing).

The topological filter makes use of *morphological operators*. Morphological operators are so called because they carry out elaborations on the shape of an object. Standard operations include dilation (accretion), erosion, opening and closing. Dilation causes regions belonging to the foreground to grow (thicken), while erosion shrinks and thins them (Szeliski 2010). Topological filters consist of n openings followed by n closures, where n is the number of iterations with which it is possible to parameterize the topological filters. The *opening* consists of a first phase of erosion of border pixels, during which those pixels that belong to the object and that are surrounded by at least one background pixel are assigned to the background, and of a second phase of growth, in which those pixels of backgrounds that are surrounded by pixels belonging to the object are assigned to the object. With this process, those pixel segments that, at the end of the segmentation, sprouted from the objects, are

removed with erosion and are not reconstructed with the growth because they are not connected with the element structure. Then there is the *closure*, which consists of a first phase of growth followed by a phase of erosion. After segmentation, incorrectly segmented areas may remain inside the object (displayed as variably extended areas without orange pixels but actually belonging to the erythrocyte), but the growth of the pixels belonging to the background and surrounded by pixels belonging to the object solves the error assigning such areas to the object RBC itself; the subsequent erosion does not remove the pixels newly added because they are connected with the pixels of the object structure.

Since sometimes the topological filter is not enough, the *anti-segment filter* is applied. Thanks to it, segments extraneous to the cell are detected and cut. These segments are like bridges that can connect small residues of plasma proteins to the cellular perimeter. In the first part of the anti-segment filter, the software extracts the contour of the result of the instance classification filtered by the topological filter and divides it according to the median vertical line, obtaining two semi-profiles (right semi-contour and left semi-contour). When the software detects a non-progressive profile by recognizing "jumps", it cuts the segments that protrude horizontally from the semi-contour and carries on the detection of the progressive profile. Therefore, segments that protrude from the semi-contour are recognized as segments of pixels not belonging to the cellular perimeter and are attributed to the background. In the second phase of the anti-segment filter, the result of the instance classification filtered by the topological filter is divided according to the median horizontal line, obtaining two other semi-profiles (upper semi-contour and lower semi-contour). The analysis is repeated as described above for the vertical segments (Fig. 3.11).

It is possible to iterate topological filters in an arbitrary way, just by typing a digit in the *number of iterations* textbox. For example, with n = 1, the aperture filter removes 2-pixel thick segments, while with n = 2 it removes 4-pixel thick segments. To prevent removing objects of interest it is in general advisable not to exceed 4 iterations (which corresponds to exclusion of objects with linear dimensions up to 8 pixels). It should be noted that the request for n iterations yields repeated applications of the opening filter for n times followed by n following applications of the closing filter.

These procedures can be performed only after the instance classification has taken place, that is, only after the sets of pixels have been recognized as individual elements. It is clear that, since the instance classification excludes objects (instances) having an area smaller than the expected area values of an erythrocyte, such filters operate more efficiently and quickly than applying them to the result of the initial segmentation, which yields many unconnected segments that are not eligible as erythrocytes.

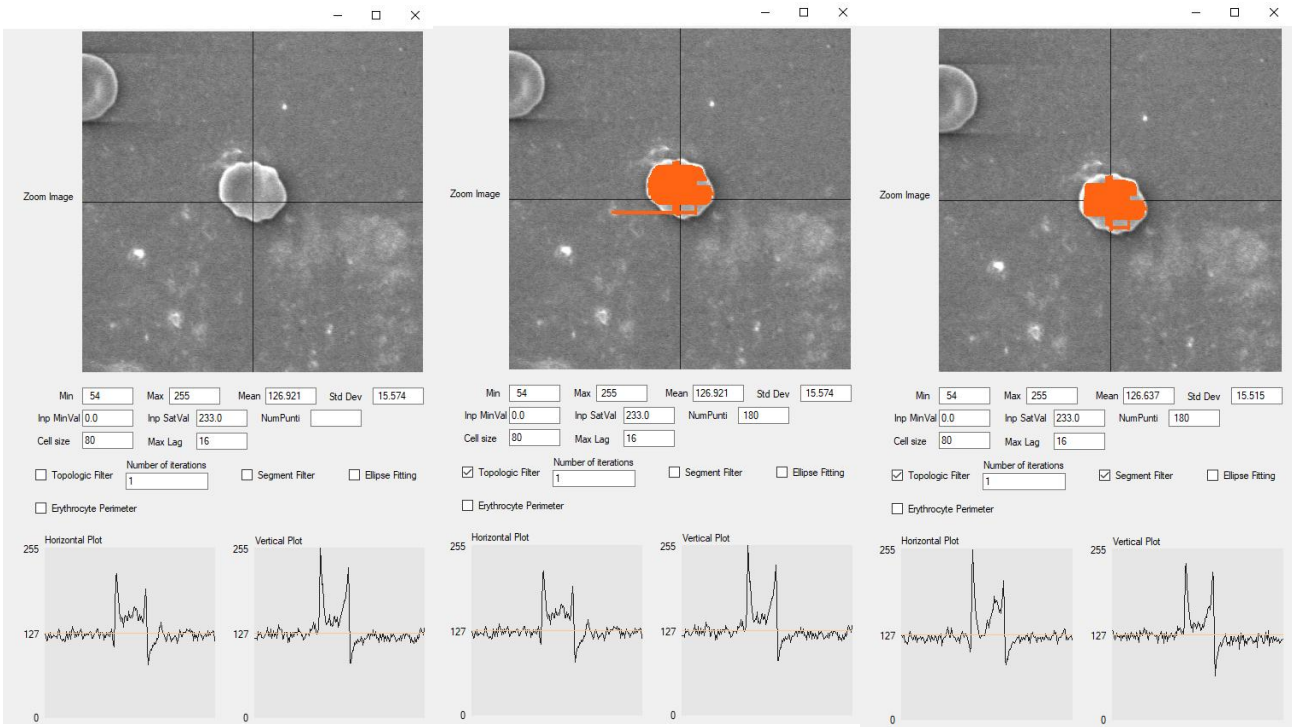

Figure 3.11 - Application of topological and anti-segment filters. The image on the left shows an erythrocyte in the zoom window without the application of any filter. In the image in the center, obtained following the application of the topological filter, it can be seen an imperfect segmentation that leaves segments of pixels sprouting from the erythrocyte. In the image on the right, it can be seen how, after the application of the topological and anti-segment filters, extraneous segments have been completely eliminated.

3.6.7. Filtering: discussion

Tomari et al. (2014), in their work about developing a computer-assisted system to automate the process of identifying erythrocytes in blood smear images, used morphological operators to remove unnecessary elements from the segmented image. In particular, a sequence of two times of erosion, two times of dilation and contour filling algorithms was applied to reduce noise and holes inside the cell. Wąsowicz et al. (2017) in their study about a computerized system for automatic counting and classification of erythrocytes in images acquired under a light microscope, used morphological operations at two different moments of the erythrocyte separation procedure. In the first moment, they applied morphological operators such as dilation and erosion, to remove background noise and give prominence to the central part of the erythrocytes, and in the second moment, after carrying out other image pre-processing procedures, they performed morphological operations to fill holes in the image and erase excessively small objects. Morphological operators were also used for the segmentation of erythrocytes in the study by Bhowmick et al. (2013), having the objective to address quantitative microscopic approach for automated screening of erythrocytes in anaemic cases using SEM images of unstained blood cells. In particular, morphological opening operator is being used to eliminate the unwanted and distorted cells from the image. IdentiCyte program, specifically designed

to quickly count and identify RBC from a series of light microscope images, discard from the image of elements that are too small occurs thanks to the measurement of their area. This way debris are removed from the image (Garnier et al., 2019).

In conclusion, it is possible to state that the selected combination of mathematical operators underlaying our filtering methods for an accurate recognition of RBC is, among others previously used by other authors, the best one suited for the specific type of SEM micrographs used in our work.

3.6.8. Ellipse fitting

Following filtering, the **ellipse fitting** takes place, an operation with which the algorithm computes the ellipse that best approximates the identified RBC. The software superimposes on the set of orange pixels an elliptical shape with a couple of free parameters (two ellipse's semi-axes and the ellipse's center). The dimensions of the two semi-axes and the center of the ellipse are then modified until the best fit is obtained, i.e. the best overlap area of this theoretical shape over the segments identified as belonging to the RBC. In this way, the result of the instance classification is refined. In fact, at the end of the segmentation, a partially incorrectly recognized RBC could appear. In this case, if the algorithm tried to superimpose an ellipse on the classified region, an ellipse of smaller or larger dimensions than expected would be obtained, determining the exclusion of this element from subsequent proceedings (Fig. 3.12).

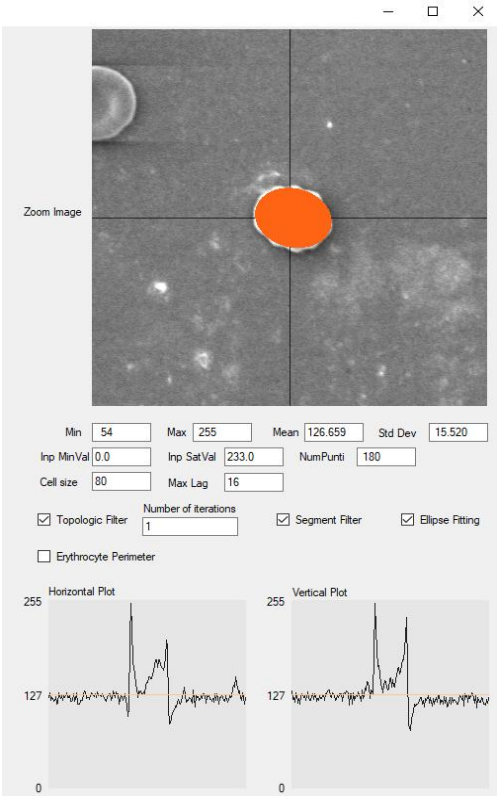

Figure 3.12 - Ellipse fitting. To improve the result of instance classification, the algorithm computes and superimposes an ellipse on the erythrocyte that best represents the erythrocyte itself.

Filtering and ellipse fitting processes have been inserted because it was thought that it is much better to remove a potential cell whose instance-classification procedure is not accurate, rather than try to process it and run the risk of introducing a wrong information. In fact, when a cell is thrown away randomly, the odds of throwing away a healthy cell or a diseased cell exactly follow the statistic of the disease (there is no bias in the statistic). On the contrary, accepting a wrongly segmented cell at the beginning and then obtaining an incorrect classification can give rise to problems.

3.6.9. Detection of erythrocyte perimeter

The ellipse fitted can adapt to erythrocyte geometry but imperfectly: it does not follow the cellular contour accurately. To solve this problem, the ellipse perimeter is deformed so that each point is moved forward or backward radially until it meets the actual cellular contour (the brightest part of the cellular profile, represented by the maximum peak on the plots). With the process of detection of erythrocyte perimeter, a red outline appears on erythrocyte contour (Fig. 3.13). Fig. 3.14 shows how the graphical interface of the software appears in a second phase of its development, with the addition of the functions just described.

By testing the software at this phase of development, it was observed that it recognizes RBC and highlights them with a red contour with a rather high success rate. This can be affirmed thanks to an evaluation of the software ability of single erythrocytes detection in SEM micrographs. The total of erythrocytes recognized by the software was 2475 out of a total of 3000 erythrocytes manually counted: the percentage of erythrocytes recognized in average was therefore 83.08% (Tab. 3.1). This kind of analysis was necessary to establish if this first phase of software development had reached the optimization and so if it was possible to continue with the subsequent steps of development.

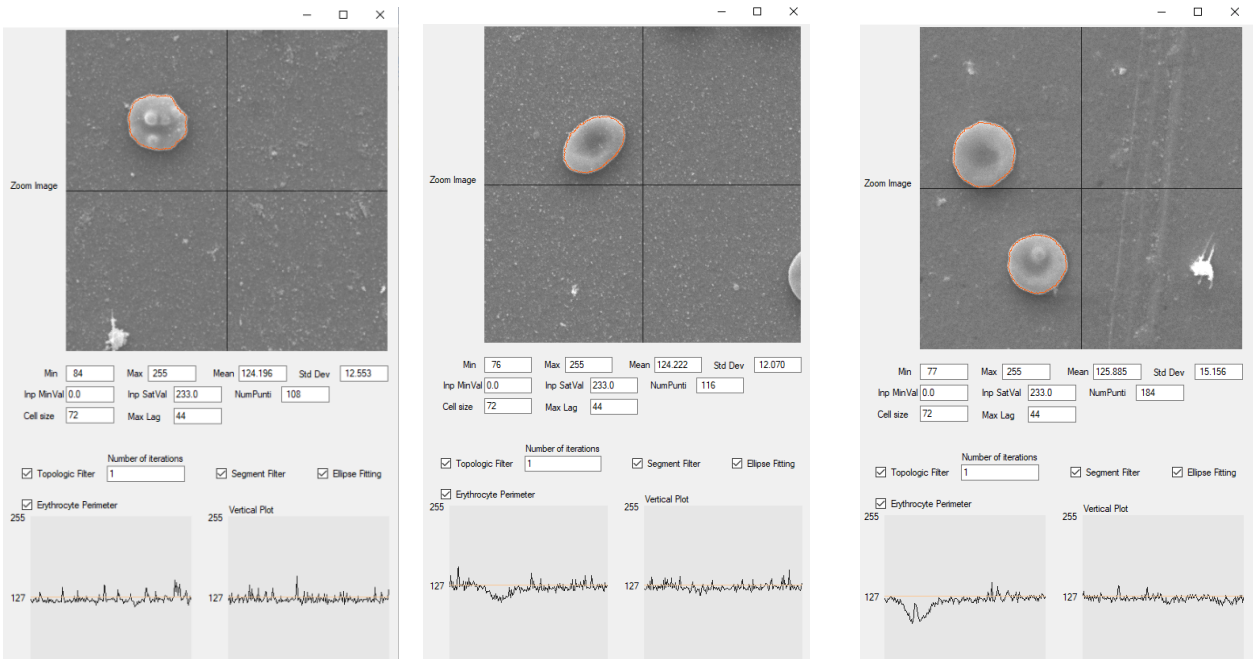

Figure 3.13 – Detection of erythrocyte perimeter. When one or more erythrocytes are displayed in the zoom box and the operator requests their processing, a red line appears following the erythrocyte outline (all the textboxes related to filtering, ellipse fitting and erythrocyte perimeter must be selected).

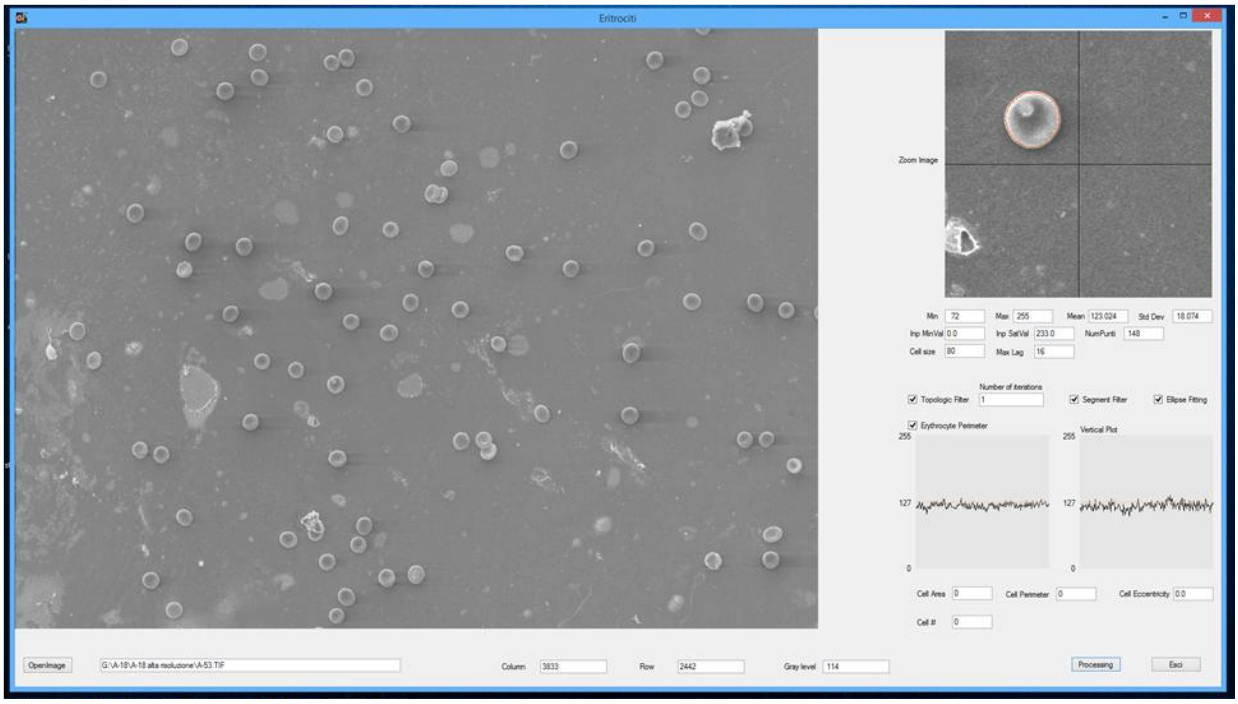

Figure 3.14 - Software window in a newer development version. It can be seen how the size of the zoom box has increased. New textboxes have also been added: *Std Dev* (standard deviation of the pixel intensity value in the zoom box), *Inp MinVal* (minimum input value, referred to the whole image), *Inp SatVal* (value of input saturation, referred to the whole image), *Max lag* (distance between the first minimum and the first maximum and between the second maximum and the second minimum of the plot). These last two parameters can be modified by the operator. Below these functions, checkboxes relating to the two filters, ellipse fitting and erythrocyte perimeter were added. Other textboxes have also been added below the plots: they are related to the first cellular morphological parameters and for the cell number. The column, row and gray level textboxes have been moved lower, below the whole image.

sample number	images analyzed	detected erythrocytes	counted erythrocytes
1	21	688	1054
2	23	819	876
3	68	968	1070
3	**112**	**2475**	**3000**

Table 3.1 - Results of single erythrocytes processing in SEM micrographs for the evaluation of their correct detection by the software. The table shows the data for each sample in terms of the number of images analyzed, the number of erythrocytes correctly detected by the software, the number of erythrocytes counted manually. The last row shows the sums of these data for the total samples analyzed.

3.7. Computation of erythrocyte morphological parameters

The next step in the software development was to devise formulas and algorithms for the accurate calculation of some cellular morphological parameters. These parameters were chosen as they were considered useful for the discrimination and classification of the abnormal erythrocyte morphotypes most frequently observed in the previously analyzed and classified ASD blood samples. At this

purpose, software interface has been modified with the addition of textboxes relating to the RBC's morphological parameters. When an erythrocyte is displayed and detected in the zoom window, the operator can click with the left mouse button on erythrocyte itself to view values relating to its morphological parameters within the corresponding textboxes (Fig. 3.15). This software development step is also extremely important, as the ability of the extracted object's features (represented by cellular morphological parameters) to uniquely represent the object, starting from the available information, influences the effectiveness of individual erythrocyte subclasses recognition (Tomari et al., 2014).

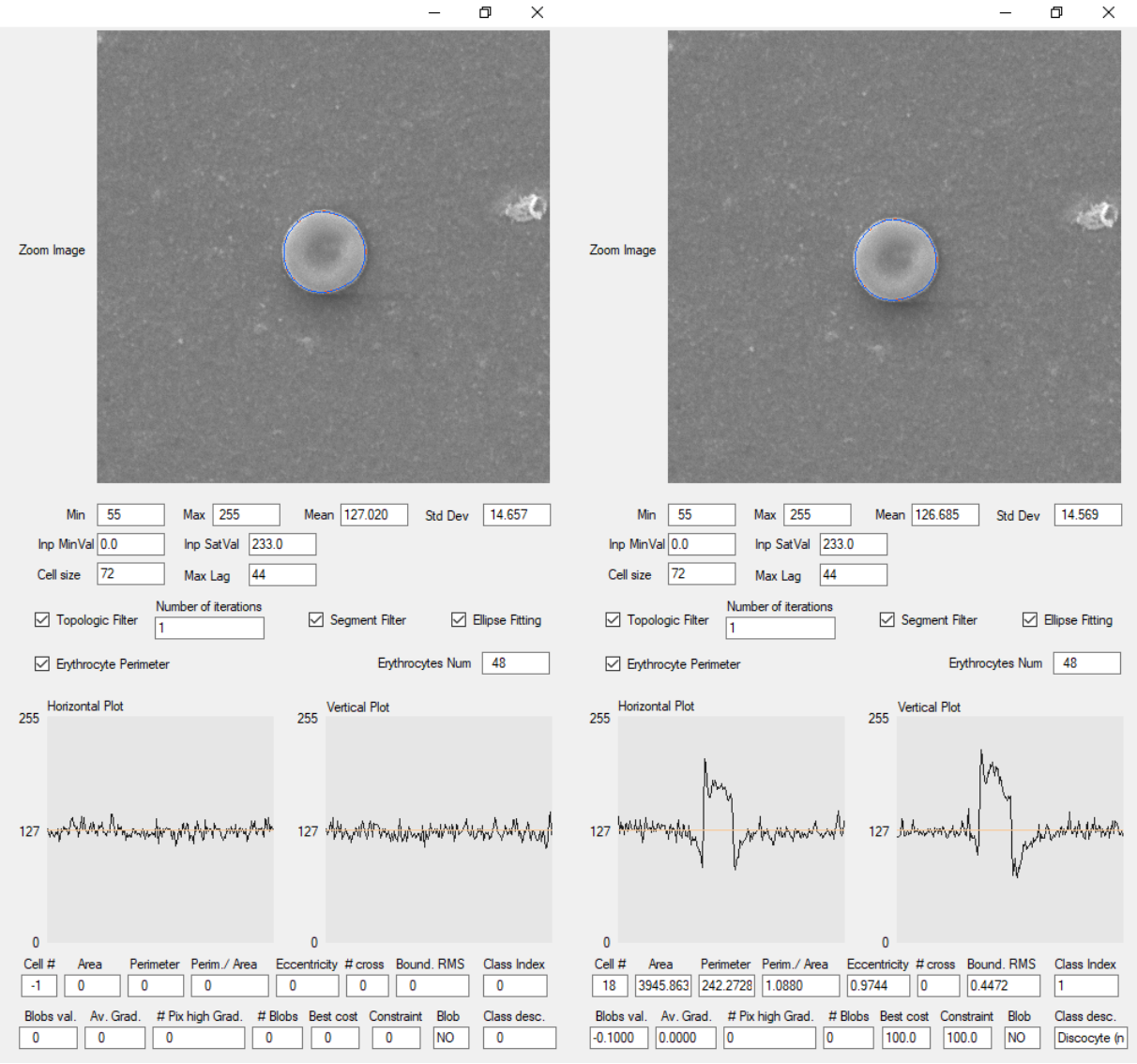

Figure 3.15 - Morphological parameters. As software development progressed, textboxes related to cellular morphological parameters have been added in its interface (Area, Perimeter, Perim./Area, Eccentricity, #crosses, Bound. RMS, Blobs, Av. Grad., #Pix high Grad., #Blobs, Best cost, Constraint, Blob). After clicking anywhere inside the RBC in the zoom window, values relating to morphological parameters are displayed. The difference between before (figure on the left) and after (figure on the right) having clicked can be seen by observing contents of textboxes related to cellular morphological parameters.

3.7.1. Perimeter

During the computation of erythrocyte perimeter, the software completes the entire circle of the cell contour with an angular step that allows the movement of one pixel at a time. Sometimes, however, cell perimeters go back angularly, with respect to the cell center: always moving in the same direction along the perimeter (for example: counterclockwise, in the direction in which the angle increases) sometimes the angle decreases for short distances, in correspondence with cellular contour's spines or irregularities. In the progression made when sampling the superimposed ellipse's perimeter, however, the angle always increases. This discrepancy causes gaps on the cellular perimeter (by going to debug one can realize their presence). The presence of such gaps gives rise to a series of cascading problems such as considering an unsatisfactory number of contour pixels (either a few pixels or too many pixels on the actual contour). A calculation function was developed; it identifies these gaps within the reconstructed contour and attempts to fill them by linear interpolation. This method consists in drawing a line that joins the two pixels at the ends of the gap. The gap is usually 2-3 pixels large, so the result obtained by linear interpolation in most cases represents an acceptable approximation of perimeter shape. When the gap is larger, the line no longer represents a good approximation of the cell perimeter, and the program rejects the reconstruction of the gap with this method. In these cases, the program reports an error in the perimeter reconstruction.

Another aspect that needs to be emphasized is that the perimeter is reconstructed using the 8-connected mode. This means that, for each pixel, the immediately adjacent pixels are connected horizontally (right, left), vertically (below, above) and diagonally (Szeliski, 2020). Using this mode, sometimes two pixels connected diagonally are found on the perimeter. Then to be more precise in the calculation algorithm it is necessary to consider that the distance between the two pixels is no longer 1 but $\sqrt{2}$.

In the perimeter calculation algorithm, there is also a function that can be asked if any pixel is inside or outside the cell perimeter. Thanks to this function it is possible to establish if a pixel is mistakenly considered as internal to the cell when it is actually external (or vice versa). This entails several advantages, including that of being able to determine the cellular area by counting the pixels inside the perimeter.

3.7.2. Area

The area represents the set of pixels contained within the erythrocyte perimeter. To be more precise in the calculation of this parameter, an approximate correction was made to the area calculated as a set of pixels contained within the erythrocyte perimeter, by subtracting half of the perimeter. This

was done because each of perimeter's pixel is ideally half inside and half outside the erythrocyte area. In fact, in theory the perimeter is a thin line with zero thickness that passes through the center of perimeter pixels, while the erythrocyte perimeter has actually its own extension. For a greater accuracy, it has been considered that along the erythrocyte perimeter there may be angular points at which cusps are formed. In that case, not half, but 3/4 of pixels are assigned outside the perimeter. For the purpose of erythrocytes morphological classification, the area represents an important parameter for the discrimination of microcytes and macrocytes with respect to discocytes (Fig. 3.16).

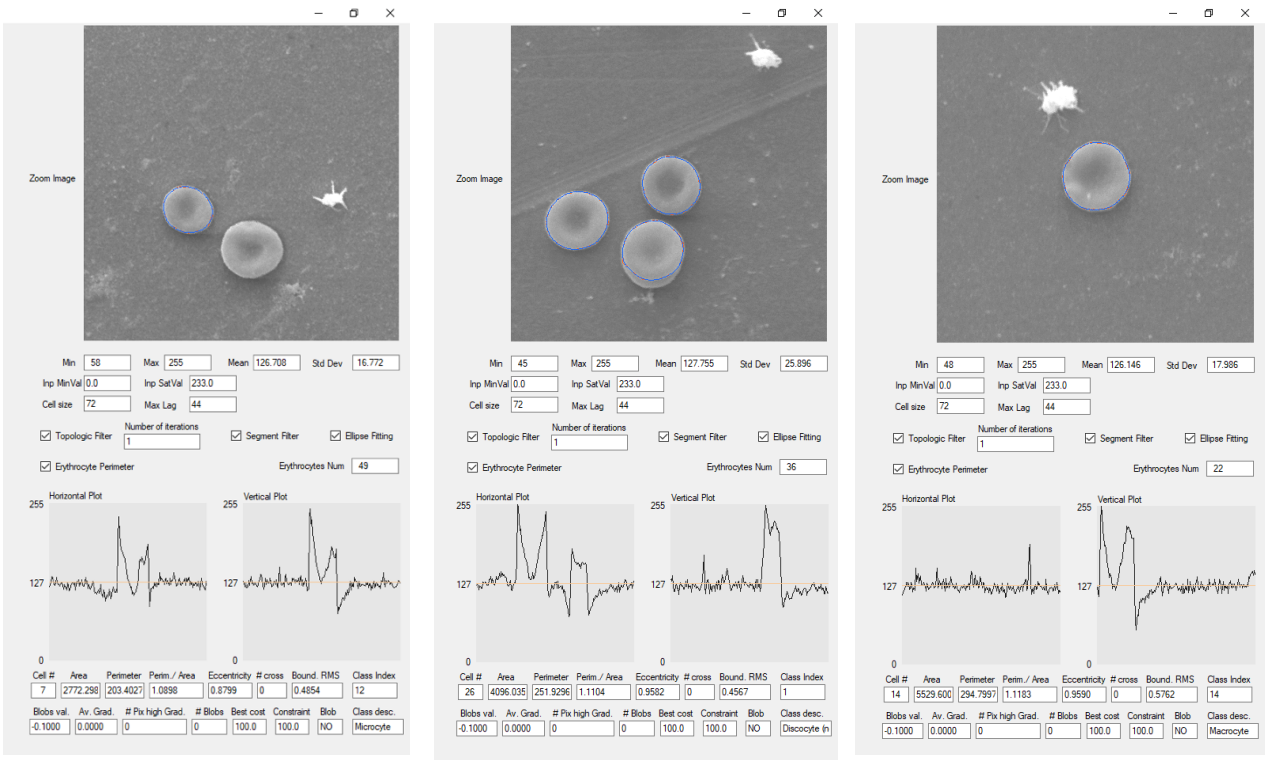

Fig. 3.16 - Morphological parameters: area and perimeter. It can be seen how the area and perimeter values in the case of a discocyte (central figure) are intermediate between those of a microcyte (figure on the left) and a macrocyte (figure on the right).

3.7.3. Eccentricity

Eccentricity indicates the elongation degree of an erythrocyte. To measure the eccentricity, starting from the perimeter, the software searches for the longest axis (major axis) of the erythrocyte, then considers the orthogonal direction in space, then looks for the distance to be framed (minor axis). Thus, a major axis and a minor axis are established: the ratio between the two axes is the measure of eccentricity. Eccentricity represents an essential parameter for the discrimination of elliptocytes (Fig. 3.17).

3.7.4. Perimeter/area ratio

Another parameter considered as important for classification and discrimination between morphotypic and morphologically abnormal erythrocytes is the perimeter/area ratio. For this measurement, the following calculation was used:

$$\frac{perimeter^2 \,/\, area}{4\pi}.$$

The perimeter/area ratio is intended to represent an important feature for classifying abnormal erythrocytes such as those with a jagged outline (echinocytes). In detail, we are interested in understanding when the perimeter increases consistently for the same area. In the case of echinocytes, which have irregular contours and surface spiny protusions, the perimeter/area ratio increases compared to a discocyte of comparable size, due to the greater length of the perimeter. Furthermore, the perimeter/area ratio could help in the identification of elliptocytes. In fact, with the same perimeter, the area of an elliptocyte can decrease and therefore the perimeter/area ratio can increase (Fig. 3.17).

3.7.5. Number of crosses and Boundary RMS

Number of crosses (*#crosses*) and boundary RMS (Root Mean Square; *Bound. RMS*) are two other measures that are effective to analyze the irregularity of erythrocyte perimeter and therefore useful to identify abnormal cells. The pair of the two values reveals most of the red cell abnormalities frequently observed in some pathological blood samples under consideration. To understand the functioning of these two indicators, it must be pointed out that the software performs an upstream operation: it carries out a "smoothed" version of erythrocyte perimeter. Following the processing of erythrocyte images, the real perimeter is displayed in red, while the smoothed perimeter in blue. *Boundary RMS* represents the mean square deviation between the two curves (the two perimeters) in the space. The value of this indicator tends to 0 in healthy cells. *#crosses* instead represents the number of times the real perimeter intertwines on the smoothed perimeter. To validate the intersections, the part circumscribed by the intersection is required to have a minimum area (and if not, the result is zero intersections). Using the software, it was noted that the number of crosses is typically greater than 1 in abnormal cells (Fig. 3.18). The Boundary RMS value rises in each case when the cell begins to develop anomalies in its boundary.

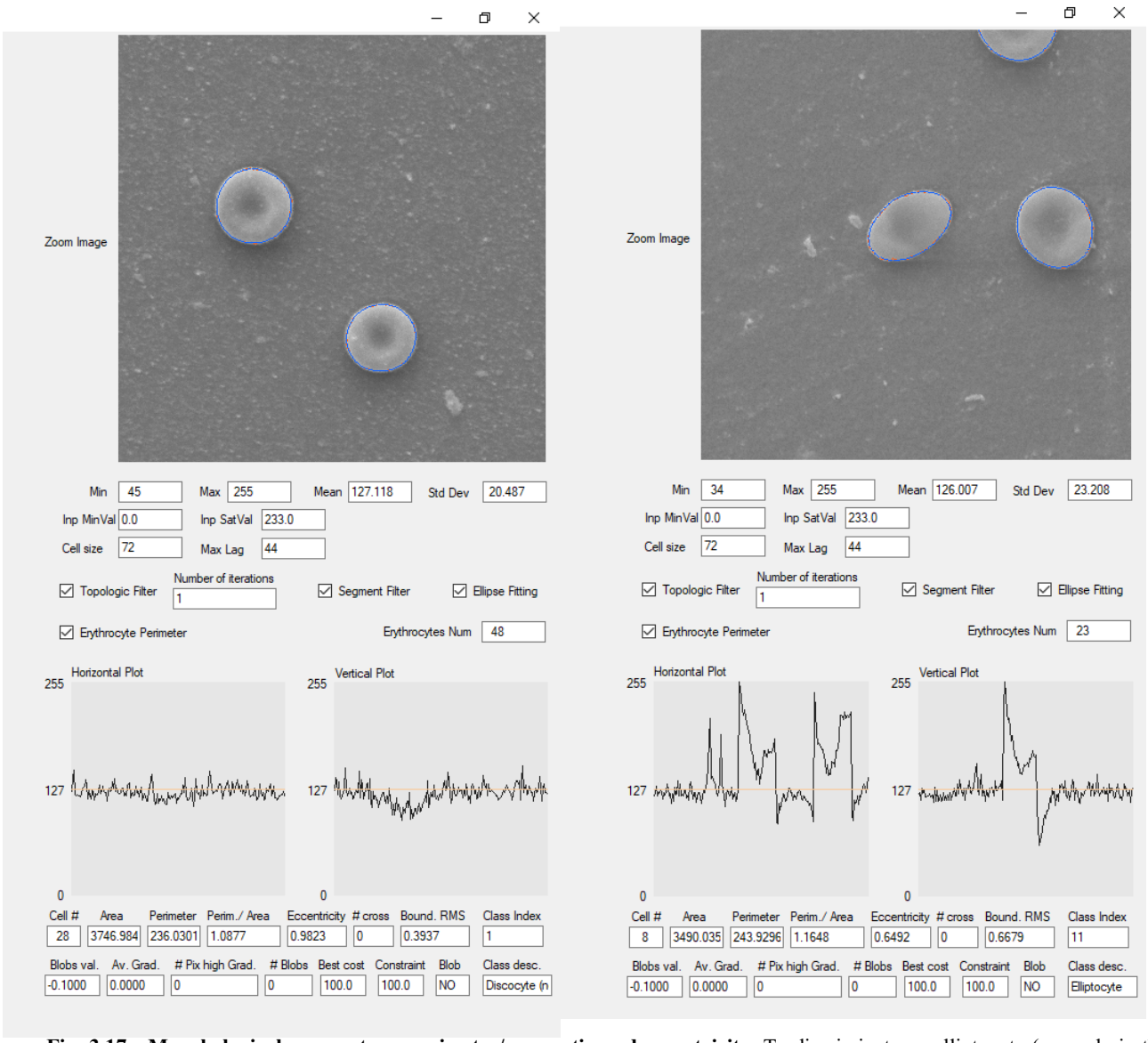

Fig. 3.17 - Morphological parameters: perimeter/area ratio and eccentricity. To discriminate an elliptocyte (example in the figure on the right) from a discocyte (example in the figure on the left) it is important to consider, between the morphological parameters, perimeter/area ratio and eccentricity. Generally, in case of elliptocytes the value of perimeter/area ratio is greater, while that of eccentricity is lower than in case of discocytes.

3.7.6. Blobs

It was decided to indicate with the term "blobs" the irregularities which resemble protuberances found sometimes in abnormal RBC (such as acanthocytes and target cells) of pathological blood samples taken into consideration. To detect blobs in a cell, the software considers a fairly extensive list of parameters: blobs value, average gradient in the cellular area, number of pixels with high gradient within the cellular area, numbers of blobs, cost and constraint. To compute *blobs val. (blobs value)*, *Av. Grad (average gradient in the cellular area)*, and *#Pix high Grad (number of pixels with high gradient within the cellular area)*, the software considers the minimum value, the average value

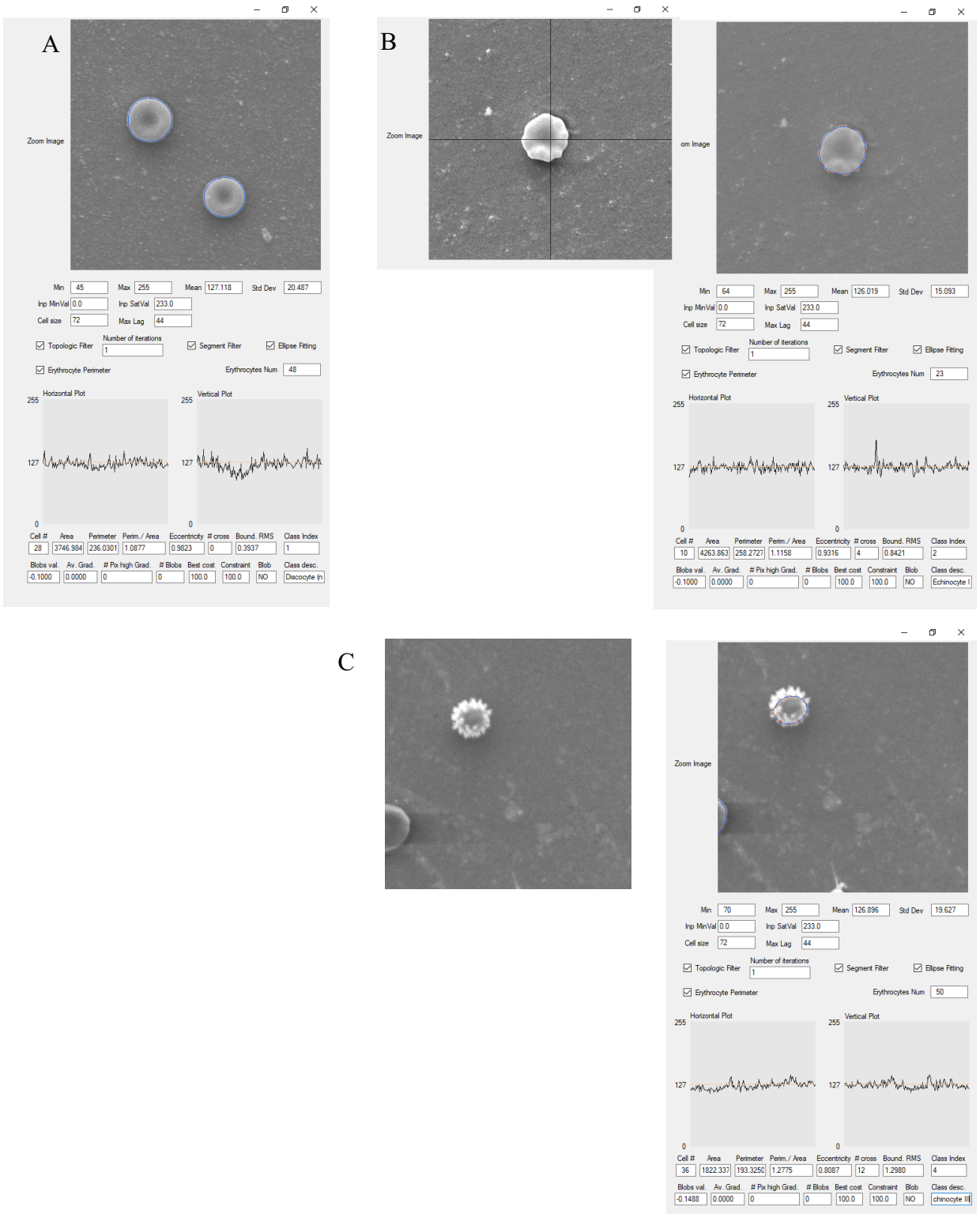

Figure 3.18 - Morphological parameters for echinocytes recognition. To discriminate an echinocyte from a discocyte, it is important to consider, between the morphological parameters, Perim./Area ratio, #crosses and Boundary RMS. In this image it can be seen how the values of these three parameters progressively increase passing from a discocyte (A) to an echinocyte I (B) up to an echinocyte III (C).

and the maximum value of gray level on the cell boundary and also the minimum, average and maximum value of gray level within the cell.

Blobs value equal to 0 should occur for cells completely free from blobs, while a blobs value equal to 1 should occur for cells completely full of blobs. To obtain a blobs value equal to 0, one of the following conditions must be false: (1) the maximum value within the cell is greater than the mean value of the boundary, (2) the maximum value within the cell is greater than or equal to 85% of the maximum value calculated on the contour. If both conditions are true, and therefore the cell contains some blobs, the software calculates the *blobs value* as follows:

$$\frac{maximum\ value\ of\ internal\ averages - average\ value\ of\ the\ perimeter}{maximum\ value\ of\ the\ perimeter - average\ value\ of\ the\ perimeter}\ ^{5}.$$

Therefore, the perimeter's grayscale value is used as a reference point to establish blobs value. It was so decided, as the value of the perimeter's gray level varies from cell to cell. It was considered the maximum value of the internal averages and not the absolute maximum value, because otherwise the software would be too sensitive to variability: there may be very intense pixels inside the cell due to acquisition errors or image noise, which generate extremes.

Instead, to establish the *number of high gradient pixels within the cellular area*, the gradient threshold is first constructed. This was done starting from the following calculation:

$$1{,}15 * the\ maximum\ gray\ level\ on\ the\ perimeter - minimum\ of\ gray\ level\ averages\ inside\ the\ cell\ .$$

This gives an idea of the maximum gradient in the cellular area, that is, the maximum "jump" in terms of pixel intensity that occurs from the inside of the cell towards its boundary. 15% of this value is then considered as a threshold to establish whether the gradient measured inside the cell is high or not. It is believed that the set of parameters for detecting blobs inside the cell and that one for detecting contour irregularities may be important for recognition of acanthocytes (Fig. 3.19).

However, testing the software on SEM images it was found that the blobs recognition procedure developed as just described did not generate completely satisfactory results. In fact, sometimes the software did not recognize protuberances inside the cell, generating false negatives, other times it exchanged normal shadows for these structures, generating false positives. Therefore, it was thought, to improve blobs recognition, to add a new procedure which consists in fitting an ellipse on the blob's contours. This ellipse has got some parameters of freedom: position of the center (which can be moved on the cell), two semi-axes (which can increase or decrease) and the rotation angle of the

[5] To calculate the brightness internal averages the software scans the entire cell's inner part (reaching a distance from the cell center equal to 90% of its radius); for each point, a small window (3x3 or 4x4 pixels in size) around the point is considered and its average brightness is constructed. Therefore, as many brightness averages are obtained as the number of pixels within the cell considered.

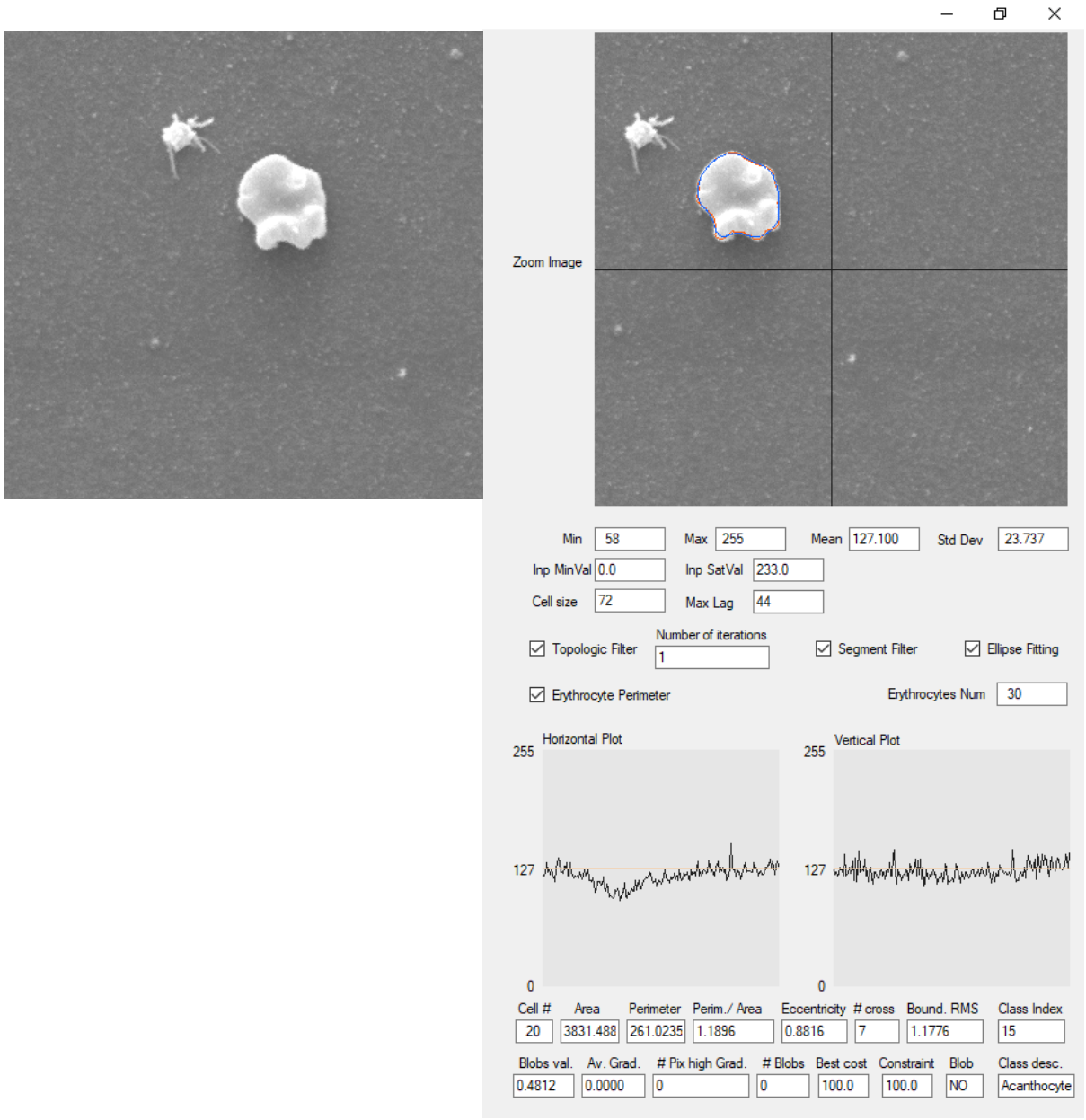

Fig. 3.19 - Morphological parameters for acanthocytes recognition. From this figure it can be seen how, in the case of an acanthocyte, the values of the following morphological parameters are high: Perim./Area, #crosses, Bound. RMS, Blobs val.

ellipse major axis. Some new parameters relating to blobs recognition procedure were therefore taken into consideration: number of blobs (*#blobs*), cost function (*Best cost*), constraint function (*Constraint*). *Cost function* indicates how much ellipse function resembles the blob's outline in the image, giving a difference between the two objects. When the deviation is minimal, it means that the ellipse has been optimized and has undergone the best adaptation to the blob's contour. *Constraint function*, on the other hand, requires that the blob's (ellipse's) central point be a minimum of brightness in the image, that is, the value of the surrounding pixels is higher than that of the central pixel. Again, a lower value indicates a better agreement. At this stage of software development, there were six parameters to consider for blobs detection, making it very difficult to manually evaluate

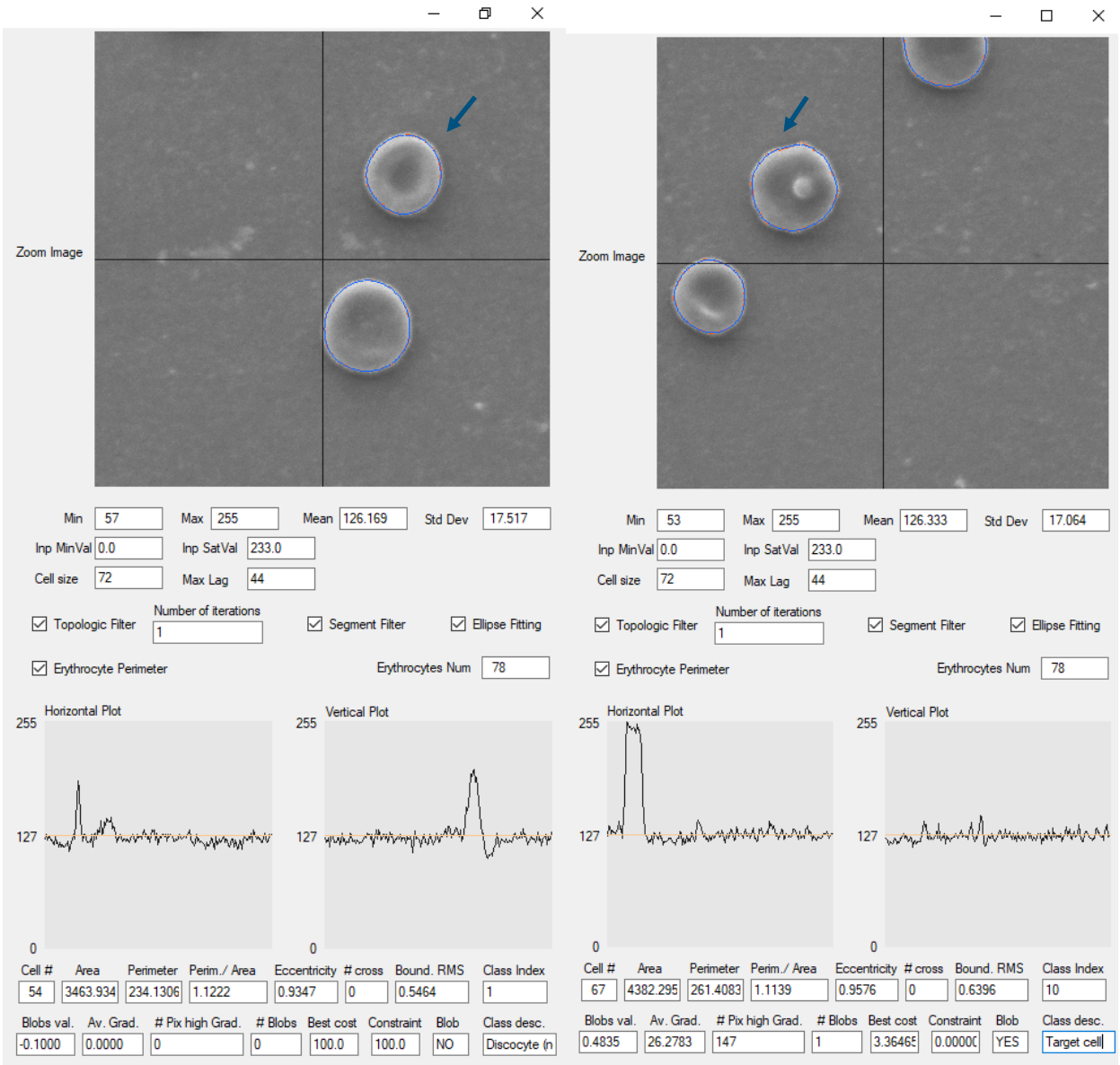

Figure 3.20 - Morphological parameters for blob detection. In the figure on the left (discocyte) one can see: (1) the values of *Blobs val.*, *Av. Grad.*, *#Pix high Grad.*, *#Blobs* parameters tend to zero, (2) the values of *Best cost* and *Constraint* parameters are maximum: this indicates the absence of blobs, as reported by the last of the textboxes for morphological parameters. In the figure on the right (target cell) one can see: (1) the values of *Blobs val.*, *Av. Grad.*, *#Pix high Grad.* parameters are high, (2) the *#Blobs* parameter indicates the presence of 1 blob, (3) the values of *Best cost* and *Constraint* parameters are low: this indicates overall the presence of blobs, as reported by the last of the textboxes for morphological parameters.

processing results. Therefore, it was devised a new parameter to try to perform an overall blobs classification; a new textbox (*Blob*) was added: "Yes" or "No" is displayed, depending on the presence and absence of blobs respectively (Fig. 3.20).

3.7.7. Morphological parameters: discussion

As for our software, in the work by Bacus et al. (1976) the *area* was considered as one of the features useful for the separation of different erythrocyte categories. In this case, the area was described as the number of pixels enclosed by cell boundary. For the discrimination of macrocytes, Chandrasiri e

Samarasinghe (2014) instead used the *Diameter Area Factor*, corresponding to the ratio between the cell diameter and the area and also a factor calculated as the ratio between the area of central pallor and the area. Khot e Prasad (2012) used area values compared to the threshold values to discriminate macrocytes and microcytes, while for the identification of sickle and drop-shaped cells they extracted the minor axis, the major axis and the area. One of the erythrocyte indices used by Albertini et al. (2003) to discriminate 7 morphological classes from RBC images acquired under a light microscope processed with image processing software was the *dimensional index*. It was based on the area (in pixels) of the selection made using the software's rectangular tool that encloses an erythrocyte. In the work by Bhowmick et al. (2012), area (number of pixel present in the segmented SEM image of erythrocytes) and perimeter (number of boundary pixel present in the binary erythrocytes image) were among the geometric extracted features of erythrocytes in SEM images. They were calculated as follow:

- $area = \sum_x \sum_y f(x,y)$

where f(x,y) represent the pixel value corresponding to the (x,y) position of the binary erythrocytes image f(x,y)=1; if f(x,y)∈object else f(x,y)=0; otherwise;

- $perimeter$: $\sum_x \sum_y f(x,y)\ \ x,y \in Boundary\ region$.

Regarding our *perimeter/area ratio* calculated just through this formula, notably it would not provide a suitable result for our purpose, as this ratio just changes according to the size of the cell (in particular, as the size of the erythrocyte increases, the ratio decreases). For example, in the case of a circle, the ratio between perimeter and area is $2\pi r/\pi r^2$ and therefore $2/r$. To solve this problem, the perimeter was squared in the calculation, carrying out the ratio between the perimeter squared and the area. In this way, for example in the case of a perfectly circular cell, the ratio is $4\pi^2r^2 / \pi r^2$ and therefore 4π. This number is fixed and does not depend on the circle size. We were also interested in the fact that the measurement of perimeter/area ratio with its corrections results in a number around the unit value, in order to easily verify the presence of anomalies. For this purpose, the perimeter squared/area ratio was divided in the calculation by the value that this ratio assumes for a perfect circle (4π). It must be considered that even for a perfectly round cell, the value of the perimeter/area ratio with its corrections will never be equal to 1, but always a little greater than 1. This is because the formulas described above for calculating the ratio between perimeter/area (including normalization by the factor 4π) are exact in a continuous space, but not in a discrete space such as that of pixels. In this type of space, the coordinates (area, radius, perimeter) do not vary continuously but in jerks. In an ideal continuous space, on the contrary, the image with which we relate is made up

of infinitely small pixels and for this reason the perimeter/area ratio with its corrections would be equal to 1 for an exactly round cell. In the study by Bacus et al. (1976) a parameter similar to our perimeter/area ratio was taken into consideration for the separation of different erythrocyte categories: *circularity*. It is described as the number of perimeter pixels squared divided by the area. This results in a constant of 3π for perfect circles and a larger number for other shapes.

In several works, one of the features used for erythrocytes identification is the measurement of the roundness of an object. This parameter was represented by the following formula

$$4\pi * area/\ perimeter^2.$$

It was used by: Marzuki et al. (2017) to identify abnormal cells in cases of thalassemia (*roundness)*, Bhowmick et al. (2012) for thalassemia screening (*compactness*), Sharma et al. (2016) to detect sickle cell anaemia and thalasssaemia (*metric value*), Bala and Doegar (2015) for automatic detection of sickle cell (*form factor*). In the work by Tomari et al. (2014) for the development of a computer-assisted system to automate the process of detecting and identifying erythrocytes from blood smear images, a similar feature - *compactness* - was used. Compactness is based on information derived from perimeter and area and it provides information on how the object is formed in terms of the smoothness of the circular shape. When the compactness value becomes high, it means that the shape of the object is more complex.

Regarding our morphological parameter of *eccentricity*, before arriving at the decision to measure it in the way previously described, other attempts were made. Initially it was thought to measure the eccentricity starting from the already fitted ellipse. It was then found that this method was not adequate, as the first fitted ellipse did not give guarantees to cover the cellular area correctly. It was therefore decided to operate in such a way as to superimpose an ellipse on the real cellular perimeter and starting from it to measure the eccentricity. Even this method was not always adequate in accurately measuring eccentricity, since sometimes RBC are not symmetrical and in those cases the ellipse was not able to represent the cells correctly. Also in the work of Bacus et al. (1976), eccentricity was considered as one of the features useful for the separation of different erythrocyte categories. Again, eccentricity is described as a measure of the ratio of width to length of oblong cells. In the work by Chandrasiri and Samarasinghe (2014), a *Shape Area Factor* was defined to determine the oval or circular erythrocyte shape state. This factor was given by the ratio between the greater and the shorter length of the rectangle that encloses the erythrocyte. Unfortunately, this way to estimate the eccentricity of a closed curve (loop) only works when the ellipse major axis is parallel to one of the two rectangle sides, i.e. horizontal or vertical. Marzuki et al. (2017) used erythrocyte

eccentricity (E) to identify abnormal cells in cases of thalassemia. This parameter was given by the equation:

$$E = \sqrt{(major\ axis^2\ - minor\ axis^2)}\ /\ major\ axis.$$

Eccentricity value was between 0 and 1: if the value is equal to 0 it means that the shape is a circle, while if the value is equal to 1, the shape resembles a linear segment. Eccentricity in the work of Bhowmick et al. (2012) is calculated in the same way to the one just described. A similar parameter, called *aspect ratio*, has been used by Sharma et al. (2016) for the detection of sickle cell anemia and thalassemia. It was defined as the ratio between major axis and minor axis. The aspect ratio of a circle is 1 and as the circularity of the shape decreases the aspect ratio increases. It is worth to note that the eccentricity definition adopted by our software was quite different, as shown in the following equation.

$$E = \frac{minor\ axis}{major\ axis}$$

With this definition $E = 1$ corresponds to a perfect circle, and the parameter again belongs to the [0;1] interval.

In the work by Bacus et al. (1976), a feature similar to our morphological parameters of *boundary RMS* and *#crosses* parameters was considered for the separation of different erythrocyte categories: *spicularity* (number of spicules on the boundary).

Regarding the *blob* fitting procedure, optimization algorithms were used to search for the minimum of a defined objective function. In our case, the minimum of the function is obtained when the ellipse is centered on the brightest area of the cell. Between an absolute optimization algorithm (which obtains the absolute minimum of the function) and a relative optimization algorithm (which searches for a relative minimum), the latter type was chosen. An absolute optimization algorithm obtains the absolute minimum of the function, while in the case of a relative optimization algorithm one indicates the approximate values around which the algorithm must look for the minimum - this will find a relative minimum and only occasionally an absolute minimum. A relative rather than absolute optimization algorithm was preferred since the latter are very slow and therefore difficult to use. In the work by Bacus et al. (1976), in a similar way with respect to our work, the authors used, for the separation of the different erythrocyte categories, the *"target"* feature as a measure of the distribution of gray levels in the center of the cell.

3.8. Semi-automatic classification of erythrocyte morphotypes

3.8.1. Extension of processing to the whole image

After establishing cellular morphological parameters crucial for discriminating between healthy and abnormal erythrocytes, the next step in software development was to extend the process of erythrocyte detection from single-cell readings (images in the zoom box) to the whole image. This represented a first step towards automation: it was no longer necessary to click on each cell manually to process it. The goal of extending calculation to the whole image was to allow processing, counting, calculation of morphological parameters and classification of all the cells in the image.

To extend the calculation for erythrocytes detection to the whole image, it was necessary to apply to the whole image the contrast and brightness optimization process, initially carried out only on the image in the zoom box. After the software update, the procedure just described is performed during image loading: when the image is displayed in the software window, the contrast and brightness optimization has already been carried out. At this point, framing a small image in the zoom box, it no longer needs to be modified for brightness and contrast parameters. To perform the brightness and contrast optimization calculation on the whole image, the program builds two new images: one about local *average values* (of the gray level) on the whole image and the other about local *standard deviation* (of the gray level). To do this, the software computes for any image pixel the local average and the standard deviation, estimating them from a (moving) window centered on the considered image point. The software then repeats this calculation for all the pixels of the image, obtaining the mean and the standard deviation images. These mean and standard deviation images are then used to adjust brightness and contrast across the entire image. Since local information is also considered in this calculation, the software capabilities in erythrocytes detection stayed comparable to the initial ones.

At this point in the software development, a new button was added at the software window's bottom right: *Full Img Processing* (Full Image Processing). By clicking on this button, it is possible to process the entire image: after a calculation time of 2-3 minutes, individual detected erythrocytes' boundaries are highlighted on the main image. A new textbox was also added to program window's right column: *Erythrocyte Num* (Erythrocyte Number). It allows to immediately view what is the number of erythrocytes detected by the software in the whole image. By clicking anywhere on the main image, the image region that has got as its center the point on which the click was made, appears in the zoom box at its natural resolution. Detected erythrocytes in this region of the image appear with their boundaries already highlighted (Fig. 3.21). As previously happened, by clicking with the left mouse

button on a cell in the zoom box, values corresponding to the cellular morphological parameters are displayed in the appropriate textboxes at the bottom right of the software window.

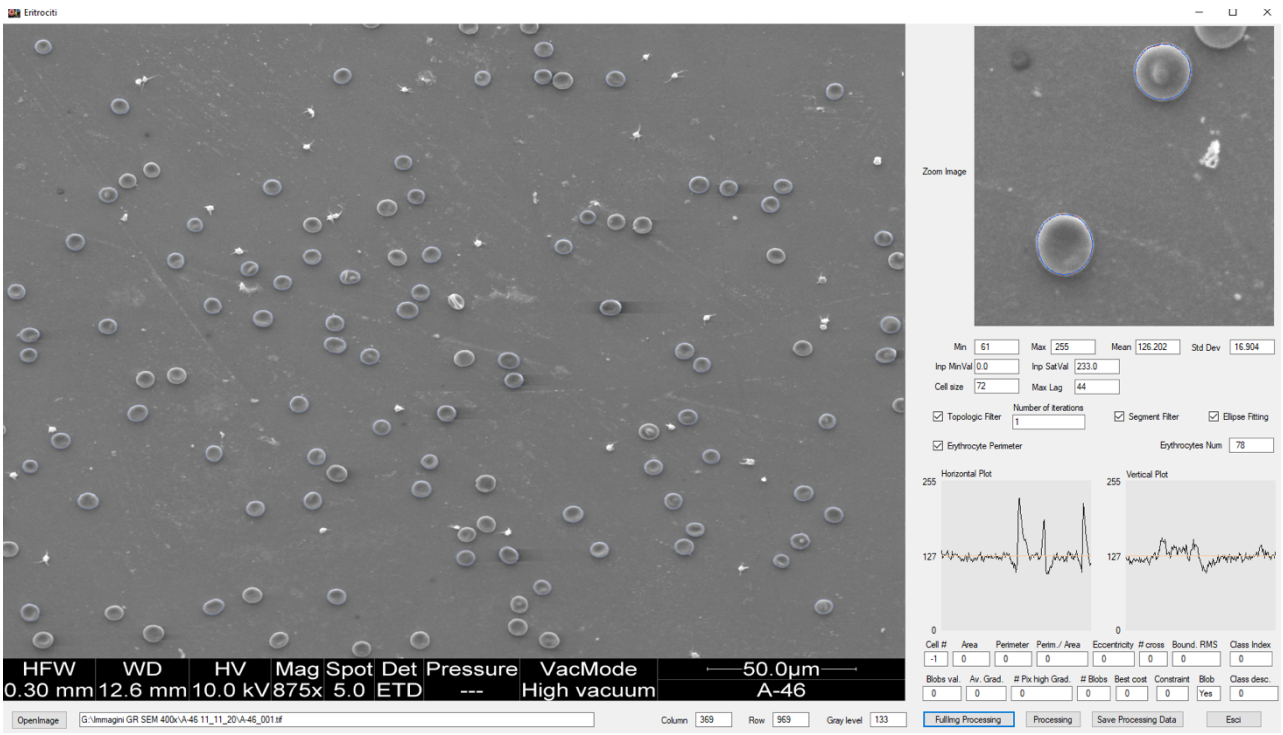

Figure 3.21 - Extension of the calculation to the whole image. In the software window, on the right, one can see two new buttons: *Full Img Processing* and *Erythrocyte Num*. After a single click on the *Full Img Processing* button: (1) erythrocytes detected automatically by the software are highlighted in the main image, (2) the number of erythrocytes automatically detected is displayed in the appropriate textbox.

3.8.2. Extension of processing to the whole image: discussion

The extension of the erythrocyte detection to the whole image in a single step requested to define the contrast and brightness optimization algorithm for the whole image, which was instead initially carried out only on the image in the zoom box. It could not be possible to divide the whole image into many small images and apply contrast and brightness optimization to each. In fact, this method would have posed the problem of non-intact cells in the small images (cells are not, in this case, neither all on a small image, nor on the other). So, applying this method would have meant deleting about half of the cells. There was therefore a need to apply brightness and contrast optimization directly to the entire image. If this operation is not carried out well, "jumps" may be produced along the image. That is, if for example a small image located at the top is optimized differently from one located at the bottom, the program detects "jumps" when these images are then seen close to each other. Initial attempts to adjust brightness and contrast applied to the whole image caused worsening in cell recognition, because the individual small images were low in contrast and therefore flat. With the

final solution found, the average value and standard deviation images are used to adjust the brightness and contrast of the entire image, also taking local information with it. So, with this solution, detection capabilities of RBC should have remained comparable to what they were at the beginning. To verify this, an evaluation of erythrocyte automatic detection process was performed.

3.8.3. Evaluation of erythrocyte automatic detection process

Thanks to extension of the processing to the whole image, it was possible to test the software ability to detect erythrocytes in SEM images. For this purpose, erythrocytes were manually divided into four categories: automatically detected, correctly detected, incorrectly detected (false positives), not detected (false negatives; Suppl. Tab. 10). Incorrectly detected erythrocytes almost always correspond to two or more superimposed cells (stacks). Since the cells are located on a dark background, the change in brightness between one cell and the background is much higher than the change in brightness between the two cells. As a result, the contours separating the cell from its background are much clearer than those separating the two cells from each other. This sometimes results in unsatisfactory contours and, consequently, in incorrect cell recognition (Figure 3.22). Not detected erythrocytes presumably result from unsuccessful processes of filtering, ellipse fitting, or perimeter recognition. Of all the outlines detected, 96.45% were recognized correctly (with the remaining 3.55% of false positives). The efficiency rate of the software in identifying all erythrocytes in SEM images (percentage of erythrocyte correctly detected VS erythrocyte manually counted) was found to be 68.11%. Percentage of false negatives is instead 27.82% (Tab. 3.2). Therefore, it can be inferred a whole method sensitivity of 71% (95% CI: 70.21-71.78%), with a positive predictive value of 96.45% (95% CI: 70.21-71.78%). This erythrocyte recognition step can tolerate a relatively large number of false negatives. In fact, this type of error, if distributed in a completely random fashion among the different morphometric classes of erythrocytes, will simply lead to a reduction in the total number of RBC *per* image available for subsequent processing without influencing in any way the final estimated distribution.

Category	Total for 380 images in 10 samples	Percentage
correctly detected	9216	96.45%
incorrectly detected (false positives)	339	3.55%
not detected (false negatives)	3764	27.82%

Table 3.2 - Results of evaluation of erythrocyte automatic detection process on 380 selected images in 10 samples. Column 2 shows the total number of blood cells detected in each category across all images. Column 3 is the percentage of each category compared to the total number of RBC automatically detected for RBC correctly detected and false positives, and to the total number of RBC counted manually, for false negatives.

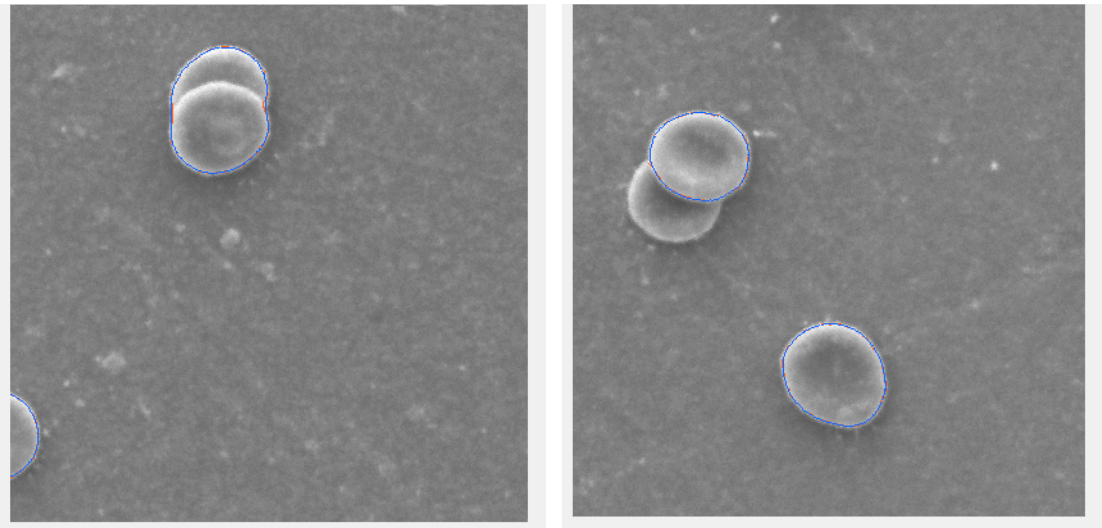

Figure 3.22. False positives and correctly recognized erythrocytes. The figure on the left shows an example of a false positive in erythrocytes detection by the software (the software considers two partially overlapping erythrocytes as a single element), while the figure on the right shows how sometimes the software is able to correctly recognize an erythrocyte even if it is partially overlapping to other one.

3.8.4. Software training step: classification of erythrocytes automatically detected

For the development of the semi-automatic classifier, a training step was firstly necessary. During this phase, erythrocytes automatically detected by the software in SEM micrographs were assigned manually to the morphological classes they belong to. Thanks to a further step forward in software development, it is possible to see a fraction of the image in the zoom box when the mouse cursor is moved over the whole image. By clicking with the right mouse button on the large image, the zoom image at the top right is fixed and stops scrolling. This allows the user to: (1) click with the left button of the mouse on a RBC in the zoom box to see the values of its morphological parameters displayed in the textboxes at the bottom right, (2) click with the right button of the mouse on a red blood cell in the zoom box to set its state. The possible states are the morphological classes to which red blood cells belong (discocyte, echinocyte I, echinocyte II, echinocyte III, acanthocyte, spherocyte, stomatocyte, leptocyte, knizocyte, target cell, elliptocyte, microcyte, macrocyte, other anomaly), the "undefined" state (initially set for all RBC automatically detected) and the “deleted” status (to be selected when the software, making a mistake, identifies a stack of cells or another object as an erythrocyte). It is possible to assign to each erythrocyte its status by clicking with the left mouse on the appropriate wording in the drop-down menu. Following this operation of supervised erythrocyte classification, the erythrocyte class and the corresponding index can be displayed in the new textboxes of the software window (Fig. 3.23). To see again the image at the top right scrolling by moving the mouse over the main image, simply click with the left mouse button on the latter.

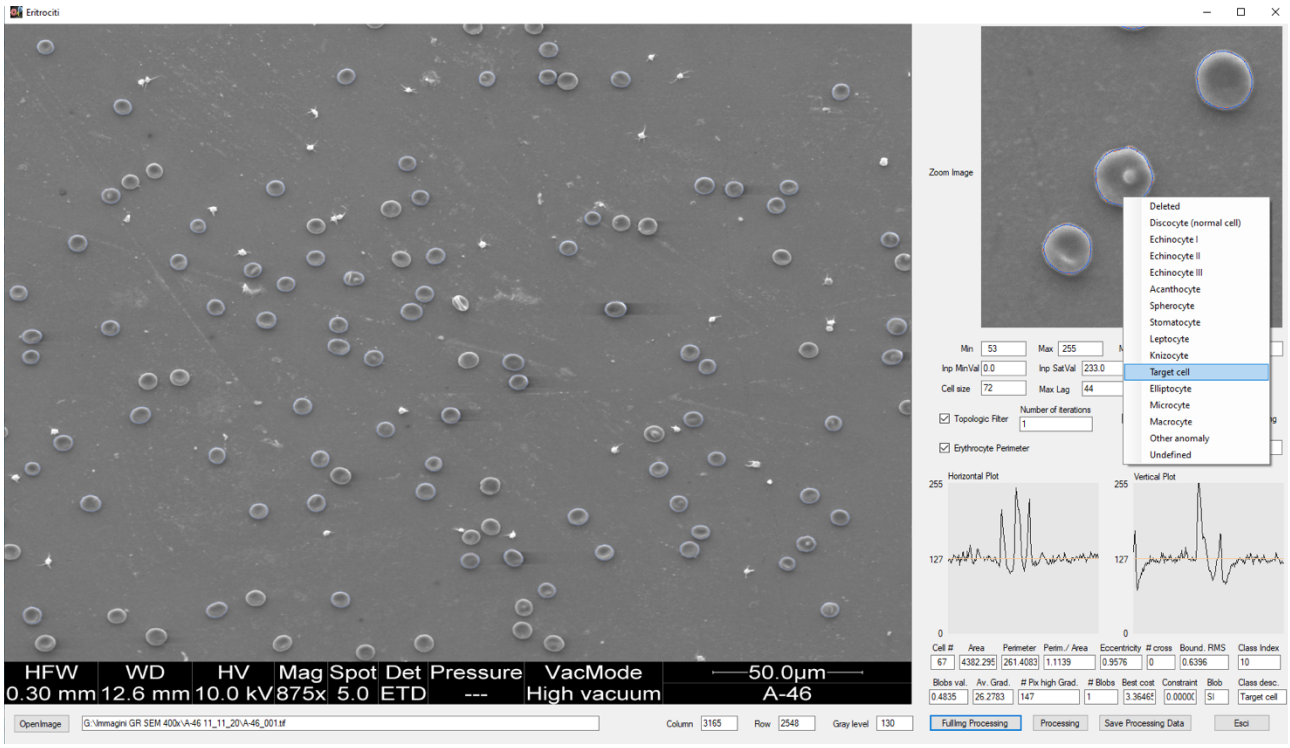

Figure 3.23 - Classification of erythrocytes automatically detected. In this image it can be seen the drop-down menu: thanks to it, it is possible to manually set the morphological class to which the automatically detected erythrocytes belong or to delete an element from the analysis (if the software has made a detection error). After this process, the class index and the class description are displayed in the appropriate textboxes at the bottom right of software interface. The new button *Save processing data* allows to save the supervised classification data of the entire image.

3.8.5. Software training step: saving of processing data

At the end of erythrocyte supervised classification process for each image, the operator must save the data obtained as a result of processing and classification, thanks to the new button at the software interface window's bottom right *Save Processing Data* (Fig. 3.23). By clicking on this button, a dialog box appears. In this box, the operator can choose the format for saving the data (a CSV archive, which will be opened with the Excel software, or a text archive), enter the file name and choose the folder in which to save it. In the file saved (both in the case of the text format and of the CSV format), each line (apart from that of the header) corresponds to an erythrocyte recognized by the software. For each erythrocyte, the corresponding progressive number, the description of its class, the corresponding index and a series of numerical data are displayed. The first of these numerical data represent the x and y coordinates of RBC's center within the image. This information allows to easily find a specific RBC within the micrograph in the software window. Indeed, by moving the mouse cursor on the main image it is possible to observe the row and column values in the corresponding textboxes. The other processing data are related to the erythrocytes morphological parameters previously described together with the values related to the two semiaxes, the angle (that describes

how much the major semiaxis is rotated with respect to the x-axis of the image), maximum diameter (which represents the segment of maximum length passing through the center of the ellipse that joins two points belonging to the ellipse's contour) and minimum, maximum, and average pixel intensity level calculated on the cell perimeter and inside the cell (these latter six new data were added with the aim of helping recognition of specific classes - for example, leptocytes - or to differentiate spherocytes and microcytes). In this way, the association is made between a certain set of numerical values, corresponding to the identified cellular morphological parameters, and a specific erythrocyte in the SEM image, named according to its corresponding morphological class (Fig. 3.24).

3.8.6. Construction of scatterplots graphs

The next step in the work was the construction of scatterplot graphs starting from most of the processing data saved for each image analyzed by the software and classified by the operator. These graphs allow to see how in a two-dimensional diagram the different morphometric classes arranged their points, each corresponding to an erythrocyte. For example, in the most representative of the graphs constructed (Fig. 3.25), it can be immediately noted that microcytes, macrocytes, discocytes and elliptocytes separate quite well, even if with a small overlapping area between discocytes and microcytes. Scatterplot graphs made it possible to get an initial idea of the separation of erythrocyte populations and to understand the precision limits on which it was necessary to work on.

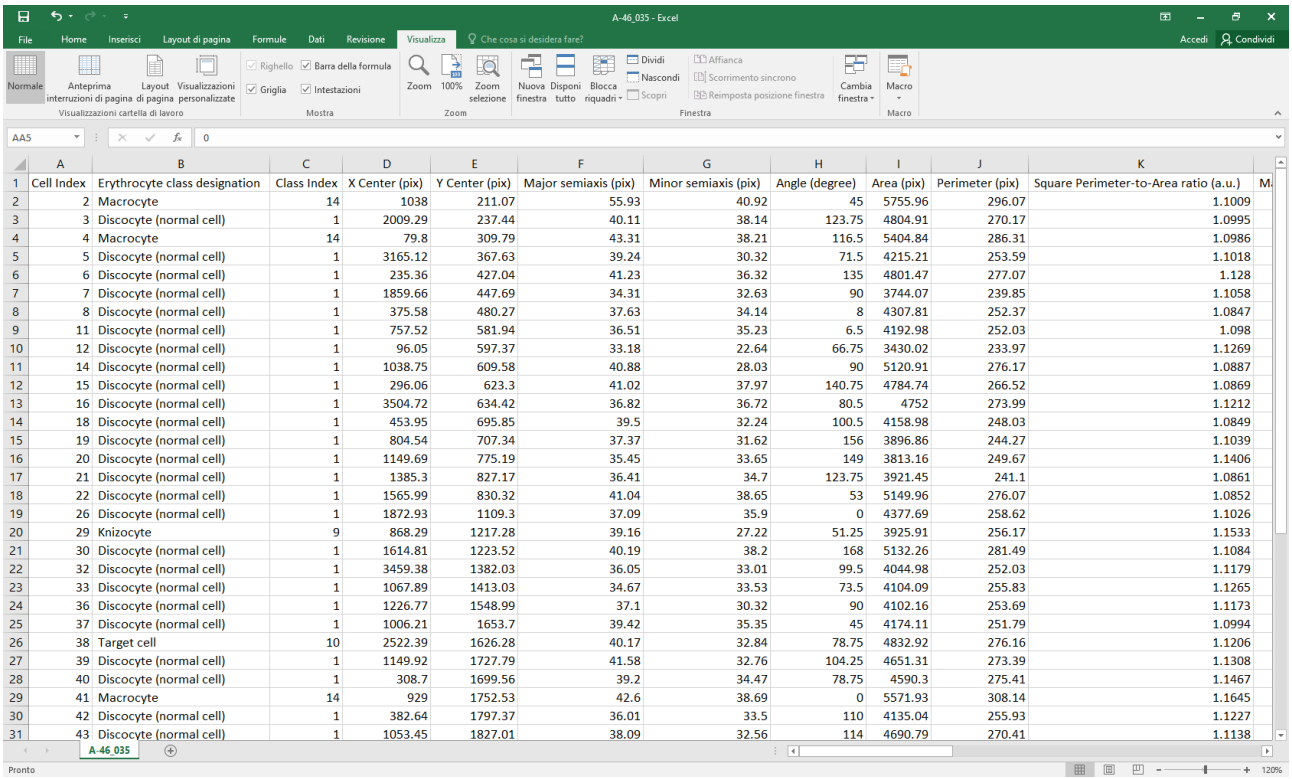

A-46_035 - Excel

Cell Index	Erythrocyte class designation	Class Index	X Center (pix)	Y Center (pix)	Major semiaxis (pix)	Minor semiaxis (pix)	Angle (degree)	Area (pix)	Perimeter (pix)	Square Perimeter-to-Area ratio (a.u.)
2	Macrocyte	14	1038	211.07	55.93	40.92	45	5755.96	296.07	1.1009
3	Discocyte (normal cell)	1	2009.29	237.44	40.11	38.14	123.75	4804.91	270.17	1.0995
4	Macrocyte	14	79.8	309.79	43.31	38.21	116.5	5404.84	286.31	1.0986
5	Discocyte (normal cell)	1	3165.12	367.63	39.24	30.32	71.5	4215.21	253.59	1.1018
6	Discocyte (normal cell)	1	235.36	427.04	41.23	36.32	135	4801.47	277.07	1.128
7	Discocyte (normal cell)	1	1859.66	447.69	34.31	32.63	90	3744.07	239.85	1.1058
8	Discocyte (normal cell)	1	375.58	480.27	37.63	34.14	8	4307.81	252.37	1.0847
11	Discocyte (normal cell)	1	757.52	581.94	36.51	35.23	6.5	4192.98	252.03	1.098
12	Discocyte (normal cell)	1	96.05	597.37	33.18	22.64	66.75	3430.02	233.97	1.1269
14	Discocyte (normal cell)	1	1038.75	609.58	40.88	28.03	90	5120.91	276.17	1.0887
15	Discocyte (normal cell)	1	296.06	623.3	41.02	37.97	140.75	4784.74	266.52	1.0869
16	Discocyte (normal cell)	1	3504.72	634.42	36.82	36.72	80.5	4752	273.99	1.1212
18	Discocyte (normal cell)	1	453.95	695.85	39.5	32.24	100.5	4158.98	248.03	1.0849
19	Discocyte (normal cell)	1	804.54	707.34	37.37	31.62	156	3896.86	244.27	1.1039
20	Discocyte (normal cell)	1	1149.69	775.19	35.45	33.65	149	3813.16	249.67	1.1406
21	Discocyte (normal cell)	1	1385.3	827.17	36.41	34.7	123.75	3921.45	241.1	1.0861
22	Discocyte (normal cell)	1	1565.99	830.32	41.04	38.65	53	5149.96	276.07	1.0852
26	Discocyte (normal cell)	1	1872.93	1109.3	37.09	35.9	0	4377.69	258.62	1.1026
29	Knizocyte	9	868.29	1217.28	39.16	27.22	51.25	3925.91	256.17	1.1533
30	Discocyte (normal cell)	1	1614.81	1223.52	40.19	38.2	168	5132.26	281.49	1.1084
32	Discocyte (normal cell)	1	3459.38	1382.03	36.05	33.01	99.5	4044.98	252.03	1.1179
33	Discocyte (normal cell)	1	1067.89	1413.03	34.67	33.53	73.5	4104.09	255.83	1.1265
36	Discocyte (normal cell)	1	1226.77	1548.99	37.1	30.32	90	4102.16	253.69	1.1173
37	Discocyte (normal cell)	1	1006.21	1653.7	39.42	35.35	45	4174.11	251.79	1.0994
38	Target cell	10	2522.39	1626.28	40.17	32.84	78.75	4832.92	276.16	1.1206
39	Discocyte (normal cell)	1	1149.92	1727.79	41.58	32.76	104.25	4651.31	273.39	1.1308
40	Discocyte (normal cell)	1	308.7	1699.56	39.2	34.47	78.75	4590.3	275.41	1.1467
41	Macrocyte	14	929	1752.53	42.6	38.69	0	5571.93	308.14	1.1645
42	Discocyte (normal cell)	1	382.64	1797.37	36.01	33.5	110	4135.04	255.93	1.1227
43	Discocyte (normal cell)	1	1053.45	1827.01	38.09	32.56	114	4690.79	270.41	1.1138

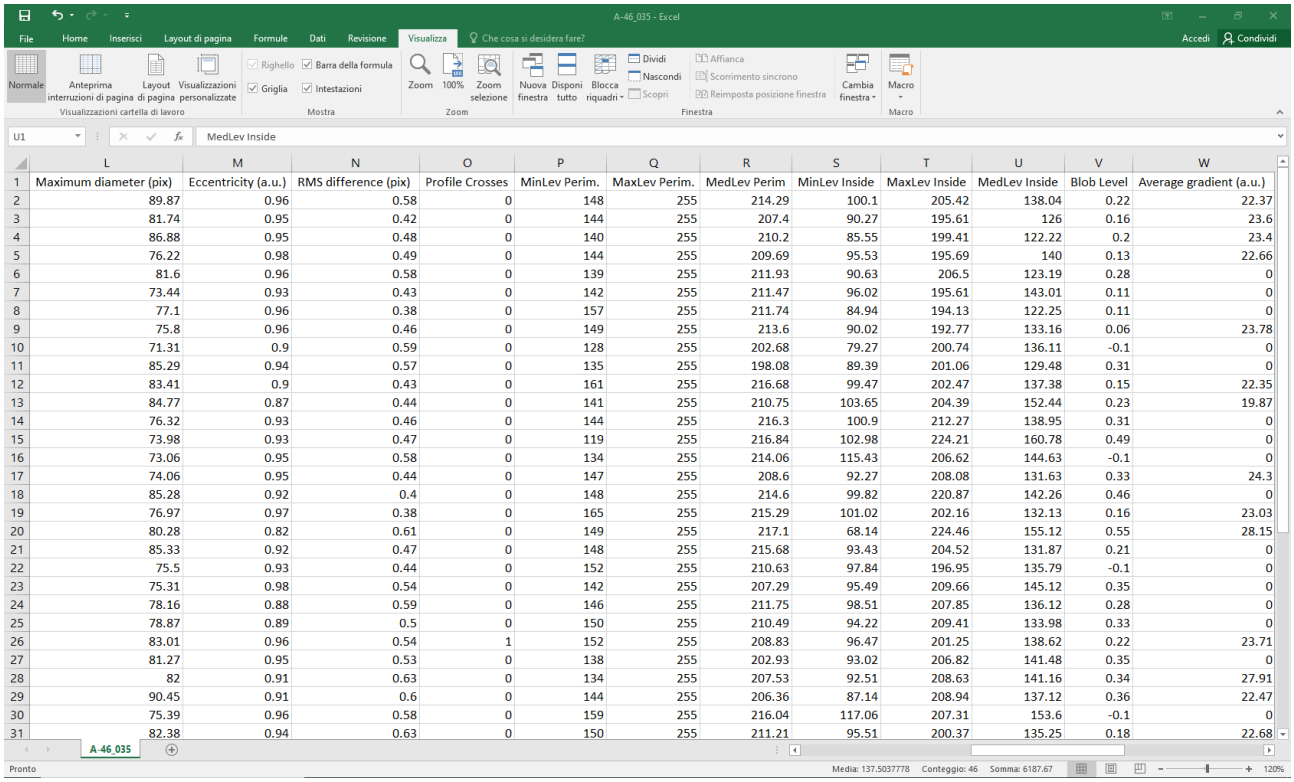

A-46_035 - Excel

File Home Inserisci Layout di pagina Formule Dati Revisione Visualizza Che cosa si desidera fare? Accedi Condividi

Normale | Anteprima interruzioni di pagina | Layout di pagina | Visualizzazioni personalizzate | Visualizzazioni cartella di lavoro
Righello | Barra della formula | Griglia | Intestazioni | Mostra
Zoom | 100% | Zoom selezione | Zoom
Nuova finestra | Disponi tutto | Blocca riquadri | Dividi | Nascondi | Scopri | Affianca | Scorrimento sincrono | Reimposta posizione finestra | Cambia finestra | Finestra
Macro | Macro

U1 | MedLev Inside

	L	M	N	O	P	Q	R	S	T	U	V	W
1	Maximum diameter (pix)	Eccentricity (a.u.)	RMS difference (pix)	Profile Crosses	MinLev Perim.	MaxLev Perim.	MedLev Perim	MinLev Inside	MaxLev Inside	MedLev Inside	Blob Level	Average gradient (a.u.)
2	89.87	0.96	0.58	0	148	255	214.29	100.1	205.42	138.04	0.22	22.37
3	81.74	0.95	0.42	0	144	255	207.4	90.27	195.61	126	0.16	23.6
4	86.88	0.95	0.48	0	140	255	210.2	85.55	199.41	122.22	0.2	23.4
5	76.22	0.98	0.49	0	144	255	209.69	95.53	195.69	140	0.13	22.66
6	81.6	0.96	0.58	0	139	255	211.93	90.63	206.5	123.19	0.28	0
7	73.44	0.93	0.43	0	142	255	211.47	96.02	195.61	143.01	0.11	0
8	77.1	0.96	0.38	0	157	255	211.74	84.94	194.13	122.25	0.11	0
9	75.8	0.96	0.46	0	149	255	213.6	90.02	192.77	133.16	0.06	23.78
10	71.31	0.9	0.59	0	128	255	202.68	79.27	200.74	136.11	-0.1	0
11	85.29	0.94	0.57	0	135	255	198.08	89.39	201.06	129.48	0.31	0
12	83.41	0.9	0.43	0	161	255	216.68	99.47	202.47	137.38	0.15	22.35
13	84.77	0.87	0.44	0	141	255	210.75	103.65	204.39	152.44	0.23	19.87
14	76.32	0.93	0.46	0	144	255	216.3	100.9	212.27	138.95	0.31	0
15	73.98	0.93	0.47	0	119	255	216.84	102.98	224.21	160.78	0.49	0
16	73.06	0.95	0.58	0	134	255	214.06	115.43	206.62	144.63	-0.1	0
17	74.06	0.95	0.44	0	147	255	208.6	92.27	208.08	131.63	0.33	24.3
18	85.28	0.92	0.4	0	148	255	214.6	99.82	220.87	142.26	0.46	0
19	76.97	0.97	0.38	0	165	255	215.29	101.02	202.16	132.13	0.16	23.03
20	80.28	0.82	0.61	0	149	255	217.1	68.14	224.46	155.12	0.55	28.15
21	85.33	0.92	0.47	0	148	255	215.68	93.43	204.52	131.87	0.21	0
22	75.5	0.93	0.44	0	152	255	210.63	97.84	196.95	135.79	-0.1	0
23	75.31	0.98	0.54	0	142	255	207.29	95.49	209.66	145.12	0.35	0
24	78.16	0.88	0.59	0	146	255	211.75	98.51	207.85	136.12	0.28	0
25	78.87	0.89	0.5	0	150	255	210.49	94.22	209.41	133.98	0.33	0
26	83.01	0.96	0.54	1	152	255	208.83	96.47	201.25	138.62	0.22	23.71
27	81.27	0.95	0.53	0	138	255	202.93	93.02	206.82	141.48	0.35	0
28	82	0.91	0.63	0	134	255	207.53	92.51	208.63	141.16	0.34	27.91
29	90.45	0.91	0.6	0	144	255	206.36	87.14	208.94	137.12	0.36	22.47
30	75.39	0.96	0.58	0	159	255	216.04	117.06	207.31	153.6	-0.1	0
31	82.38	0.94	0.63	0	150	255	211.21	95.51	200.37	135.25	0.18	22.68

A-46_035

Pronto | Media: 137.5037778 | Conteggio: 46 | Somma: 6187.67 | 120%

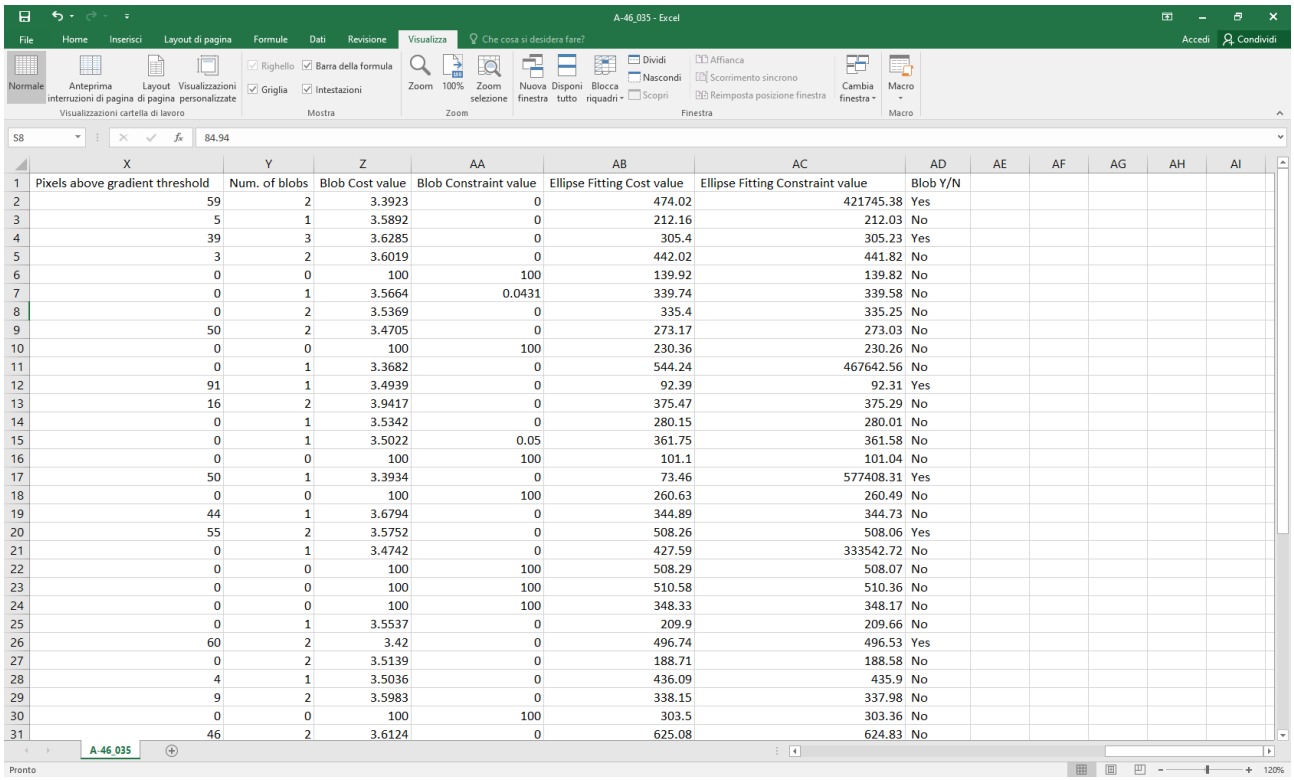

A-46_035 - Excel

File Home Inserisci Layout di pagina Formule Dati Revisione Visualizza Che cosa si desidera fare? Accedi Condividi

Normale | Anteprima interruzioni di pagina | Layout di pagina | Visualizzazioni personalizzate | Visualizzazioni cartella di lavoro
Righello | Barra della formula | Griglia | Intestazioni | Mostra
Zoom | 100% | Zoom selezione | Zoom
Nuova finestra | Disponi tutto | Blocca riquadri | Dividi | Nascondi | Scopri | Affianca | Scorrimento sincrono | Reimposta posizione finestra | Cambia finestra | Finestra
Macro | Macro

S8 | 84.94

	X	Y	Z	AA	AB	AC	AD	AE	AF	AG	AH	AI
1	Pixels above gradient threshold	Num. of blobs	Blob Cost value	Blob Constraint value	Ellipse Fitting Cost value	Ellipse Fitting Constraint value	Blob Y/N					
2	59	2	3.3923	0	474.02	421745.38	Yes					
3	5	1	3.5892	0	212.16	212.03	No					
4	39	3	3.6285	0	305.4	305.23	Yes					
5	3	2	3.6019	0	442.02	441.82	No					
6	0	0	100	100	139.92	139.82	No					
7	0	1	3.5664	0.0431	339.74	339.58	No					
8	0	2	3.5369	0	335.4	335.25	No					
9	50	2	3.4705	0	273.17	273.03	No					
10	0	0	100	100	230.36	230.26	No					
11	0	1	3.3682	0	544.24	467642.56	No					
12	91	1	3.4939	0	92.39	92.31	Yes					
13	16	2	3.9417	0	375.47	375.29	No					
14	0	1	3.5342	0	280.15	280.01	No					
15	0	1	3.5022	0.05	361.75	361.58	No					
16	0	0	100	100	101.1	101.04	No					
17	50	1	3.3934	0	73.46	577408.31	Yes					
18	0	0	100	100	260.63	260.49	No					
19	44	1	3.6794	0	344.89	344.73	No					
20	55	2	3.5752	0	508.26	508.06	Yes					
21	0	1	3.4742	0	427.59	333542.72	No					
22	0	0	100	100	508.29	508.07	No					
23	0	0	100	100	510.58	510.36	No					
24	0	0	100	100	348.33	348.17	No					
25	0	1	3.5537	0	209.9	209.66	No					
26	60	2	3.42	0	496.74	496.53	Yes					
27	0	2	3.5139	0	188.71	188.58	No					
28	4	1	3.5036	0	436.09	435.9	No					
29	9	2	3.5983	0	338.15	337.98	No					
30	0	0	100	100	303.5	303.36	No					
31	46	2	3.6124	0	625.08	624.83	No					

A-46_035

Pronto | 120%

Figure 3.24: File saved of processing data. In the file saved of processing data, each row (apart from that of the header) corresponds to an erythrocyte recognized by the software. Numerical data corresponding to the morphological parameters previously described are displayed for each erythrocyte.

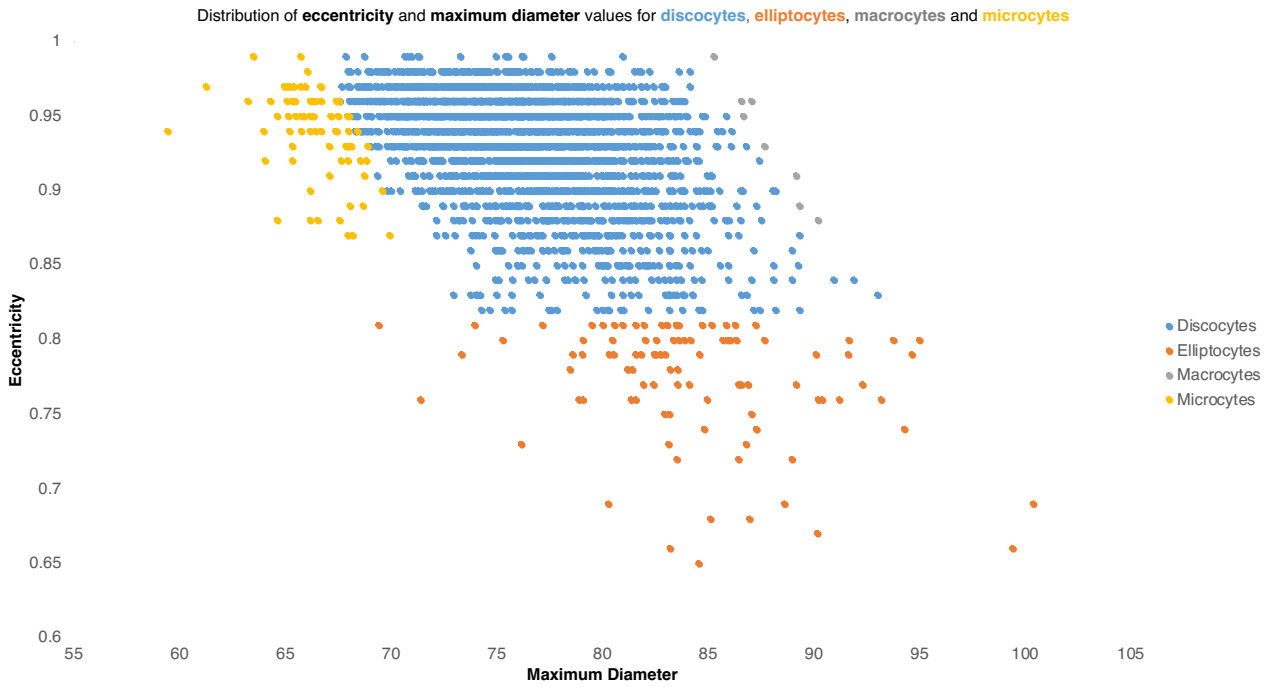

Fig. 3.25 - Distribution of discocytes, elliptocytes, macrocytes and microcytes according to eccentricity and maximum diameter. In this scatterplot graph it can be noted that microcytes, macrocytes, discocytes and elliptocytes separate quite well, even if with a small overlapping area between discocytes and microcytes.

3.8.7. Erythrocyte morphotypes classifier

After the construction of the erythrocyte morphotypes classifier, a new button (*Classification*) was added to the software interface at the bottom right. This button was linked to erythrocytes detected in the image loaded into the software. It allows to perform automatic classification of erythrocytes after the *Processing* or *Full Img Processing* function have been performed. After executing the classification command, it is possible to click on an erythrocyte detected in the zoom image to view its predicted classification: the classification textbox is automatically filled by replacing the word "undefined" with the word corresponding to the morphological class to which the erythrocyte belongs. A new summary table was also added, in which the probabilities for the processed cell of belonging to each morphological erythrocyte class can be read (Fig. 3.26).

In this new version of the software, a new checkbox was also added (*Ignore Radiometric Parameters*), just below the probability summary table. This checkbox instructs the classification algorithm to ignore those parameters which may depend on the radiometry of the image. It is important because if contrast and brightness were changed between the acquisition of the training dataset and the processed image, no valid statistical information is available for radiometric

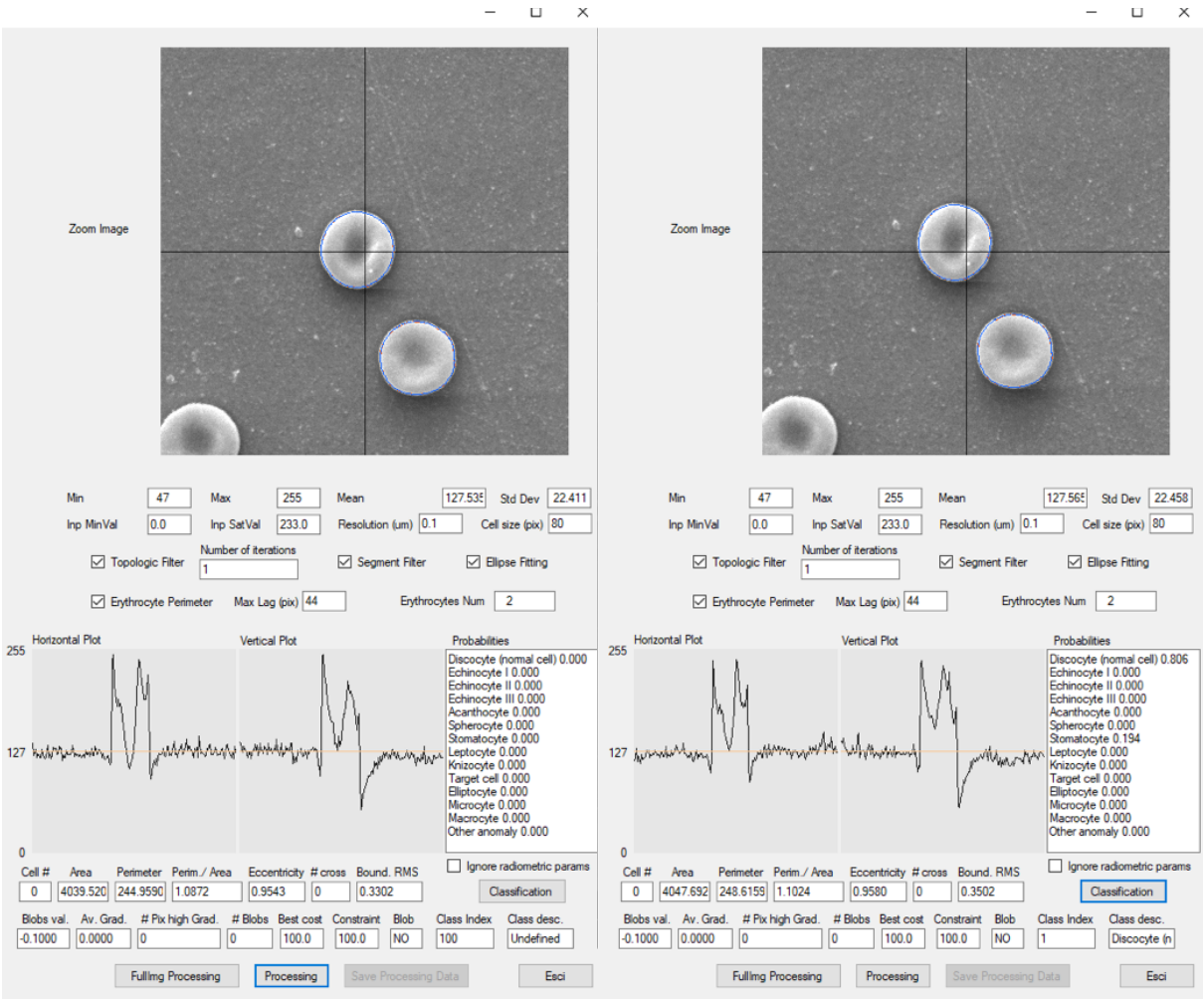

Figure 3.26 - Automatic classification. The new *Classification* button can be noted at the bottom right of the software graphical interface. It can be also noted that, before performing the automatic classification, the state assigned to the erythrocyte just processed is undefined (figure on the left), while after clicking on *Classification* button, *class index* and *class description* are automatically assigned to the erythrocyte (figure on the right). To the right of the transects it can be also seen a new summary table in which the probabilities for the erythrocyte of belonging to each morphological class can be read.

parameters. Typically, classification can be tried first including all parameters and then, if recognition problems are noticed, radiometric parameters can be excluded. After the checkbox has been selected or deselected, the classification button must be clicked again.

Differently from image intensity data, space-like or geometrical parameters (e.g.: cell area, perimeter, and eccentricity) can be easily corrected when image spatial resolution changes between the training and classification phases. The software can correctly manage space scale variations, as the user is requested to insert into a dedicated textbox – labeled *Resolution (um)* – the spatial resolution of the image currently processed. This is the explicit indication of the image resolution, that is, the spatial dimension of a pixel in micrometers. The default value is 0.08586. Inserting a new value automatically updates the adjacent textbox, called *Cell size (pix)*. The update takes 6 micrometers as the default average size of an erythrocyte. The smaller a pixel is (as an absolute scale), the larger the area of the erythrocytes will be, thus their perimeter, maximum diameter, etc. The

algorithm uses this resolution when correcting the value of space-like parameters to match the values of these parameters with respect to the spatial resolution of the statistical parameterization data of the erythrocyte classes. Figure 3.27 shows how the graphical interface of the new software version looks like.

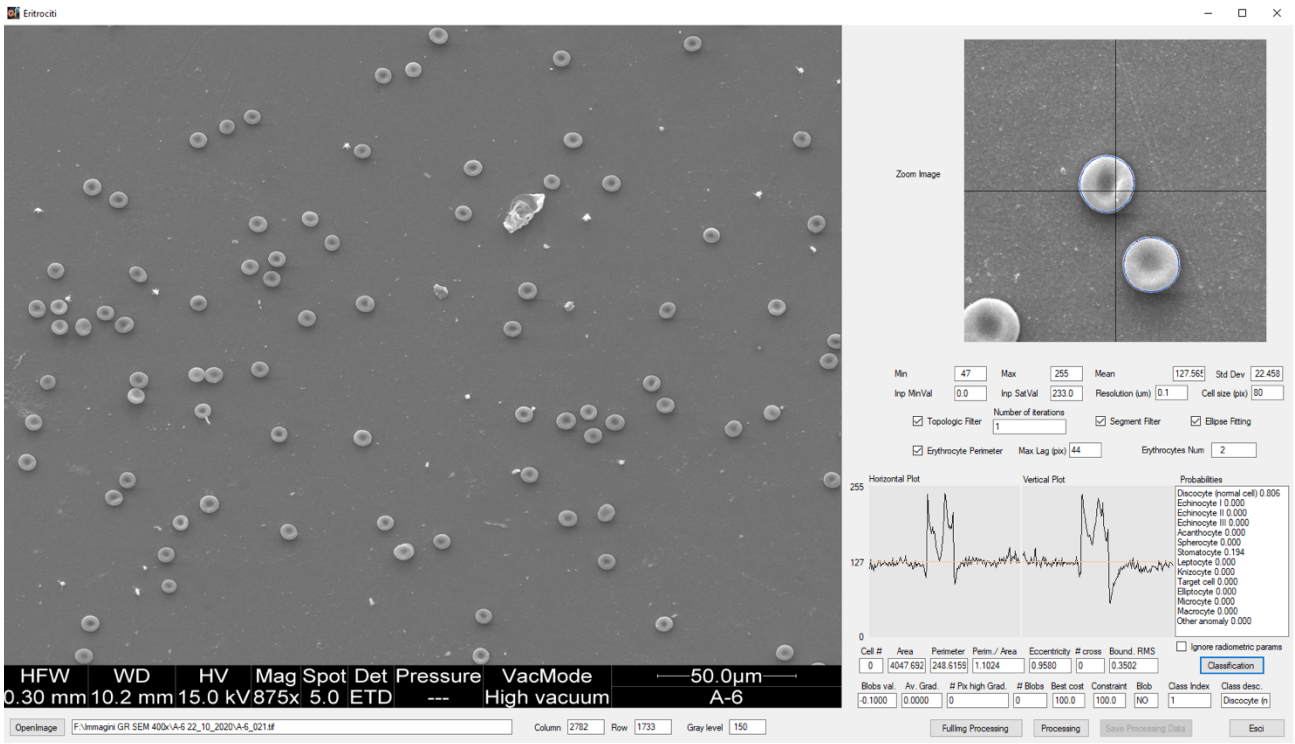

Figure 3.27 - Graphical interface of the updated software version with the possibility of automatic erythrocyte classification. Apart from the new elements already described (*Classification* button and probabilities table), in this figure it can be noted: a new textbox (*Resolution (um)*) and a new checkbox (*Ignore radiometric params*). The *Max Lag (pix)* textbox has been moved close to the *Erythrocyte Perimeter* checkbox.

3.8.8. Erythrocyte morphotypes classifier: discussion

The possibility of using Bayes classification alone for semi-automatic classification of erythrocytes was excluded. Bayes classification minimizes the total probabilities of error (sum of false positives and false negatives). In this respect, it is the best classification possible, statically giving the best performance. However, whenever one of the two possible classes is very rare, Bayes classification scheme always assigns the element to the least rare class. The Neyman-Pearson classification criterion, on the other hand, tends to minimize not the probability of false positives and false negatives, but only the probability of false negatives, subject to the constraint that the number of false positives does not grow excessively. The problem of the Neyman-Pearson classification criterion is establishing the thresholds of a priori probabilities (likelihood ratio), a problem that cannot be solved analytically because it is mathematically too complex. Bayesian classification was instead chosen by

Bhowmick et al. (2013) for automated classification of anemia, along with its sub-class, using SEM images of unstained blood cells. Several authors (Kim et al., 2001; Tomari et al., 2014; Wąsowicz et al., 2017) used neural networks to classify the blood cells in blood smear images. Instead, Sharma et al. (2016) used a K-Nearest Neighbor classifier to detect sickle cell anaemia and thalassaemia.

Actually, it is incorrect to state that the variables relating to all morphological parameters except 5 (area, perimeter, maximum diameter, eccentricity and boundary RMS) are statistically independent. However, it was still decided to construct a multivariate probability density only for a maximum of 5 parameters, because if, for example, a multivariate probability density with dimension 16 (how many morphological parameters are in all) were constructed, it would be necessary to work with square matrices of dimensions 16, making the work complicated and time-consuming.

In the case of the IdentiCyte program, a library of examples of cell identifications has been built (examples of cells from each class are placed in the folder corresponding to that category). Subsequently, through the compilation process, all the images in the library folders are read and transformed and the results are saved in a file, as is the case of our software. This phase can be considered analogous to the training step of our software. Finally, RBC are identified using the eigenfaces method. It uses a principal component analysis to extract features from the library of pre-identified cells. These features can be used to compare new images to those in the library and determine which is most similar. The program IdentiCyte shows the morphological classification of RBC a little differently than in our software: images that have already been identified can be viewed with labels over cells to show the identifications (Garnier et al., 2019).

3.8.9. Erythrocytes semi-automatic classification

The latest version of the software contains a new button (*Open Test File*) and a new textbox used to open the test files consisting of morphological parameter's values of erythrocytes belonging to a specific morphological class (Fig. 3.28,3.29). After having opened the test file with the appropriate button, it is necessary to click on the *Classification* button to obtain the classification of the erythrocytes reported in the test file. At this point the program generates the *Classification.tx*t file in its folder; in this file the classification results are reported (Fig. 3.30; this file is also generated when the operator classifies an image). This operation was performed for the erythrocyte test files belonging to the morphological classes of discocytes, echinocytes I, spherocytes, stomatocytes, knizocytes, target cells, elliptocytes, microcytes and macrocytes to evaluate the efficiency of the automatic classifier. The remaining morphological classes were not taken into consideration as for these classes there were not enough elements (erythrocytes) in the processing data generated during the training

TestDiscocitiA - Blocco note di Windows

File Modifica Formato Visualizza ?

```
1241
4304.34 281.33  1.2096  81.22   0.85    0.53    0       128     255     210     93.35   216.57  134.23  0.44    0       0
3996.28 245.44  1.0953  77.01   0.91    0.61    0       156     255     210.88  103.39  206.56  142.09  0.26    19.89   39
3879.81 240.37  1.0886  73.98   0.95    0.45    0       156     255     220.79  108.08  209.14  144.8   0.19    0       0
5244.53 278.94  1.0865  89.36   0.87    0.56    0       136     255     204.61  96.08   203.63  137.7   0.29    22.19   17
4412.96 278.07  1.1808  80.16   0.91    0.6     0       142     255     205.25  98.41   228.94  150.42  0.63    22.56   156
4614.65 270.69  1.1241  82.01   0.92    0.52    0       147     255     214.03  98.35   220.36  142.1   0.46    0       0
4711.04 273.93  1.1258  82.42   0.93    0.64    0       143     255     204.13  98.53   216.91  135.9   0.47    0       0
3999.12 263.76  1.1766  77.03   0.92    0.57    0       144     255     209.15  114.12  217.05  145.14  0.41    19.42   85
5209.98 308.03  1.2038  86.49   0.94    0.72    0       129     255     211.08  90.63   219.58  140.93  0.48    0       0
3800.23 249.54  1.1419  74.53   0.9     0.67    0       134     255     187.54  90      198.43  124.41  0.35    0       0
4970.45 273.1   1.0928  84.31   0.93    0.5     0       150     255     215.88  99.88   205.05  131.1   0.2     0       0
4195.66 254.68  1.1092  78.16   0.91    0.53    0       137     255     211.83  90.04   200.59  131.84  0.19    22.61   54
4980.33 271.34  1.0846  86.4    0.88    0.44    0       135     255     212.22  97      205.29  132.65  0.24    24.43   97
3972.69 242.62  1.0859  74.67   0.94    0.4     0       138     255     213.78  87.57   196.85  131.38  0.13    22.16   59
4609.45 265.1   1.1015  82.57   0.9     0.49    0       141     255     215.06  84.96   194.19  130.52  0.08    22.7    81
4767.86 268.27  1.096   83.24   0.92    0.59    0       145     255     211.31  93.02   202.38  139.21  0.22    23.89   40
3976.61 250.78  1.1218  74.63   0.95    0.5     0       134     255     205.95  90.06   207.89  129.83  0.35    0       0
4461.04 261.93  1.1063  82.64   0.86    0.46    0       148     255     207.77  91.9    201.59  132.67  0.24    0       0
4927.21 269.59  1.0834  84.2    0.93    0.48    0       139     255     209.64  94      206.84  134.69  0.3     23.49   135
4436.86 258.27  1.0938  78.41   0.94    0.46    0       135     255     202.14  90.61   205.29  127.69  0.34    24      85
4392.75 266.51  1.1343  78.29   0.95    0.52    0       140     255     202.68  93.86   208.77  131.86  0.38    0       0
4122.69 250.62  1.1011  77.37   0.9     0.41    0       136     255     209.35  84.67   196.38  125.46  0.17    23.32   90
4068.04 253.93  1.1231  78.6    0.86    0.56    0       145     255     196.52  97.22   187.76  123.75  -0.1    0       0
4351.74 258.52  1.1055  77.47   0.96    0.5     0       136     255     207.16  83.49   196.23  133.75  0.19    25.68   115
4741.62 274.76  1.1256  82.49   0.91    0.46    0       138     255     208.08  79.33   195.89  127.56  0.19    27.28   130
3461.28 233.44  1.1193  73.78   0.84    0.56    0       147     255     212.92  96.27   206.76  150.78  -0.1    0       0
```

Linea 1, colonna 1 | 100% | Windows (CRLF) | UTF-8

Figure 3.28 – Example of text file used to test the efficiency of erythrocyte morphotypes classifier. Each line - which represented an erythrocyte - consists of erythrocyte morphological parameters' values (the exception is the first line where only the number of total elements considered in the file itself is displayed). These values were extrapolated from the processing data of the training step.

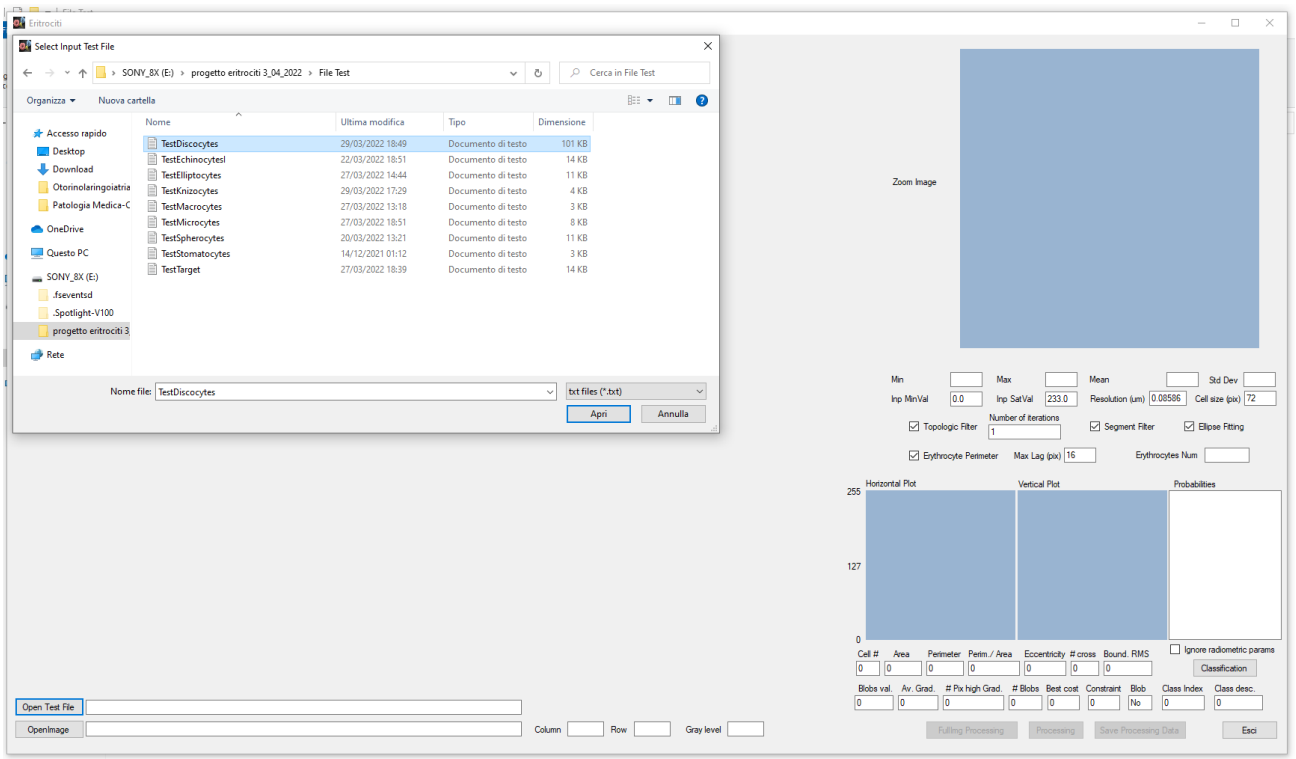

Figure 3.29 - Graphical interface of the software as it appears after clicking on the "Open Test File" button. Just above the *Open Image* button the presence of the new *Open Test File* button and the related textbox can be seen. The dialog box that opens after clicking on the new button can be also noted. It allows to select the desired test file for the subsequent classification.

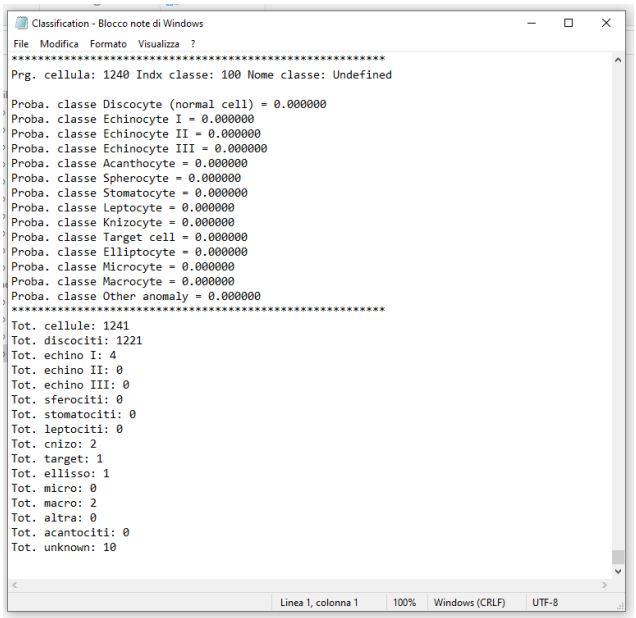

Figure 3.30 – Example of a *Classification.txt* file produced following the automatic classification of a test file. The summary file called *Classification.txt* reports the salient data of the classification carried out: first the list of individual cells with the different probabilities, then the overall summary.

step. Results of the test operation were organized in a confusion matrix (Tab. 3.3). In addition to the morphological classes previously mentioned, in the Tab. 3.3 a row relating to the "undefined" category can be also seen: an instance of morphological parameters is set to the undefined status when its probability to belong to various classes shows a small change between the first and the second most probable classes (uncertainty), or when the likelihood of obtaining that combination of morphological parameters is negligible (the instance is an outlier). The last three rows in the Tab. 3.3 report the estimates of true positives, false negatives and unknown rates regarding the classification of any morphological class. Sensitivity and accuracy values of the software for individual morphotype classes are shown in Tab. 3.4. The data confirm high accuracy of the software for identifying elliptocytes (91.45%), macrocytes (94.44%) and microcytes (98.57%) with acceptable accuracy for target cells (70.97%) and echinocytes I (76.52%) spherocytes (86.21%), discocytes (87.79%), while accuracy was found to be insufficient (<60%) for knizocytes (54.84%) and stomatocytes (58.97%).

	Discocytes	Echinocytes I	Spherocytes	Stomatocytes	Knizocytes	Target cells	Elliptocytes	Microcytes	Macrocytes	FP (%)
Tot	**1241**	**180**	**133**	**35**	**39**	**156**	**149**	**104**	**35**	
Discocytes	1208	61	24	2	4	71	1	5	0	**8.108**
Echinocytes I	1	88	0	0	0	23	1	2	0	**1.303**
Spherocytes	0	0	100	0	5	1	0	10	0	**0.772**
Stomatocytes	1	0	0	23	2	2	4	7	0	**0.772**
Knizocytes	3	2	0	0	17	7	1	1	0	**0.676**
Target cells	4	2	0	0	0	22	0	3	0	**0.434**
Elliptocytes	1	3	0	4	5	0	139	0	0	**0.627**
Microcytes	0	1	0	0	0	0	0	69	0	**0.048**
Macrocytes	1	0	0	0	0	2	0	0	34	**0.145**
Undefined	22	23	9	6	6	28	3	7	1	**4.730**
	1241	180	133	35	39	156	149	104	35	
TP (%)	**97.341**	**48.889**	**75.188**	**65.714**	**43.590**	**14.103**	**93.289**	**66.346**	**97.143**	
FN (%)	**0.886**	**38.333**	**18.045**	**17.143**	**41.026**	**67.949**	**4.698**	**26.923**	**0.000**	
Unknown (%)	**1.773**	**12.778**	**6.767**	**17.143**	**15.385**	**17.949**	**2.013**	**6.731**	**2.857**	

Table 3.3 - Result of automatic classification test. The first row and the first column show the erythrocyte morphological classes taken into consideration for the automatic classification test. The second row shows the total number of cells classified for each erythrocyte class. Subsequently, the assignments (classification) provided by the classification algorithm are shown in the individual columns. Below are shown the total number of cells classified for each erythrocyte class, followed by the percentages of true positive (TP) and false negatives (FN) and unknown relating to the class in question against all the other classes as a whole. The last column reports the total percentage of false positives (FP) of each class, summed up on all tests and normalized to the total number of classifications (2072).

Erythrocyte morphological class	Sensitivity (%)	95% Confidence interval (C.I.)	Accuracy (%)	95% Confidence interval (C.I.)
Knizocytes	51.52	33.54 – 69.20	54.84	36.03 – 72.68
Stomatocytes	79.31	60.28 – 92.01	58.97	42.10 – 74.43
Target cells	17.19	11.10 – 24.86	70.97	51.96 – 85.78
Echinocytes I	56.05	47.92 – 63.95	76.52	67.71 – 83.92
Spherocytes	80.65	72.58 – 87.19	86.21	78.57 – 91.91
Discocytes	99.10	98.39 – 99.55	87.79	85.94 - 89.47
Elliptocytes	95.21	90.37 – 98.05	91.45	85.82 – 95.37
Macrocytes	100	89.72 – 100	94.44	81.34 – 99.32
Microcytes	71.13	61.05 – 79.89	98.57	92.30 – 99.96

Table 3.4 - Results of automatic classification test: sensitivity and accuracy values. Note: data are calculated not accounting "undefined" morphotypes.

3.8.10. Erythrocytes semi-automatic classification: discussion

In the current availability of numerous data regarding individual human operator classification, it is interesting to note how this software is able to intercept erythrocyte morphological categories, albeit with different degrees of efficiency. About this, we point out that the most frequent erythrocyte class (discocytes) has a false negative rate far below one (0.886%), an essential condition for any attempt to perform autonomous classification of SEM images. The low number of true positives related to target cells is due to the currently modest efficiency of the software in detecting blobs (Tab. 3.5), despite the numerous attempts we tried to improve this aspect of the software and despite the high number of morphological parameters related to blobs that the software can calculate. In addition, about the different degrees of efficiency of the software in intercepting abnormal erythrocyte morphotypes, let us note that not all classes of morphological anomalies have the same weight in terms of correlation with a specific pathology. In fact, in the future it will be worth asking whether a certain shape character classified in a more or less efficient way by the software is significant for the pathology to be intercepted, before performing an initial test of the software for diagnostic purposes.

Category	Total for 28 target cells in 2 samples	Percentage
False negatives	21	75%
True positives	7	25%

Table 3.5 – Evaluation of software's ability to recognize blobs. False negatives: target cells with unrecognized blobs. True positives: target cells with recognized blobs.

3.8.11. Computer-assisted tool for erythrocyte phenotyping in SEM micrographs: final discussion

Several published works on erythrocyte classification have focused on classification of erythrocytes into normal or abnormal, limited number of erythrocyte shapes, or on correlation with specific disease processes based on the combination of extracted morphological features from RBC (Yturralde et al., 2020). However, several previous publications (Agrawal and Verma, 2015; Ali et al., 2013; Tomari et al., 2014; Zheng et al., 2004) have described their methods and results without making their software readily available. On the other hand, there are some commercially available hematology analyzers (or automatic cell counters, which are the most common high-tech devices used to perform various types of tests on human blood samples): HemaCAM by Fraunhofer Institute for Integrated Circuits IIS, Germany (*HemaCAM®*), Vision Hema by West Medica, Germany (*Vision Hema® Assist - Automatic Cell Imaging System by West Medica*), EasyCell by Medica corporation, USA (*Hematology Imaging System*, 2014), and CellaVision® DM9600 by CellaVision, Sweden (*CellaVision® DM9600*). Most of these systems are specialized in the detection of white blood cells, while CellaVision is specialized for the automatic detection and classification of morphological abnormalities in RBC. However, reports published for erythrocytes classification with CellaVision demonstrate limited specificity and variable accuracy without re-classification by operators (Criel et al., 2016; Egelé et al., 2016).

The software that has been presented in this thesis is the first computer-assisted tool to be designed specifically for identification of RBC morphotypes in SEM micrographs from ASD patients' blood samples. In order to discover if erythrocyte morphological alterations may be used as a component of a screening for early ASD diagnosis, it is necessary to analyze many blood samples, and for each of them, to count and classify a large number of erythrocytes. Owning and being able to use a computerized system for erythrocyte morphometric analysis would relieve operators from manual search and classification of erythrocyte shapes during SEM analysis, a time-consuming and tedious work. Despite the flaw represented by the low sensitivity of the software in identifying all the RBC in SEM micrographs, this tool has the great advantage of high reproducibility. Indeed, results from manual classification are subject to strong variability of objective and subjective operators' conditions which affects the results, determining their instability. Conversely, automatic classification processes are not subject to this type of variability. Another important advantage of using a computerized morphometric analysis system is the calculation speed. In fact, manual classification requires a generally long execution time, which is not susceptible of optimization. Instead, automatic classification can be optimized through more powerful computers and more efficient software

implementations. Another positive aspect of our software is the large number of computers on which it is potentially executable. Indeed, our software can be run from a Windows executable: this point is important because currently windows has an 82.45% market share on desktop computers (Garnier et al., 2019). This makes our software different from the program Cytomine, for which exists only instruction to use it on Linux-based operating systems. Another advantage of our software is its extreme simplicity of use for operators, thanks to its user-friendly interface and the few operations that must be carried out to get the final result. For example, unlike the method used by McInerney and Terzopoulos (2000) and that by Park and Keller (2001), our software does not require careful initial setup for the discrimination between significant and non-significant contours. The power of our software lies in the possibility of classifying many dozens of cells just by clicking on three buttons (one for image opening, one for processing and the last one for classification). This makes our software different from the programs CellProfiler and CellProfiler Analyst (the first one applies image processing, the second one uses machine learning techniques to count and identify cells; Carpenter et al. 2006; Jones et al. 2008). These programs, even if powerful, are not very user friendly: there are many modules, each of which has several options to parse. Furthermore, both these two separate pieces of software need to be run to get complete results. Another software which has been developed and published for public use is BlobFinder. Differently from our software, this program only counts cells without classifying them (Allalou and Wählby, 2009). Another software which has been developed to count and identify RBC from a series of microscope images is the program IdentiCyte developed by Garnier et al. (2019). In this program, for RBC recognition users are given the ability to change the value of minimum pixel area for an object to be considered a cell, together with other key variables in the operation of the program itself. This is similar to what happens with our software, which require initial definition of the cellular size value in pixel and other few parameters. However, while IdentiCyte focused on the discrimination from discocytes only two erythrocyte categories (spherocytes and echinocytes) and the related transition phases, our software also focuses on the classification of other morphological categories (for example microcytes, macrocytes, elliptocytes, stomatocytes, knizocytes). Furthermore, IdentiCyte was developed for light microscopy images, unlike our software which was developed specifically for SEM micrographs.

Our research will continue by producing further software training data, in order to try to reach a sufficient number of elements also regarding the erythrocyte morphological classes of echinocytes II, echinocytes III, acanthocytes and leptocytes. In the future it will also be interesting to calculate the possible variability of the software efficiency in the classification of erythrocyte morphotypes, starting from different portions of the dataset, and then to compare this data with those of intra-operator variability already calculated for the manual SEM analysis of erythrocyte morphotypes.

Further studies are also needed to establish whether our software has got the potential to perform well also on RBC photos acquired through light microscope with interferential contrast. In conclusion, it is possible to say that our software for erythrocyte phenotyping in SEM micrographs has very good chances to become a powerful laboratory tool with many potential applications ranging from many diagnostic purposes to basic research in hematology.

4. CONCLUSIONS

This thesis work concerns a pioneering sector that begins the exploration aimed at finding new biomarkers for an early diagnosis of ASD, basing on SEM morphological analysis of RBC. One of the goals achieved by this work is the optimization of a new protocol, based on the acupuncture method, for blood samples preparation aimed at SEM morphological analysis of RBC. After having obtained, by the local ethics committee, a favorable opinion and the authorization to proceed for the research project about erythrocyte morphological changes in pediatric ASD patients, preliminary results from blood samples analysis at SEM were produced. This meant the possibility of starting to prepare a red blood cells morphometric dataset at SEM of ASD patients and healthy volunteers. Considering the limited number of blood samples available so far, this first part of the present thesis work should be considered as the basis for future research that eventually will allow to calculate the statistical significance of the possible differences in erythrocyte morphology between ASD patients and healthy controls. Then it will be possible to continue the research to determine at what age the erythrocyte morphological changes begin to appear in ASD patients and to establish, by retrospective analysis with respect to the clinical diagnosis of ASD, whether this occurs earlier than the neuropsychiatric diagnosis of the disease. Answering these questions is of seminal importance to know if the presence of erythrocyte morphological alterations in ASD patients can be considered as a biomarker to be included in a screening aimed at early ASD diagnosis. Indeed, it is desirable for the future the possibility of combining information obtained from erythrocytes morphometric tests with other data, for example molecular data concerning lipid and protein components of the erythrocyte membrane, to define a reliable set of laboratory tests useful for ASD diagnostics.

This study also investigated the intra-operator variability of the RBC morphological analysis by SEM, while still remains to clarify the nature of the inter-operator variability of this kind of analysis. Observations from studying intra-operator variability of the RBC morphological analysis by SEM strongly suggest the need of a high number of replicate counts and supports the key relevance of implementing reliable computer-assisted algorithms and machine learning systems in order to discover potential novel disease biomarkers based on SEM analysis of peripheral blood micro-samples. Indeed, the most consistent part of this thesis concerns the development, operation and validation of a computer-assisted tool that has been shown to be capable of detection and semi-automatic classification of erythrocytes in SEM micrographs. Future development of the work will be to classify, through this software, erythrocytes in SEM micrographs acquired from blood micro-samples, allowing the system to associate, to each subject, a distribution of erythrocytes among the

several morphometric classes. In the future it would be very interesting to compare these data with those obtained from the manual RBC classification at SEM of the same set of samples. Since the final aim of the study is to provide an automated predictive tool that can reveal potential pathological conditions, the definition of the patient's status will depend on the frequency of RBC in the different morphological classes. Based on the frequency of erythrocytes with altered morphology in the blood sample, it will be possible to hypothesize the patient's pathological state. We believe that, if the hypothesis about erythrocyte morphological alterations as an early biomarker of ASD will be validated, this software could become a very useful tool in the hands of families and clinicians to identify individuals at risk of developing ASD. Furthermore, our software will be able to find application not only in ASD diagnostics, but also in basic research studies, concerning for example the effects of alterations in RBC membrane's cortical cytoskeleton or lipid composition on changes in erythrocyte shape.

5. ACKNOWLEDGEMENTS

I thank my Prof. Tutor, Professor Lupetti, for the trust he has placed in me since day one, for making his laboratory available to me and for the time and patience needed to supervise my PhD. I also thank him for giving me autonomy and freedom in working methods, for always recognizing my merits, making me feel appreciated and esteemed, but also for pointing out mistakes when necessary.

I thank Prof. Barducci for the fruitful work of developing the new software, to which I was lucky enough to collaborate. I thank him for his great ability in explaining with clarity and simplicity topics that are actually complex and far from my background and for his infinite patience in answering exhaustively all my doubts or questions.

I thank Eugenio, because I owe almost all of my practical skills in electron microscopy to him. I thank him for being - with kindness, friendliness, serenity, patience and professional experience - my point of reference in the research activity, always ready to deal with me when I needed.

I thank the volcanic prof. De Felice for having had the idea from which this ambitious project started, for having put in contact the other protagonists of this adventure, forming a new team, and, of course, for his skills put at the service of this thesis work. I thank Silvia for her exquisite helpfulness, and I am grateful to her for always showing empathy towards me and for helping me with his knowledge and professional experience. I thank the brilliant prof. Hayek, for the contagious passion and enthusiasm he put into this project. I thank all the colleagues of the Child Neuropsychiatry Unit of USL Umbria 2 in Terni, for carrying out the difficult task of recruiting and collecting the biological material essential for our research.

I thank Alessandro for his invaluable and very valid technical support. I thank David, for coming to meet me with his help (above all allowing me to use his computer), for all the opinions and advice. I thank them and all the colleagues of the "ground floor coffee", for the essential moments of pause and socializing. I thank my colleagues Mariangela, Ambra and Veronica for helping me with their skills and professional experience - when I needed clarification, advice or to observe in order to learn. I thank them, Dalia, Annalisa, Claudia and Domenico, for their support (*because it is known that the PhD course often requires it!)*. I also thank them for all the moments spent together – above all our unforgettable lunch breaks, based on sushi / Ravioli Wang (and not only). In particular, I thank Veronica also for having been, with her professional skill and innumerable human qualities, the best laboratory neighbor I could wish for, and also for having been a little bit like a mentor for me, from the first day of my internship with prof. Callaini up to now. In particular, I also thank Ambra, always sunny and full of energy, for making me feel welcomed and accepted from the first day of this journey.

It was amazing to have shared with her my everyday life of a PhD student: without her everything would not have been the same. I also thank Mariadonata, Felice and Sara who worked on this project before me or with me, thus laying solid foundations for this thesis work.

I thank my family for always believing in me and trusting me, even when I wasn't able to do that. I am happy to have shared with them, even from a distance, literally every day of these years, making them participate in the addition of every piece of the puzzle. I thank my parents for their teachings transmitted since I was a child, thanks to which I was able to develop the qualities that allowed me to complete this path. There are no words to thank them for all the opportunities they gave me, and also for never making me feel alone, bearing my every *sclero* and bad moment. Moreover, I thank in particular my brother Vincenzo, with his acute intelligence and concreteness, and my sister Giulia, with her wisdom and joviality, for always being there when I needed it.

Thanks to my grandfather and my extended family for their affection, for making me feel the warmth and the joy of being together every time I "came down" in these years. In particular, I thank Francesca, with her generosity and sensitivity, for having always been by my side over these years, even when I “seemed unachievable”. In particular, I also thank my aunt Maria for her sincere and constant interest in me, for often offering to me her help with generosity and openness.

I thank Serena for giving me the opportunity to experience the beauty of a true friendship with a wonderful person as she is. Although, more than a friend, she is a sister to me. With her, the joy from achieving all the small goals in this path was doubled, the sadness due to the moments of discouragement halved. I could tell her my every little failure, feeling that her esteem for me stayed unchanged and this was priceless. I thank her for making me feel, even in those cases, always welcomed and understood and never judged. I carry with me her wise advice and our loud laughter.

I thank Giulia for having been with me from the beginning of our university career until now. I am happy to have reached important academic goals together with her. Her coming back to Siena a year ago was pure oxygen for me and I am grateful to her for always including me in her group. I thank her and Giuliana for always making me feel *at home away from home*; I am happy to have reasoned together on important choices regarding our future, and to share heart troubles and joy. I thank - albeit late - them, Clara, Veronica and Elena for having been awesome friends in university life, always together shoulder to shoulder (from university lessons to exams, from sports to dinners and outings on Saturday nights, up to celebrations of the great goals). Although each of us has now taken its own path, these memories are imprinted in my mind and heart.

I thank all my friends in Salerno for the moments of leisure and fun spent together with my every return to homeland. I thank in particular the two Fede, Chiara and Sara for being my friends of all time. It was a joy to have celebrated birthdays and graduations together, to have spent together Easter

Mondays, Christmas' Eves, New Years, Halloweens and innumerable pizzas. I am also grateful to them for having faced and overcome together less happy moments in recent years, strengthening our bond. It has been great to grow up together and I hope we will always continue to do so.

Finally, I thank the Rotary Club Rotary Club Chianciano, Chiusi, Montepulciano, Rotary Club Valdelsa, Kiwanis Club Siena for choosing to finance part of this project. Their contribution was fundamental.

6. BIBLIOGRAPHY

- Abruzzo, P.M., Ghezzo, A., Bolotta, A., Ferreri, C., Minguzzi, R., Vignini, A., Visconti, P., Marini, M., 2015. Perspective biological markers for autism spectrum disorders: advantages of the use of receiver operating characteristic curves in evaluating marker sensitivity and specificity. Dis. Markers 2015. https://doi.org/10.1155/2015/329607
- Adollah, R., Mashor, M.Y., Mohd Nasir, N.F., Rosline, H., Mahsin, H., Adilah, H., 2008. Blood cell image segmentation: a review, in: Abu Osman, N.A., Ibrahim, F., Wan Abas, W.A.B., Abdul Rahman, H.S., Ting, H.-N. (Eds.), 4th Kuala Lumpur International Conference on Biomedical Engineering 2008, IFMBE Proceedings. Springer Berlin Heidelberg, Berlin, Heidelberg, pp. 141–144. https://doi.org/10.1007/978-3-540-69139-6_39
- Agrawal, P., Verma, P., 2015. Automated detection and counting of red blood cell using image processing techniques. Int. J. Sci. Res. Manag. 3, 2692–2695.
- Albertini, M.C., Teodori, L., Piatti, E., Piacentini, M.P., Accorsi, A., Rocchi, M.B.L., 2003. Automated analysis of morphometric parameters for accurate definition of erythrocyte cell shape. Cytom. PartA J. Int. Soc. Anal. Cytol. 52, 12–18. https://doi.org/10.1002/cyto.a.10019
- Ali, J., Ahmad, A., George, L.E., Der, C.S., Aziz, S., 2013. Red blood cell recognition using geometrical features. Int. J. Comput. Sci. Issues 10, 90–94.
- Allalou, A., Wählby, C., 2009. BlobFinder, a tool for fluorescence microscopy image cytometry. Comput. Methods Programs Biomed. 94, 58–65. https://doi.org/10.1016/j.cmpb.2008.08.006
- Antonelou, M.H., Kriebardis, A.G., Velentzas, A.D., Kokkalis, A.C., Georgakopoulou, S.-C., Papassideri, I.S., 2011. Oxidative stress-associated shape transformation and membrane proteome remodeling in erythrocytes of end stage renal disease patients on hemodialysis. J. Proteomics 74, 2441–2452. https://doi.org/10.1016/j.jprot.2011.04.009
- Arganda-Carreras, I., Legland, D., 2014. Classic Watershed (IJPB-plugins).
- Babitha, R., Gunasekaran, R., 2016. Impact of waist circumference on red blood cells size in obese adults. Int. J. Res. Med. Sci. 4, 3449–3454. https://doi.org/10.18203/2320-6012.ijrms20162310
- Bacus, J.W., Belanger, M.G., Aggarwal, R.K., Trobaugh, F.E., 1976. Image processing for automated erythrocyte classification. J. Histochem. Cytochem. 24, 195–201. https://doi.org/10.1177/24.1.1254916
- Bala, S., Doegar, A., 2015. Automatic detection of sickle cell in red blood cell using watershed segmentation. Int. J. Adv. Res. Comput. Commun. Eng. 4, 488–491.

- Barducci, A., Pippi, I., 1999. Object recognition by edge analysis: a case study. Opt. Eng. 38, 284–294. https://doi.org/10.1117/1.602087
- Baron-Cohen, S., 2006. Two new theories of autism: hyper-systemising and assortative mating. Arch. Dis. Child. 91, 2–5. https://doi.org/10.1136/adc.2005.075846
- Berliner, S., Rogowski, O., Aharonov, S., Mardi, T., Tolshinsky, T., Rozenblat, M., Justo, D., Deutsch, V., Serov, J., Shapira, I., Zeltzer, D., 2005. Erythrocyte adhesiveness/aggregation: A novel biomarker for the detection of low-grade internal inflammation in individuals with atherothrombotic risk factors and proven vascular disease. Am. Heart J. 149, 260–267. https://doi.org/10.1016/j.ahj.2004.05.058
- Bessis, M., 1974. Corpuscles - Atlas of Red Blood Cell Shapes. Springer-Verlag, Berlin.
- Bessis, M., Weed, R.I., 1973. Living Blood Cells and their Ultrastructure. Springer-Verlag, Berlin, Heidelberg, New York.
- Bessis, M., Weed, R.I., Leblond, P.F. (Eds.), 1973. Red Cell Shape. Springer-Verlag, New York, Heidelberg, Berlin. https://doi.org/10.1007/978-3-642-88062-9
- Bester, J., Buys, A.V., Lipinski, B., Kell, D.B., Pretorius, E., 2013. High ferritin levels have major effects on the morphology of erythrocytes in Alzheimer's disease. Front. Aging Neurosci. 5. https://doi.org/10.3389/fnagi.2013.00088
- Bhowmick, S., Das, D.K., Maiti, A.K., Chakraborty, C., 2013. Structural and textural classification of erythrocytes in anaemic cases: A scanning electron microscopic study. Micron 44, 384–394. https://doi.org/10.1016/j.micron.2012.09.003
- Bhowmick, S., Das, D.K., Maiti, A.K., Chakraborty, C., 2012. Computer-aided aiagnosis of thalassemia using scanning electron microscopic images of peripheral blood: a morphological approach. J. Med. Imaging Health Inform. 2, 215–221. https://doi.org/10.1166/jmihi.2012.1092
- Bolotta, A., Battistelli, M., Falcieri, E., Ghezzo, A., Manara, M.C., Manfredini, S., Marini, M., Posar, A., Visconti, P., Abruzzo, P.M., 2018a. Oxidative stress in autistic children alters erythrocyte shape in the absence of quantitative protein alterations and of loss of membrane phospholipid asymmetry. Oxid. Med. Cell. Longev. 2018. https://doi.org/10.1155/2018/6430601
- Bolotta, A., Visconti, P., Fedrizzi, G., Ghezzo, A., Marini, M., Manunta, P., Messaggio, E., Posar, A., Vignini, A., Abruzzo, P.M., 2018b. Na+, K+-ATPase activity in children with autism spectrum disorder: Searching for the reason(s) of its decrease in blood cells. Autism Res. 11, 1388–1403. https://doi.org/10.1002/aur.2002
- Brecher, G., Bessis, M., 1972. Present status of spiculed red cells and their relationship to the discocyte-echinocyte transformation: A critical review. Blood 40, 333–344.

- Brett, D., Warnell, F., McConachie, H., Parr, J.R., 2016. Factors affecting age at ASD diagnosis in UK: no evidence that diagnosis age has decreased between 2004 and 2014. J. Autism Dev. Disord. 46, 1974–1984. https://doi.org/10.1007/s10803-016-2716-6
- Brian, J.A., Bryson, S.E., Zwaigenbaum, L., 2015. Autism spectrum disorder in infancy: developmental considerations in treatment targets. Curr. Opin. Neurol. 28, 117–123. https://doi.org/10.1097/WCO.0000000000000182
- Brunsting, A., Mullaney, P., 1972. Light scattering from coated spheres: model for biological cells. Appl. Opt. 11, 675–680.
- Buttarello, M., 2016. Analizzatori ematologici a flusso: basi tecnologiche, modalità di valutazione, qualità analitica e nuove informazioni. Biochim. Clin. 40, 180–194.
- Buys, A.V., Van Rooy, M.J., Soma, P., Van Papendorp, D., Lipinski, B., Pretorius, E., 2013. Changes in red blood cell membrane structure in type 2 diabetes: a scanning electron and atomic force microscopy study. Cardiovasc. Diabetol. 12, 1–7. https://doi.org/10.1186/1475-2840-12-25
- Carpenter, A.E., Jones, T.R., Lamprecht, M.R., Clarke, C., Kang, I.H., Friman, O., Guertin, D.A., Chang, J., Lindquist, R.A., Moffat, J., Golland, P., Sabatini, D.M., 2006. CellProfiler: image analysis software for identifying and quantifying cell phenotypes. Genome Biol. 7, 1–11. https://doi.org/10.1186/gb-2006-7-10-r100
- CellaVision® DM9600, n.d.
- Chandrasiri, S., Samarasinghe, P., 2014. Automatic anemia identification through morphological image processing, in: 7th International Conference on Information and Automation for Sustainability. Presented at the 2014 7th International Conference on Information and Automation for Sustainability (ICIAfS), IEEE, Colombo, Sri Lanka, pp. 1–5. https://doi.org/10.1109/ICIAFS.2014.7069561
- Ciccoli, L., De Felice, C., Paccagnini, E., Leoncini, S., Pecorelli, A., Signorini, C., Belmonte, G., Guerranti, R., Cortelazzo, A., Gentile, M., Zollo, G., Durand, T., Valacchi, G., Rossi, M., Hayek, J., 2013. Erythrocyte shape abnormalities, membrane oxidative damage, and β-actin alterations: an unrecognized triad in classical autism. Mediators Inflamm. 2013. https://doi.org/10.1155/2013/432616
- Ciccoli, L., De Felice, C., Paccagnini, E., Leoncini, S., Pecorelli, A., Signorini, C., Belmonte, G., Valacchi, G., Rossi, M., Hayek, J., 2012. Morphological changes and oxidative damage in Rett Syndrome erythrocytes. Biochim. Biophys. Acta BBA - Gen. Subj. 1820, 511–520. https://doi.org/10.1016/j.bbagen.2011.12.002
- Ciccoli, L., Signorini, C., Alessandrini, C., Ferrali, M., Comporti, M., 1994. Iron release, lipid

peroxidation, and morphological alterations of erythrocytes exposed to acrolein and phenylhydrazine. Exp. Mol. Pathol. 60, 108–118.

- Cortelazzo, A., Felice, C., Guerranti, R., Leoncini, R., Barducci, A., Leoncini, S., Signorini, C., Zollo, G., Pecorelli, A., Gagliardi, A., Armini, A., Paccagnini, E., Gentile, M., Bini, L., Durand, T., Galano, J.-M., Rossi, M., Ciccoli, L., Hayek, J., 2015. Erythrocyte cytoskeletal-plasma membrane protein network in rett syndrome: effects of ω-3 polyunsaturated fatty acids. Curr. Proteomics 12, 217–226. https://doi.org/10.2174/1570164612041601191535 11
- Criel, M., Godefroid, M., Deckers, B., Devos, H., Cauwelier, B., Emmerechts, J., 2016. Evaluation of the Red Blood Cell Advanced Software Application on the CellaVision DM96. Int. J. Lab. Hematol. 38, 366–374.
- Cruz, J.C.D., Garcia, R.G., Avilledo, M.I.D., Buera, J.C.M., Chan, R.V.S., Espana, P.G.T., 2019. Microscopic image analysis and counting of red blood cells and white blood cells in a urine sample, in: ICBET' 19. Presented at the 9th International Conference on Biomedical Engineering and Technology, Association for Computing Machinery (ACM) Press, Tokyo, Japan, pp. 113–118. https://doi.org/10.1145/3326172.3326185
- Dawson, G., 2008. Early behavioral intervention, brain plasticity, and the prevention of autism spectrum disorder. Dev. Psychopathol. 20, 775–803. https://doi.org/10.1017/S0954579408000370
- Deng, L., Yang, H., Meng, W., Chen, Y., Hu, G., Liu, H., 2018. Ultrastructural changes in red blood cells in aortic dissection patients under extracorporeal circulation: Atomic force microscopy study. Int. J. Artif. Organs 41, 452–459. https://doi.org/10.1177/0391398818784272
- Devi, S.S., Kumar, R., Laskar, R.H., 2015. Recent advances on erythrocyte image segmentation for biomedical applications, in: Das, K.N., Deep, K., Pant, M., Bansal, J.C., Nagar, A. (Eds.), Proceedings of Fourth International Conference on Soft Computing for Problem Solving, SocProS 2014. Springer India, New Delhi, pp. 353–359.
- Durant, T.J.S., Olson, E.M., Schulz, W.L., Torres, R., 2017. Very deep convolutional neural networks for morphologic classification of erythrocytes. Clin. Chem. 63, 1847–1855. https://doi.org/10.1373/clinchem.2017.276345
- Egelé, A., Stouten, K., van der Heul-Nieuwenhuijsen, L., de Bruin, L., Teuns, R., van Gelder, W., Riedl, J., 2016. Classification of several morphological red blood cell abnormalities by DM96 digital imaging. Int. J. Lab. Hematol. 38, e98–e101. https://doi.org/10.1111/ijlh.12530
- Estes, A., Munson, J., Rogers, S.J., Greenson, J., Winter, J., Dawson, G., 2015. Long-Term outcomes of early intervention in 6-year-old children with autism spectrum disorder. J. Am. Acad. Child Adolesc. Psychiatry 54, 580–587. https://doi.org/10.1016/j.jaac.2015.04.005

- Fang, Z., Jiang, C., Tang, J., He, M., Lin, X., Chen, X., Han, L., Zhang, Z., Feng, Y., Guo, Y., Li, H., Jiang, W., 2016. A comprehensive analysis of membrane and morphology of erythrocytes from patients with glucose-6-phosphate dehydrogenase deficiency. J. Struct. Biol. 194, 235–243. https://doi.org/10.1016/j.jsb.2015.10.015
- Ferreira, T., Rasband, W., 2012. ImageJ User Guide.
- Fessler, M.B., Rose, K., Zhang, Y., Jaramillo, R., Zeldin, D.C., 2013. Relationship between serum cholesterol and indices of erythrocytes and platelets in the US population. J. Lipid Res. 54, 3177–3188. https://doi.org/10.1194/jlr.P037614
- Ford, J., 2013. Red blood cell morphology. Int. J. Lab. Hematol. 35, 351–357.
- Fortunato, M., 2016. Ottimizzazione del protocollo di allestimento di campioni ematici per analisi morfologiche al microscopio elettronico a scansione finalizzate alla diagnosi precoce di autismo (Tesi di laurea magistrale in biologia sanitaria (LM-6)). Università di Siena.
- Fossum, K.L., Williams, L., Garon, N., Bryson, S.E., Smith, I.M., 2018. Pivotal response treatment for preschoolers with autism spectrum disorder: Defining a predictor profile. Autism Res. 11, 153–165. https://doi.org/10.1002/aur.1859
- Frustaci, A., Neri, M., Cesario, A., Adams, J.B., Domenici, E., Dalla Bernardina, B., Bonassi, S., 2012. Oxidative stress-related biomarkers in autism: systematic review and meta-analyses. Free Radic. Biol. Med. 52, 2128–2141. https://doi.org/10.1016/j.freeradbiomed.2012.03.011
- Gallagher, P.G., 2005. Red cell membrane disorders. ASH Educ. Program Book 2005, 13–18. https://doi.org/10.1182/asheducation-2005.1.13.
- Garnier, G.F.G., Manderson, C.A., Giri, S., Garnier, G., 2019. IdentiCyte: Simple red blood cell identification software. SoftwareX 9, 223–229. https://doi.org/10.1016/j.softx.2019.02.006
- Ghezzo, A., Visconti, P., Abruzzo, P.M., Bolotta, A., Ferreri, C., Gobbi, G., Malisardi, G., Manfredini, S., Marini, M., Nanetti, L., Pipitone, E., Raffaelli, F., Resca, F., Vignini, A., Mazzanti, L., 2013. Oxidative stress and erythrocyte membrane alterations in children with autism: correlation with clinical features. PLoS One 8, e66418. https://doi.org/10.1371/journal.pone.0066418
- Greenwalt, T.J., 2006. The how and why of exocytic vesicles. Transfusion (Paris) 46, 143–152. https://doi.org/10.1111/j.1537-2995.2006.00692.x
- Hegde, R.B., Prasad, K., Hebbar, H., Sandhya, I., 2018. Peripheral blood smear analysis using image processing approach for diagnostic purposes: A review. Biocybern. Biomed. Eng. 38, 467–480. https://doi.org/10.1016/j.bbe.2018.03.002
- HemaCAM®, n.d. . Fraunhofer Institute for Integrated Circuits IIS.
- Hematology Imaging System, 2014. Medica Corporation.

- Jasenovec, T., Radosinska, D., Celusakova, H., Filcikova, D., Babinska, K., Ostatnikova, D., Radosinska, J., 2019. Erythrocyte deformability in children with autism spectrum disorder: correlation with clinical features. Physiol. Res. 68, S307–S313. https://doi.org/10.33549/physiolres.934349
- Jones, T.R., Kang, I.H., Wheeler, D.B., Lindquist, R.A., Papallo, A., Sabatini, D.M., Golland, P., Carpenter, A.E., 2008. CellProfiler Analyst: data exploration and analysis software for complex image-based screens. BMC Bioinformatics 9, 1–16. https://doi.org/10.1186/1471-2105-9-482
- Kandasami, P., Srinath, S., Seshadri, S.P., Girimaji, S.C., Kommu, J.V.S., 2017. Lost time—Need for more awareness in early intervention of autism spectrum disorder. Asian J. Psychiatry 25, 13–15. https://doi.org/10.1016/j.ajp.2016.07.021
- Kasari, C., Gulsrud, A., Paparella, T., Hellemann, G., Berry, K., 2015. Randomized comparative efficacy study of parent-mediated interventions for toddlers with autism. J. Consult. Clin. Psychol. 83, 554. https://doi.org/10.1037/a0039080
- Kass, M., Witkin, A., Terzopoulos, D., 1988. Snakes: active contour models. Int. J. Comput. Vis. 1, 321–331. https://doi.org/10.1007/BF00133570
- Kaur, K., Chauhan, V., Gu, F., Chauhan, A., 2014. Bisphenol A induces oxidative stress and mitochondrial dysfunction in lymphoblasts from children with autism and unaffected siblings. Free Radic. Biol. Med. 76, 25–33. https://doi.org/10.1016/j.freeradbiomed.2014.07.030
- Khot, S., Prasad, R., 2012. Image analysis system for detection of red blood cell disorders using artificial neural network. Int. J. Eng. Res. 1, 1–14.
- Kim, K., Jeon, J., Choi, W., Kim, P., Ho, Y.-S., 2001. Automatic cell classification in human's peripheral blood images based on morphological image processing. Presented at the Australian Joint Conference on Artificial Intelligence, Springer, Berlin, Heidelberg, pp. 225–236.
- Kubitschek, H., 1960. Electronic measurement of particle size. Res. Lond. 13.
- Lim, G., Wortis, M., Mukhopadhyay, R., 2002. Stomatocyte-discocyte-echinocyte sequence of the human red blood cell: Evidence for the bilayer-couple hypothesis from membrane mechanics. Proc. Natl. Acad. Sci. 99, 16766–16769. https://doi.org/10.1073/pnas.202617299
- Lindeberg, T., 2011. Edge detection. Encycl. Math.
- Lord, C., Rutter, M., DiLavore, P.C., Risi, S., Luyster, R.J., Gotham, K., Bishop, S.L., Guthrie, W., 2012. Autism Diagnostic Observation Schedule - Second Edition. Western Psychological Services, Torrance, CA.
- Loyola-Leyva, A., Loyola-Rodríguez, J.P., Figueroa, Y.T., González, F.J., Atzori, M., Cervera, S.B., 2019. Altered erythrocyte morphology in Mexican adults with prediabetes and type 2 diabetes

mellitus evaluated by scanning electron microscope. Microscopy 68, 261–270. https://doi.org/10.1093/jmicro/dfz011

- Loyola-Leyva, A., Loyola-Rodríguez, J.P., Terán-Figueroa, Y., González, F.J., Atzori, M., Camacho-Lopez, S., 2020. Hypercholesterolemia associated with erythrocytes morphology assessed by scanning electron microscopy in metabolically unhealthy individuals with normal-weight and obesity. Obes. Med. 20. https://doi.org/10.1016/j.obmed.2020.100292
- Lucantoni, G., Pietraforte, D., Matarrese, P., Gambardella, L., Metere, A., Paone, G., Bianchi, E.L., Straface, E., 2006. The red blood cell as a biosensor for monitoring oxidative imbalance in chronic obstructive pulmonary disease: an ex vivo and in vitro study. Antioxid. Redox Signal. 8, 1171–1182. https://doi.org/10.1089/ars.2006.8.1171
- Maitra, M., Kumar Gupta, R., Mukherjee, M., 2012. Detection and counting of red blood cells in blood cell images using Hough transform. Int. J. Comput. Appl. 53, 18–22. https://doi.org/10.5120/8505-2274
- Malpica, N., de Solórzano, C.O., Vaquero, J.J., Santos, A., Vallcorba, I., García-Sagredo, J.M., del Pozo, F., 1997. Applying watershed algorithms to the segmentation of clustered nuclei. Cytom. J. Int. Soc. Anal. Cytol. 28, 289–297. https://doi.org/10.1002/(SICI)1097-0320(19970801)28:4<289::AID-CYTO3>3.0.CO;2-7
- Manzur-Jattin, F., Álvarez-Ortega, N., Moneriz-Pretell, C., Corrales-Santander, H., Cantillo-García, K., 2016. Eriptosis: mecanismos moleculares y su implicación en la enfermedad aterotrombótica. Rev. Colomb. Cardiol. 23, 218–226. https://doi.org/10.1016/j.rccar.2015.09.004
- Marzuki, N.I.B.C., bin Mahmood, N.H., bin Abdul Razak, M.A., 2017. Identification of thalassemia disorder using active contour. Indones. J. Electr. Eng. Comput. Sci. 6, 160–165. https://doi.org/10.11591/ijeecs.v6.i1.pp160-165
- Mazalan, S.M., Mahmood, N.H., Razak, M.A.A., 2013. Automated red blood cells counting in peripheral blood smear image using circular Hough transform. Presented at the 2013 1st International Conference on Artificial Intelligence, Modelling & Simulation (AIMS), IEEE, Kota Kinabalu, pp. 320–324. https://doi.org/10.1109/AIMS.2013.59
- McInerney, T., Terzopoulos, D., 2000. T-snakes: Topology adaptive snakes. Med. Image Anal. 4, 73–91. https://doi.org/10.1016/S1361-8415(00)00008-6
- MedCalc Software Ltd., 2021. . Ostend, Belgium.
- Mullaney, P., Dean, P., 1969. Cell sizing: a small-angle light-scattering for sizing particles of low relative refractive index. Appl. Opt. 8, 2361–2362.
- Nithyaa, A.N., Premkumar, R., Kanchana, D., Krishnan, N.A., 2013. Automated detection and

classification of blood diseases, in: Malathi, R., Krishnan, J. (Eds.), Recent Advancements in System Modelling Applications, Lecture Notes in Electrical Engineering. Springer India, India, pp. 393–404. https://doi.org/10.1007/978-81-322-1035-1_34

- Pallotta, V., Naro, F., Gevi, F., D'Alessandro, A., Zolla, L., 2014. Supplementation of anti-oxidants in leucofiltered erythrocyte concentrates: assessment of morphological changes through scanning electron microscopy. Blood Transfus. 12, 421–424. https://doi.org/10.2450/2014.0272-13
- Palmer, L., Briggs, C., McFadden, S., Zini, G., Burthem, J., Rozenberg, G., Proytcheva, M., Machin, S.J., 2015. ICSH recommendations for the standardization of nomenclature and grading of peripheral blood cell morphological features. Int. J. Lab. Hematol. 37, 287–303. https://doi.org/10.1111/ijlh.12327
- Park, J., Keller, J.M., 2001. Snakes on the watershed. IEEE Trans. Pattern Anal. Mach. Intell. 23, 1201–1205. https://doi.org/10.1109/34.954609
- Parletta, N., Niyonsenga, T., Duff, J., 2016. Omega-3 and omega-6 polyunsaturated fatty acid levels and correlations with symptoms in children with attention deficit hyperactivity disorder, autistic spectrum disorder and typically developing controls. PLoS One 11, e0156432. https://doi.org/10.1371/journal.pone.0156432
- Pianigiani, S., 2018. Sviluppo di un sistema informatico per il riconoscimento e la classificazione automatici di eritrociti umani in micrografie SEM (Tesi di laurea magistrale in biologia (LM-6)). Università degli Studi di Siena, Dipartimento di Scienze della Vita.
- Pierre, R.V., 2002. Red cell morphology and the peripheral blood film. Clin. Lab. Med. 22, 25–61. https://doi.org/10.1016/S0272-2712(03)00066-0
- Pretorius, E., Bester, J., Vermeulen, N., Alummoottil, S., Soma, P., Buys, A.V., Kell, D.B., 2015. Poorly controlled type 2 diabetes is accompanied by significant morphological and ultrastructural changes in both erythrocytes and in thrombin-generated fibrin: implications for diagnostics. Cardiovasc. Diabetol. 14, 1–20. https://doi.org/10.1186/s12933-015-0192-5
- Pretorius, E., Bester, J., Vermeulen, N., Lipinski, B., Gericke, G.S., Kell, D.B., 2014a. Profound morphological changes in the erythrocytes and fibrin networks of patients with hemochromatosis or with hyperferritinemia, and their normalization by iron chelators and other agents. PLoS One 9, e85271. https://doi.org/10.1371/journal.pone.0085271
- Pretorius, E., Kell, D.B., 2014. Diagnostic morphology: biophysical indicators for iron-driven inflammatory diseases. Integr Biol 6, 486–510. https://doi.org/10.1039/C4IB00025K
- Pretorius, E., Lipinski, B., 2013. Thromboembolic ischemic stroke changes red blood cell morphology. Cardiovasc. Pathol. 22, 241–242. https://doi.org/10.1016/j.carpath.2012.11.005

- Pretorius, E., Olumuyiwa-Akeredolu, O.O., Mbotwe, S., Bester, J., 2016. Erythrocytes and their role as health indicator: Using structure in a patient-orientated precision medicine approach. Blood Rev. 30, 263–274. https://doi.org/10.1016/j.blre.2016.01.001
- Pretorius, E., Swanepoel, A.C., Buys, A.V., Vermeulen, N., Duim, W., Kell, D.B., 2014b. Eryptosis as a marker of Parkinson's disease. Aging 6, 788–819. https://doi.org/10.18632/aging.100695
- Pretorius, E., Vermeulen, N., Bester, J., Lipinski, B., Kell, D.B., 2013. A novel method for assessing the role of iron and its functional chelation in fibrin fibril formation: the use of scanning electron microscopy. Toxicol. Mech. Methods 23, 352–359. https://doi.org/10.3109/15376516.2012.762082
- Radosinska, J., Vrbjar, N., 2016. The role of red blood cell deformability and Na,K-ATPase function in selected risk factors of cardiovascular diseases in humans: focus on hypertension, diabetes mellitus and hypercholesterolemia. Physiol. Res. S43–S54. https://doi.org/10.33549/physiolres.933402
- Rogowska, J., 2009. Overview and fundamentals of medical image segmentation, in: Bankman, I.N. (Ed.), Handbook of Medical Image Processing and Analysis. Academic Press, pp. 69–85.
- Rogowski, O., Berliner, S., Zeltser, D., Serov, J., Ben-Assayag, E., Justo, D., Rozenblat, M., Kessler, A., Deutsch, V., Zakuth, V., Shapira, I., 2005. The erythrosense as a real-time biomarker to reveal the presence of enhanced red blood cell aggregability in atherothrombosis. Am. J. Ther. 12, 286–292.
- Rose, S., Melnyk, S., Pavliv, O., Bai, S., Nick, T.G., Frye, R.E., James, S.J., 2012. Evidence of oxidative damage and inflammation associated with low glutathione redox status in the autism brain. Transl. Psychiatry 2, e134–e134. https://doi.org/10.1038/tp.2012.61
- Rossignol, D.A., Frye, R.E., 2012. A review of research trends in physiological abnormalities in autism spectrum disorders: immune dysregulation, inflammation, oxidative stress, mitochondrial dysfunction and environmental toxicant exposures. Mol. Psychiatry 17, 389–401. https://doi.org/10.1038/mp.2011.165
- Ruggeri, B., Sarkans, U., Schumann, G., Persico, A.M., 2014. Biomarkers in autism spectrum disorder: the old and the new. Psychopharmacology (Berl.) 231, 1201–1216. https://doi.org/10.1007/s00213-013-3290-7
- Russell, P., Batchelor, D., Thornton, J., 2001. SEM and AFM: complementary techniques for high resolution surface investigations. Veeco Metrol. Group.
- Salzman, G., Crowell, J., Martin, J., Trujillo, T., Romero, A., Mullaney, P., LaBauve, P., 1975. Cell classification by laser light scattering: identification and separation of unstained leukocytes. Acta Cytol. 19, 374–377.

- Schopler, E., Van Bourgondien, M., Wellman, G., Love, S., 2010. Childhood Autism Rating Scale, Second Edition. Western Psychological Services, Los Angeles, CA.
- Sharma, V., Rathore, A., Vyas, G., 2016. Detection of sickle cell anaemia and thalassaemia causing abnormalities in thin smear of human blood sample using image processing. Presented at the 2016 International Conference on Inventive Computation Technologies (ICICT), IEEE, Coimbatore, India, pp. 1–5. https://doi.org/10.1109/INVENTIVE.2016.7830136
- Shen, L., Zhao, Y., Zhang, H., Feng, C., Gao, Y., Zhao, D., Xia, S., Hong, Q., Iqbal, J., Liu, X.K., Yao, F., 2019. Advances in biomarker studies in autism spectrum disorders, in: Guest, P.C. (Ed.), Reviews on Biomarker Studies in Psychiatric and Neurodegenerative Disorders, Advances in Experimental Medicine and Biology. Springer International Publishing, Cham, pp. 207–233. https://doi.org/10.1007/978-3-030-05542-4_11
- Simpson, L.O., 1989. Blood from healthy animals and humans contains nondiscocytic erythrocytes. Br. J. Haematol. 73, 561–564. https://doi.org/10.1111/j.1365-2141.1989.tb00298.x
- Singer, K., Fisher, B., Perlstein, M., 1952. Acanthocytosis: a genetic erythrocyte malformation. Blood 7, 577.
- Swanepoel, A.C., Pretorius, E., 2012. Scanning electron microscopy analysis of erythrocytes in thromboembolic ischemic stroke. Int. J. Lab. Hematol. 34, 185–191. https://doi.org/10.1111/j.1751-553X.2011.01379.x
- Szeliski, R., 2020. Computer vision: algorithms and applications, Second. ed. Springer.
- Szeliski, R., 2010. Computer Vision: Algorithms and Applications. Springer.
- Tomari, R., Zakaria, W.N.W., Jamil, M.M.A., Nor, F.M., Fuad, N.F.N., 2014. Computer aided system for red blood cell classification in blood smear image. Procedia Comput. Sci. 42, 206–213. https://doi.org/10.1016/j.procs.2014.11.053
- Turchetti, V., Leoncini, F., Matteis, C.D., Trabalzini, L., Guerrini, M., Forconi, S., 1998. Evaluation of erythrocyte morphology as deformability index in patients suffering from vascular diseases, with or without diabetes mellitus: correlation with blood viscosity and intra-erythrocytic calcium. Clin. Hemorheol. Microcirc. 18, 141–149.
- Turchetti, V., Matteis, C.D., Leoncini, F., Trabalzini, L., Guerrini, M., Forconi, S., 1997. Variations of erythrocyte morphology in different pathologies. Clin. Hemorheol. Microcirc. 17, 209–215.
- Vargas, D.L., Nascimbene, C., Krishnan, C., Zimmerman, A.W., Pardo, C.A., 2005. Neuroglial activation and neuroinflammation in the brain of patients with autism. Ann. Neurol. Off. J. Am. Neurol. Assoc. Child Neurol. Soc. 57, 67–81. https://doi.org/10.1002/ana.20315
- Vision Hema® Assist - Automatic cell imaging system by West Medica, n.d. . MedicalExpo.

- Vromen, J., McCane, B., 2009. Red blood cell segmentation from SEM images. Presented at the 2009 24th International Conference Image and Vision Computing New Zealand (IVCNZ), IEEE, Wellington, New Zealand, pp. 44–49. https://doi.org/10.1109/IVCNZ.2009.5378364
- Wang, R., 2017. Curved surface feature extraction and texture analysis based on curvelet transform for red blood cell image. Presented at the 2nd International Conference on Artificial Intelligence: Techniques and Applications (AITA 2017), pp. 347–352. https://doi.org/10.12783/dtcse/aita2017/16042
- Wang, R., 2011. Red Blood Cell classification through shape feature extraction and PSO-CSVM classifier design. Presented at the 2011 7th International Conference on Advanced Information Management and Service (ICIPM), IEEE, Jeju, pp. 107–111.
- Wąsowicz, M., Grochowski, M., Kulka, M., Mikołajczyk, A., Ficek, M., Karpieńko, K., Cićkiewicz, M., 2017. Computed aided system for separation and classification of the abnormal erythrocytes in human blood. Presented at the The Second International Conference "Biophotonics-Riga 2017," International Society for Optics and Photonics, Riga, Latvia, p. 105920A. https://doi.org/10.1117/12.2297218
- Westerman, M.P., Bacus, J.W., 1983. Red Blood Cell morphology in sickle cell anemia as determined by image processing analysis: the relationship to painful crises. Am. J. Clin. Pathol. 79, 667–672. https://doi.org/10.1093/ajcp/79.6.667
- Yturralde, E.M., Bulseco-Damian, K., Geraldino, N., 2020. Comparison of digital image analysis and conventional microscopy in evaluating erythrocyte morphology in peripheral blood smears. Philipp. J. Pathol. 5, 10–18. https://doi.org/10.21141/PJP.2020.03
- Zarra, F., 2017. Implementazione di una metodica per il monitoraggio morfologico degli eritrociti a fini diagnostici. (Tesi di Laurea Triennale in Scienze Biologiche (L-13)). Università degli Studi di Siena, Dipartimento di Scienze della Vita.
- Zeiler, M.D., Fergus, R., 2014. Visualizing and understanding convolutional networks. Presented at the European conference on computer vision, Springer, Cham, pp. 818–833.
- Zheng, Q., Milthorpe, B.K., Jones, A.S., 2004. Direct neural network application for automated cell recognition. Cytom. PartA J. Int. Soc. Anal. Cytol. 57A, 1–9. https://doi.org/10.1002/cyto.a.10106

7. SUPPLEMENTRY MATERIAL

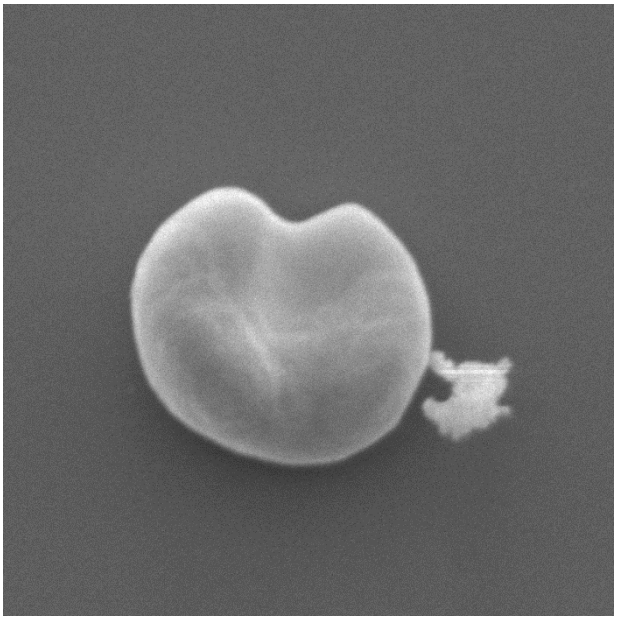

Supplementary figure 1 - Bite cell: RBC with a peripheral arcuate defect (bite).

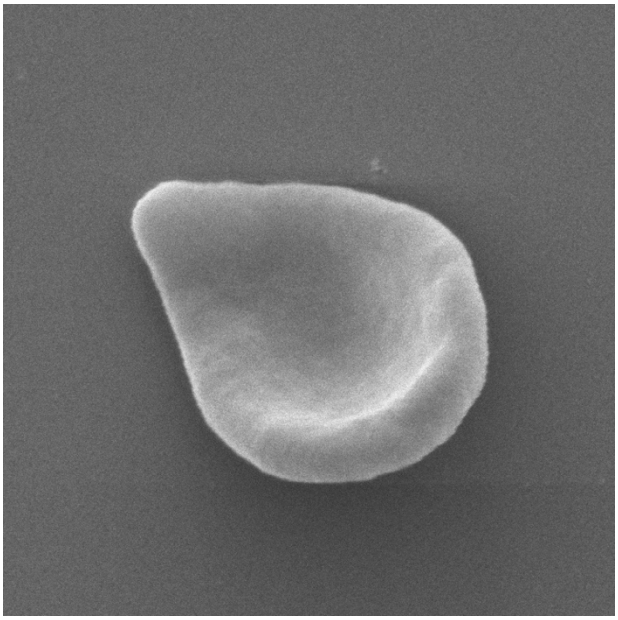

Supplementary figure 2 - Dacryocyte: erythrocyte with a single spicule, wide and tapered, which gives the cell the shape of a drop.

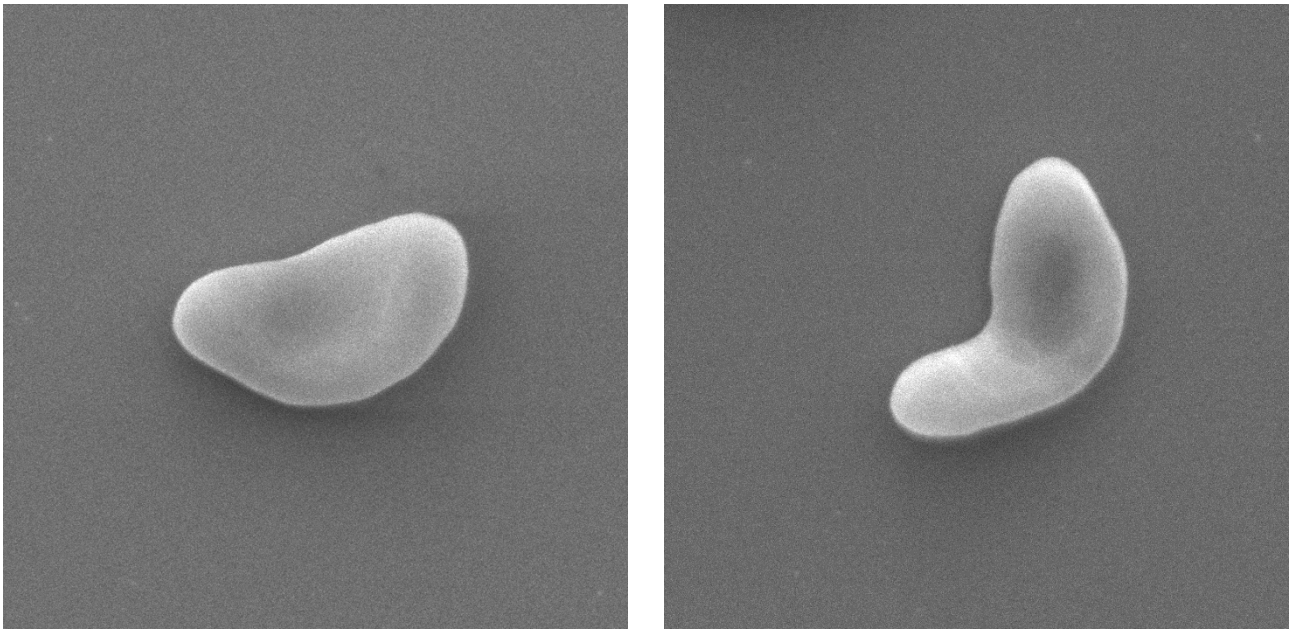

Supplementary figure 3 - Schistocytes: fragments of red blood cells.

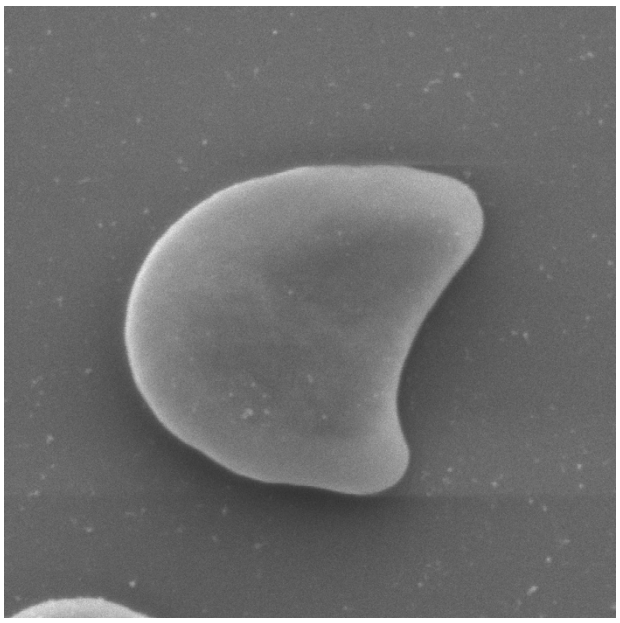

Supplementary figure 4 – Helmet-shaped red blood cell.

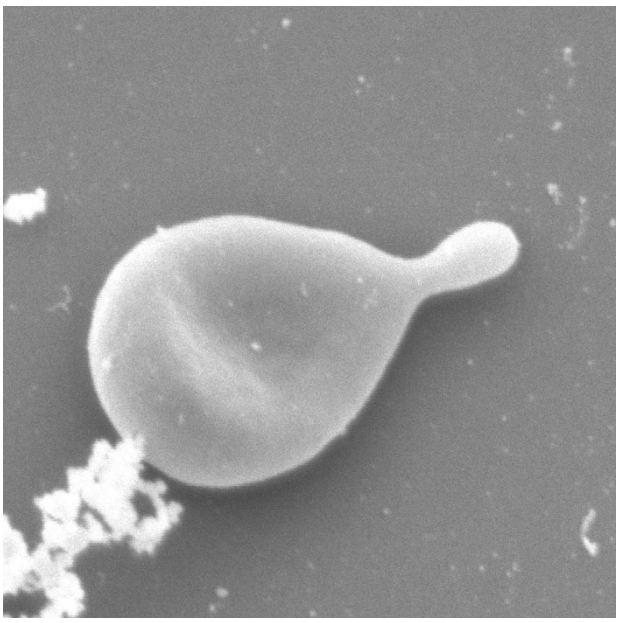

Supplementary figure 5 – Filamentous red blood cell.

# sample	echinocytes I	echinocytes II	echinocytes III	acanthocytes	spherocytes	sphero-stomatocytes	stomatocytes	leptocytes
1	0.10	0.00	0.00	0.00	0.29	0.10	0.00	0.00
	0.90	0.00	0.00	0.00	0.30	0.20	0.60	0.10
	0.60	0.00	0.00	0.00	1.69	0.00	0.60	0.00
2	0.10	0.00	0.00	0.00	9.65	2.29	1.79	0.00
	0.10	0.00	0.00	0.00	15.45	1.00	1.20	0.30
	0.20	0.00	0.00	0.00	12.48	1.60	2.10	0.00
3	0.40	0.00	0.00	0.10	2.79	0.90	0.50	0.00
	0.69	0.00	0.00	0.00	5.80	0.20	0.49	0.00
	0.30	0.00	0.00	0.10	3.66	0.20	0.99	0.10

# sample	knizocytes	target cells	elliptocytes	microcytes	macrocytes	other anomalies	total abnormal morphotypes	discocytes
1	2.94	0.00	2.16	0.59	0.00	2.85	9.03	90.97
	2.60	0.10	3.00	0.50	0.20	3.40	11.89	88.11
	3.58	0.30	3.28	0.80	0.10	2.59	13.53	86.47
2	17.61	0.20	1.79	1.29	0.00	6.27	41.00	59.00
	15.25	0.10	0.50	0.00	0.00	10.37	44.27	55.73
	17.47	0.70	0.80	0.10	0.00	7.49	42.91	57.09
3	8.28	0.60	6.79	1.70	0.00	5.89	27.94	72.06
	11.50	3.64	3.05	0.20	0.00	6.78	32.35	67.65
	11.29	3.56	4.06	0.59	0.00	7.62	32.48	67.52

Supplementary Table 1 - Triplicate measurements of RBC morphological analysis at SEM on 3 different blood samples as assessed by the same operator. Values are in percent. These data were used to gauge intra-assay variability.

#	total erythrocytes	echinocytes I	echinocytes I %	echinocytes II	echinocytes II %	echinocytes III	echinocytes III %	spherocytes	spherocytes %
1	1005	1	0.1	0	0.00	0	0.00	2	0.20
2	1008	0	0.00	0	0.00	0	0.00	1	0.10
3	1000	0	0.00	1	0.10	1	0.10	2	0.20
4	1008	9	0.89	1	0.10	0	0.00	0	0.00
5	1032	2	0.19	0	0.00	0	0.00	3	0.29
6	1019	0	0.00	0	0.00	0	0.00	1	0.10
7	1007	16	1.59	1	0.10	0	0.00	1	0.10
Average			**0.40**		**0.04**		**0.01**		**0.14**

#	stomatocytes	stomatocytes %	leptocytes	leptocytes %	knizocytes	knizocytes %	target cells	target cells %	elliptocytes
1	4	0.40	0	0.00	15	1.49	1	0.10	24
2	0	0.00	2	0.20	8	0.79	2	0.20	21
3	7	0.70	1	0.10	12	1.20	0	0.00	45
4	0	0.00	0	0.00	3	0.30	5	0.50	26
5	1	0.10	0	0.00	1	0.10	0	0.00	16
6	4	0.39	0	0.00	2	0.20	0	0.00	15
7	17	1.69	0	0.00	6	0.60	0	0.00	22
Average		**0.47**		**0.04**		**0.67**		**0.11**	

#	elliptocytes %	microcytes	microcytes %	other anomalies	other anomalies %	totale abnormal morphotypes	total abnormal morphotypes %	discocytes	discocytes %
1	2.39	3	0.30	0	0.00	50	**4.98**	955	95.02
2	2.08	1	0.10	0	0.00	35	**3.47**	973	96.53
3	4.50	1	0.10	0	0.00	70	**7.00**	930	93.00
4	2.58	2	0.20	0	0.00	46	**4.56**	962	95.44
5	1.55	1	0.10	0	0.00	24	**2.33**	1008	97.67
6	1.47	1	0.10	0	0.00	23	**2.26**	996	97.74
7	2.18	0	0.00	0	0.00	64	**6.36**	943	93.64
Average	**2.39**		**0.13**		**0.00**		**4.42**		**95.58**

Supplementary Table 2 - SEM morphological analysis of 7 blood samples from healthy volunteers enrolled for the pilot study.

#	total erythrocytes	echinocytes I	echinocytes I %	echinocytes II	echinocytes II %	echinocytes III	echinocytes III %	spherocytes	spherocytes %
1	1001	43	4.30	4	0.40	3	0.30	3	0.30
2	1020	41	4.02	2	0.20	1	0.10	0	0
3	1023	20	1.96	10	0.98	2	0.20	0	0.00
4	1070	45	4.21	2	0.19	3	0.28	1	0.09
5	1020	103	10.10	17	1.67	0	0.00	2	0.20
6	883	40	4.53	7	0.79	0	0.00	4	0.45
7	1039	18	1.73	3	0.29	1	0.10	4	0.38
8	1013	34	3.36	5	0.49	0	0.00	1	0.10
9	1017	43	4.23	10	0.98	0	0.00	4	0.39
10	1017	9	0.88	1	0.10	1	0.10	5	0.49
11	1387	112	9.02	27	2.22	11	0.89	8	0.69
12	1002	51	5.09	1	0.10	0	0.00	5	0.50
13	1006	100	9.94	2	0.20	6	0.60	14	1.39
14	1006	8	0.80	0	0.00	0	0.00	1	0.10
15	1020	2	0.20	0	0.00	0	0.00	1	0.10
Average	%		**4.29**		**0.57**		**0.17**		**0.35**

#	stomatocytes	stomatocytes %	leptocytes	leptocytes %	knizocytes	knizocytes %	target cells	target cells %	elliptocytes
1	0	0.00	2	0.20	9	0.90	24	2.40	22
2	0	0.00	0	0.00	0	0.00	13	1.27	11
3	0	0.00	0	0.00	1	0.10	37	3.62	2
4	0	0.00	0	0.00	1	0.09	32	2.99	5
5	0	0.00	0	0.00	0	0.00	7	0.69	32
6	0	0.00	2	0.23	1	0.11	18	2.04	11
7	0	0.00	2	0.19	3	0.29	16	1.54	18
8	8	0.79	5	0.49	13	1.28	44	4.34	14
9	1	0.10	1	0.10	1	0.10	6	0.59	48
10	0	0.00	2	0.20	2	0.20	32	3.15	5
11	9	0.64	2	0.11	4	0.24	52	3.72	34
12	0	0.00	2	0.20	9	0.90	31	3.09	20
13	3	0.30	52	5.17	33	3.28	89	8.85	18
14	0	0.00	2	0.20	6	0.60	16	1.59	28
15	2	0.20	0	0.00	5	0.49	6	0.59	3
Average		**0.13**		**0.47**		**0.57**		**2.70**	

#	elliptocytes %	microcytes	microcytes %	other anomalies	other anomalies %	total abnormal morphotypes	total abnormal morphotypes %	discocytes	discocytes %
1	2.20	0	0.00	0	0.00	114	**11.39**	887	88.61
2	1.08	0	0.00	0	0.00	69	**6.76**	951	93.24
3	0.20	3	0.29	1	0.10	76	**7.43**	947	92.57
4	0.47	0	0.00	0	0.00	89	**8.32**	981	91.68
5	3.14	2	0.20	4	0.39	167	**16.37**	853	83.63
6	1.25	8	0.91	0	0.00	91	**10.31**	792	89.69
7	1.73	1	0.10	2	0.19	68	**6.54**	971	93.46
8	1.38	4	0.39	0	0.00	128	**12.64**	885	87.36
9	4.72	2	0.20	4	0.39	120	**11.80**	897	88.20
10	0.49	0	0.00	0	0.00	57	**5.60**	960	94.40
11	2.50	6	0.38	4	0.26	267	**20.67**	1120	79.33
12	2.00	0	0.00	0	0.00	119	**11.88**	883	88.12
13	1.79	0	0.00	0	0.00	317	**31.51**	689	68.49
14	2.78	0	0.00	1	0.10	62	**6.16**	944	93.84
15	0.29	0	0.00	8	0.39	27	**2.65**	993	97.35
Average	**1.73**		**0.16**		**0.12**		**11.34**		**88.66**

Supplementary Table 3 - SEM morphological analysis of 15 blood samples from ASD patients enrolled for the pilot study.

#	total erythrocytes	echinocytes I	echinocytes I %	echinocytes II	echinocytes II %	echinocytes III	echinocytes III %	acanthocytes	acanthocytes %	spherocytes	spherocytes %
1	1002	7	0.70	0	0.00	0	0.00	0	0.00	29	2.89
2	1003	0	0.00	1	0.10	0	0.00	0	0.00	9	0.90
3	1019	1	0.10	0	0.00	0	0.00	0	0.00	3	0.29
4	1008	0	0.00	0	0.00	0	0.00	0	0.00	6	0.60
Average	**%**		**0.20**		**0.03**		**0.00**		**0.00**		**1.17**

#	sphero-stomatocytes	sphero-stomatocytes %	stomatocytes	stomatocytes %	leptocytes	leptocytes %	knizocytes	knizocytes %	target cells	target cells %	elliptocytes
1	0	0.00	2	0.20	0	0.00	3	0.30	12	1.20	14
2	1	0.10	0	0.00	0	0.00	2	0.20	18	1.79	9
3	1	0.10	0	0.00	0	0.00	30	2.94	0	0.00	22
4	2	0.20	0	0.00	0	0.00	3	0.30	11	1.09	1
Average		**0.10**		**0.05**		**0.00**		**0.94**		**1.02**	

#	elliptocytes %	microcytes	microcytes %	macrocytes	macrocytes %	other anomalies	other anomalies %	total abnormal morphotypes	total abnormal morphotypes %	discocytes	discocytes %
1	1.40	5	0.50	2	0.20	9	0.90	83	**8.28**	919	91.72
2	0.90	1	0.10	1	0.10	6	0.60	48	**4.79**	955	95.21
3	2.16	6	0.59	0	0.00	29	2.85	92	**9.03**	927	90.97
4	0.10	3	0.30	1	0.10	13	1.29	40	**3.97**	968	96.03
Average	**1.14**		**0.37**		**0.10**		**1.41**		**6.52**		**93.48**

Supplementary Table 4 - SEM morphological analysis of 4 healthy volunteers' blood samples prepared through the optimized protocol.

#	total erythrocytes	echinocytes I	echinocytes I %	echinocytes II	echinocytes II %	echinocytes III	echinocytes III %	acanthocytes	acanthocytes %	spherocytes	spherocytes %
1	1001	0	0.00	0	0.00	0	0.00	0	0.00	579	57.84
2	1002	0	0.00	0	0.00	0	0.00	1	0.10	100	9.98
3	1002	0	0.00	0	0.00	0	0.00	0	0.00	264	26.35
4	1001	0	0.00	0	0.00	0	0.00	0	0.00	349	34.87
5	1003	1	0.10	0	0.00	0	0.00	0	0.00	398	39.68
6	1000	0	0.00	0	0.00	0	0.00	0	0.00	455	45.50
7	1005	1	0.10	0	0.00	0	0.00	0	0.00	236	23.48
Average			**0.03**		**0.00**		**0.00**		**0.01**		**33.96**

#	sphero-stomatocytes	sphero-stomatocytes %	stomatocytes	stomatocytes %	leptocytes	leptocytes %	knizocytes	knizocytes %	target cells	target cells %	elliptocytes
1	4	0.40	10	1.00	0	0.00	6	0.60	0	0.00	5
2	33	3.29	18	1.80	0	0.00	33	3.29	17	1.70	2
3	38	3.79	9	0.90	0	0.00	78	7.78	3	0.30	3
4	27	2.70	61	6.09	0	0.00	108	10.79	0	0.00	3
5	35	3.49	43	4.29	5	0.50	77	7.68	1	0.10	25
6	17	1.70	16	1.60	3	0.30	35	3.50	0	0.00	12
7	45	4.48	19	1.89	13	1.29	80	7.96	8	0.80	13
Average		**2.84**		**2.51**		**0.30**		**5.94**		**0.41**	

#	elliptocytes %	microcytes	microcytes %	macrocytes	macrocytes %	other anomalies	other anomalies %	total abnormal morphotypes	total abnormal morphotypes %	discocytes	discocytes %
1	0.50	2	0.20	0	0.00	14	1.40	620	**61.94**	381	38.06
2	0.20	4	0.40	1	0.10	40	3.99	249	**24.85**	753	75.15
3	0.30	5	0.50	0	0.00	86	8.58	486	**48.50**	516	51.50
4	0.30	0	0.00	1	0.10	190	18.98	739	**73.83**	262	26.17
5	2.49	0	0.00	2	0.20	41	4.09	628	**62.61**	375	37.39
6	1.20	1	0.10	0	0.00	15	1.50	554	**55.40**	446	44.60
7	1.29	0	0.00	3	0.30	42	4.18	460	**45.77**	545	54.23
Average	**0.90**		**0.17**		**0.10**		**6.10**		**53.27**		**46.73**

Supplementary Table 5 - SEM morphological analysis of the first 7 blood samples from ASD patients enrolled for the clinical study.

#	total erythrocytes	echinocytes I	echinocytes I %	echinocytes II	echinocytes II %	echinocytes III	echinocytes III %	acanthocytes	acanthocytes %	spherocytes	spherocytes %
1	1001	0	0.00	0	0.00	0	0.00	0	0.00	101	**10.09**
2	1001	0	0.00	0	0.00	0	0.00	0	0.00	279	**27.87**
3	1024	1	0.10	0	0.00	0	0.00	0	0.00	89	**8.69**
Average			**0.03**		**0.00**		**0.00**		**0.00**		**15.55**

#	sphero-stomatocytes	sphero-stomatocytes %	stomatocytes	stomatocytes %	leptocytes	leptocytes %	knizocytes	knizocytes %	target cells	target cells %	elliptocytes
1	7	0.00	0	0.70	0	0.00	9	0.90	4	0.40	14
2	0	0.00	2	0.20	0	0.00	14	1.40	3	0.30	13
3	6	0.59	2	0.20	0	0.00	13	1.27	2	0.20	43
Average		**0.20**		**0.37**		**0.00**		**1.19**		**0.30**	

#	elliptocytes %	microcytes	microcytes %	macrocytes	macrocytes %	other anomalies	other anomalies %	total abnormal morphotypes	total abnormal morphotypes %	discocytes	discocytes %
1	1.40	6	0.60	3	0.30	8	0.80	152	15.18	849	84.82
2	1.30	2	0.20	3	0.30	9	0.90	325	32.47	676	67.53
3	4.20	1	0.10	2	0.20	20	1.95	179	17.48	845	82.52
Average	**2.30**		**0.30**		**0.27**		**1.22**		**21.71**		**78.29**

Supplementary Table 6 - SEM morphological analysis of 3 blood samples from healthy volunteers to check effects of the anticoagulant solution on the amount of spherocytes.

total erythrocytes	echinocytes I	echinocytes I %	echinocytes II	echinocytes II %	echinocytes III	echinocytes III %	acanthocytes	acanthocytes %	spherocytes	spherocytes %
1017	0	0.00	0	0.00	0	0.00	0	0.00	233	**22.91**

sphero-stomatocytes	sphero-stomatocytes %	stomatocytes	stomatocytes %	leptocytes	leptocytes %	knizocytes	knizocytes %	target cells	target cells %	elliptocytes
0	0.00	6	0.59	2	0.20	31	3.05	7	0.69	10

elliptocytes %	microcytes	microcytes %	macrocytes	macrocytes %	other anomalies	other anomalies %	total abnormal morphotypes	total abnormal morphotypes %	discocytes	discocytes %
0.98	3	0.29	1	0.10	15	1.47	308	30.29	709	69.71

Supplementary Table 7 - SEM morphological analysis of one blood samples from healthy volunteer to check effects of the anticoagulant solution from the same stock used for the first 7 pathological samples of the clinical study on the amount of spherocytes.

total erythrocytes	echinocytes I	echinocytes I %	echinocytes II	echinocytes II %	echinocytes III	echinocytes III %	acanthocytes	acanthocytes %	spherocytes	spherocytes %
922	3	0.33	1	0.11	0	0.00	0	0.00	14	**1.52**

sphero-stomatocytes	sphero-stomatocytes %	stomatocytes	stomatocytes %	leptocytes	leptocytes %	knizocytes	knizocytes %	target cells	target cells %	elliptocytes
0	0.00	0	0.00	0	0.00	5	0.54	26	2.82	10

elliptocytes %	microcytes	microcytes %	macrocytes	macrocytes %	other anomalies	other anomalies %	total abnormal morphotypes	total abnormal morphotypes %	discocytes	discocytes %
1.08	1	0.11	1	0.11	6	0.65	67	7.27	855	92.73

Supplementary Table 8 - SEM morphological analysis of one blood samples from healthy volunteer to check effects of the re-prepared anticoagulant solution on the amount of spherocytes.

#	total erythrocytes	echinocytes I	echinocytes I %	echinocytes II	echinocytes II %	echinocytes III	echinocytes III %	acanthocytes	acanthocytes %	spherocytes	spherocytes %
8	1002	4	0.40	0	0.00	0	0.00	0	0.00	4	0.40
9	1005	12	1.19	0	0.00	0	0.00	0	0.00	22	2.19
10	1002	4	0.40	0	0.00	0	0.00	1	0.10	28	2.79
11	1001	0	0.00	0	0.00	0	0.00	0	0.00	85	8.49
12	1005	1	0.10	0	0.00	0	0.00	0	0.00	97	9.65
Average	**%**		**0.42**		**0.00**		**0.00**		**0.02**		**4.70**

#	sphero-stomatocytes	sphero-stomatocytes %	stomatocytes	stomatocytes %	leptocytes	leptocytes %	knizocytes	knizocytes %	target cells	target cells %	elliptocytes
8	2	0.20	3	0.30	0	0.00	2	0.20	14	1.40	12
9	8	0.80	6	0.60	0	0.00	7	0.70	10	1.00	13
10	9	0.90	5	0.50	0	0.00	83	8.28	6	0.60	68
11	2	0.20	6	0.60	0	0.00	24	2.40	29	2.90	17
12	23	2.29	18	1.79	0	0.00	177	17.61	2	0.20	18
Average		**0.88**		**0.76**		**0.00**		**5.84**		**1.22**	

#	elliptocytes %	microcytes	microcytes %	macrocytes	macrocytes %	other anomalies	other anomalies %	total abnormal morphotypes	total abnormal morphotypes %	discocytes	discocytes %
8	1.20	10	1.00	1	0.10	14	1.40	66	**6.59**	936	93.41
9	1.29	17	1.69	0	0.00	28	2.79	123	**12.24**	882	87.76
10	6.79	17	1.70	0	0.00	59	5.89	280	**27.94**	722	72.06
11	1.70	25	2.50	0	0.00	32	3.20	220	**21.98**	781	78.02
12	1.79	13	1.29	0	0.00	63	6.27	412	**41.00**	593	59.00
Average	**2.55**		**1.64**		**0.02**		**3.91**		**21.95**		**78.05**

Supplementary Table 9 - SEM morphological analysis of the last 5 blood samples from ASD patients enrolled for the clinical study.

# sample	# image	manually counted	automatically detected	correctly detected	incorrectly detected (false positives)	not detected (false negatives)
1	35	2071	1425	1379	46	582
2	49	1760	1313	1229	84	403
3	29	893	572	565	7	321
4	20	1033	629	586	43	404
5	75	1851	1417	1366	51	417
6	34	1532	903	896	7	629
7	29	1038	910	898	12	128
8	32	1743	1135	1092	43	608
9	24	833	510	494	16	223
10	53	777	741	711	30	49
10	**380**	**13531**	**9555**	**9216**	**339**	**3764**

Supplementary Table 10 - Results of the overall processing of SEM images for the evaluation of erythrocyte detection by the software. The table shows the data for each sample in terms of the number of images analyzed, the number of erythrocytes manually counted, the number of erythrocytes automatically detected, the number of erythrocytes correctly detected, the number of erythrocytes incorrectly detected (false positives), and the number of not detected erythrocytes (false negatives). In the last row are reported their relative sums for the total of images analyzed for all the 10 samples.